Ultrafast Electron Dynamics at Alkali/Ice Structures Adsorbed on a Metal Surface

Im Fachbereich Physik
der Freien Universität Berlin
eingereichte Dissertation

Michael Meyer

October 2011

This work was done between August 2007 and October 2011 in the group of Professor Martin Wolf at the Physics Department of the Freie Universität Berlin and the Department of Physical Chemistry at the Fritz-Haber-Institut der Max-Planck-Gesellschaft.

Berlin, October 2011

Erstgutachter: Prof. Dr. Martin Wolf

Zweitgutachter: Prof. Dr. Martin Weinelt

Datum der Disputation: 30.11.2011

Abstract

The goal of this work is to study the interaction between excess electrons in water ice structures adsorbed on metal surfaces and other charged or neutral species, like alkali ions, or chemically reactive molecules, like chlorofluorocarbons (CFC), respectively. The excess electrons in the ice can interact with the ions directly or indirectly via the hydrogen bonded water molecules. In both cases the presence of the alkali influences the population, localization, and lifetime of electronic states of excess electrons in the ice adlayer. These properties are of great relevance when considering the highly reactive character of the excess electrons, which can mediate chemical reactions by dissociative electron attachment (DEA).

The influence of alkali adsorption on electron solvation and transfer dynamics in ice structures is investigated for two types of adsorption configurations using femtosecond time-resolved two-photon photoelectron spectroscopy. In the first system alkali atoms are coadsorbed on top of a wetting amorphous ice film adsorbed on Cu(111). At temperatures between 60 and 100 K alkali adsorption leads to the formation of positively charged alkali ions at the ice/vacuum interface. The interaction between the alkali ions at the surface and the dipole moments of the surrounding water molecules results in a reorientation of the water molecules. As a consequence new electron trapping sites, *i.e.* at local potential minima, are formed. Photoinjection of excess electrons into these alkali-ion covered amorphous ice layers, results in the trapping of a solvated electron at an alkali-ion/water complex. In contrast to solvation in pure amorphous ice films, where the electrons are located in the bulk of the ice layer, solvated electrons at alkali-ion/water complexes are located at the ice/vacuum interface. They exhibit lifetimes of several picoseconds and show a fast energetic stabilization. With ongoing solvation, *i.e.* pump-probe time delay, the electron transfer is mediated by tunneling through a potential barrier which is determined by the thickness of the ice layer.

In the second system electron solvation at small alkali/water clusters directly prepared at the metal substrate is investigated. In these experiments the average number of water molecules in such a cluster can be controlled so that the population and stabilization dynamics of excess electrons can be investigated as a function of D_2O coverage. Two main effects are observed: (i) the alkalis are solvated by a reorientation of the surrounding solvent molecules in the cluster; and (ii) above a critical number of water molecules per alkali excess electrons can localize at the clusters where they are energetically stabilized. This critical ratio depends on the type of alkali and is inversely proportional to the alkali-induced dipole moment.

Finally, it is demonstrated that trapped electrons in crystalline ice adsorbed on Ru(001) can very efficiently mediate chemical reactions *via* dissociative electron attachment. When electronegative molecules like $CFCl_3$ are coadsorbed with crystalline ice a DEA process between trapped electrons and $CFCl_3$ molecules occurs, resulting in the formation of $\cdot CFCl_2$ radicals and Cl^- anions. These results suggest that photoexcited trapped electrons can play an important role in heterogeneous chemical processes on ice surfaces and could thus be relevant in the polar stratosphere chemistry.

Kurzfassung

Das Ziel dieser Arbeit ist es, die Wechselwirkung zwischen Überschusselektronen und anderen geladenen oder neutralen Spezies wie Alkaliionen, oder chemisch reaktive Moleküle wie Fluorchlorkohlenwasserstoffe (FCKW), in D_2O Eis auf Metalloberflächen zu untersuchen. Die Überschusselektronen im Eis können mit den Ionen direkt oder indirekt über die Wassermoleküle interagieren. In beiden Fällen führen die Ionen zu einer Beeinflussung der Populationsdynamik und des Lokalisierungsorts der Überschusselektronen in der Eisadsorbatschicht. Diese Eigenschaften sind von großer Bedeutung, da diese Elektronen sehr effizient chemische Reaktionen durch dissoziative Elektronenanlagerung (DEA) vermitteln können.

Der Einfluss der Adsorption von Alkaliatomen auf die Elektronentransfer- und Solvatisierungsdynamik an den D_2O/Cu(111)-Grenzflächen ist für zwei verschiedene Adsorptionskonfigurationen mit Hilfe zeitaufgelöster Zwei-Photonen Photoemissionsspektroskopie untersucht worden. Im ersten experimentellen Ansatz werden die Alkaliatome auf eine geschlossene amorphe Eisschicht adsorbiert, was im Temperaturbereich zwischen 60 und 100 K zur Bildung von positiv geladenen Alkaliionen an der Eis-Vakuum-Grenzfläche führt. Die Wechselwirkung zwischen den Ionen an der Eisoberfläche und den Dipolmomenten der umgebenden Wassermoleküle führt zu einer Umorientierung der Wassermoleküle, so dass neue Bindungsstellen bzw. Potentialminima entstehen, die das Anlagern von photoangeregten Überschusselektronen an die Alkaliionen-Wasser-Komplexe ermöglichen. Im Gegensatz zur Solvatisierung in reinem amorphen Eis, in dem die Elektronen im Volumen der Eisschicht gebunden sind, befinden sich die solvatisierten Elektronen an den Alkaliionen-Wasser-Komplexen an der Eisoberfläche. Sie weisen Lebensdauern von mehreren Pikosekunden auf und zeigen eine schnelle energetische Stabilisierung. Mit fortlaufender Solvatisierung wird der Elektronentransfer zurück zum Metall durch das Tunneln durch eine Potentialbarriere bestimmt, deren Dicke durch die Dicke der Eisschicht gegeben ist.

Im zweiten experimentellen Ansatz wird die Elektronensolvatisierung an kleinen Alkaliatom-Wasser-Clustern untersucht, die direkt an der Metalloberfläche präpariert werden. Das macht es in diesen Experimenten möglich, die mittlere Zahl der Wassermoleküle in einem solchen Cluster einzustellen, und so die Populations- und Stabilisierungsdynamik der Überschusselektronen als Funktion der Wasserbedeckung zu untersuchen. Zwei wesentliche Effekte werden beobachtet: (i) die Alkaliionen werden durch eine Umorientierung der umgebenden Wassermoleküle solvatisiert, und (ii) oberhalb einer kritischen Anzahl von Wassermolekülen pro Alkaliatom können Überschusselektronen an den Cluster gebunden werden. Dieses Verhältnis ist umgekehrt proportional zu dem Dipolmoment, welches das Alkaliatom induziert.

Ferner wird gezeigt, dass Überschusselektronen in kristallinem Eis auf Ru(001) sehr effizient chemische Reaktionen durch DEA-Prozesse anregen können. So können $CFCl_3$ Moleküle, die auf der kristallinen Eisschicht adsorbiert sind, nach Anlagerung eines in der Eisschicht eingefangenen Elektrons zu $\cdot CFCl_2$ Radikalen und Cl^- Ionen dissoziieren. Dieses Ergebnis legt nahe, dass diese Elektronen eine wichtige Rolle in heterogenen chemischen Prozessen auf Eisoberflächen in der Stratosphärenchemie spielen können.

Contents

List of Figures

List of Tables

1 Introduction

Interactions of electrons with matter lead to a huge variety of physical and chemical processes that are of fundamental relevance in physics, chemistry, and biology. When an electron is injected into a polar molecular medium the solvent molecules will react in such a way that the energy of the system is minimized. This process is known as solvation. Additional reaction pathways are opened when the solvent molecules are in contact with a metal or semi-conductor substrate so that electron transfer through interfaces can occur. This so-called heterogenous electron transfer (HET) is of vital importance in technologically relevant fields such as organic optoelectronics and nanoscale molecular devices [Zhu04]. The situation becomes more complex when the solvent media is not homogenous anymore but contains other charged or neutral species or reactive molecules. In the latter case excess electrons in the polar environment can be attached to reactive molecules at the solvent/vacuum interface such as chlorofluorocarbons (CFC) and lead to their dissociation by dissociative electron attachment (DEA) [Lu10]. As these different aspects of electron solvation and charge transfer play an important role in this thesis the concepts of (i) electron solvation, (ii) heterogenous electron transfer and excess electron dynamics in thin adlayers, and (iii) interactions between excess electrons and coadsorbed charged or neutral species will be briefly introduced.

The first observation related to solvated electrons however was made for liquid ammonia already in 1808, where after the addition of potassium a blue color of the liquid was observed [Dav08]. Later, this observation was attributed to light absorption by excess electrons in the solution, which are surrounded by a cavity formed by NH_3 molecules [Kra08]. Excess charges in polar media are screened by reorientation of the surrounding molecular dipoles. This process leads to a localization and energetic stabilization of the charge. Generally, the most important solvent is water, where electron solvation has been extensively studied for excess electrons in liquid water [Lon90, Sil98, Emd98, Lae00] and gas phase cluster[Bra04, Ver05b, Tur05a]. Solvation can as well occur for other charged species in polar solvents like alkali or halogen ions, see for example [Hen02].

More recently electron solvation has been studied for ultrathin ice films or clusters condensed on single crystal metal substrates [Stä08a]. This surface science approach yields several advantages compared to studies in the liquid or the gas phase. The samples are prepared under ultra high vacuum (UHV) conditions, which allows for a precise and reproducible preparation and a systematic characterization of the adlayers. In addition, the structure of the prepared layers can be modified in a controlled way by variation of the preparation conditions, *e.g.* sample temperature, coverage, or adsorption of impurity atoms/molecules, in order to investigate the influence of the structure on the electron dynamics at the metal/adsorbate interface. Furthermore, the excess electrons are generated in the metal substrate from where they are injected into the molecular adlayer, whereas they are generated by photoexcitation of the solvent molecules in the case of liquids or gas phase cluster. The generated photo hole is screened in the metal so that it does not interact with the excited electron. The excitation of electrons in the substrate yields the advantage that the electron dynamics can be observed without the presence of dissociated water molecules. Indeed, electron solvation dynamics in thin adlayers are a model system for HET because the coupling strength between the donor and the acceptor state, which is determining the transfer rate, is transiently changing. It has been shown that solvated electrons in thin ice layers on a metal surface subsequently localize, leading to an increasing confinement of their wave function, and accordingly to a reduction of the back transfer rate to the metal substrate [Gah02, Bov03]. Hence, the study of electron solvation dynamics at ice/metal interfaces allows the investigation of HET as a function of coupling strength.

So far only homogenous solvent adlayers have been discussed. However, especially the presence of additional charged species such as alkali ions can strongly influence the properties of excess electrons in the polar solvent. Screening effects of the alkali ions (Na^+, K^+, Cs^+) are expected to influence the population, localization, and lifetime of electronic states of excess electrons. In order to discriminate between spectroscopic signatures of electron and/or ion solvation occurring in the presence of positively charged alkali ions and solvated electrons that occur in pure water it is a prerequisite to know the contribution of the latter one, which has been studied before [Stä08a].

In the case of stratospheric or atmospheric chemistry the alkali ions can play a significant role. It is known that heterogeneous reactions on the surface of icy particles in stratosphere strongly participate in the chemistry involving pollutants [Rav97, Gar98]. In addition, excess electrons in ice are expected to actively participate in the reactivity of water ice surfaces under ionizing radiation in the stratosphere. Especially their role in the depletion of the ozone layer is controversially discussed [Lu10, Gro11]. The highly reactive character of these species has been demonstrated in the case of CFCs deposited on amorphous or crystalline water films, where the dissociation of surface CFC is triggered in an efficient way by excess electrons in the ice during electron [Lu99a, Lu01b] or UV photon irradiation [Ryu06]. The photoinjection of excess electrons from an electron donor into polar molecular ice and their subsequent dynamics of localization and lifetime are therefore fundamental steps for the understanding of the interactions between ionizing particles and ices of polar molecules.

In the framework of the thesis time- and angle-resolved two-photon photoelectron (2PPE) spectroscopy has been performed to investigate the electron dynamics in ice structures adsorbed on metal surfaces especially in the presence of positively charged alkali ions. 2PPE is a pump-probe technique that brings many advantages compared to optical spectroscopy besides its surface sensitivity. It allows for the investigation of occupied and also of unoccupied electronic states below the vacuum level of the sample. Furthermore, absolute binding energies and absolute energetic positions of electronic states with respect to the Fermi level of the metal substrate can be determined knowing the employed photon energies of pump- and probe pulse. In addition, the parallel momentum of the photoemitted electrons can be measured by performing angle-resolved

2PPE measurements, yielding information on the degree of localization of the electronic wave function of the excess electrons.

This work focuses on the interaction between excess electrons in ice structures adsorbed on metal surfaces and coadsorbed alkali atoms/ions or CFC molecules. In chapter 2 an overview of electron solvation in liquid water (section 2.1) and at water ice/metal interfaces (section 2.2) is given. Here previous work done in the group of Prof. M. Wolf on electron solvation in amorphous ice on Cu(111) (section 2.2.1) and electron trapping in crystalline ice on Ru(001) (section 2.2.2) is summarized. Possible chemical reactions of alkali ions and CFC molecules with water molecules or excess electrons in the polar environment are discussed in the next two sections. The succeeding sections introduce the properties of the metal substrates and the adsorbates investigated. In chapter 3 the major experimental technique, time-resolved 2PPE spectroscopy, and the experimental setup, laser system and UHV system, is introduced. Finally, experimental details on the sample preparation and characterization are given in section 3.4.

The experimental results on electron-transfer and -solvation dynamics at alkali/ice structures adsorbed on Cu(111) are presented in chapters 4 and 5. First, it is shown that coadsorption of sub-monolayer alkali coverages (<0.15 ML) on top of a wetting amorphous ice layer leads to pronounced changes in the dynamics of excess electrons. For alkali adsorption temperatures between 60 and 100 K the autoionization of the alkali atoms leads to positively charged ions at the ice/vacuum interface, which results in the appearance of a new species of solvated electrons at alkali-ion/water cluster at the ice surface. Compared to solvated electrons in pure ice, these electrons exhibit much longer residence times of several picoseconds in the polar layer. The charge transfer of these electrons back to the metal substrate is mediated by tunneling through a potential barrier formed by the ice film, as revealed by ice thickness-dependent measurements. For alkali adsorption temperatures below 60 K the autoionization is hindered and the highest occupied molecular orbital of the alkali atom in the ice environment is observed (section 4.2). The experiments presented in chapter 5 show that alkali atoms which are directly adsorbed on the metal surface can be hydrated by subsequently deposited water molecules that preferentially bind to the alkali sites. In addition, following the transient change of the electronic structure as a function of water coverage reveals interesting changes as the water coverage increases. Most notably, a new electronic state appears, which is attributed to excess electrons at the alkali-water-cluster that are stabilized by the response of the polar environment. Finally, an example for the ability of excess electrons in polar adlayers to trigger chemical reactions is given in section 6. Here, it is shown that trapped electrons in crystalline ice, which present an extraordinary long lifetime on the order of minutes and are located at the ice/vacuum interface, can induce the dissociation of a CFC molecule, *via* a dissociative electron attachment, resulting in the formation of Cl^- anions at the ice surface.

2 Investigated Systems and Processes

This chapter presents fundamental concepts on which this thesis on electron solvation in alkali/ice structures is based.
In the first part of this chapter in section 2.1 the focus of the discussion lies on electron solvation in polar molecular environments, and especially on molecular layers adsorbed on a metal surfaces in section 2.2. Here an overview of the electron transfer and solvation dynamics in amorphous and crystalline ice structures is given. The following section discusses the ability of such solvated or trapped electrons to drive chemical reactions on ice surfaces. Photoinduced processes driven by optically excited electrons are closely related to processes which are driven by primary low-energy electrons and they actively participate to the photo-reactivity of water ice surfaces. In section 2.2.4 an overview of the standard of knowledge of the influence of positively charged ions, *e.g.* alkali ions, on the properties of such doped water ice-surfaces and the possible effects on their chemical reactivity is presented.

In the second part the electronic properties of the metal substrates Cu(111) and Ru(001) (section 2.3) as well as the elementary properties of the adsorbate water are introduced(section 2.4). They are of fundamental interest as the metal substrates serve as an electron donor and acceptor in the presented experiments, *i.e.* in the electron injection process into the molecular layer and the decay of the population of excited states, respectively. Besides the bulk electronic structure of the substrate the surface electronic structure and the image potential is of special interest in photoemission experiments. These properties are as well addressed in section 2.3.

Finally, the excited states of chemisorbed alkali atoms on a metal surface are introduced in section 2.5. Due to a partial charge transfer from the alkali species to the substrate an unoccupied resonance evolves. Such systems in the presence of water have been investigated in the framework of this thesis.

2.1 Electron Solvation in Water

When an excess electron is added to a polar environment the electric field of the charge will interact with the dipole moments of the solvent molecules. This interaction leads to a reorientation of the polar molecules and an energetically stabilization of the charge, a process which is called electron solvation. Although more than 200 years have passed since the first reported observation of solvated electrons recognized by the blue color of liquid ammonia containing contaminations [Dav08] the nature of excess electrons is still of continuing interest and a complete understanding is not settled, yet [1]. 50 years ago solvated electrons [2] have also been observed for the first time in liquid water [Har62].

The generation of excess charges in water can occur via different pathways. A direct photoexcitation of the solvent molecules lead to its ionization. In the condensed phase, water ice can be seen as a large band-gap insulator [Guo02]. Its ionization requires overcoming its ionization potential of 8 eV, *via* a single- or a multi-photon process. Another way to provide excess charges is to add them to the system by adding electron donor atoms or molecules (*e.g.* alkali atoms). However, the presence of charged molecules or ions can influence the electron solvation dynamics as will be reported in this work for alkali ions in water ice (see chapter 4). Finally, low-kinetic energy electrons generated by UV irradiation can also be directly captured by the water network.

A simple but very successful model to describe the optical properties of solvated electrons in water is the so called Kevan or cavity model [Kev81, Lud04, Mar10]. Like depicted in the upper right panel of Fig.2.1 the electron is surrounded by spherical cavity formed by six octrahedrally distributed water molecules. One of the H-atoms of every molecule surrounding the electron is pointing towards the solvated electron forming the first solvation shell with a radius of roughly 4 Å in equilibrium [Zha06b]. However, alternative models for the structure of solvated electrons have also been proposed. Based on DFT calculations Zhan *et al.* also proposed a cavity containing six water molecules [Zha03]. But in contrast to the Kevan model the electron forms two strong electron-hydrogen bonds of the $e^-\cdots$H-O type with the hydrogen-bonded water cluster and two of the hydrogen bonds in the neutral water cluster are broken. In another alternative model description the solvation occurs via the formation of a solvent anion complex [Mar99]. Recently, these cavity models have been challenged by molecular dynamic simulations using rigorously derived pseudopotential [Lar10]. Instead of residing in a cavity *Larsen et al.* found that the hydrated electron is occupying a region of enhanced water density with a diameter of $\sim$ 1 nm.

Either residing in a cavity or in a region with higher water density the optical adsorption spectrum of solvated electrons can be modeled with a good quantitative agreement to experimental spectra. The absorption has a maximum at 1.725 eV and is rather broad (0.84 eV) [Zha06b] as shown in the lower right panel of Fig. 2.1. The absorption spectrum is dominated by the transition of the solvated electron from its

---

[1] One hundred years later this observation has been explained by the absorption of excess electrons residing in a cavity formed by ammonia molecules [Kra08].

[2] Solvated electrons are also referred to us hydrated or ammoniated electrons when they are solved in water or ammonia, respectively.

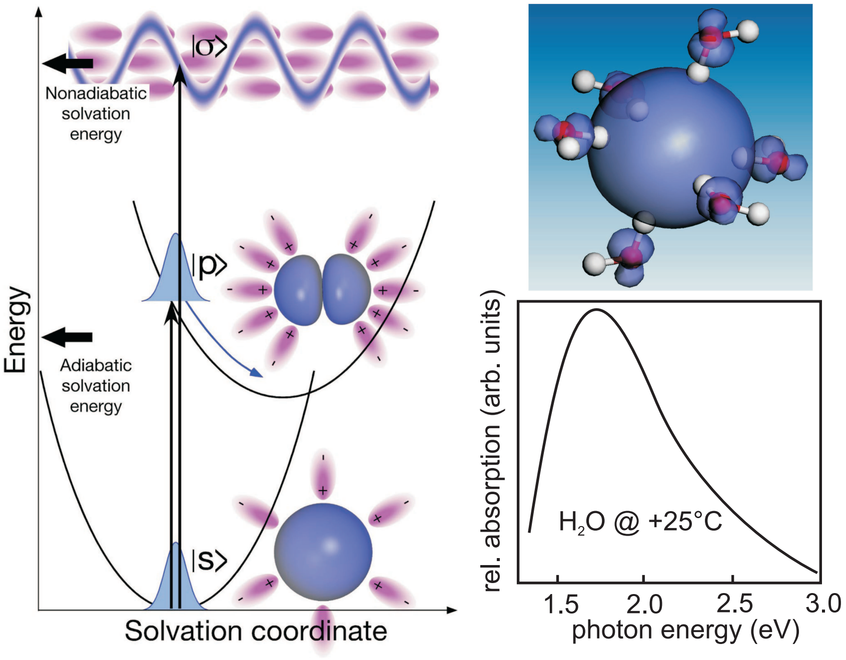

Figure 2.1: Left: energy diagram of the solvation and electronic excitation of excess electrons in water. The electron can be excited from its ground state to a p-like state and to a higher lying delocalized conduction band (adopted from [Zha06b]). Upper Right: Kevan model of the solvated electron. (adopted from [Zha06b]) Lower Left: optical absorption spectrum of liquid water (modified from [Sch68]).

s-like electronic ground state to the p-like first three excited states (see left panel of Fig.2.1). The absorption of photons with energies above 3.1 eV leads to the population of the delocalized conduction band in liquid water [Ass99, Son01]. Furthermore, the optical excitation leads to a displacement along the inertial solvation coordinate. As a consequence the relaxation occurs to vibrationally excited levels, involving H_2O libration, resulting in a broadening of the spectrum [Bal99]. Besides the structure of the solvated electron in liquid water also the interpretation of its relaxation dynamics is a field of ongoing interest and controversy. The vertical transition from the s-like ground state to the p-like excited states happens on a faster timescale then the surrounding water molecules can relax to their new equilibrium position after the transition. By measuring the transient adsorption spectrum three distinct timescales can be observed. However, the interpretation of these three decay processes is not unambiguous. *Barbara et al.* attribute the initial changes in the transmission spectra to librational motion[3] of

---

[3] A librational motion is a hindered rotation of the molecules. As in water every water molecule interacts with its neighboring molecules by hydrogen bonds it has a preferred orientation and can

the solvent molecules on a ~ 35-80 fs time scale, as it presents a strong isotope effect by substituting hydrogen with deuterium atoms [Yok98]. This process is followed by a nonadiabatic internal conversion to the ground state on the 200-300 fs time scale. In the last step the long-time relaxation of the s-like ground state takes place on a 1 ps time scale. In the interpretation of Larsen and coworkers the relaxation pathway involves first a rapid internal conservation followed by slow ground state cooling [Lar10], which is in contradiction to the mechanism discussed above.

Great effort has been invested in the investigation of the solvation dynamics of electrons in water anion clusters. Such $(H_2O)_n{}^-$ clusters of defined size n are frequently used to study electron solvation dynamics in finite systems [Ver05b] [4]. For a long time the binding energy of the hydrated electron couldn't be determined directly in bulk water. Hence, it is often derived from the extrapolation of the vertical binding energy (VBE)[5] of $(H_2O)_n{}^-$ clusters to infinite cluster size [Coe90]. It was found that the VBE depends linear on $n^{-\frac{1}{3}}$ [Ver05b]. A comparison of experimental binding energies as a function of the size of the cluster n is presented in Fig.2.2. Furthermore, it is still controversially discussed in theory and experiment whether the excess electron resides in the bulk or at the surface of these clusters or both [Bar88, Bar93, Pai04, Ver05b, Tur05a, Ver05a, Tur05b, Coe06]. Up to now there is no agreement between experiment and theory in how far the transition from a surface to an interior solvation site depends on the cluster size and on its structure [Fri08, Tur05a, Ver05b]. Neumark and coworkers found in their photoelectron spectra from $(H_2O)_n{}^-$ clusters three different isomers with different VDEs as depicted in

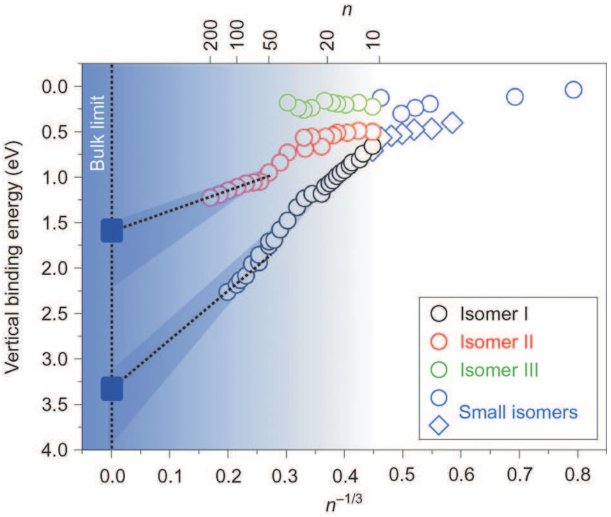

Figure 2.2: Experimental VBEs of hydrated electrons in $(H_2O)_n{}^-$ clusters of various sizes. Adopted from [Sie10].

---

therefor not freely rotate.

[4] n stands for the number of water molecules in the anionic cluster.

[5] In literature on hydrated electrons in anionic water clusters the synonym vertical detachment energy (VDE) is frequently used.

Fig.2.2 [Ver05b, Kam06]. Isomer I clusters are believed to contain solvated electrons which are bound at interior sites, whereas isomers II and III are attributed to surface bound electrons.

Recently, Siefermann *et al.* have performed photoelectron spectroscopy measurements on liquid water jets [Sie10]. They state that they can now unequivocally prove the existence of solvated electrons bound at the water surface and in bulk water, with VBE of 1.6 eV and 3.3 eV, respectively (see Fig.2.2). Extrapolating the VDEs for the three different cluster isomers mentioned above indeed show that the data for isomer I converge to the VBE measured for the bulk solvated electrons and that the VDEs for isomers II and III converge to the VBE of the state of the electron at the liquid surface.

In this last section an overview of electron solvation in liquid water and anionic waters clusters of different sizes has been given. The very active research and the controversial discussions in the last years prove that electron solvation processes are still of great interest as justified by the relevance of charge solvation in various fields ranging from biology to atmospheric chemistry. The focus in the following section lies on electron solvation dynamics at water ice-metal interfaces and previous works on this subject.

2.2 Electron Solvation at Water Ice/Metal Interfaces

Electron solvation occurs both in polar liquids or clusters as well as in the condensed phase of polar solvents adsorbed on a metal- or semiconductor surface. The electron transfer and solvation dynamics of different solvents such like water [Gah02, Bov03, Stä08a] alcohol [Li06], nitrils [Ge00, Szy05], and ammonia layers [Stä08b] at various metal and semiconductor interfaces [Zha06a, Zha06b] have been studied extensively. In contrast to the electron solvation studies in liquids or clusters the presence of an interface offers another possibility for the generation of an excess charge. By photoexcitation of electron-hole (e-h) pairs in the substrate electrons can be injected in the molecular adlayer. In this scheme the substrate serves as the chromophore and electron source and the solvation dynamics of the excess electron can be observed without the influence of electron-donating atoms or ions. The understanding of the pure electron solvation dynamics is the fundamental prerequisite to investigate the the influence of positively charged ions on the electron dynamics of these systems. In the following section the current understanding of electron solvation dynamics in water ice will be discussed. As will be shown later, the dynamics depend strongly on the morphology of the ice films. Therefore, the first part of this section concentrates on the ultrafast dynamics in amorphous ice on Cu(111), whereas the second part focuses on the considerable slower dynamics of crystalline ice on Ru(001).

2.2.1 Electron Solvation Dynamics in Amorphous Ice on Cu(111)

The ultrafast electron dynamics at ice-metal interfaces are characterized by four elementary steps. The initial photoexcitation of electrons in the metal substrate is followed by charge injection into the adsorbate layer. Consecutively, the electron localizes at preexisting potential minima where an energetic stabilization occurs. Finally, the electron decay back to unoccupied metal states with a finite probability. In the following these steps will be introduced in detail. A representative data set of a time-resolved two-photon photoemission (2PPE) measurement of a 4 bilayer (BL) thick amorphous D_2O layer [6]is shown in Fig.2.3.a. The 2PPE intensity is plotted in a false color representation as a function of energy with respect to the Fermi level of the Cu(111) substrate (left axis) and as a function of pump-probe time delay (bottom axis). The spectra exhibit two distinct features, a broad continuum e_{CB} around zero time delay and at $E - E_F = 2.9$ eV a distinct peak e_S that is shifting to lower energies with increasing time delay. As can be directly seen from the spectrum in 2.3, the intensity of both spectral signatures decreases with increasing time delay. Whereas e_{CB} decays within the duration of the laser pulses the long-living feature e_S can be observed for several hundred fs. Time-and angle resolved photoemission data is presented in Fig.2.3. It was shown before by angle-dependent 2PPE that the continuum e_{CB} (solid markers in Fig.2.3b)) exhibits a quasi-free electron like dispersion with an effective mass equal

---

[6] Details on the preparation of ice layers and 2PPE is given in chapter 3.

to the free electron mass $m_{eff} = 1.0(2) \cdot m_e$ [Bov03]. The dispersion indicates the delocalized character of this band. The peak e_S (open symbols) shifts to lower energies with time delay and shows an apparently negative dispersion[7] which becomes stronger with increasing time delay. This behavior suggests that the electron wave function of this state becomes progressively localized.

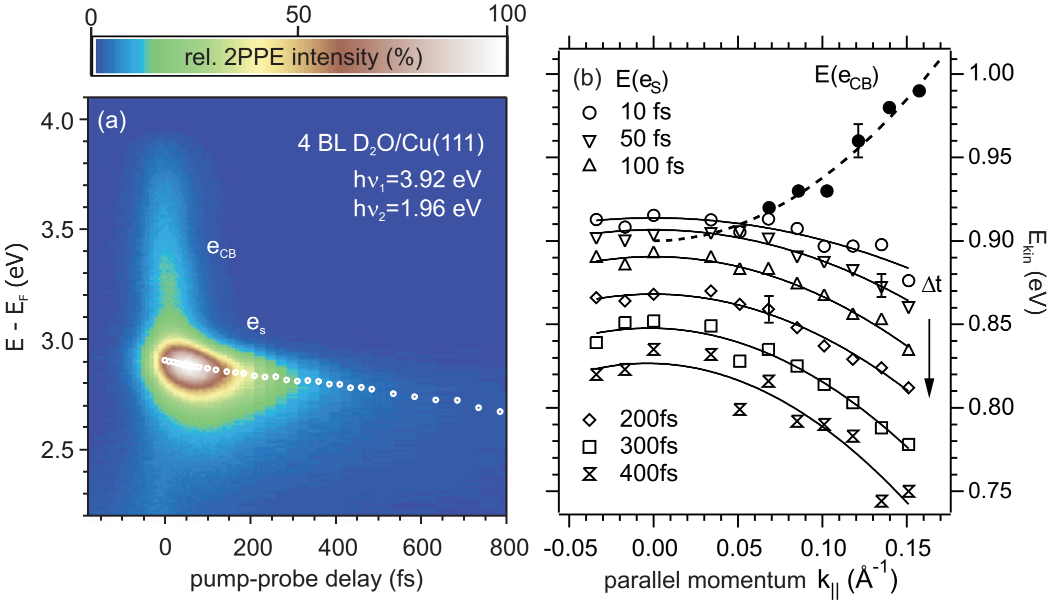

Figure 2.3: Angle- and time-resolved 2PPE spectra of amorphous D_2O on Cu(111). (a): 2D false color representation of the 2PPE intensity as a function of pump-probe delay and the intermediate state energy with respect to the Fermi level. The white circles mark the peak maximum of the spectral distribution of the solvated electrons e_S. (b): Angle- and time-resolved 2PPE of D_2O/Cu(111): dispersion of the conduction band e_{CB} (solid markers) and solvated electrons e_S for different time delay Δt (open symbols). Modified from [Bov03]

On the basis of the presented time- and angle-resolved 2PPE experiments on amorphous D_2O on Cu(111), the underlying fundamental processes of charge transfer, localization, energetic stabilization and electron back transfer will be discussed. Fig.2.4 presents a schematic representation of these elementary steps.

(1) In a first step photo absorption in the metal substrate leads to generation of e-h pairs. As a consequence of the wide band gap of ice of 8.2 eV [Shi77], which

---

[7] The apparently negative dispersion of e_S is a result of the finite bandwidth, $\Delta k_{\|}$, of the interfacial electrons in momentum space and the experimental fact that the spectra are taken at a specific angle and not a specific $\Delta k_{\|}$. The origin of the apparent negative dispersion is described in more detail in [Bov03].

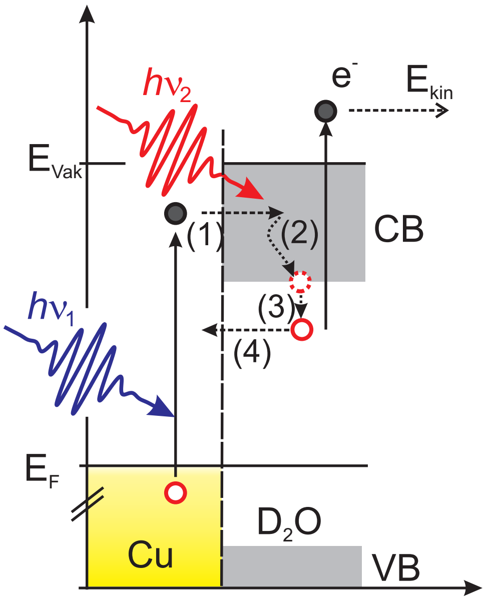

Figure 2.4: Schematic representation of the elementary processes of electron solvation in amorphous D_2O at metal interfaces: The absorption of photon with energy $h\nu_1$ creates excited electrons in the metal. (1) The photoexcited electrons are injected into the D_2O layer via the ice conduction band. (2) They localize in pre-existing potential minima at or below the band bottom. (3) Due to a molecular rearrangement the excess electrons are energetically stabilized. (4) Concurrently, the electron population decays back to unoccupied metal states. These electron dynamics are probed by a second, time-delayed laser pulse $h\nu_2$, which excites the electrons above the vacuum energy, where their kinetic energy is measured by an electron time-of-flight spectrometer.

makes a photoexcitation within the ice layer very unlikely for photon energies below the band-gap, all photoexcited electrons originate from the Cu(111) crystal. The excited electrons can then be injected into the D_2O layer due to wave function overlap of delocalized states of the metal with the conduction band (CB) of ice. The feature e_{CB} in the spectrum in Fig.2.3a) is assigned to the CB of the ice layer, because of it's free-electron like behavior, characteristic for a delocalized state. The fast decay of the electrons in the ice conduction band within the duration of the laser pulses indicates a strong electronic coupling between CB electrons and unoccupied metal states. The strong coupling leads to an efficient charge injection of excited electrons into the ice adlayer *via* the conduction band.

(2) and (3) The excess electrons in the CB can localize at pre-existing traps at or below the band bottom. These potential minima can for instance originate from weak or broken hydrogen bonds [Nor07]. The trapping of the excess electrons is reflected by the non-positive dispersion of the spectral signature e_S. The apparent negative dispersion is explained by the finite bandwidth of the solvated electrons in k-space and the rather broad peaks in energy, which is explained in detail in [Bov03]. The transient localization of the excess charge is driven by a reorientation of the surrounding water molecules. The reorientation of the water dipole moments in the vicinity of the excess electron also leads to an energetic stabilization of the electron. This stabilization is observed as an energetic shift of the maximum of the e_S peak with increasing time delay (see Fig.2.3a)). The localization and energetic stabilization of excess electrons are characteristic properties of electron solvation in polar liquids. Therefore the spectral

feature e_S can be assigned to solvated electrons in amorphous D_2O ice layers.

(4) The population of the solvated electron state continuously decays back to the metal substrate. The ongoing screening of the excess charge from the Cu(111) substrate caused by the continuous rearrangement of surrounding water molecules leads to a subsequent reduction of their decay probability and to an increase of their lifetime in the ice. As a consequence the population of e_S decays non-exponentially and can be observed up to 1 ps.

In addition to the above mentioned population and energetic stabilization of the solvated electron states, an important parameter to consider is their localization within the molecular ice. Indeed, such electrons either reside in the bulk of an ice film or at the vacuum-ice interface. The binding site of a solvated electron is not solely determined by the spatial distribution of attractive sites but its relevance is also influenced by the population probability of these potential sites. To address the question of the solvation site experiments have been performed where the electrostatic environment of the excess charge is influenced by adsorption of a dielectric medium such like xenon atoms [Stä07a, Mey08]. For closed amorphous ice layers solvated electrons are embedded in the bulk of the layer [Mey08]. For D_2O coverages with a mass equivalent of less than 2 BL ice clusters are formed on Cu(111). In this case the adsorption of Xe atoms leads to a strong change in the binding energy of the solvated electrons which indicates that they reside at the ice-vacuum interface [Stä07a, Mey08]. The binding site of excess electrons strongly depends on the ice morphology and the local arrangement of the water molecules as will be shown in the next section on electron solvation in crystalline ice.

2.2.2 Electron Trapping in Crystalline Ice on Ru(001)

As already mentioned in the previous section the electron dynamics in water ice depend strongly on the morphology and structure of the adsorbate. Experiments have been performed showing that structural changes, which occur during the crystallization of amorphous layers of polar molecules, *e.g.*, water and ammonia, can lead to drastic changes of the respective electron dynamics [Gah04, Stä07b, Bov09, Stä11]. The present section reports on the dynamical evolution from femtoseconds to minutes of an excess electron in crystalline ice structures adsorbed on Ru(001) substrate.

The left panel of Fig.2.5 presents a series of 2PPE spectra of crystalline D_2O on Ru(001) taken at different time delays between pump- and probe-pulse. At intermediate state energies of $E - E_F = 3.2$ eV and $E - E_F = 3.8$ eV spectral signatures of the n = 1, 2 image-potential states(IPS) are resolved. It is known for metal-molecules interfaces that IPS may exist, which are delocalized parallel to the interface and bound with respect to the vacuum level [Ech04]. They exhibit lifetimes of $\tau_1 \leq 5$ fs and $\tau_2 = 50$ fs, respectively. The state observed at $E - E_F = 2.2$ eV is attributed to long-living trapped electrons at the ice/vacuum interfaces and will be referred to as e_T. It exhibits a significantly different behavior than the IPS. The first and most striking difference is the

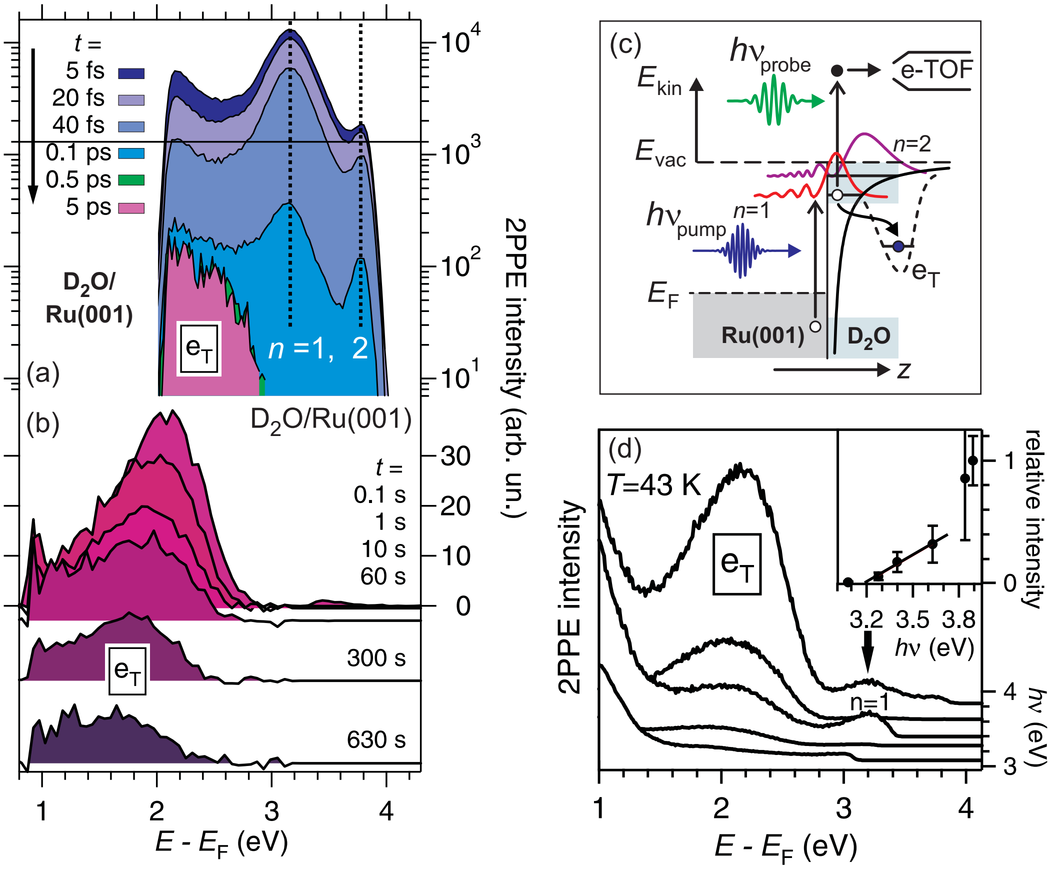

Figure 2.5: Trapped electrons in crystalline D$_2$O/Ru(111). (a) Time-resolved 2PPE spectra at the indicated pump-probe delays on a 2 BL crystalline D_2O adlayer adsorbed on Ru(001). (b) 2PPE spectra with time delays of seconds. (c) Schematic representation of the pump-probe excitation and electron trapping in crystalline ice. (d) Single color 2PPE spectra taken for different UV photon energies. The inset displays the intensity of the e_T peak as a function of photon energy normalized to the intensity for $h\nu = 3.9$ eV. Modified from [Bov09]

extraordinary long lifetime of this excited state. Fig.2.5.b shows the complete spectral signature of e_T which can be followed over 17 orders of magnitude. Such an enormous lifetime of an excited state in front of a metal surface indicate that the trapped electron has to be highly localized and very efficiently screened from the substrate. Secondly, the temporal evolution of e_T shows a large stabilization of ~ 0.6 eV within 10 min and spans over all observed timescales.

The photo injection process was investigated by varying the photon energy $h\nu_{pump}$ of the pump pulse. Respective spectra are presented in Fig.2.5.d as a function of $h\nu_{pump}$. A threshold photon energy of $h\nu_{pump} = 3.2$ eV is necessary to generate electrons in e_T, which coincides with the energy of the n = 1 IPS. This behavior leads to the conclusion that, for photon energies above the threshold energy, electrons are injected into the laterally delocalized n = 1 IPS from where they can get trapped in the ice layer (cf. Fig.2.5.c)[8]. The trapping of the excited electrons has to occur at pre-existing traps as the residence time of the electrons in the first IPS is only ≤ 5 fs which would be not enough time for a molecular reorientation of the surrounding water molecules. In contrast a dynamic polaron formation can be ruled out as this would also require a longer formation time for lattice distortions [Ge98].

Long-living electrons in crystalline ice have been found for all coverages above 1 BL D_2O/Ru(111), which forms a $\sqrt{3} \times \sqrt{3}$ ordered wetting layer. For coverages exceeding 1 BL crystalline ice clusters are formed on top of the first wetting layer [Kim05, Haq07]. It shall be noted that for comparable coverages of amorphous ice no electrons with such an outstanding residence time are found. Upon adsorption of Xe overlayers the e_T peak in the 2PPE spectra is quenched. This clearly shows that the trapping sites for excess electrons reside at the ice/vacuum interface. After thermal desorption of the Xe rare gas layer the e_T peak recovers. Hence, the e_T sites have not been destroyed but rather blocked by Xe atoms[9]. Anyhow, the extremely long lifetime of the trapped electrons can not be explained by coherent tunneling of a quasi-free electron through a potential barrier with a height which is determined by the IPS. For a barrier height of 1 eV and a thickness of 1.9 nm which is given by the height of the first wetting layer and the ice clusters above at a coverage of 2 BL decay times in the order of μs would be achieved. But the trapped electrons also experience a time-dependent energetic stabilization during the hydration process caused by the rearrangement of the surrounding water molecules. As a consequence the potential barrier height increases and trapped electrons are very effectively screened from the metal substrate which strongly reduces the tunneling probability. The time-dependent population decay and energetic stabilization of the trapped electron can be described in terms of a continuous nuclear reorganization during which the electron relaxes deeper into the trap passing through adjacent conformational substates[10].

Additionally, microscopic insight into the initial trapping sites has been gained by *ab intio* calculations based on first-principle density functional theory by A. Rubio and coworkers [Bov09]. In order to allow a lateral localization of the electron at defect sites a large surface cell consisting of a 4 × 4 surface unit cell of ice $I_h(0001)$ in 3 layers and a vacuum region with 10 BL is used. Different defects have been investigated such like vacancies (a missing water molecule), divacancies, and orientational defects in the first bilayer and admolecules to the surface bilayer. Details on defects in crystalline ice are discussed in section 2.4.1. The binding energy of the excess charge is calculated with respect to the configuration without the trapping site. In Fig.2.6a. the geome-

---

[8] Angle-dependent 2PPE experiments confirmed the localized character of the trapped electrons [Bov09].

[9] More details on the determination of the binding site of trapped electrons will be given in the result section as it was also investigated in the framework of the present thesis.

[10] The temporal evolution and the temperature-dependence of the energetic stabilization of e_T are very well modeled based on a dynamic stabilization among conformational substates described by a harmonic potential as a function of a multidimensional nuclear coordinate. For details see [Stä07b, Bov09]

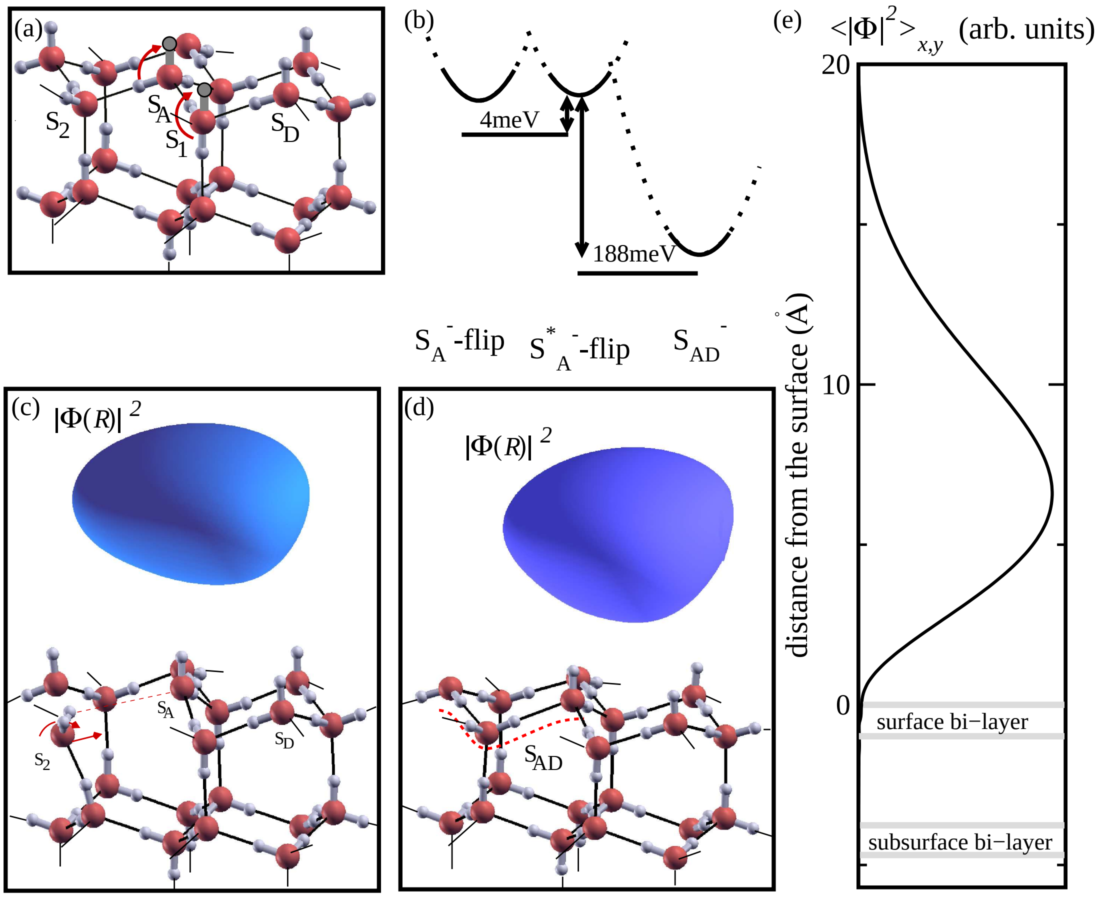

Figure 2.6: Orientational defects at crystalline ice interfaces: (a,c,d) ice structure and orientational defects created by flipping of OD bonds and the following reorientation of their neighboring D_2O molecules. (b) Energy of orientational defects and its stabilization. (e) In-plane average of the density of the excess electron as a function of the distance from the surface. Adopted from [Bov09].

try of the ice surface and exemplary orientational defects S_1 and S_A are shown. As a measure of the relevance of a defect type its formation energy is calculated. For the surface vacancies and a divacancy, the calculated formation energies are too high to be responsible for the abundance of the observed trapping sites and can therefore be ruled out. The most favorable orientational defect with a formation energy of 0.25 eV is the reoriented water molecule S_A such that an OD-bond points towards the vacuum(S_A-flip). The molecule assumes a S_D-configuration and a Bjerrum L-defect is created in between the S_A and the neighboring D_2O molecule, accompanied by a sideways reconstruction of the under-coordinated water neighbor S_2 (see Fig.2.6.c). Alternatively, the nearest neighbor of the subsurface layer S_1 can reorient giving rise to another orientational defect(S_1-flip) with a larger formation energy. Both kind of defects lead to the reconstruction of the natural hydrogen-bonds as shown in Fig.2.6.d. The resulting defect labeled S_{AD} leads to a binding energy gain of the trapped electron of 0.19 eV (see Fig.2.6.b). In the presence of the excess electron, S_{AD} even has a negative formation energy and its dynamical creation would stabilize the electron-ice complex at the surface. Excess electrons bind to such defects in a laterally well localized state as shown for S_A-flip and S_{AD} in Fig.2.6.c,d. The in-plane average of the excess electron density along the surface normal at the S_A-flip defect is depicted in Fig.2.6.e. It reveals that the excess electron is mainly located in front of the ice surface and that the wave function overlap of the trapped electron with the ice is small.

In the preceding two subsection an overview of electron solvation in amorphous and crystalline ice adsorbed on a metal substrate has been given. The knowledge of the electron dynamics and binding characteristics of excess electrons in ice layers is a key ingredient for the understanding of their interaction with coadsorbed atoms or molecules. In the following subsection the chemical reactive interaction of chlorofluorocarbons with trapped(solvated) electrons in crystalline(amorphous) ice is discussed.

2.2.3 Electron Induced Dissociation of Chlorofluorocarbons Coadsorbed with Water

The dissociative electron attachment to $CFCl_3$ coadsorbed on crystalline ice structures have been investigated in the framework of the present thesis. Due to the particular properties of trapped electrons in crystalline ice, which have been introduced in section 2.2.2, the DEA of $CFCl_3$ in the presence of crystalline ice is very efficient. The results are discussed in chapter 6.

Radiation-induced processes in molecular ices are of high relevance in numerous fields, from atmospheric chemistry and astrochemistry to (photo) catalysis [Gar05, Lu10]. Besides effects induced directly by excitation with UV or VUV photons or ionizing particles, many indirect processes can be involved. Adsorption of cosmic-rays can lead to the generation of secondary electrons which can then drive chemical reactions. In the dissociative electron attachment (DEA)[11] process a free, unbound electron with low kinetic energy ($E_{kin} \leq 20\ eV$) resonantly attaches to a molecule AB, resulting in the formation of a transient negative ion AB^*, which then dissociates into a neutral A and an anionic fragment B^-:

$$e^- + AB \rightarrow AB^{*-} \rightarrow A + B^-. \tag{2.1}$$

In ices, the formed fragments can desorb, recombine, or react with other molecules and therefore trigger a more complex chemistry in condensed phase. In Fig.2.7 the potential energy curves for a dissociative electron attachment process are displayed for a gaseous molecule (g) and a chlorofluorocarbon adsorbed on an ice surface (s). The lowering of the transient anion state is due to the stabilizing polarization potential formed by the surrounding water molecules. The latter potential energy curve is lowered by ~ 1.3 eV [Lu02]. The low energy electron can for instance be a free electron or a weakly bound electron in water ice.

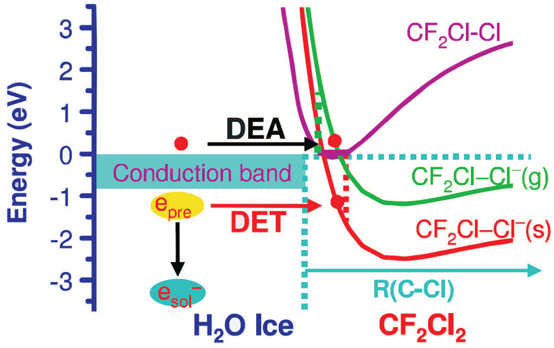

Figure 2.7: Potential energy curves for dissociative electron attachment (DEA) of a free electron with nearly 0 eV kinetic energy to CF_2Cl_2 in the gas phase (g) and for dissociative electron transfer (DET) to CF_2Cl_2 adsorbed on an ice surface. Adopted from [Lu10].

---

[11] A distinction between DEA and dissociative electron transfer (DET) will not be made in this thesis as both are very similar. For a description of the differences between DEA and DET see [Lu10].

Surface photochemistry involving condensed chlorofluorocarbons (CFCs) has attracted considerable attention because of their role in atmospheric ozone depletion [Pra90, Row91, Lu01b]. A large part of the stratospheric chemistry occurs mainly heterogeneously, on the surface of water ice particles [Rav97, Gar98]. Accordingly, the photoinduced dissociation of these adsorbed molecules is of great interest in the understanding of the chemical mechanisms in the stratospheric medium. It is known that the emission of CFCs causes ozone depletion by the release of chlorine atoms [12] via solar photolysis following this equation [Mol74, Too91]:

$$CF_2Cl_2 + h\nu \rightarrow Cl + CF_2Cl. \tag{2.2}$$

In addition to the direct induced dissociation, in the framework of the photochemical model for ozone depletion, the dissociation of CFCs by capture of electrons produced by cosmic rays in ice particles in polar stratospheric clouds is discussed [Lu01b, Pat02, Lu10].

CFCs present a high cross section for DEA of ballistic electrons with a kinetic energy near 0 eV [Ill79, Kla01]:

$$e^-[0eV] + CF_2Cl_2 \leftrightarrow CF_2Cl_2^{*-} \rightarrow Cl^- + CF_2Cl. \tag{2.3}$$

Such an electron can attach to the molecule, leading to the formation of a transient negative ion $\mathrm{CF_2Cl_2^{*-}}$. This transient species can now either decay via the autodetachment of the electron, or by the C-Cl bond cleavage and the formation of a $\mathrm{Cl^-}$ ion. The electron induced cross section of the DEA process 2.3 is 10^4 times higher than the direct photodissociation cross section of 2.2 [Ill79].

The dissociation of CFCs on ices has been studied extensively in the past decade due to its potential relevance for the ozone depletion [Lu99a, Lu01a, Lu01b, Lu01c, Far04, Lu04, Ryu06, Wan08, Lu09, Bha10]. Lu and Madey investigated the DEA of chlorofluorocarbons in the presence of polar ice films consisting of water or ammonia by means of an electron stimulated desorption ion angular distribution detector with time-of-flight capability. This technique allows to measure total yields of a specific ion species upon an electron bombardment [Lu99a]. The bombardment with 250 eV electrons generates low-energy secondary electrons in the metal with a maximum in the electron energy distribution between 0 and 2 eV. As already mentioned earlier these low-energy electrons can trigger the dissociation of CFCs following the reaction 2.3. The relative $\mathrm{Cl^-}$ yield as a function of water and ammonia coverages for various $\mathrm{CF_2Cl_2}$ pre-coverages are presented in Fig.2.8. For the lowest $\mathrm{CF_2Cl_2}$ coverage coadsorbed with $\mathrm{H_2O}$, the $\mathrm{Cl^-}$ yield exhibits a maximum enhancement by approximately two orders of magnitude at about 1.3 ML of water. The effect is even more pronounced for the coadsorbtion of NH_3, where the enhancement is more than a factor of 10^4. The $\mathrm{Cl^-}$ yield decreases with increasing water coverages due to elastic and inelastic scattering as the desorbing $\mathrm{Cl^-}$ ions pass through the water layer. The fact that the $\mathrm{Cl^-}$

---

[12] The chlorine atoms act as an ozone-scavenger and destroys ozone in the simplest example by a (Cl,ClO) reaction chain [Mol74]:
$Cl + O_3 \rightarrow ClO + O_2$
$ClO + O \rightarrow Cl + O_2$.

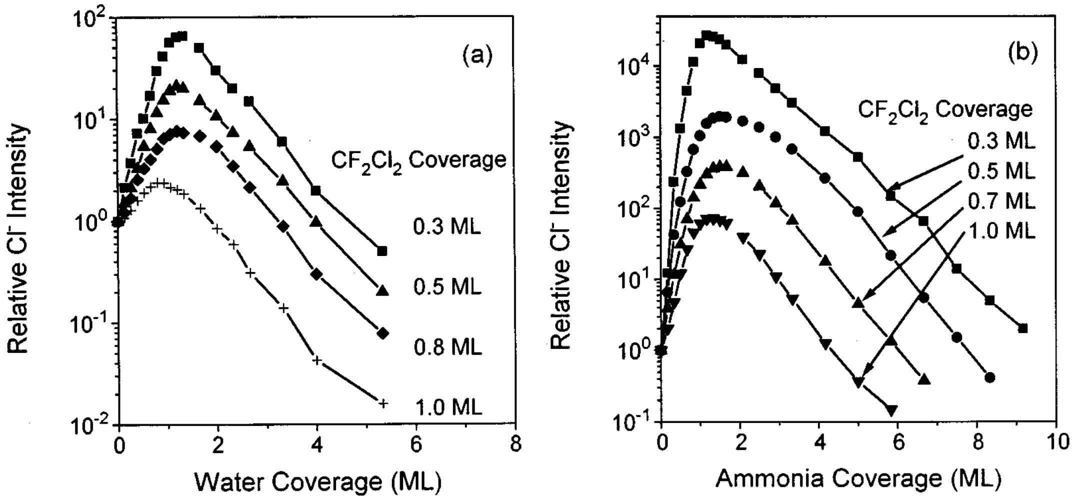

Figure 2.8: Enhancement of electron-induced dissociation of CFCs coadsorbed with water and ammonia ices: Relative Cl^- yield from 250 eV electrons incident onto different amounts of CF_2Cl_2 precovered Ru(001) as a function of water (a) and ammonia (b) coverage. The data is normalized to the initial value for zero water or ammonia coverage and was taken at a sample temperature of 25 K. Adopted from [Lu99a].

enhancement effect is strongest at the lowest CF_2Cl_2 coverage has been attributed to a competing deexcitation channel. The dissociative $CF_2Cl_2^{*-}$ is transferred into a stabilized $CF_2Cl_2^-$ which decreases the dissociation probability. With decreasing CF_2Cl_2 coverage the deexcitation channel becomes less significant. The strong enhancement of the Cl^- yield is explained by the presence and attachment of solvated electrons in the polar molecular layer. In contrast to non-polar molecules, where excess electrons remain quasi-free and exhibit only a short residence time [Fer91], excess electrons in a polar medium exhibit lifetimes ranging from several hundred femtoseconds to even minutes, as discussed in section 2.2.1 and 2.2.2. Accordingly, the Cl^- yield is smaller for CF_2Cl_2 coadsorbed with non-polar molecules or atoms, such like CH_4, and rare gases, Ar, Kr, and Xe, where an enhancement by a factor of ~ 10 has been observed [Lu99b]. Similar experiments have been performed by Ryu *et al.* for $CFCl_3$ coadsorbed on top of amorphous ice films [Ryu06]. Employing 2PPE spectroscopy they observed a decrease of the solvated electrons lifetime as a function of $CFCl_3$ coverage. The lifetime of the solvated electron decreases from its initial decay time of 120 fs to about 80 fs at a $CFCl_3$ coverage of 0.1 ML. This effect is attributed to a dissociative electron transfer to the $CFCl_3$ molecules. The solvated electrons are transferred by tunneling to the anionic state of $CFCl_3$, which is than dissociating into a $CFCl_2$ radical and a Cl^- ion.

2.2.4 Water Coadsorbed with Alkali Atoms

As discussed in the previous section excess electrons in ice have a strong influence on the dissociation efficiency of CFCs and are therefore considered to be relevant in stratospheric chemistry potentially leading to the destruction of the ozone layer. In the stratosphere, ice particles contain a sizeable amount of positive ions, originating from NaCl brought by the ocean evaporation of from Na or K atoms brought by meteor sputtering into the atmosphere [Pla03]. It is a question of interest how such positively charged species influence the stabilization and localization of excess electrons in the ice. These are key parameters for the understanding of the interactions between ionizing particles and ices of polar molecules. In addition, impurities are abundant in condensed water and will modify the energetics and dynamics of electron solvation. For instance, screening effects of excess charges in the ices, such as positively charged impurities (e.g., alkali ions Na^+, K^+, Cs^+, and so forth), are expected to influence the population, localization, and lifetime of electronic states of excess electrons and therefore also the reactivity of such systems under ionizing irradiation. It is therefore important to study their role on secondary-electron-induced reactivity under ionizing radiation. In the following, interactions between neutral alkali atoms and water ice will be presented. In particular, the processes leading to the presence of alkali cations in the ice will be discussed as a function of system parameters like temperature and alkali surface density.

Alkali atoms in contact with liquid water lead to a well known exothermic reaction, yielding MOH and H_2 following the formula:

$$2M + 2H_2O \rightarrow 2(M^+OH^-) + H_2, \tag{2.4}$$

where M denotes an alkali metal atom. However, the underlying process for this reaction, where the valence *s* electron of the alkali plays an active role, is not well understood [Bor04]. The chemistry of alkali atoms on solid water has been investigated by Krischok *et al.* and Borodin *et al.* in an ultraviolet photoemission spectroscopy (UPS) and metastable impact electron spectroscopy (MIES) study [Kri03, Bor04][13]. In MIES electrons from the substrate surface are ejected by an Auger-like charge exchange process, referred to as Penning ionization, between metastable He atoms and the surface [Har97]. MIES is a very surface sensitive technique as the He atoms impinge the surface with near-thermal kinetic energy of 60 - 100 meV. In the left panel of Fig.2.9 a series of MIES spectra are presented for different amounts of Na deposition on three layers of ice on a TiO_2 substrate kept at 130 K. The topmost spectra are taken before Na exposure and exhibit three distinct features which are attributed to molecular water,*i.e.* the three highest occupied water orbitals $1b_1$, $3a_1$ and $1b_2$. The Na coverage dependent changes can be summarized in three Na coverage regimes.

- At low Na coverages only the three features attributed to intact water molecules ($1b_1$, $3a_1$ and $1b_2$) appear in the spectra. The 3s orbital of atomic Na is not observed indicating that the Na is ionized.

---

[13] The interaction of alkali atoms and water has also been investigated by others experimentally and theoretically [Bla90, Par00, Cha01, Gün02, Gün03, Fer03, Gle04, Pol07].

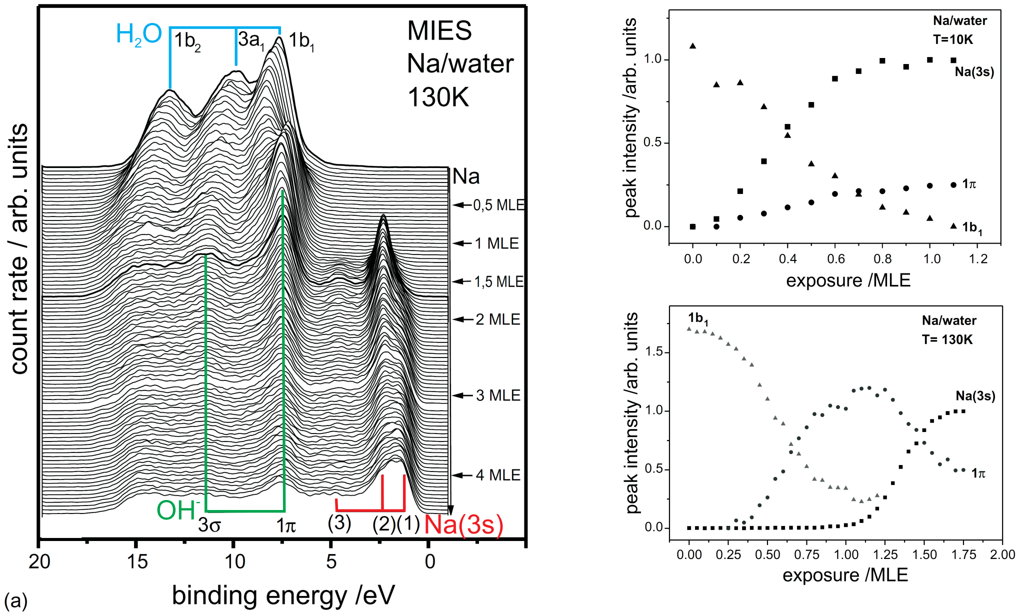

Figure 2.9: (left): MIES spectra for different Na coverages adsorbed on three layers of ice at a substrate temperature of 130 K. (right): Intensities of the MIES peaks associated with water ($1b_1$), OH (1π) and 3s electron of Na as a function of sodium exposure at substrate temperatures of 10 K and 130 K. Modified from [Kri03].

- In the intermediate coverage regime the sodium is still ionized (no 3s orbital). But the spectra are now dominated by the emission from the OH 1π and 3σ orbitals, whereas the intensity of the signatures for intact water molecules decreases, suggesting that the water molecules in the surface become replaced by OH species from the reaction with Na.

- At high Na coverages the 3s orbital becomes the dominant feature of the MIES spectra, indicating that Na atoms remain neutral at the surface and are not further ionized.

The evaporation of Na to the solid water induces an efficient dissociation of water molecules and OH^- and Na^+ are formed. The right panel of Fig.2.9 depicts the intensities of the molecular water ($1b_1$), the OH (1π), and Na(3s) peak as a function of Na exposure for different sample temperatures. At 10 K the Na signal is already observed for 0.25 ML and the feature of the OH species is comparable small. Clearly, the reaction between Na and water does not take place efficiently anymore at 10 K. The activation threshold for water dissociation in alkali metal doped ice films is estimated to be around 100 K [Gün02]. Also the Na coverage is crucial for the dissociation. Below a critical coverage of 0.15 ML Na and a critical temperature of 100 K the water molecules remain intact [Gle04], while the Na is ionized to Na^+ and the 3s electron is directly transferred from the Na adsorbate to the metal substrate via resonant tunneling through the relatively thin SW film.

The adsorption of different alkali atoms, e.g Lithium, Natrium, and Potassium, on thick ice films[14] supported on a Cu(111) substrate has been studied by photoemission (PE) spectroscopy and DFT calculations by Vondrak *et al.* [Von06a, Von06b, Von09]. For all investigated alkali atoms a drastic decrease in the threshold for photoemission from the ice film was observed for low alkali coverages compared to photoemission from undoped ice films, where the PE threshold is 8.7 eV [Bar78]. Although physical properties of these three alkali atoms, such like the ionization potential IP or the atomic radius r_a differ significantly, the photon energy dependent PE cross-section shows a very similar behavior. The ionization energy and the atomic radius of the three alkali atoms are summarized in table 2.2.

The total photoemission yield of the water ice surface doped with Li, Na, and K as a function of photon energy is depicted in Fig.2.10. The PE yield increases exponentially between 2.1 and 3.5 eV for Potassium doped water, 2.5 and 3.25 eV for Lithium doped water, and 2.3 and 3.0 eV for Natrium doped water. There is a tendency of decreasing PE threshold for heavier alkali metals, however compared with the given error of $\pm 0.2 eV$ it is only a slight effect. In addition, also the energy distribution of the photoemitted electrons is similar presenting a broad ($\sim 2eV$) and asymmetric peak, at an initial energy of no more than 2.6 eV below the vacuum level. Vondrak *et al.* explain the strong similarities among the different alkali doped ice films with a common initial state. The initial state when the alkali atom adsorbs on the ice film is proposed to be a metastable form of a solvated electron loosely associated with its parent alkali atom. The metastable character of this state was proven to be correct by employing time-dependent measurements of its temporal evolution. In all three cases the PE cross section was observed to decay uniformly with time. The initial state formed when Li adsorbs on the ice film decays much faster than for Na or K with a first-order rate coefficient of $1.4 \times 10^{-2} s^{-1}$. The faster decay is explained by a more efficient diffusion of the Li into the ice film.

Table 2.1: Ionization energy and atomic radius of Li, Na, and K from [Lid93].

	Lithium	Natrium	Potassium
ionization energy (eV)	5.39	5.13	4.34
atomic radius (Å)	2.05	2.23	2.77

Furthermore, quantum chemistry calculations have been performed to explain the origin of the metastable state and decay channel which leads to the decreasing PE signal with time [Von06a, Von09]. Fig.2.11 illustrates several optimized structures consisting

---

[14] In order to minimize the influence of the substrate the experiments have been performed on 3000 L thick crystalline ice films.

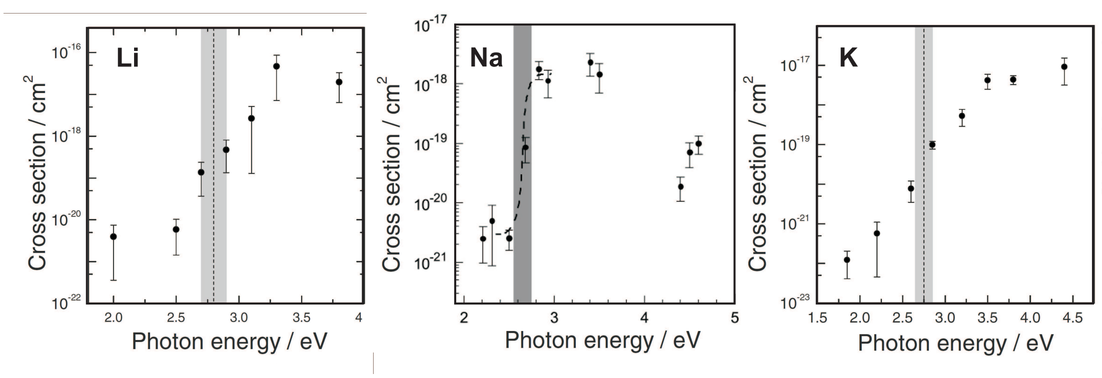

Figure 2.10: Photon energy dependence of the photoemission yield of the water ice surface doped with (left) 0.05 ML Li, (middle) 0.02 ML Na, and (right) 0.02 ML of K. The corresponding cross-section of the undoped ice film is $< 10^{-22} cm^2$. Modified from [Von06b, Von09].

of 18 H_2O molecules, which have been achieved using the B3LYP/6-311+g level of theory. The structure of the first local minimum on the potential energy surface when the Na atom approaches the ice surface is shown in Fig.2.10.(a) and (b) in a side and top view, respectively. Here the Na atom lies above the ice surface and is bound symmetrically to the O atoms of the three water molecules in the surface ring. The 3*s* orbital of the Na, which is a large component of the HOMO, is getting delocalized. However, the calculated PE threshold is higher than the observed experimentally one. When the optimization is started with the Na atom in the surface hexagonal ring, the ice structure gets distorted (cf. Fig.2.10.(c) and (e)). The present structure has a stronger binding energy than that in (a) and (b) of $96 kJmol^{-1}$. However, the calculated vertical ionization potential is 3.0 eV which is in very good agreement with the measured PE threshold. In this structure the HOMO is delocalized over 8 Å in diameter. In the structure presented in Fig.2.10(e) the Na atom resides in between the first and second water layer. The Na 3*s* electron is delocalized at an H_2O molecule with a dangling surface H atom. The O-H bond is significantly stretched from 0.96 to 2.1 Å and the Na is almost fully ionized. Although the energy is $30 kJmol^{-1}$ higher than in (c) and (d) this structure can be reached by thermal activated rearrangement of the water molecules. The authors propose that the elongated O-H bond breaks resulting in the formation of H_2, leaving NaOH in the ice [Von06a]. This reaction is believed to result in the observed decay of the PE signal with time. Very similar results have been achieved for K on ice. The larger decay rate of K compared with Na is consistent with its lower ionization potential. In contrast with Na and K, for Li no stretched surface O-H bond occurs and accordingly no fully ionization of Li takes place. The faster decay of the PE signal in the case of Li is explained in terms of a rapid diffusion of Li atoms into the bulk of the ice, which is facilitated by the smaller atomic radius of Li (cf. table 2.2).

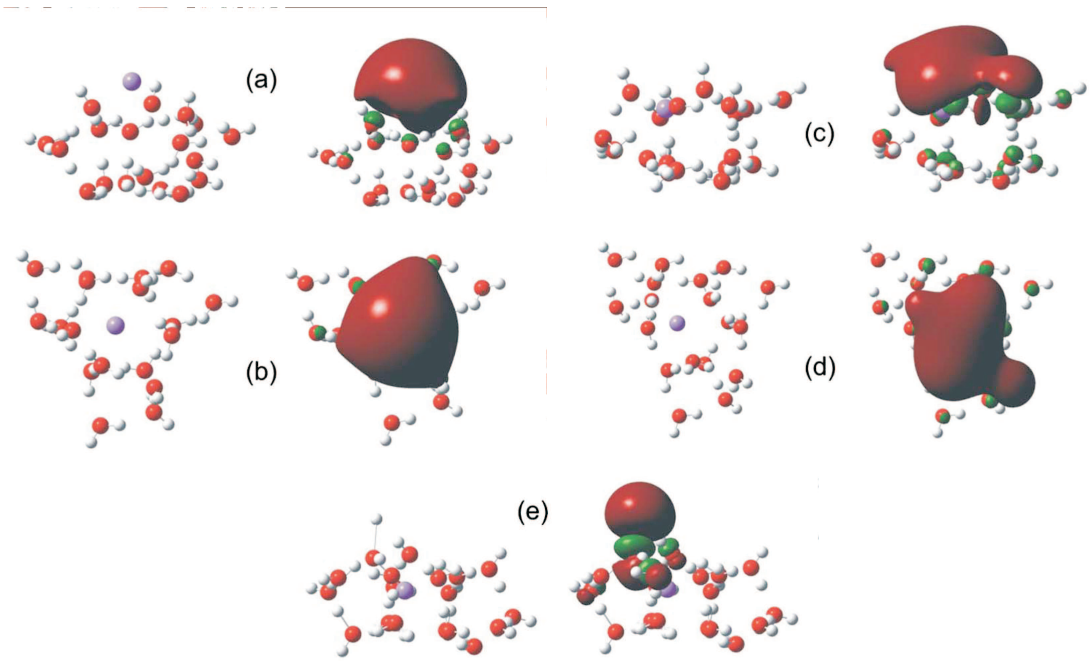

Figure 2.11: Calculated structures of a Na atom bound to a model ice surface consisting of 18 H_2O molecules. The white spheres are H atoms, the red spheres are O atoms, and the purple sphere is the Na atom. The red and green orbitals are the HOMO. For details see the text. Adopted from [Von06a].

Summarizing the preceding subsection, the adsorption of alkali metal atoms on a water ice surface leads to the liberation of the *ns* valence electron into the water environment, resulting in the formation of alkali ions. Depending on the sample temperature and alkali coverage this electron transfer results in the exothermic dissociation of surrounding water molecules to form OH^- ions and to the formation of an alkali hydroxide. For low temperatures and low alkali coverages the water dissociation is suppressed. In this case the valence electron of the alkali atom is delocalized over 2-3 water molecules in the vicinity of its parent ion. However, this electron can subsequently be stabilized by the surrounding water molecules so that an alkali ion remains at the surface. In chapter 4 the influence of coadsorbed alkali atoms on the dynamics of excess electrons in amorphous D_2O on Cu(111) will be discussed. It will be shown that excess electrons can be bound to alkali-ion/water cluster at the ice/vacuum interface, where the electrons are efficiently screened from the metal substrate, resulting in lifetimes of several picoseconds in the ice, and energetically stabilized by the surrounding water molecules. In addition, the adsorption of potassium atoms at temperatures below 50 K enables the observation of the 4s electron of the K atom.

2.3 Electronic Properties of the Metal Substrate

All the experiments in the present thesis have been performed on the metals Cu(111) and Ru(001). The properties of the metal substrates and their surfaces is important for several reasons. First of all, they serve as a template for the atomic or molecular adlayers and therefor influence their structure. Secondly, the substrate acts as an electron donor from where electrons can be excited and transferred into unoccupied electronic states of the adsorbate. Hence, the observed electron dynamics can be influenced by the electronic properties of the metal substrate. Also features of the bare metal, *e.g.* surface- and image potential states, or signatures of the bulk band structure, can be present in the 2PPE spectra. In the following a description of the electronic structure of both substrates is given as well as a short introduction to surface states and image potential states.

2.3.1 Structure and Electronic Properties of Cu(111)

Copper crystalizes in a face centered cubic (fcc) structure with a lattice constant of a=3.61 Å [Kit05]. The band structure and the density of states of the noble metal with the electron configuration [Ar]3d^{10}4s^{1} is depicted in Fig.2.12. The completely occupied d-bands lie 5-2 eV below the Fermi level E_F. In contrast to the localized electrons in the d-bands which exhibit a flat dispersion the dispersion of the electrons in the sp-band can be described as a parabola of a quasi-free electron gas. The sp-band ranges from 8.6 eV below E_F at the $\overline{\Gamma}$ point up to states above the vacuum level E_{Vac}. The position of the d-bands and the available unoccupied states in the sp-band are responsible for the yellowish color of Cu. The absorption of photons with energies of

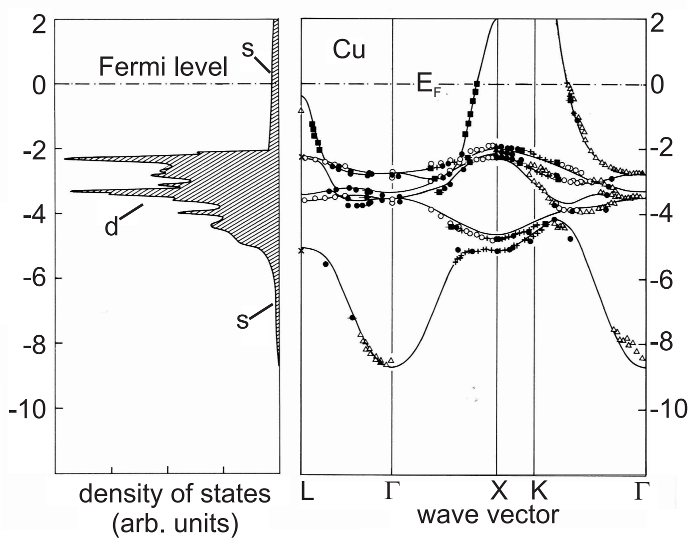

Figure 2.12: Bulk band structure along high symmetry points in the Brioullin zone derived from theoretical and experimental investigations and calculated density of states of Cu [Eck84]. Adopted from [Iba90].

hν $\geq$2 eV leads to an electronic transition of d-band electrons into the states in the sp-band above E_F, whereas photons with lower energies are reflected. The Cu(111) surface exhibits an orientational band gap in the projected surface band structure around the center of the surface Brioullin zone at the $\overline{\Gamma}$ point. As can be seen in Fig.2.13 the band gap ranges from the upper edge of the occupied states at 0.85 eV below E_F to 4.08 eV above the Fermi level. The work function Φ, which is defined as the energetic difference between E_F and E_{Vac}, of the Cu(111) is 4.9 eV [Fau95, Kno98]. In the region of the band gap surface states and adsorbate-induced states can only exist if their wave function is located in front of the surface and is exponentially damped inside the bulk. The penetration depth of such states is smallest in the middle of the band gap and converges to infinity at the band edges [Smi85]. The broken periodicity of the lattice at the Cu (111) surface gives rise to an occupied surface state and unoccupied image potential states. Both states are delocalized within a plane parallel to the surface and form two-dimensional bands as depicted in the right panel of Fig.2.13. The surface state is partially occupied and lies symmetrical around $\overline{\Gamma}$ at 0.39 eV below E_F. The surface state plays an important role for the electron dynamics at the bare and adsorbate covered Cu(111) surface. On the one hand due to the high probability density of the SS at the surface (cf. left panel of Fig.2.13) electrons from the surface state can be efficiently transferred to other interfacial states either originating from the substrate or from adsorbates. In the case of the first image-potential state the electron transfer from the surface state is the dominant excitation pathway [Kno98]. On the other hand the unoccupied part of the surface state at larger values of $k_{\|}$ offers a large phase space for the relaxation of excited electrons.

A charge located in front of polarizable surfaces interacts with the polarization charge it induces at the surface. This interaction can be described by an attractive Coulomb potential which corresponds to the classical image-potential [Lan73]:

$$V_{IP}(z) = -\frac{e^2}{4(z - z_{im})}, \tag{2.5}$$

where z_{im} is the image-plane position[15]. The image potential of the Cu(111) surface is plotted in the left panel of Fig.2.13. This one dimensional potential confines electrons only in the direction normal to the surface, parallel to the surface the electrons are delocalized. If the substrate offers a projected band gap in the vicinity of the vacuum level electrons are trapped by the image potential and their wave function decays exponentially into the metal (left panel of Fig.2.13). The relaxation of the image potential states occurs on an femtosecond timescale by elastic and inelastic scattering [Ech04]. These states form a Rydberg like series of bound states at the surface:

$$E_n = E_{Vac} - \frac{Ry}{(n+a)^2} = E_{Vac} - \frac{0.8504\ eV}{(n+a)^2}\ with\ n = 1,2,3,... \tag{2.6}$$

Here, Ry is the Rydberg unit of energy, and n denotes the quantum number of the system and the number of nodes of the wave function in front of the metal surface. The

---

[15] The image plane is located half an atomic layer distance outside the last atomic layer [Smi89].

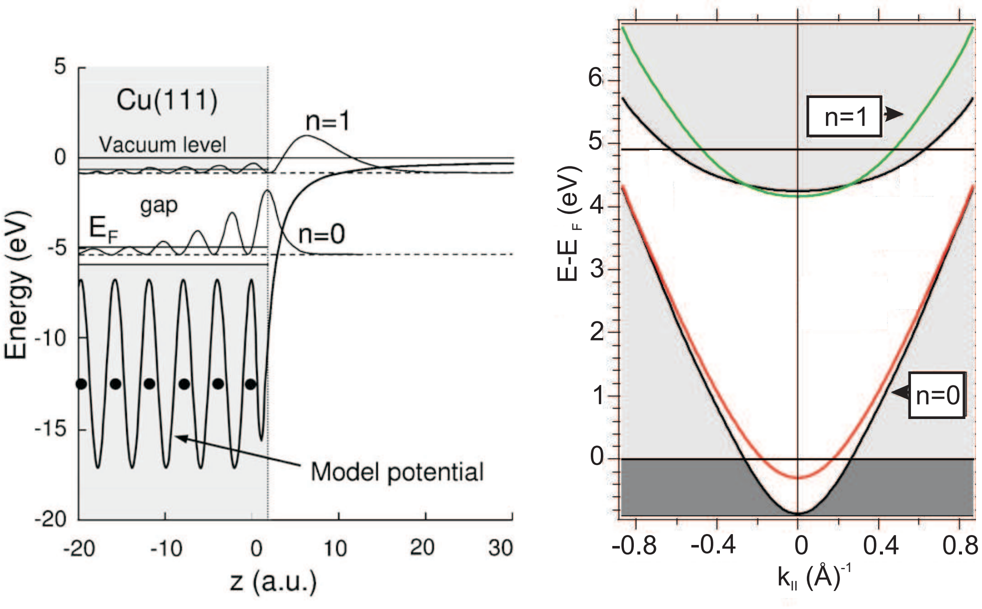

Figure 2.13: (Left): 1D model potential and probability density for the surface state (n=0) and the first image potential state (n=1) at the Cu(111) surface at $\overline{\Gamma}$. (Adopted from [Ech04]). (Right): Projected bulk band structure in [111] direction with calculated dispersion for the surface and the first image potenital state. (Based on [Smi85]).

fact that the potential barrier formed by the band gap of the metal is not infinitely high and allows a finite penetration of the wave function into the metal is taken into account by the so-called quantum defect a [Ech78]. The dispersion of both states can be described analog to the behavior of free electrons with an effective mass m^*:

$$E(\vec{k}) = \frac{\hbar^2 k^2}{2m^*}. \tag{2.7}$$

As the probability density of the n = 1 IPS is mostly located in the vacuum (cf. Fig.2.13 its dispersion basically follows that one of a free electron and $m^* \approx m_e$. The dispersion of the n = 0 SS, in contrast, resembles more the dispersion of the bulk bands,due to the larger overlap of the probability density of the surface state with bulk states. IPS with quantum numbers $n \geq 2$ are degenerated with the unoccupied sp-band. Therefore, they are referred to as image-potential resonances.

Although the n = 1 IPS lies in the Cu(111) band gap it exhibits a rather short lifetime of ∼ 20 fs [Kno98, Ech04], which is caused by the fact that it is at the band edge. With increasing quantum number n the maximum of the probability density of the IPS wave function shifts away from the surface. Hence, as the lifetime is inversely proportional to the fraction of the wave function inside the metal, it scales in good approximation with n^3 [Ech00]. However, as the n = 2 IPS is degenerated with bulk states and consequently posses a larger phase space for scattering, its lifetime is only 14 fs [Ech04].

2.3.2 Electronic Structure of Ru(001)

Ruthenium is a hcp (hexagonal closed packed) single crystal with a lattice constant of $a = 2.71$ Å [Kit05]. The Ru(001) surface consists of hcp layers with an ABAB stacking. The atomic electron configuration is [Kr] $4d^7$ $5s^1$. In Fig.2.14 the calculated projected bulk band structure and the integrated density of states of Ru(001) is depicted. In contrast to copper, the valence d-band is not fully occupied and hence crossing the Fermi level up to 1.5 eV above E_F. As a consequence the density of states has a maximum at ~ 1 eV above E_F. This high density of unoccupied states around the Fermi level strongly influences the electron dynamics of Ru(001). Electrons in excited states experience a huge phase space for electron-electron scattering, which results in a fast relaxation dynamics compared to Cu(111) [Kno98, Lis04]. This effect was also observed for solvated electrons in water on Ru(001), where the initial decay of the solvated electron population is, with $\tau_1^{Ru} = 34$ fs, considerably faster than for D_2O/Cu(111), with $\tau_1^{Cu} = 140$ fs [Stä07b].

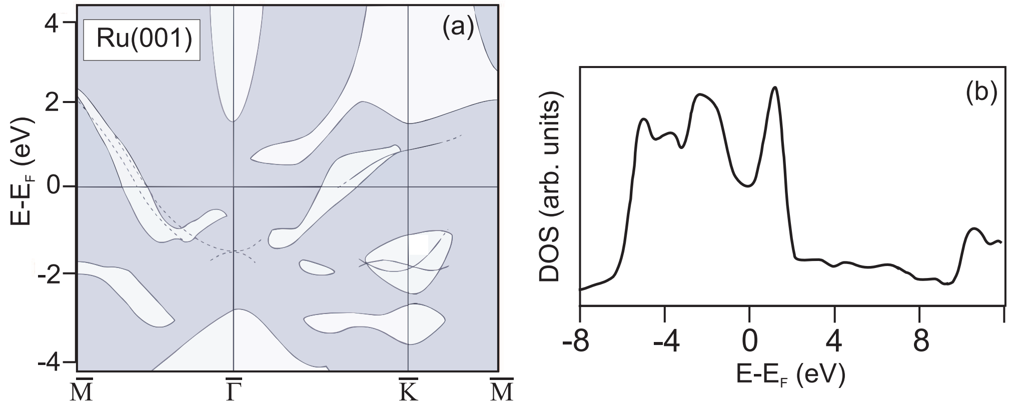

Figure 2.14: (a): Projected bulk band structure of Ru(001) modified from [Pel00]. (b): Integrated density of states showing a maximum 1 eV above the Fermi level. Modified from [Sei00].

The orientational sp-band gap at the Ru(001) surface around $\overline{\Gamma}$ ranges from 1.6 eV to 11 eV above E_F. The work function of Ru(001) is 5.4 eV [Ber00]. Opposite to the case for Cu(111) the band gap also crosses the vacuum level. Hence, the image potential states are not degenerated with bulk bands. A series of IPS up to $n = 7$ was observed [Gah04]. As expected from theory [Ech00] the lifetime of the IPS increases with increasing quantum number, because the maximum probability density shifts away from the surface reducing the wave-function overlap with the substrate.

2.4 Properties of Ice/Metal Interfaces

All the experiments on electron solvation and transfer dynamics conducted in this work were performed at ice-metal interfaces. The present section will introduce the properties of the adsorbate water and the metal substrates Cu(111) and Ru(001).

2.4.1 Physical Properties and Structures of Water

Water is fundamental for many different processes in nature and it spans over a huge variety of different fields. On a macroscopic level water in all its states of agreation, *e.g.* liquid water, water ice, water vapor, and as small particles in clouds, plays a key role in worlds climate. Water is the main absorber of the sunlight in the stratosphere, mainly in the infrared, and contributes significantly to the greenhouse effect. On the other hand due to cloud formation reflecting the sunlight it attenuates global warming [Cha]. But also on a microscopic scale water is irreplaceable, such like in human cells, which are mainly consisting of water. Here the ability of water to act as a solvent is fundamental as many biochemical reactions take place only within aqueous solutions.

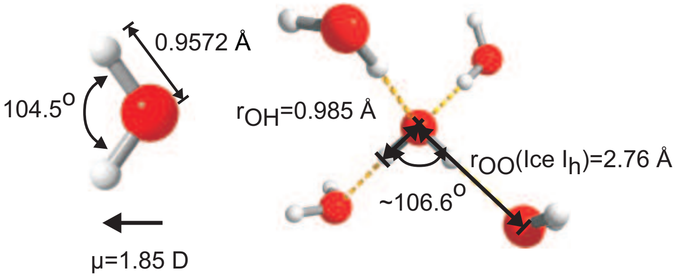

Figure 2.15: The water molecule and its structure in hydrogen bonding: Geometry of single water molecules and water molecules in a hydrogen network based on [Lud01].

The water molecule consist of three atoms, one O ([He]$2s^2p^4$) and two H ($1s^1$). According to the LCAO (Linear Combination of Atomic Orbitals) theory, each hydrogen forms a σ type covalent bonding with the O atom, which results from the overlap between the H 1s orbital and an 2s-2p hybridized orbital of the O atom. The remaining electrons of the oxygen occupy two other valence hybrid orbitals of O, which is therefore in a sp^3 configuration. This results in a tetrahedral geometry of the H_2O molecules, with an H-O-H bond angle of 109° (cf. Fig.2.15). Because of the significant difference in the electronegativity of the H and the O atoms, the σ bonds are polarized, leading to a positive partial charge of each H atom, and a negative one of the O atom. The different center of mass of the charges leads to a permanent dipole moment of 1.85 D [Clo73], that makes water a good solvent for other polar molecules.

Among each other water molecules are connected via hydrogen bonds. The hydrogen bond is based on a electrostatic attractive force between a electropositive hydrogen atom covalently bound to an oxygen and lone pairs of another water molecule. Usually the first is referred to as proton donor and the last one as proton acceptor if only two molecules are present. A hydrogen bond is also commonly referred to as an O-H$\cdots$O. The length of the H$\cdots$O bond is almost three times longer than the length of the covalent O-H bond. The hydrogen bond leads to a broadening of the binding potential of the proton which results in a downshift of the vibrational modes and in an increase of the distance to the covalently bond oxygen atom. In liquid or solid water more hydrogen bonds are possible. As every oxygen atom has two lone pairs each one can form a hydrogen bond with a hydrogen of another water molecule. Such every water molecule can be bonded to four other water molecules via hydrogen bonds like it is depicted in Fig.2.15. The hydrogen bond is stronger than a bond mediated by the van-der-Waals interaction but weaker than a covalent bond. Typically the strength of the hydrogen bond in water is 240 meV per bond.

These particular intermolecular interactions make the phase diagram of water very rich and complex. Besides the three well-known phases under ambient conditions, *i.e.* water vapor, liquid water, and ice, at least 15 stable and metastable phases exist [Pet99, Mal09, Loe06]. However, most of these phases do only exist under very high pressures. In the low pressure regime ranging from ambient pressure down to ultrahigh vacuum conditions with p $\leq 10^{-8}$ mbar, the phase diagram can be simplified to four stable and three metastable phases as depicted in Fig.2.16. The most abundant form of ice in nature under ambient conditions is the hexagonal form of crystalline ice I_h which is known from many diffraction experiments [Pet99]. The oxygen atoms form a hexagonal lattice with four oxygen atoms per primitive unit cell. Every water molecule is accepting and donating two hydrogen bonds so that every H_2O molecule is coordinated by four more molecules (*cf.* right panel of Fig.2.15). An important property of ice I_h is the absence of a long-range proton order and thus a disorder in the orientation of the water molecules. Bernal and Fowler stated that ice is a crystal with respect to the position of oxygen atoms and a glass with respect to the position of the hydrogen atoms [Ber33]. Nevertheless, the arrangement of the protons in ice I_h fulfills the so-called Bernal-Fowler-Pauling rules [Ber33, Pau35]:

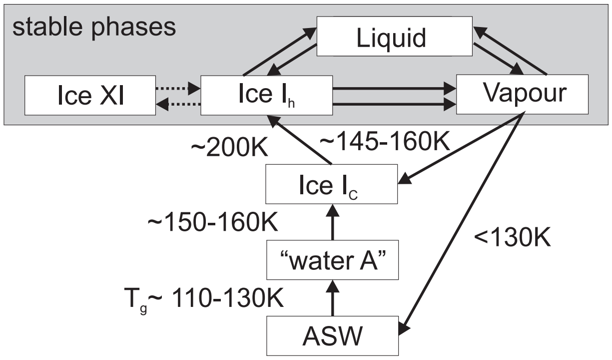

Figure 2.16: Simplified phase diagram of water in the low pressure regime with stable and metastable phases according to [Pet99].

(i) two hydrogen atoms are near each oxygen atom

(ii) on each line connecting nearest oxygen atoms there is only one hydrogen atom.

Under UHV conditions hexagonal ice I_h cannot be prepared as it requires a heating to 200 K which is beyond the temperature where desorption of water typically occurs[16] Such transition as I_h to I_c cannot be achieved. The structure and properties of cubic ice I_c are very similar to those of ice I_h. Cubic ice I_c also follows the Bernal-Fowler-Pauling rules such that the tetrahedral hydrogen bond coordination is preserved. The main difference of ice I_c in comparison to ice I_h is the different stacking order. While in ice I_h the hexagonal unit cells are stacked in a ABABAB-sequence, the stacking order in ice I_c is in an ABCABCABC order. Anyhow, the energetic differences are very small [Pet99] and so both ice modifications are not distinguishable for thin layers. As a consequence the properties of ice I_h can be transferred to ice I_c. A more detailed discussion of the structure and properties of condensed phases of water is given in a recent review by Malenkov [Mal09].

When the above mentioned ice rules are broken a point defect occurs. These defects are of great significance in a variety of different effects in water such like the conductance of water or phase transitions. Perfect crystalline ice should be an electrical insulator but in fact it has a non negligible conductivity of 0.01 μSm^{-1} [Pet99]. Furthermore, these defects can lead to fluctuations in the potential energy surface which can serve as potential trap for excess electrons. Indeed as discussed before pre-existing defects at the surface of crystalline ice adsorbed on a metal surface are the essential requirement for the existing of long-living trapped electrons at the ice/vacuum interface.

Although an ice rule is locally broken leading to a protonic point defect the oxygen atom lattice is not considerably affected and remains intact. In Fig.2.17 the different types of point defects are depicted. The ionic defects H_3O^+ and OH^- are formed if the

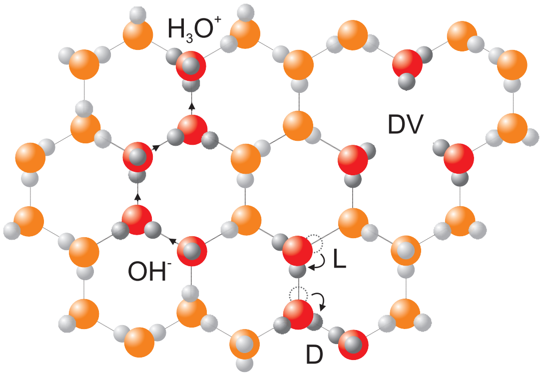

Figure 2.17: Schematic presentation of protonic point defects in ice Ice_h. Ionic defects form when the first ice rule is broken, Bjerrum defects occur when the second ice rule is violated. If a water molecule is missing in the lattice a dressed vacancy is present. (from left to right)

---

[16] More details on the desorption behavior of ice will be given in section 3.4.2.

first ice rule is broken and a proton is transferred to the neighboring water molecule. This initial step requires an energy of ~ 1.4 eV for the proton the overcome the barrier in the double-well potential of the hydrogen bonded water molecule. As long as the H_3O^+ OH^- pair is located at neighboring sites this situation is unstable. Anyhow, it can be stabilized if the neighboring molecule transfer its proton to its respective neighbor. Such the protons can move through the lattice from site to site very efficiently as despite the high activations energy for the formation of an ionic defect the activation energy of the proton motion is basically barrier less [Pet99]. Similar to the ionic defects Bjerrum defects also occur in pairs if the second ice rule is broken. In this case the water molecule is oriented in such a way that no proton (L-defect) or two protons (D-defect) are located along one of the O-O axes. Although the needed energy for the formation of a Bjerrum defect is smaller than for an ionic defect the activation energy for the diffusion of these defects is larger resulting in a smaller mobility of the L-defects. A third type of defect occurs when a water molecule is missing in the ice lattice like it is depicted in Fig.2.17 and labeled with DV.

Besides the crystalline ice I_c which was prepared in the framework of this thesis to investigate the chemical reactivity of trapped electrons with chlorofluorocarbons the second prepared ice structure in the present work is the amorphous solid water (ASW). Hence, in the following the structure of amorphous ice will be presented and properties of crystalline and amorphous ice will be discussed. Amorphous solid water[17] is prepared by condensation of water vapor onto a cold substrate at temperatures below 130 K [Jen94]. The local structure of amorphous ice and crystalline ice I_h are very similar. But in contrast to ice I_h, amorphous ice, besides the lack of a long range proton order, does not exhibit a long range order in the oxygen atom lattice. The reason for the loss of the long range order lies in the deviations from the tetrahedral geometry. On average the O-O-O bond angle deviates by 8°. It is known from X-ray and neutron scattering experiments that each water molecule is surrounded by 3.9(1) H_2O molecules [Fin02]. The structural differences are shown schematically in the insets of Fig.2.18. ASW can be seen as a liquid which is frozen in an amorphous structure where no diffusion occurs [Hal89]. The morphology of amorphous ice strongly depends on the respective preparation conditions. When deposited at low temperature ($T \leq 70K$) amorphous ice can be porous. The density of the pores strongly depends on preparation parameters like the angle between the impinging molecules and the surface normal [Ste99]. With increasing temperature ($T \geq 70$ K) the porosity of amorphous ice reduces and a compact and homogenous ice film is formed.

The electronic structure of crystalline and amorphous ice is quite similar as well but distinct differences exist. Both modifications of ice behave like a large band gap semiconductor. Delocalized states in the conduction band can be excited by photons with photon energies exceeding ~ 11 eV. The creation of excitons lead to adsorption in the ultra-violet with a maximum at 8.6 eV [Shi77]. Anyhow, the presence of defects

---

[17] Throughout this thesis ASW and amorphous ice will be used as a synonym for each other as now other amorphous phase than ASW is discussed in this work.

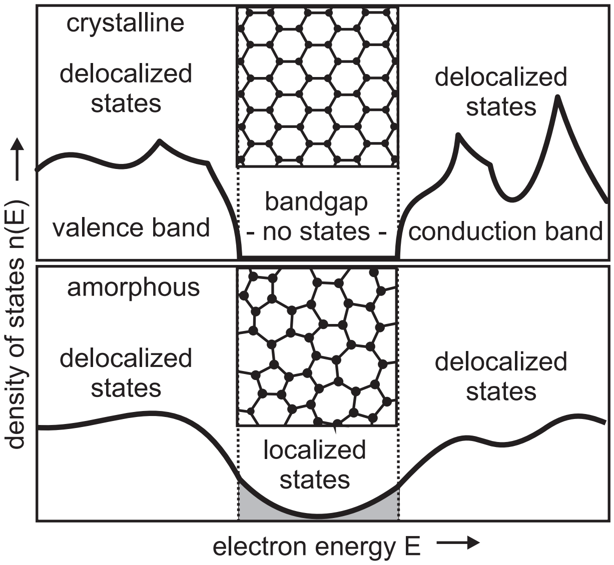

Figure 2.18: Band structure of amorphous and crystalline ice. The lattice distortions in amorphous ice smears sharp features in the band structure and the band edges. Anderson localization gives rise to localized states in the band gap. Insets: Schematic presentation of the local structure of crystalline and amorphous ice. Based on [Zal98].

and the missing long range order in amorphous ice influence the electronic structure and give rise to Anderson localization. Deviations from the periodic structure result in less sharp Brillouin zone boundaries and defined structures in the density of states of a crystalline solid are smoothed as apparent in Fig.2.18. The band edges decay exponentially into the band gap [Gou90]. These localized electronic states only occur when the gain in binding energy of the electron overcomes the loss in its kinetic energy according to the Heisenberg's uncertainty principle. Hence it can be concluded that distinct potential energy minima in the potential energy surface are present. The Anderson localization plays also an important role for the solvated electrons in amorphous ice. As already discussed in section 2.2 the injection of an excess electron proceeds via the ice conduction band followed by the initial trapping in a pre-existing potential minimum.

2.4.2 Water Adsorbed on Metal Surfaces

The adsorption of water on well-defined, metal surfaces has been extensively studied in the last decades and is still a topic of great interest also in recent investigations. The interaction of water with a metal surface governs a huge variety of processes in many areas of science ranging from catalytic surface reactions, processes at electrodes, wetting and corrosion to its importance in fuel cell reactions. The literature describing water adsorption at solid interfaces has been summarized in excellent reviews by Thiel and Madey [Thi87], Henderson [Hen02] and recently by Hodgson and Haq [Hod09].

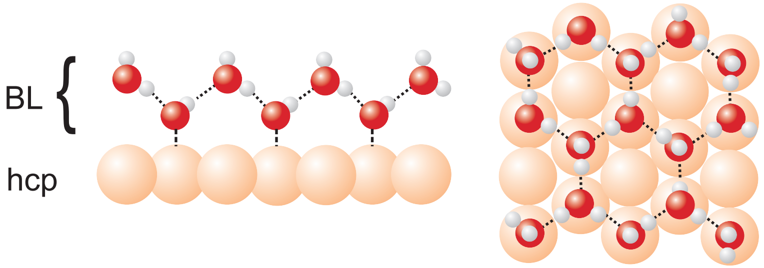

Figure 2.19: The structure of an ideal water bilayer adsorbed on a hcp metal surface in a side- and top-view.

The classical picture for the adsorption of water molecules on a metal surface is based on the concept of an ice bilayer (BL) as schematically depicted in Fig.2.19. In this structure every second water molecule is bound to the metal substrate by one lone pair of its oxygen atom. The remaining water molecules bind to the lower half bilayer via hydrogen bonds. The vertical distance between the oxygen plane in this buckled structure is ~ 0.9 Å. The partial orientation of the water dipole moments along the surface normal and a charge transfer from the molecules to the substrate result in a decrease of the work function by ~ 1 eV for Cu and Ru [Gah04]. However, the structure presented in Fig.2.19 is an ideal bilayer of bulk ice. The structure of water on a metal surface can deviate from this ideal bilayer as it is the case for the adsorption of water on Cu(111) and Ru(001) but also for other metal surfaces like Pt(111) and Ni(111).

On Pt(111) water molecules are not solely bond to the surface via the lone pairs of the oxygen atoms. Within the first BL all molecules bind directly to the surfaces through alternating metal-oxygen and metal hydrogen bonds, resulting in a flat water layer [Oga02a]. The adsorption structure of water on Ru, *i.e.* if the water molecules adsorb intact or half-dissociated, and in what orientation, is a subject of a long controversy [Hel94, Hel95, Fei02, Den03, Fei03, Pui03, Fei04, Men05]. Low energy electron diffraction (LEED) spectra show that water on Ru(001) forms a $(\sqrt{3} \times \sqrt{3})R30°$ overlayer. It was also found that the vertical distance between the oxygen atoms in the two half planes is only 0.1 Å [Hel94] and not 0.9 Å as expected from the bulk ice structure. Neither the expansion of the water layer due to the lattice mismatch nor a surface reconstruction of the Ru atoms in the first layer [Hel94, Pui03] are suitable to explain this deviation. A more reasonable explanation for the compression of the first bilayer takes into account dipole-mirror interaction and a large charge transfer to the metal substrate. Feibelman *et al.* found, on the basis of density functional theory (DFT) calculations, that the energetically most stable structure consists of a half-dissociated first layer wherein water molecules and hydroxyl fragments are hydrogen-bonded in a hexagonal structure and hydrogen atoms bind directly to the metal [Fei02]. This structure produces a $(\sqrt{3} \times \sqrt{3})R30°$ overlayer–like LEED pattern as observed by Held and Menzel [Hel94], because scattering by D atoms is weak.

However, the calculated decrease in the work function of 0.3 eV is, compared with 2PPE experiments where a decrease of 1.2 eV for the first BL was found [Gah04], too small. Theoretical studies by Meng et al., however, show that the half-dissociated structure is indeed the energetically most stable form but is kinetically not accessible because for D_2O the calculated activation barrier for dissociation is, with 0.62 eV, higher than the one for desorption, with 0.53 eV [Men05]. The different possible compositions of an intact water layer have also been controversy discussed. A structure is proposed where the hydrogen atoms of the outer water molecules point towards the metal substrate and not towards the vacuum. This structure is referred to as D-down [Den03]. A mixed D-up[18] and D-down structure is suggested by Meng *et al.* [Men05]. This mixed structure could as well explain the strong work function change upon bilayer adsorption, in contrast to a solely D-down configuration, which strongly underestimates the work function change [Men05]. Recent experiments performed by the group of A. Hodgson favor another scenario. By looking at the D_2O scissoring frequency, which is only present for intact water molecules, with reflection-absorption infrared spectroscopy they could unambiguously demonstrate the adsorption of an intact water layer [Cla04]. On the basis of helium atom scattering experiments and further

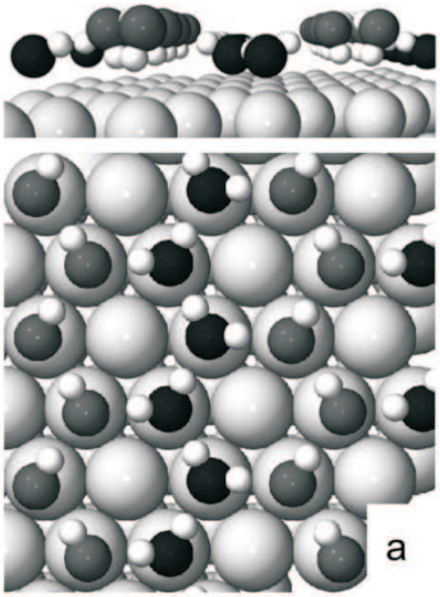

Figure 2.20: Structure of the wetting water layer on Ru(001). Chain structure showing water adsorbed ”flat” or ”H-down” in extended chains. The ”flat” water molecules have on hydrogen directed in plane along the chain and one tilted up towards the neighboring H-down chain. Adopted from [Haq06].

---

[18] Here the hydrogen atoms of the outer water molecules point towards the vacuum.

DFT calculations they propose a structure consisting of chains of flat lying molecules, bound atop Ru, in hexagonal network, and D-down chains as depicted in Fig.2.20 [Gal09, Hod09].

The growth of water films on Ru(001) can be described by the Stranski-Krasanov growth mechanism. After the completion of the wetting layer, which is fully covering the Ru(001) surface, 3D ice clusters form on top of the first bilayer [Haq07]. At temperatures of 140 K the water molecules are sufficiently mobile to form high crystallites and the wetting layer is still visible up to a coverage of ∼ 90 layers. Up to 3 BL the fraction of the wetting layer exposed decreases with increasing nominal coverage. As growth continues, the exposed fraction increases again to 60% for a coverage of 10 BL. This behavior shows the hydrophobic interaction to the wetting layer and the tendency to form 3D cluster instead of more extended 2D structures. For a nominal coverage of 10 BL crystalline ice clusters grow with a height of up to 30 layers. As already introduced in section 2.2.2 defects on top of these 3D crystalline clusters provide potential binding sites for excess electrons, which can trigger the dissociation of coadsorbed molecules as will be discussed in chapter 6.

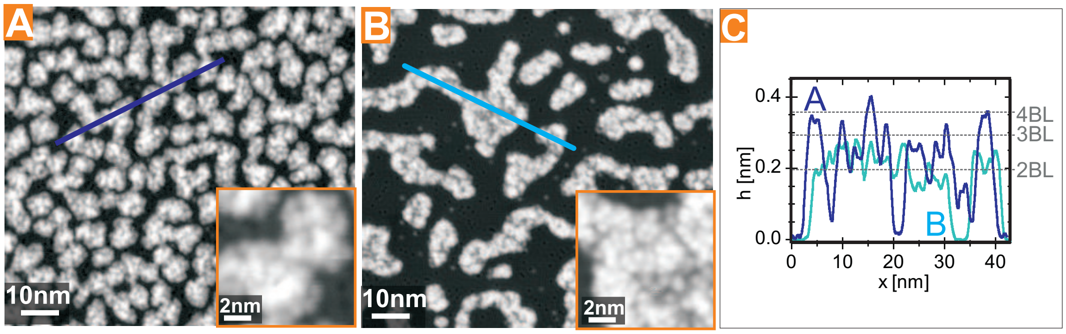

Figure 2.21: STM images of amorphous ice cluster on Cu(111): (A,B) STM images of porous and compact ice clusters adsorbed on Cu(111) with a nominal coverage of 1 BL. (C) Line scans reveal the height of the ice structures of up to 4-5 BL for porous and 2-3 BL for compact ice clusters. Modified from [Stä07a].

The growth of amorphous ice on Cu(111) differs significantly from the growth of crystalline ice on Ru(001) due to a significantly weaker water-metal interaction. A comparable interaction strength of the water-metal and the water-water bond is found by means of Thermal Desorption Spectroscopy (TDS) where predominantly zero-order desorption kinetics are observed [Bov03]. Additional information is gained by measuring the coverage dependence of the work function by 2PPE. The work function is lowered significantly upon water adsorption from $\Phi = 4.9$ eV for the clean Cu(111) surface. At a coverage of 3 BL the work function saturates at 3.95 eV, which suggests that ice adsorbs on Cu(111) initially not in a layer-by-layer growth mode. It rather takes about

3 BL before the Cu surface is completely covered by the adsorbate. Fig.2.21 presents STM images of porous and compact ice cluster on Cu(111) which have been taken by K. Morgenstern and coworkers [Stä07a]. Both images show a nominal water coverage of 1 BL. Porous cluster are prepared at 85 K, upon heating to 120 K for 2 s the cluster height shrinks from 4-5 BL to 2-3 BL for compact clusters (cf. line scans in Fig.2.21). At higher coverages (>3 BL) a smooth ice surface is observed by low-temperature STM which covers the Cu(111) surface completely [Gah03].

2.5 Electronic Properties of Chemisorbed Alkali Atoms on a Metal Surface

Alkali atoms adsorbed on a noble metal surface serve as a model system for adsorbate dynamics of chemisorbed species. The dynamics of the unoccupied alkali resonance, which is a consequence of a partial charge transfer of the alkali valence electron to the metal substrate, have been studied extensively theoretically [Bor02, But05, Gau07, Krö07] and experimentally [Fis94, Bau99, Pet00, Bor08, Zha08, Ste10].

In the low coverage regime the adsorption of alkali atoms is accompanied by significant changes of the work function. The evolution of the work function as a function of alkali coverage is depicted in Fig.2.22.(a) for Na adsorbed on a Cu(111) surface. With increasing alkali coverage the work function quickly decreases and reaches a minimum of $\Phi = 2.2eV$ at a coverage of $\sim$ 0.4 ML for Na/Cu(111). This change is due to a strong dipole moment induced by the positive alkali core and its image charge [Gau07]. In the low coverage regime, where the adsorbed alkali species do not interact with each other, it is proportional to the number of dipoles at the surface. When the alkali-alkali interaction becomes relevant, which reduces the effective dipole moment, the work function change deviates from its linear dependence on the coverage. Above half a monolayer the work function increases again until it reaches a value close to the

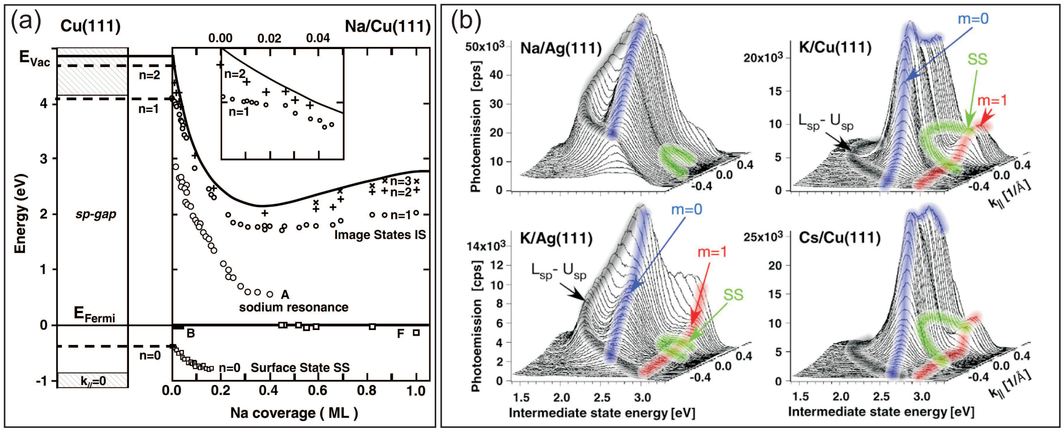

Figure 2.22: (a): Band scheme of the clean Cu(111) surface at $k_{\|} = 0$ (left) and electronic states of Na/Cu(111) as a function of Na coverage (right). Upon alkali adsorption the vacuum energy (solid line) and the binding energies of the occupied Cu(111) n=0 surface state, the unoccupied image potential states (n=1,n=2,n=3), and a Na-induced unoccupied state (A) are changing. Adopted from [Gau07], originally published in [Fis94].(b): 2PPE spectra as a function of intermediate state energy and $k_{\|} = 0$ for Na/Ag(111), K/Ag(111), K/Cu(111), and Cs/Cu(111). Highlighted are alkali localized m=0 (σ) and m=$\pm$1 (π) intermediate states, the surface state (SS) and the transition from the lower to the upper sp-band. Adopted from [Bor08].

work function of the bulk alkali metal at a coverage of about 1 ML [19]. The binding energies of the substrate-derived surface state and the first three image potential states are also strongly influenced by the adsorption of the alkali atoms. Their energetic position roughly follows the change of the vacuum energy of the system. The surface state disappears when it crosses the sp-band edge at 0.9 eV below E_F. For an alkali coverage below ~ 0.5 ML an alkali-localized resonance occurs at ~ 2 eV below the vacuum level. Typical 2PPE spectra of various alkali atoms adsorbed on Ag(111) and Cu(111) are depicted in Fig.2.22.(b). The resonance is formed by the ns and np_z valence orbitals of the alkali atom. Accordingly the alkali resonance is oriented perpendicular to the surface and exhibits a σ (m=0) symmetry (cf. blue highlighted peak in the 2PPE spectra in Fig.2.22.(b)) [Bau98, Gau07, Zha08]. Recently, Borisov *et al.* demonstrated the existence of a new alkali-induced resonance oriented parallel to the surface [Bor08]. In a joint experimental and theoretical study they assigned this resonance to an adsorbate-localized state formed by the mixing between the p and d valence orbitals of the alkali atom with a π (m=±1) symmetry (cf. red highlighted peak in the 2PPE spectra in Fig.2.22.(b)). Both alkali resonances exhibit a flat $k_\parallel = 0$ dispersion as can be seen in the angle-resolved 2PPE spectra in Fig.2.22.(b), due the weak interaction between separated alkali atoms in the low coverage regime.

The lifetime of the alkali σ resonance varies along the different alkali atoms [Bor02] and also strongly depends on the substrate [Chu06]. Along the sequence Na, K, Rb, Cs the lifetimes of the excited states increase [Bau97, Pet00, Bor02]. Three main processes contribute to the lifetime of an excited state at a metal surface:

(i) The resonant charge transfer (RCT) is an one-electron transfer process. The electron in an adsorbate state decays to an unoccupied metal state of the same energy. If the substrate provides unoccupied states at the energy of the excited adsorbate electron the RCT is usually the dominating decay channel [Gau07].

(ii) An excited electron can as well decay by an inelastic interaction, where the energy of a given electron is not conserved. Here, the excited electron scatters under excitation of an electron-hole pair of the substrate and partially transfers its energy. As multiple electrons are involved in this process, its decay rate Γ_{ee} is usually much smaller than the decay rate Γ_{RCT} of the RCT. However, it plays an important role for the decay of hot electrons or the decay of image states.

(iii) The third contribution is the electron-phonon channel, where the energy decays via electron-phonon scattering. It strongly depends on the distance of the excited state from the lattice. Usually this process is weaker than the other two decay channels.

The decay of the excited state of an adsorbed alkali atom on Cu(111) is mainly governed by the RCT. Both decay times follow the trend of the polarizability of the alkalis, which increases along the sequence Na, K, Rb, and Cs. Table 2.2 summarizes the

---

[19] With increasing alkali coverage the interaction of neighboring alkali atoms increases and the alkali adlayer becomes metallic. For Na/Cu(111) this transition occurs at 0.4 ML, where the sodium resonance lies below E_F and is therefor occupied (peak labeled with (F) in Fig.2.22.(a). Once the monolayer is completed quantum well states have been observed in these systems [Car97, Joh02, Hof03]

calculated values for the one-electron decay rate Γ_{RCT}, the inelastic electron-electron decay rate Γ_{ee}, and the corresponding level lifetime $\tau = \frac{\hbar}{\Gamma_{RCT}+\Gamma_{ee}}$.

Table 2.2: Decay rate of the first excited state of the alkali/Cu(111) systems taken from [Bor02]

	Na/Cu(111)	K/Cu(111)	Rb/Cu(111)	Cs/Cu(111)
Γ_{RCT} (meV)	70	16	10	7
Γ_{ee} (meV)	22	18	17	15
τ (fs)	7	19	24	30

Compared to alkali atoms on a free electron metal surface the calculated and experimentally observed lifetimes of the first excited state of alkali/Cu(111) are significantly longer [Bor01]. The long lifetime is a consequence of a ”quasi” blocking of the RCT by the projected band gap of the Cu(111) surface (L-band gap), so that the total decay rate of the excited state is dominated by the inelastic interaction with bulk electrons. Fig.2.23 depicts the wave-packet propagation for the first excited state in Cs/Cu(111) (a) and Cs adsorbed on a free-electron metal surface (b) as a function of coordinates parallel and perpendicular to the surface and the respective surface electronic band structures. The RCT decay of the excited state is an energy conserving transition that

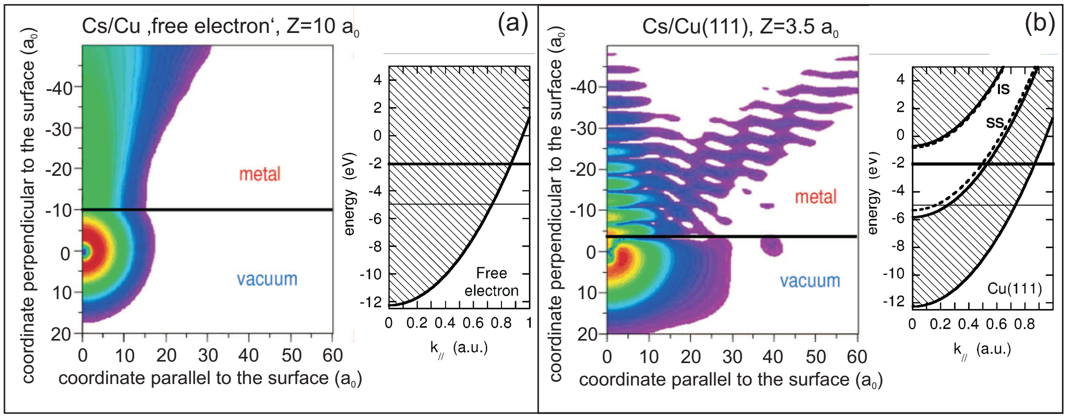

Figure 2.23: Wave-Packet for the Transient State in the Cs/Free-Electron (a) and Cs/Cu(111) (b) Metal Surface System. The red areas correspond to large probabilities for the electron. The Cs atom center is at the origin of coordinates. (a) The RCT decay of the excited state favors transitions to metal states around $k_{\|}=0$, which is possible in the surface electronic band structure of an free electron metal. (b) This is impossible on Cu(111), since there is not any $k_{\|}=0$ Cu state in resonance with the Cs state energy. Thus, the RCT decay can only populate large $k_{\|}$ states resulting in a drastic reduction of the RCT rate as compared with the free-electron case. Modified from [Chu06].

favors transitions to metal states around $k_{\|}$=0 (cf. Fig.2.23.(b)). However, the Cs state (black line in the surface electronic band structure in Fig.2.23.(b)) lies at $k_{\|}$=0 in the projected band gap of the Cu(111) surface. The excited electron can only decay to the surface state at larger $k_{\|}$ or to the bulk band. Accordingly, the RCT decay can only occur to electronic states at large values of $k_{\|}$ leading to a drastic reduction of the RCT rate as compared with the free-electron case.

The long lifetime of the excited electron in the alkali resonance of Cs/Cu(111) makes it a promising candidate for electron mediated surface reactions. Indeed, it was shown by Petek et al [Pet00] that an atomic motion in a copper-cesium bond-breaking process can be induced by laser excitation. Figure 2.24.(a) presents the potential energy surface for Cs on Cu(111). Initially, the Cs is at equilibrium position in its ground state (red curve) as a positively charged ion. By absorption of a photon of the pump pulse an electron from the substrate is transferred to the excited state (blue curve). As photoexcitation is faster than the nuclei motion the transition occurs vertically and the system evolves along the nuclei coordinate away from the surface. The motion of the wave packet can be observed because the change in the Cu-Cs distance is accompanied by a decrease in the energetic position of the alkali resonance (cf. Fig.2.24.(a). The resulting 2PPE spectra are plotted in Fig.2.24.(b) and show a clear shift of the

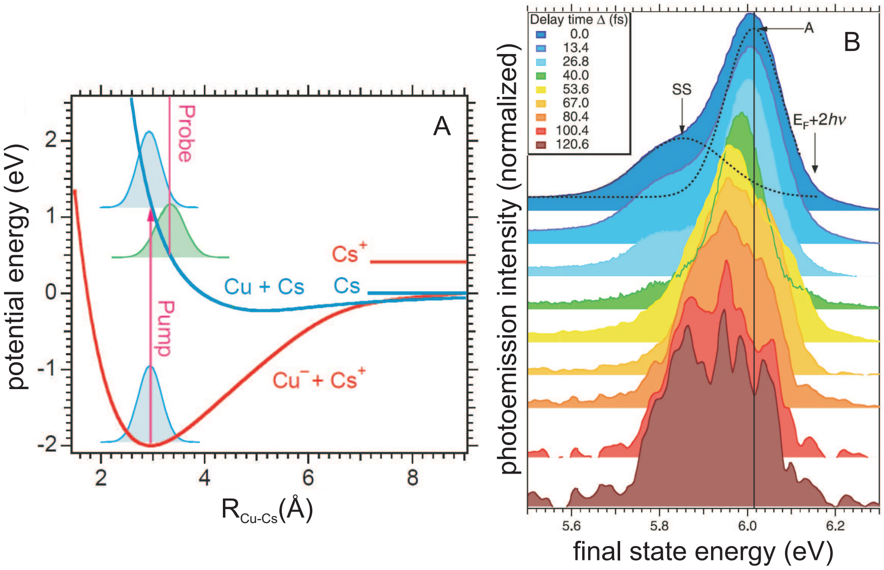

Figure 2.24: Adsorbate Atom Motion of Cs adsorbed on Cu(111). (A): Potential energy surface for Cs/Cu(111) as a function of the Cu-Cs internuclear coordinate R_{Cu-Cs}. The pump pulse excites the system, and the evolving wave packet can be probed by a time-delayed probe pulse. (B) 2PPE spectra of Cs/Cu(111) as a function of pump-probe delay. The contribution of the surface state and the alkali resonance are marked with SS and A, respectively. Modified from [Pet00].

electron distribution corresponding to the alkali-induced state A towards lower energies consistent with the dissociative motion of the Cs atoms. Although the excited state lifetime in Na/Cu(111) is considerably shorter than for Cs/Cu(111) a similar behavior has also been observed for the lighter alkali atoms [Weg09]. The energy shift of the maximum of the alkali resonance is slightly faster for Na Σ_{Na}=-1.95 meV/fs than for Cs Σ_{Cs}=-1.60 meV/fs.

After having introduced the investigated systems and the fundamental processes of electron solvation in water ice adsorbed on metal surfaces and possible reactions triggered by these excess charges, the experimental technique and the corresponding setup, sample preparation and data analysis will be presented in the following chapter.

3 Experimental Methods

In this chapter experimental details on time-resolved 2PPE measurements of ice-metal interfaces and related issues are presented. The first section provides a description of the employed technique, namely time-resolved two-photon photoelectron spectroscopy. In the following the experimental setup is presented. Details on the optical setup including the femtosecond laser system, the UHV chamber equipped with standard surface science tools and the electron time-of-flight (TOF) spectrometer are given. Finally the sample preparation and characterization procedures are discussed.

3.1 Photoelectron Spectroscopy

Photoemission spectroscopy (PES) is a well-established method to investigate the occupied electronic structure of solids and interfaces. In addition, information about the final (unoccupied) states can be obtained. The short mean free path of the escaping photoelectrons in the solid makes PES especially suitable to investigate surface phenomena. Absorption of a photon excites electrons above the vacuum level of the system where they are detected with regard to their kinetic energy E_{kin} and emission angle α [Hüf95]. Together with the knowledge of the photon energy $h\nu$ one can then deduce their binding energy E_i and dispersion parallel to the surface[20] $k_{\|}$. The kinetic energy of the photo electron is given by:

$$E_{kin} = h\nu - (E_i - E_F) - \Phi, \tag{3.8}$$

where Φ is the work function and E_F is the Fermi level of the system. Furthermore, the symmetry of the investigated state can be accessed by polarization-dependent measurements.

In the sudden approximation it is assumed that the photoemission from an initial N-particle system to the final N-1 electron state occurs much faster than the electronic system relaxes the excited electronic state. This assumption is closely related to Koopmanns' theorem where the measured ionization energy $E - E_F$ is equal to the orbital energy of the N electron state [Koo34]:

$$E - E_F \simeq \epsilon. \tag{3.9}$$

This one electron scenario is a simplification of the process and neglects for example many-body and electron relaxation effects. Many-body effects have to be considered especially in materials that are strongly correlated and where Coulomb interactions of electrons play a significant role. Electron relaxation describes the fact that when an electron is emitted from a N-particle system, the remaining N-1 electrons relax into a new energy state with a lower energy of $\epsilon_{N-1} - \delta E_{relax}$ so that:

$$\epsilon_N \neq \epsilon_{N-1}, \tag{3.10}$$

---

[20] Further details on dispersion measurements are given in section 3.1.3.

where ϵ is the orbital energy of the respective state. Nevertheless, the corrections for electron-electron correlation effects δE_{corr} and the corrections for the relaxation of the orbitals δE_{relax} are comparable but of opposite sign so that the Koopman's theorem (3.9) provides a reasonable approximation for the binding energies in photoemission.

3.1.1 One- and Three-Step Model of Photoemission

For a detailed description of the photoemission process one needs to consider many-body effects as all initial and final states have to be addressed. Nevertheless, phenomenological models which simplify the problem have been developed. Fig. 3.1 depicts an illustration of the three- and one-step model of photoemission [Hüf95]. Especially the three-step model has proven to be extremely useful.

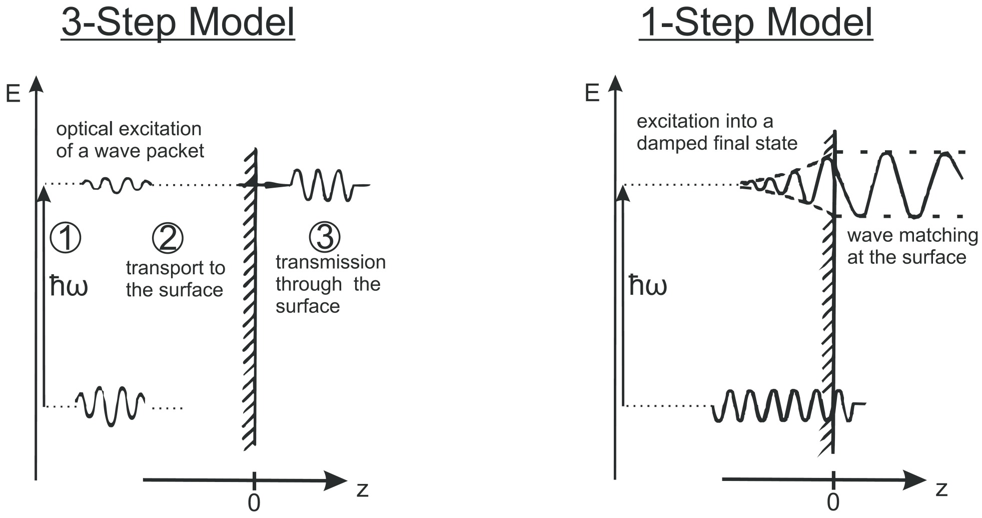

Figure 3.1: One- and three-step model of photoemission. Three-step model: (1) Photoexcitation of an electron followed by (2) its travel to the surface and (3) transmission into the vacuum. One-step model: Coupling of a Bloch state, residing int the crystal by the optical field to a freely propagating wave that decay exponentially into the bulk. Adopted from [Hüf95].

Three-Step Model

The three-step model separates the photoemission process into three distinct and independent parts [Ber64a, Ber64b].

1. In the first step an electron is locally excited from an initial to a final state within the band structure of the substrate by adsorption of a photon. The momentum of

the photon can be neglected so that the transition occurs vertical and conserves momentum.

2. The second step involves the transport of the electron to the surface, where scattering events occur, electron-defect and mainly e-e scattering, which reduce the number of electrons reaching the surface. The inelastic scattered electrons, which experienced a variation of their energy and momentum, contribute to the background of the photoemission signal. Furthermore, the scattering induces the energy-dependent mean free path of the electrons and their escape depth of 5 - 100 Å determines the surface sensitivity of photoemission spectroscopy.
3. In the last step the electron escapes through the surface and propagates in the vacuum to the detector. In this process the component of the momentum parallel to the surface $k_\parallel$ is conserved in a translational invariant (periodic) system, whereas its perpendicular component $k_\perp$ is reduced by the work function of the system.

In the three-step model the photoemission current is given by:

$$I_{PE}(k_\parallel, E_{kin}) = T(E_{kin})D(E_i)D(E_f)M_{if}\int_0^\infty f(E_i)A(k_\parallel, E_i)e^{-z/z_0}dz \ , \tag{3.11}$$

where T is a transmission function, D describes the density of states of the initial E_i and final state E_f, M_{if} is the respective transition matrix elements, f is the distribution function, A is the one-particle spectral function, and z_0 is the mean escape depth [Sch03].

One-Step Model

In the one-step model a Bloch wave (initial state) inside the crystal is optically coupled to a plane wave in the vacuum (final state), which is decaying exponentially inside the bulk (cf. right panel of Fig.3.1). The penetration depth is given by the elastic mean free path. This can as well be described as the time reversal of the LEED process, where an electron is impinging on the metal surface with an energy-dependent penetration depth. The advantage of the one step model is that good theories already exists that can describe the LEED process very accurately and can now be used for photoemission as well. Due to this similarity the final states in photoemission are also termed inverse LEED states Ψ_{LEED} and the photo current is proportional to:

$$I_{PE}(k_\parallel, E_{kin}) \propto \sum |\langle \Psi_{LEED}(E_f)|W|\Psi_i\rangle|^2 A(k_\parallel, E_i) \ . \tag{3.12}$$

Here, the operator W describes the interaction of the vector potential $\vec{A}$ of the optical field with the electrons and can be approximated by:

$$W = A_0\delta(E_f - E_i)\vec{e}\cdot\vec{r} \ , \tag{3.13}$$

where A_0 is the amplitude of the light wave, $\vec{e}$ its polarization vector, and E_i and E_f are the initial and final state energies, respectively.

3.1.2 Two-Photon Photoemission

Supplementary to the ability of investigating the occupied electronic structure of a system by one photon PES, Two-Photon Photoemission Spectroscopy (2PPE) provides the possibility to study unoccupied electronic states between the Fermi- and the vacuum-level of the system [Fau95, Pet97]. In the 2PPE process an electron from below the Fermi level is excited by absorption of a photon to an unoccupied intermediate state, located below the vacuum level of the system. Subsequently, absorption of a second photon excites the electron above the vacuum level, where it can propagate freely and is detected by a TOF spectrometer. In contrast to direct photoemission 2PPE is a 2nd order non-linear process and, therefore, requires high laser intensities. These high spatial and temporal photon densities are achieved by employing pulsed lasers with femtosecond pulse duration. Details on the generation of short laser pulses and the employed laser system are given in section 3.2. On the one hand, the photon energies are chosen to be large enough such that all intermediate states of interest can be excited and that all these states can as well be probed by exciting them above the vacuum level. On the other hand, in most cases the photon energies should be smaller than the work function of the system in order to avoid direct photoemission from states below the Fermi level[21]

Excitation Mechanism

Several different excitation channels are possible in the 2PPE process and need to be considered when analyzing a 2PPE spectrum. Three different excitation mechanism are depicted in Fig.3.2. The first mechanism depicts a direct excitation and population of an intermediate state (a). A first photon with the photon energy $h\nu_1$ excites an electron from below the Fermi level into the real intermediate state where the population of this state is probed by absorption of a second photon with $h\nu_2$ which excites the electron into the final state. A real final state in the vacuum is always available since the states above the vacuum level form a continuum of states. If no real intermediate state is in resonance with the initial state the excitation of an electron from below the Fermi level into the final state can occur *via* a virtual intermediate state (c). Photoemission via virtual intermediate states arises from the transient second order polarization in the presence of the strong laser fields used in 2PPE. It can be visualized as simultaneous absorption of two photons. As apparent from Fig.3.2 (a) and (c) both excitations can lead to the same final state energy. Nevertheless, a discrimination of both mechanism is possible on the basis of their different behavior upon changing the pump photon energy $h\nu_1$. If the excitation occurs *via* virtual intermediate states the position of the according peak in the 2PPE spectrum shifts by $\Delta h\nu$, when the pump photon energy is changed by the same amount $\Delta h\nu$. The position of the peak is not changing in the spectrum when excitation proceeds via a real intermediate state. The ability to

---

[21] The excitation probability for direct photoemission is significantly higher than the one for a two- or even three-photon process. As a consequence a spectrum taken with a photon energy higher than the work function would be strongly overlapped by the one-photon signal. Nevertheless, it is as well possible to detect direct and two-photon photoemission electron in one spectrum.

discriminate the two excitation pathways by changing the pump photon energy is only given in case that the involved states do not exhibit a dispersion along $k_\perp$, as it is for instance the case for surface states. The third possibility describes a non-resonant and indirect excitation of a real intermediate state and is depicted in Fig.3.2 (b). Here, the intermediate state is populated *via* inelastic scattering processes with other electrons, defects or phonons from another intermediate state. Due to the scattering processes involved the momenta of the scattered electrons is not conserved.

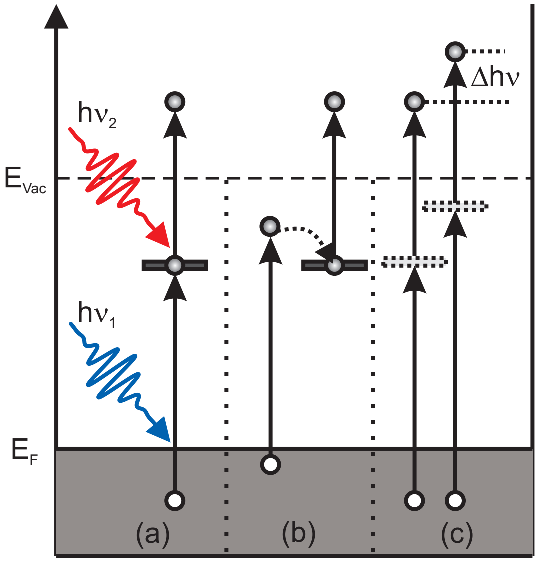

Figure 3.2: 2PPE excitation mechanism: (a) Direct resonant excitation *via* a real intermediate state. (b) Non-resonant excitation involves secondary scattering processes. (c) Indirect excitation *via* a virtual intermediate state. The processes can be distinguished by their different photon energy dependence. For further details see text.

Time-Resolved Two-Photon Photoemission

A further advantage of 2PPE spectroscopy is the ability to directly investigate the temporal evolution of an electronic relaxation after an optical excitation. The basic principle of a time-resolved 2PPE experiment is depicted in Fig.3.3. The experiments are conducted in a pump-probe scheme and the time resolution is achieved by delaying pump- and probe-pulse in time with respect to each other. An unoccupied intermediate state is excited by absorption of a first photon. A second photon, which is delayed in time by Δt, excites the electron above E_{Vac}. In this way the transient population of the intermediate state is probed by varying the time delay Δt. The assignment of the photons to pump- and probe-pulse is not unambiguous as the order of arrival of the laser pulses can also be reversed. Within this thesis all experiments were conducted using visible (VIS) and ultraviolet (UV) photons. Usually, the UV photons served as the pump-pulse and the VIS photons as the probe-pulse[22]. Accordingly, in the time-resolved 2PPE spectra this photon order is at the "positive" side of the time zero,

---

[22] The excitation of the system with UV photons allows for an investigation of unoccupied intermediate state at higher energies above the Fermi level, *e.g.* image potential states.

where both laser pulses arrive simultaneously at the sample. The reverse order is in the following referred to ”negative” time delays. The achieved time resolution in these experiments lies at approximately 1/10 of the laser pulse duration. The pulse duration lies, depending on the employed laser source and photon energy, in the range of 50 - 60 fs, so that a time resolution of around 5 fs was achieved. The temporal delay between the laser pulses is realized by sending one beam over a computer controlled delay stage[23].

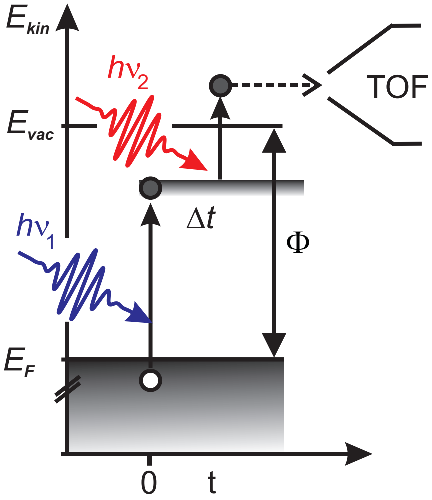

Figure 3.3: Scheme of time-resolved 2PPE spectroscopy. An electron from below the Fermi level is excited to an intermediate bound state by absorption of a photon with the photon energy hν_1. The transient population of this state is probed by absorption of a second photon with hν_2. The kinetic energy of the photoemitted electrons is analyzed in a time-of-flight (TOF) spectrometer. The pump-probe time delay Δt enables the time resolution.

3.1.3 Time-of-Flight Spectrometer and Energy- and Momentum Conversion

The 2PPE spectra were recorded using a linear time-of-flight spectrometer. A detailed description of the spectrometer and the signal processing can be found in [Kno97, Hot99, Gah04] and is only briefly reported here. The main part of the spectrometer is a field-free flight tube allowing for the unperturbed propagation of the photo-emitted electrons. The spectrometer is surrounded by a μ-metal shielding to screen the electrons from external magnetic fields. The laser light can enter and exit the spectrometer by drill holes in the shielding. In order to avoid electrical fields caused by inhomogeneities of the work function of the employed materials, the flight tube and its conical entrance tip is made of graphite coated aluminum. The sample is positioned such, that the laser beams hit the sample surface under an angle of 45° with respect to the spectrometer axis on a spot that is 3 mm away from the entrance tip. After passing through the flight tube the electrons are detected by a pair of micro channel plates. The resulting voltage pulse is coupled out of the vacuum by a capacitor and serves as the ”stop”-pulse for the determination of the flight time. The ”start” pulse comes from a leakage pulse

---

[23] Details on the optical beam path are given in section 3.2.

of the *RegA* (cf. Fig.3.7), which is detected by a fast photo diode.

The work function difference of the spectrometer ($\Phi \simeq 4.45$ eV) and the sample can be compensated by applying a bias voltage between the sample and the grounded flight-tube. The resulting potential difference eU is given by the work function of the sample Φ_{sample} and the spectrometer Φ_{spec} and the applied bias voltage U_{bias}:

$$eU = \Phi_{sample} - \Phi_{spec} + eU_{bias}. \tag{3.14}$$

Fig.3.4 shows a potential diagram between sample and spectrometer. The bias voltage U_{bias} is used to compensate for the work function differences of the sample and the spectrometer, allowing even the detection of the slowest photoelectrons. Neglecting the short acceleration of the electrons by this potential the kinetic energy of the photo emitted electrons is given by:

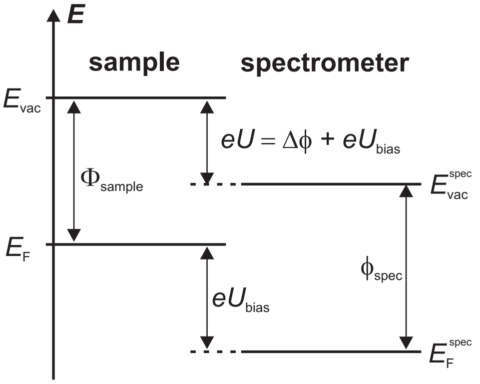

Figure 3.4: Potential gradients between Sample and Spectrometer. The sample can be biased with a voltage U_{bias}, whereas the spectrometer is permanently grounded. The kinetic energy is always measured with respect to the vacuum level of the spectrometer E_{vac}^{spec}.

$$E_{kin} = \frac{1}{2} m_e \left(\frac{L}{(t_m - t_0)} \right)^2 - eU, \tag{3.15}$$

where L is the total traveling distance of the electrons of 300 mm. The actual flight time t differs from the measured flight time t_m by a constant offset t_0, that is mainly given by the runtime of "start"-signal in the electronics. The unknown constant t_0 can be derived from a series of measurements with different bias voltages since the bias voltage U_{bias} and the measured flight time occur with different powers in equation 3.15. The conversion from flight time to energy requires to re-scale the intensities according to:

$$P(E) = \left| \frac{dE}{dt} \right|^{-1} P(t) = \frac{t^3}{m_e L^2} P(t). \tag{3.16}$$

The width of the secondary edge in the spectrum is a good measure for the energy resolution of the spectrometer. It is independent of the spectral width of the laser pulse and thus provides an upper bound for the spectrometer resolution. For electrons with a kinetic energy of up to 1 eV and between 1-3 eV the energy resolution is 13 and 25 meV, respectively [Hot99, Gah04].

The sample can be rotated in the spectrometer by ± 16° with respect to the surface normal enabling angle-resolved 2PPE measurements. In this way information on the electron momentum $\hbar k_{\|}$ parallel to the surface plane can be gained. As the momentum of the absorbed photon can be neglected and the Cu(111) surface is translational symmetric, $k_{\|}$ is conserved. The electron momentum $k_{\|}$ can be calculated by:

$$k_{\|}(\varphi, E_{kin}) = sin(\varphi)\sqrt{\frac{2m_e}{\hbar^2}E_{kin}}, \tag{3.17}$$

where φ is the emission angle of the photo electrons with respect to the surface normal.

3.1.4 Data Analysis

Photoelectron Spectra and Energy Scaling

The 2PPE spectrum of a clean Cu(111) surface is depicted in Fig.3.5 and shows the 2PPE intensity as a function of the kinetic energy of the photoemitted electrons. The spectrum exhibits a characteristic feature of the Cu(111) surface and two additional features which are a global signature in all PES spectra. The peak $E_{kin} \simeq 1.2$ eV originates from electron which are excited out of the occupied Cu(111) surface state by adsorption of two UV photons. Furthermore, the spectrum presents two cut-offs. Their position is determined by the Fermi- and vacuum-level of the sample and by the employed photon energies as depicted in Fig.3.5. In equilibrium at T=0 K all electronic states in a metal are occupied up to the Fermi energy E_F so that only electrons below or at the Fermi level can be photoexcited. Hence, the electrons with the highest kinetic energy in the spectrum originate from electrons from the Fermi level that were excited by absorption of at least two photons. The high energy cut-off in the spectrum is referred to as Fermi edge. For multi photon processes all combinations of photons, $n \cdot h\nu_1 + m \cdot h\nu_2$ [24] can lead to a Fermi edge in the spectrum, so that several Fermi edges can be observed especially when two-color experiments are performed. The second cut-off at the low-energy side of the spectrum originates from electrons which have just sufficient energy to exactly overcome the sample's work function after absorption of two photons. On the basis of the position of the Fermi- and secondary-edge and the knowledge of the used photon energy one is now able to determine energy scales which are related to properties of the investigated system like the Fermi energy and the vacuum energy.

The measured kinetic energies are obtained by measuring the flight time of an electron in the detector, described in detail in section 3.1.3, and converting it into the kinetic energy of the photo emitted electron. The measured kinetic energy $\tilde{E}_{kin}$ corresponds to the "real" kinetic energy E_{kin}, the energy gain by the applied bias voltage

---

[24] n and m are positive integers. Higher order Fermi edges with n or m > 1 are as well observable, although the probability of multi-photon process decreases with the number of involved photons, which leads to a significant reduction of the 2PPE intensity.

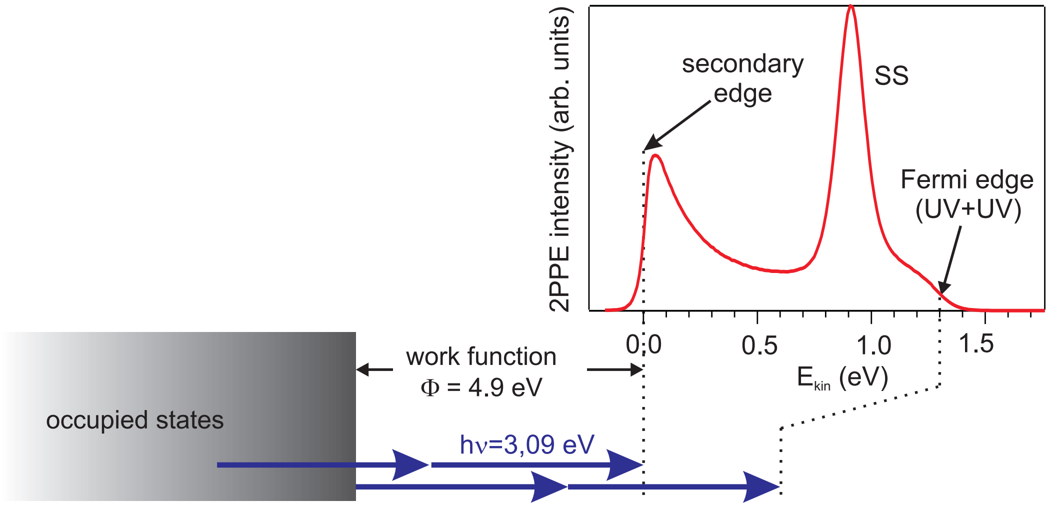

Figure 3.5: Exemplary 2PPE spectrum of Cu(111). Besides the Cu(111) surface state (SS) the spectra exhibits two features, which are referred to as secondary edge at the low energy side and Fermi edge at higher energies. The secondary edge originates from electrons which just overcome the vacuum level of the system, whereas the Fermi edge arises from electron excited from the Fermi level of the sample by two UV photons.

eU and the difference of the work function of the spectrometer and the sample $\Delta\Phi$:

$$\tilde{E}_{kin} = E_{kin} + eU + \Delta\Phi. \tag{3.18}$$

As described before, the secondary edge in the spectrum can be attributed to the vacuum level of the sample, whereas the Fermi edge is related to the Fermi level of the investigated system. Hence, the "real" kinetic energy and the work function can be obtained from the well-defined signatures in the 2PPE spectrum. The "real" kinetic energy is:

$$E_{kin} = \tilde{E}_{kin} - \tilde{E}_{kin}(secondary\ edge), \tag{3.19}$$

and the work function of the sample is given by the energy difference between the vacuum level $\tilde{E}_{kin}$(secondary edge) and the Fermi level $\tilde{E}_{kin}$(Fermi edge) and the sum of the photon energies:

$$\Phi = \tilde{E}_{kin}(secondary\ edge) - \tilde{E}_{kin}(Fermi\ edge) + h\nu_1 + h\nu_2. \tag{3.20}$$

In addition to electrons that are excited by a photon of the pump- and probe-pulse, respectively, multi-photon excitations within one laser pulse are possible, as long as the sum of photon energies $E = \sum h\nu$ is large enough to overcome the system's work function. As a consequence, a time-resolved 2PPE spectrum contains as well temporally uncorrelated signals that are independent on the time delay between pump- and probe pulse. In time-resolved measurements this fraction is usually subtracted as a background signal.

The 2PPE spectra can be plotted as a function of different energy scales with different reference energies depending on the origin of the spectral features of interest. In the case of image-potential states one usually uses the binding energy of these states with respect to the vacuum level of the system. This choice is reasonable because these states are often "pinned" to the vacuum level and, therefore, react on changes of the work function. The binding energy with respect to the vacuum level E_{vac} is given by:

$$E - E_{vac} = \tilde{E}_{kin} - \tilde{E}_{kin}(secondary\ edge) - h\nu_{1,2}. \tag{3.21}$$

When working with a two-color setup, *i.e.* different photon energies for pump- and probe-pulse, two different binding energy scales are possible depending on which laser pulse pumped or probed the state. Subtracting $h\nu_1$ in equation 3.21 yields the binding energy axis of states excited with $h\nu_1$ and probed with $h\nu_2$.

Another reasonable reference point is the Fermi level of the system. An energy axis related to the Fermi level is especially useful when investigating unoccupied intermediate state in 2PPE and is mostly used within this thesis. The intermediate state energy describes the energy with respect to the Fermi level E_F and is given by:

$$E - E_F = \tilde{E}_{kin} - \tilde{E}_{kin}(Fermi\ edge) + h\nu_{1,2}. \tag{3.22}$$

Again, two different energy scales are possible depending on the laser pulse sequence. The intermediate state energy of electrons excited by photons with the energy $h\nu_1$ and probed by photons with $h\nu_2$ results from equation 3.22 by adding the photon energy $h\nu_1$.

As already mentioned before in section 3.1.2 both laser pulses can serve as pump- or probe pulse depending on their time delay and the origin of the electronic state. for the choice of the correct energy axis, however, this knowledge is required. One way to determine this knowledge is to vary the photon energy of one of the laser pulses like it is described in section 3.1.2. Another way to access the origin of the electronic state and the sequence of the laser pulses is achieved by employing time-resolved measurements that are directly revealing the development of the transient population after excitation by photons with $h\nu_1$ or $h\nu_2$.

Time-resolved 2PPE and Population Dynamics

Time-resolved 2PPE spectroscopy allows for the investigation of electron dynamics at adsorbate covered metal interfaces including the direct observation of the population dynamics of excited states and the temporal evolution of their binding energy. Fig.3.5 exemplarily depicts a time-resolved 2PPE measurement of 0.1 ML Cs adsorbed on Cu(111). Panel (a) presents the 2PPE intensity in a false color representation as a function of intermediate state energy $E - E_F$ (left axis) and pump-probe time delay (bottom axis). The color scale proceeds from blue, indicating low 2PPE intensity, to white, indicating high 2PPE intensity. For simplicity, this two-dimensional representation of a time-resolved 2PPE measurement will be referred to as 2D-plot. As depicted in panel (b) of Fig.3.5, ”negative” time delays correspond to electrons excited by VIS laser pulses $h\nu_2$ and probed by UV laser pulses $h\nu_1$, whereas electrons are excited and probed by the inverse pulse sequence for ”positive” time delays.

Vertical cuts through the 2D plot at fixed time delays Δt yield 2PPE spectra for given time delays. In Fig.3.6(c) 2PPE spectra at time delays of $\Delta t = 0$, 20, 60, and 100 fs are presented. On the basis of such a series of 2PPE spectra information on the spectral evolution of electronic states, like transient changes in the binding energy, can be gained. Cross correlation (XC) traces are depicted in panel (d) of Fig.3.6 as a function of time delay. The XC traces for an electronic state are obtained by integrating the 2PPE signal over a specific energy window that includes the entire intensity distribution of the state. The XC traces provide information on the population dynamics of an excited electronic state. A more detailed description of the analysis of the XC traces is given in the course of the present section.

The 2D plot in Fig.3.6(a) shows two characteristic features of an alkali/metal interface. The peak around $E - E_F = 2.5$ eV, better seen in the 2PPE spectrum at $\Delta t = 0$ fs, is associated with photo emitted electrons from the occupied Cu(111) surface state. The peak at higher intermediate state energies originates from electrons that are excited by photons with the energy $h\nu_1$ into the unoccupied alkali resonance. The population of this state is then probed by absorption of $h\nu_2$ photons. This feature clearly presents a lifetime which can as well be seen in the asymmetry of the corresponding XC trace (green symbols) in panel (d) of Fig.3.6. The XC trace is well reproduced by a fit (solid green line) that considers a single exponential decay yielding a decay time of $\tau = 24(5)$ fs. The red markers in panel (d) represent the XC of the employed laser pulses. Analyzing the pulse duration following the analysis that is discussed in section 3.2.2 yields a pulse duration of 46 fs. More details of the alkali resonance that is formed by the ns and np_z valence orbitals of the alkali atom were given in section 2.5.

In order to analytically describe the decay rates in an optically coupled 3-level system, including an initial, intermediate and final state optical Bloch equations can be employed [Lou00]. However, the dephasing parameters of the system need to be known. Nevertheless, the optical Bloch equations can be simplified to a set of classical rate equations, when the excitation is limited to non-resonant transitions. Accordingly the time-dependent 2PPE response function of an intermediate state can be described following the equation:

$$I(\Delta t) \propto \int\int dt'dt'' I_1(t') I_2(t'' - \Delta t) R(t'' - t'), \tag{3.23}$$

where I_1 and I_2 describe the transient intensity of the pump- and probe pulses and R(t) is the response function of the intermediate state. For an intermediate state with a finite lifetime the XC trace can be fitted on the basis of equation 3.23 and the population decay of the state can be written as:

$$N(\Delta t) = A \cdot exp\left[-\frac{\Delta t}{\tau}\right] + B, \tag{3.24}$$

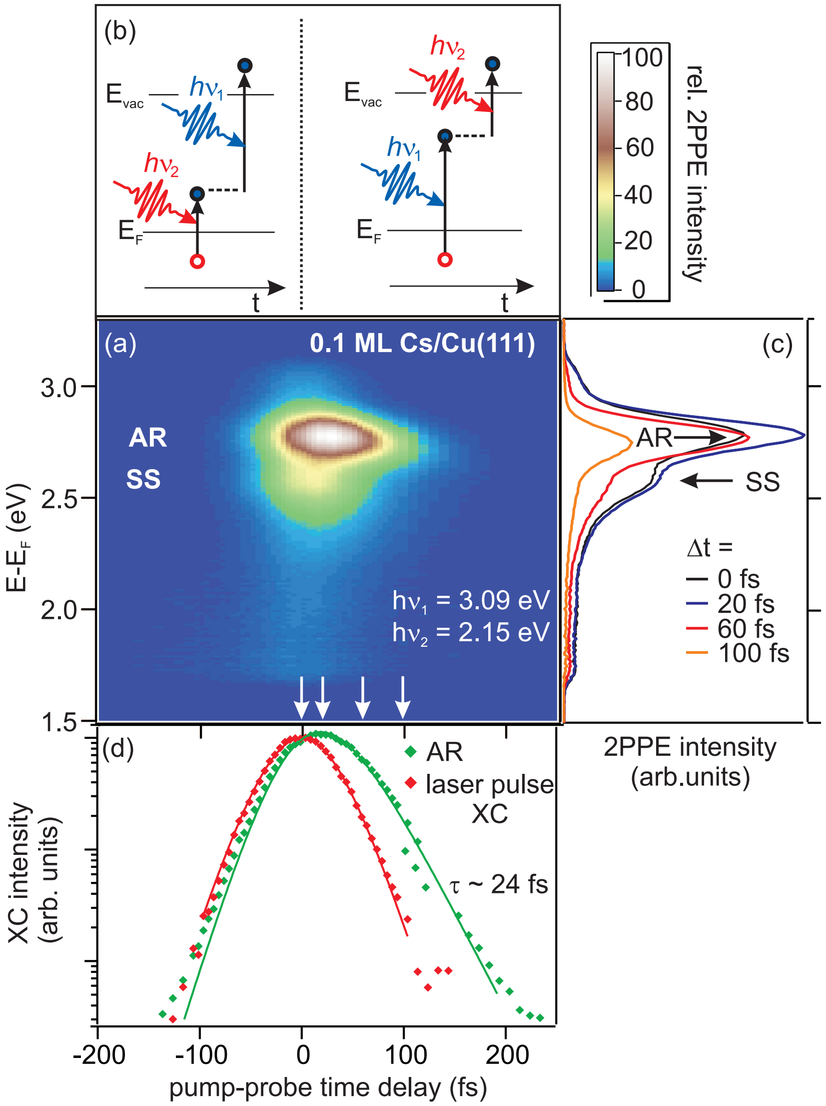

Figure 3.6: Time-resolved 2PPE spectrum of 0.1 ML Cs/Cu(111). (a) 2PPE intensity in a false color representation as a function of intermediate state energy $E - E_F$ (left axis) and pump-probe time delay (bottom axis) The white arrows mark the time delay of the 2PPE spectra presented in panel (c). (b) Scheme of the pulse sequence for "negative" delays: $h\nu_2$-$h\nu_1$ and "positive" delays: $h\nu_1$-$h\nu_2$. (c) Vertical cuts through the 2D plot taken at different time delays as indicated. The spectra exhibit different features associated to the unoccupied alkali resonance (AR) and the Cu(111) surface state (SS). (d) Cross correlation (XC) traces as a function of pump-probe delay for the state AR, which shows a clear asymmetry indicating a lifetime towards positive delay, whereas the XC of the laser pulses taken at E$_F$ is symmetric.

assuming a single exponential decay. Here, A is the amplitude, τ the decay rate and B a constant offset. By convoluting equation 3.24 with the XC of the employed laser pulses

$$F_{XC}(t) = \int dt' I_1(t) I_2(t-t') \tag{3.25}$$

the time-dependent data can be reproduced. The fit (green solid line) of the XC of the alkali resonance (green symbols) depicted in Fig.3.6 (d) was obtained following this procedure.

3.2 Laser System

Employing 2PPE spectroscopy requires the use of very short and intense laser pulses in order to provide the high temporal and spatial photon density that is needed to efficiently drive the non-linear optical processes. In this work these laser pulses are provided by a commercial, tunable femtosecond laser system from *Coherent* that consists of an oscillator with a titanium-doped sapphire (Ti:Sa) crystal (*Mira*) and a regenerative amplifier (*RegA* 9050), which are both pumped by a diode-pumped cw solid-state laser (*Verdi V-18*). Furthermore, the amplified laser pulses can pump two optical parametric amplifiers (OPA) or a home-build non-collinear optical parametric amplifier (NOPA). The laser system is schematically depicted in Fig.3.7.

3.2.1 Generation and Amplification of fs-Laser Pulses

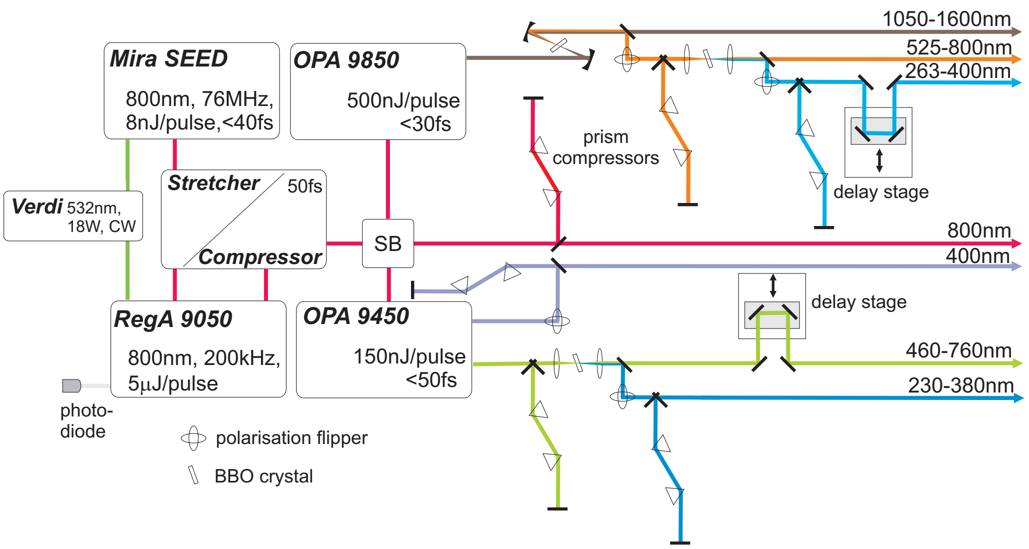

Figure 3.7: Laser System

A titanium doped sapphire crystal (Ti:Sa) serves as the active laser medium in the oscillator, where the femtosecond laser pulses are generated [Coh96]. Ti:Sa exhibits a broad, vibronic emission spectrum ranging from 670 to 1070 nm, with a maximum at 790 m. The crystal is pumped via a broad absorption band (400 - 600 nm) centered at 490 nm. Due to the long lifetime of the excited states the Ti:Sa crystal can be pumped by a cw-laser. The employed *Verdi V-18* provides cw laser light at 532 nm. A Nd:YVO_4 crystal pumped at 808 nm by two laser diodes serves as the active medium. The output is achieved by frequency doubling in a KDP crystal. By constructive interference of longitudinal modes short laser pulses are generated in the resonator of the *Mira*. Following the time-bandwidth product:

$$\frac{\lambda^2}{\Delta\lambda} = c \cdot \Delta t, \tag{3.26}$$

where λ is the central wavelength and c is the speed of light, the pulse duration is inverse proportional to the bandwidth of the mode-locked spectrum. In this oscillator mode-locking is realized with the help of the Kerr-Lens effect, which occurs for high intensities in the Ti:Sa crystal. This effect results from the intensity-dependent, non-linear fraction of the refractive index n:

$$n(\omega, I) = n_0(\omega) + n_2(\omega) \cdot I. \tag{3.27}$$

Due to the Kerr-Lens effect, the varying intensity over the spatial beam profile causes a spatial distribution of the refractive index. Hence, intense laser pulses, i.e. short laser pulses, are focussed by this lens, whereas less intense cw-modes are not focussed. By a slit in the cavity placed in the focal plane of this lens weak parts of the laser pulses are blocked. The cavity includes a prism compressor which compensates for the positive chirp, which the laser pulses experience during their travel through optical media inside the cavity, in order to keep the pulse duration short. Furthermore, a birefringent filter in the cavity allows for a variation of the central wavelength in the range from 750 to 850 nm. Based on the length of the resonator and the speed of light the *Mira* operates at a repetition rate of 76 MHz and delivers laser pulses with a duration of $\sim$ 50 fs and an energy of $\sim$ 8 nJ per pulse.

However, in order to use one of the OPA's or the NOPA the pulse energy needs to be raised by three orders of magnitude to obtain the required energy on the order of μJ. Before the *Mira* output pulses can be amplified in the *RegA* they first get stretched in time to reduce the high peak intensities, which can lead to damage in the active medium. In the *strectcher* the pulses pass through optical components with a normal group velocity dispersion (GVD)[25], which leads to a temporal stretching of the pulses to pulse durations of several nanoseconds. After the amplification the laser pulses are

---

[25] The dispersion of the group velocity v_g leads to different v_g for different spectral components of the pulse. For normal linear GVD the low energy components of the spectra (red) have a higher v_g than the high energy components (blue). To compensate this effect the laser pulses travel through an optical component with a negative GVD.

compressed in the time domain by passing through four gratings, which are introducing a negative GVD so that in addition also higher order GVD can be compensated.

Similar to the *Mira*, The *RegA* consists of a cavity with a Ti:Sa crystal that is pumped by the main fraction of the *Verdi V-18* output. During the build-up of population inversion spontaneous lasing is hindered by a quality switch (Q-switch) that reduces the quality of the cavity. At the maximum of the inversion a single laser pulse from the Mira is coupled into the cavity by an opto-acoustic modulator (cavity-dumper) and the Q-switch minimizes losses. Now the pulse is traveling through the resonator and reduces the population inversion in the Ti:Sa crystal while the laser pulse is gaining intensity. After $\sim$ 25 round trips the maximum intensity is reached and the pulse is coupled out of the cavity by the cavity-dumper. After the cavity quality is reduced again by the Q-switch a new amplification cycle can than start following the above described sequence. The intensity distribution of the re-compressed RegA output is depicted in Fig.3.8 as a function of time delay and wavelength, measured with a *Grenouille* spectrometer, which is based on the frequency-resolved optical gating (FROG) technique. With a bandwidth of $\Delta\lambda = 24.5$ nm a pulse duration of $\Delta t = 45$ fs is achieved.

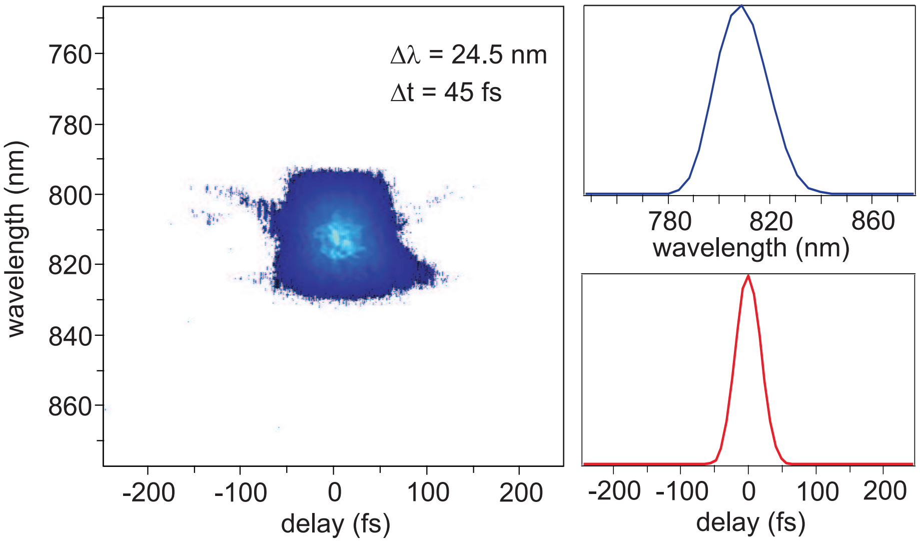

Figure 3.8: Pulse characterization of the compressed *RegA* output. Two-dimensional intensity distribution of the pulses measured with a *Grenouille* spectrometer (left panel). The intensity distribution of the pulses of the *RegA* output in the wavelength (upper right panel) and in the time domain (lower right panel).

The investigation of different samples with varying electronic properties makes it desirable to match the photon energies of pump- and probe-pulse to the requirements of the system, *e.g.* the work function. Therefore, the employed laser setup includes two optical parametric amplifiers and a non-collinear optical parametric amplifier in order to be able to tune the photon energies over the entire visible, the near-infrared and near-UV part of the light spectrum. The OPA 9450 is pumped by pulses with a central wavelength of 400 nm, that are produced by frequency-doubling of the fundamental 800 nm RegA-output in a BBO-crystal [26]. The signal output ranges from 460 to 760 nm and the achieved pulse duration are ∼ 50 fs. The NOPA produces sub-30 fs pulses in the visible spectral regime (480 - 650 nm). The shorter pulse duration is a result of the broader phase-matching region, providing a broader spectral distribution of the output pulse and hence shorter pulse duration compared to the OPA[27]. The OPA 9850 delivers laser pulses with a duration of ∼ 30 fs in the infrared part of the spectrum from 1100 - 2900 nm.

In the following the basic non-linear optical processes, like second harmonic generation (SHG), sum frequency generation (SFG), and difference frequency generation (DFG) are described. Electromagnetic waves produce in atoms or molecules in dielectric media charge displacements that induce electric dipole moments $\vec{p}(\vec{E})$. The macroscopic polarization can be expanded into a power series:

$$\vec{P}(\vec{E}) = \epsilon_0 \cdot [\chi^{(1)} \cdot \vec{E} + \chi^{(2)} \cdot \vec{E}^2 + \chi^{(3)} \cdot \vec{E}^3 + ...], \tag{3.28}$$

where χ^n is the susceptibility of n-th order, which is described by a tensor of rank $(n+1)$. χ^n depends on the symmetry of the non-linear medium and is a measure for the non-linear restoring forces, that occur during the deformation of the atomic shell by the E-M wave. Although, $\chi^{(n)} \ll \chi^{(n-1)}$ is always valid, higher order terms lead to a considerable contribution to the polarization, when the field strength of the E-M wave is high, as in the case of femtosecond laser pulses. Under the influence of light with two different frequencies ω_1 and ω_2

$$\vec{E}(\vec{\omega}) = \vec{E_1} \cdot e^{-i\omega_1 t} + \vec{E_2} \cdot e^{-i\omega_2 t} \tag{3.29}$$

the induced atomic dipole moments oscillate and produce new E-M waves with a frequency determined by the ones of the induced dipole moments. The second-order term in (3.28) yields contributions in the macroscopic polarization of the doubled frequencies of ω_1 and ω_2, their sum, and their difference frequency. The radiated waves with frequency ω propagate with a phase velocity of:

$$v_{Ph} = \frac{\omega}{k} = \frac{c_0}{n(\omega)} \tag{3.30}$$

through the non-linear medium. However, a macroscopic wave is only emitted when all microscopic components oscillate in phase. This is the case when the phase matching condition:

$$\vec{k}(\omega_1 + \omega_1) = \vec{k}(\omega_1) + \vec{k}(\omega_2) \tag{3.31}$$

is fulfilled.

In the *OPA* the *RegA* output passes through a beam splitter; 75% of the incident

---

[26] BBO: β-barium borate

[27] More details on the self-made NOPA can be found in the diploma thesis of D. Wegkamp [Weg09].

beam is reflected and serves as the pump, whereas the transmitted 25% is focused into a sapphire plate generating a broad white light continuum (seed). The wight light continuum exhibits a strong temporal chirp, which allows to select a desired spectral part by sending it via a delay stage. In a second optical path the pump pulse is generated by frequency-doubling of the fundamental 800 nm in a BBO-crystal. Pump- and seed-pulse are spatially and temporally overlapped in a second BBO-crystal. Here, the DFG process occurs and the pump-pulse (ω_1) and the seed-pulse (ω_2) are generating a photon with the difference frequency $\omega_3 = \omega_1$ - ω_2 (idler) and another photon with energy ω_2 (signal). Each pulse passes twice through this BBO-crystal to achieve higher amplification.

Most of the experiments presented in this thesis were performed using the VIS output of the OPA and either its second harmonic or the frequency-doubled output of the RegA, that served as the UV pump. In both cases the second harmonic is separated from its fundamental by a dichroic beam splitter, before the polarization of the UV light is flipped from s back to p by a periscope (cf. Fig.3.7), because the polarization of the second harmonic was changed during the SHG process in the BBO. A prism compressor setup in every beam path compensates for the positive GVD introduced by the transmitted optical components, and allows for minimizing the pulse duration for every beam path individually. The VIS laser light is guided *via* a computer controlled delay stage, which enables to control the time delay of pump- and probe-pulse with an accuracy of 0.5 fs with respect to each other. The optical setup in front of the UHV chamber is depicted in Fig.3.9. Both beam paths proceed on the same height and the laser light is focussed onto the sample kept in the UHV chamber. The in- and outcoupling windows in the UHV chamber are made from UV-transmitting MgF_2. The

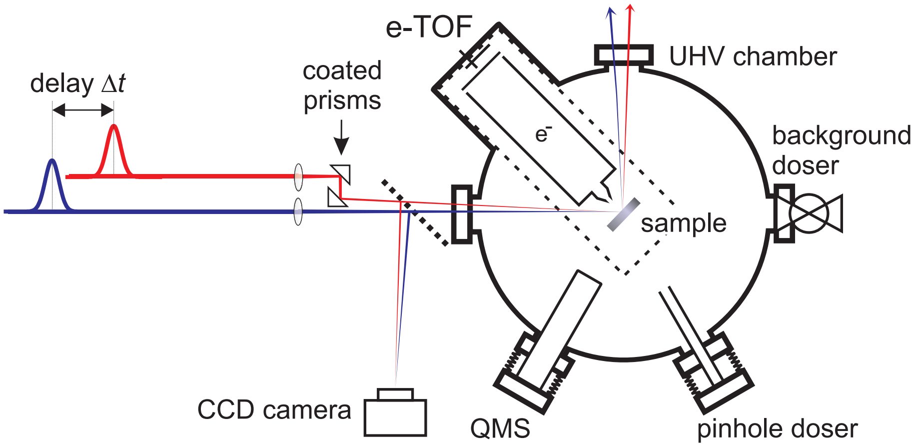

Figure 3.9: Laser setup to couple the pump- and probe laser beam into the UHV chamber. The VIS beam passes a delay stage to introduce the temporal delay. The beam profile can be taken by a CCD camera

spatial overlap of both laser beams can be controlled by a pair of reflecting prisms in the VIS beam path. A flip-mirror in front of the entrance window can be used to focus both laser beams to a position that is equivalent to the sample position in the UHV. This allows for a first adjustment of the spatial overlap by alignment of the beams through a pinhole or a rough synchronization of the beam path length by the help of a fast photo diode. In addition, the spot profiles in this sample-equivalent position can be recorded by a CCD-camera.

3.2.2 Laser Pulse Characterization

The characterization of the laser pulses by means of spot profile, laser spectrum, and pulse duration is presented in the following. For the determination of the energy scaling of the recorded 2PPE spectra it is essential to precisely know the central wave length of the laser light. The spectra of the visible and near-UV laser pulses are recorded with a fiber optic grating spectrometer (*B&M*). Typical laser spectra of a laser pulse in the visible and UV range are depicted in Fig.3.10. In the right panel of the figure the laser spectrum of the frequency-doubled *RegA*-output, which is fitted by a gaussian distribution (solid line) is shown. It has a central wave length of $\lambda = 401.5$ nm (3.09 eV) and a FWHM of $\Delta\lambda = 5.9$ nm. The left panel of Fig.3.10 depicts the laser spectrum of the OPA-output pulse in the visible spectral range. The spectral distribution is again described by a gaussian peak giving a central wave length of $\lambda = 544.6$ nm (2.28 eV) and a width of $\Delta\lambda = 8.5$ nm.

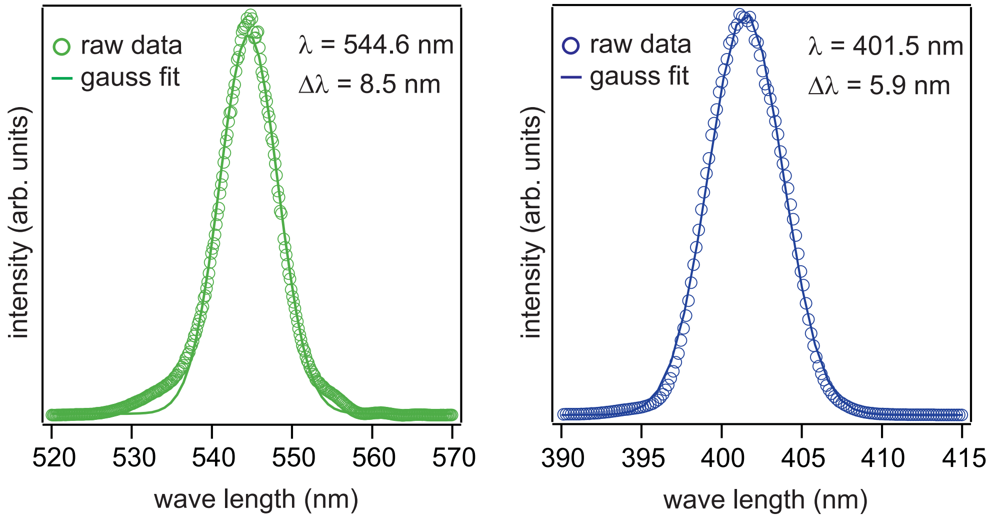

Figure 3.10: Laser spectra of typical laser pulses in the visible and UV. The intensity distribution can be described by a gauss peak (solid lines).

Information on the temporal profile of the laser pulses can be gained by 2PPE cross-correlation measurements on the sample. To reduce the effect of the finite lifetime of electronic excitations the XC traces in the time-resolved 2PPE measurement are analyzed in the spectral region with the highest intermediate state energy, as the lifetime scales with $\tau \sim \frac{1}{(E-E_F)^2}$. If no resonant excitations occur, the electrons are photo emitted via a virtual intermediate state with an infinitesimal short lifetime. In this case the time-dependent 2PPE response function of an intermediate state in equation 3.23 reduces to the cross-correlation function of two laser pulses in equation 3.25, as the response function of the intermediate state R(t) is a δ function. Hence, the cross-correlation function of two laser pulses $F_{XC}(t)$ can be written as:

$$F_{XC}(t) = \int dt' I_1(t) I_2(t-t'), \tag{3.32}$$

where I(t) is the transient laser pulse intensity. The transient envelope of the laser pulse can be described in good approximation by a gaussian distribution or a *sech*^{2}-function. For $I(t) = \frac{1}{\sqrt{2\tau}} \cdot sech^2(\frac{t}{\tau})$ and the assumption of equal pulse duration for both laser pulses the laser pulse XC can be fitted by the intensity auto-correlation function:

$$A_I(t) = \frac{\frac{t}{\tau} \cdot \cosh(\frac{t}{\tau}) - \sinh(\frac{t}{\tau})}{\tau \cdot \sinh^3(\frac{t}{\tau})}. \tag{3.33}$$

Such an analysis is exemplarily presented in Fig.3.11 for the laser pulse XC of a UV- and VIS-pulse. Fitting the XC (grey solid line) with intensity cross correlation $A_I(t)$ in equation 3.33 shows a very good consistency with the experimental data and yields a pulse duration of $\Delta\tau = 46$ fs. The minimum time–bandwidth product depends on the pulse shape, and is 0.315 for bandwidth-limited sech^2-shaped pulses, so that the transform limit for the VIS-pulse is 37 fs.

The spot profiles of the laser pulses were taken with a CCD camera located in front

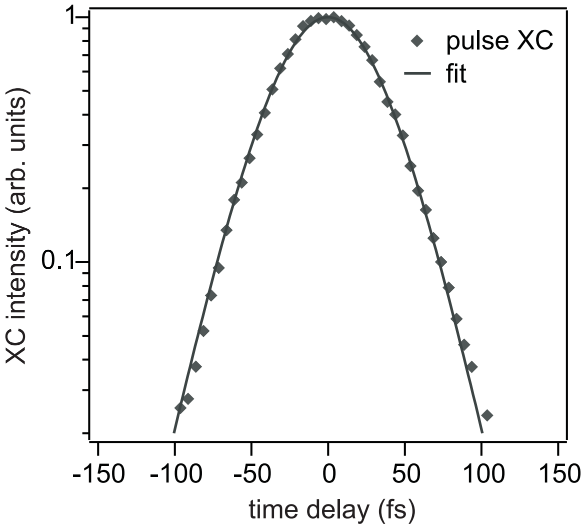

Figure 3.11: Laser pulse cross-correlation taken at the Fermi-edge of a 2PPE spectrum taken on 0.1 ML Cs/Cu(111). The fit (solid line) based on an intensity auto-correlation function of two laser pulses assuming a *sech*^{2}-like pulse envelope is in perfect agreement with the experimental data (grey diamonds). The analysis gives a laser pulse duration of $\Delta\tau = 46$ fs.

of the UHV chamber in an equivalent position with regard to the sample (cf. Fig3.9. Fig.3.12 presents two typical spot profiles of the UV- and VIS-pulses. The spot profiles can be well described by a two-dimensional gaussian intensity distribution (solid lines). The laser beams exhibit a full width at half maximum (FWHM) of 100-160 μm and 110-180 μm for the VIS-pulse and the UV-pulse, respectively. With the knowledge of the spot size and the cw-power of the laser, that is measured with power meter, one can additionally calculate other properties like the laser fluence.

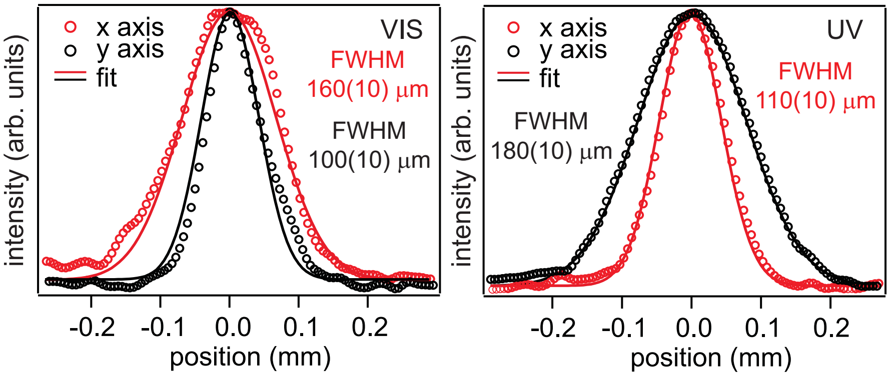

Figure 3.12: Typical spot profiles of laser pulses in the visible (left) and UV (right) spectral range. The spot profiles can be fitted using a gaussian distribution (solid lines).

3.3 UHV System

The adsorption of residual gases hinders the study of well-defined metal surfaces. To minimize the contamination these studies are performed in ultrahigh vacuum (UHV) conditions of $p \leq 10^{-9}$ mbar. At a pressure of 10^{-6} mbar the residual gas density is $n \simeq 3 \cdot 10^{16}$ molecules/m^3 and a monolayer is formed within one second on the formerly clean metal surfaces considering a mean velocity of 600 m/s and a sticking coefficient of one [Zan88].

The UHV-chamber is separated into two parts, as depicted in Fig.3.13. The upper part, preparation chamber, is equipped with surface science tools to prepare and characterize clean metal surfaces, as well as, molecular and atomic adsorbate layers. Furthermore, a sample transfer and storage system is connected to the UHV system, that allows to transfer samples without breaking the vacuum. The bottom part of the vacuum chamber, spectrometer chamber, provides an Auger spectrometer and the TOF spectrometer to acquire the 2PPE spectra. The entire UHV setup is mounted to the air-damped laser table to isolate it from unwanted vibration and to guarantee a stable beam pointing during the 2PPE measurements.

In the preparation chamber a base pressure of $p \leq 1 \cdot 10^{-10}$ mbar is achieved by employing a turbo-molecular pump (Pfeiffer). The required prevacuum for the operation of this pump is produced by an additional turbo pump (Pfeiffer), which is connected to a multi-stage membrane pump (VacuBrand). For the preparation of metal surfaces the upper chamber is equipped with an electron gun, which is used to heat the sample

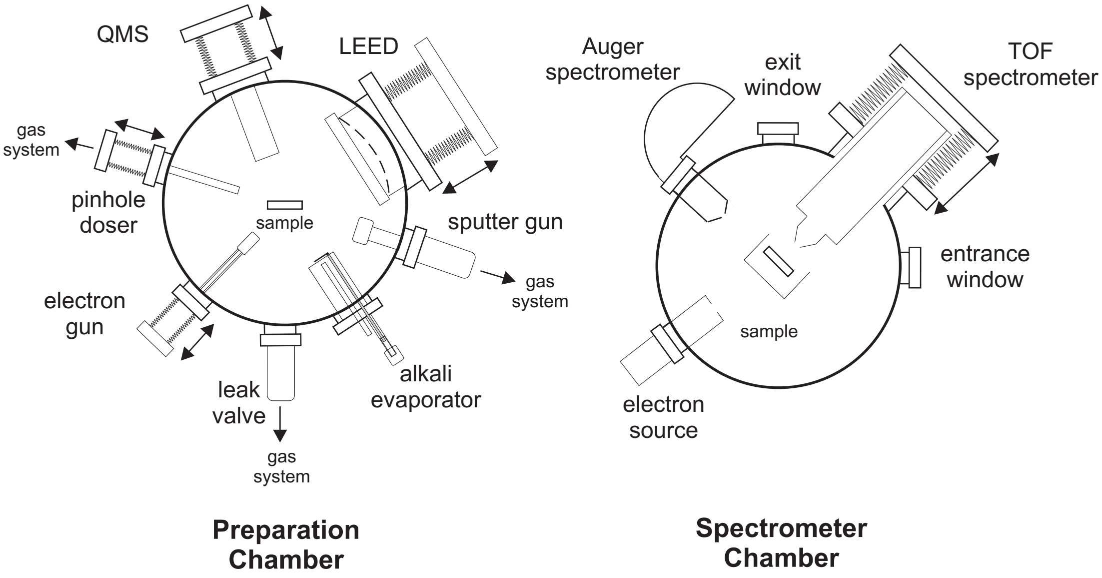

Figure 3.13: Setup of the UHV system. The UHV chamber is divided into a preparation- and a spectrometer-chamber separated by a gate valve into two independently pumped parts.

to temperatures above 900 K, where a resistivity heating is not suitable anymore[28] and a sputter gun (Specs). A low-energy electron diffraction (LEED) spectrometer (Specs) allows for the characterization of long-range order of the metal surfaces or adsorbate layers. Leak valves, a pinhole doser, and a home-build alkali evaporator enables the preparation of atomic and molecular adsorbate layers. Finally, the UHV chamber is equipped with a quadropol mass spectrometer (QMS) (MKS Instruments) for adsorbate-layer preparation and characterization, and for the residual gas analysis.

The spectrometer level of the UHV chamber is pumped by a Titanium sublimation pump (Riber) and an ion getter pump (Riber). When the gate valve is closed a base pressure of $p \leq 3 \cdot 10^{-11}$ mbar is reached. The lower part is equipped with the TOF spectrometer, that was used for the present work, and a position sensitive TOF spectrometer, which was developed during the thesis work of P. Kirchmann [Kir08].

The sample can be positioned in the UHV chamber by a motor controlled manipulator. The manipulator can be displaced laterally by ± 12.5 mm and vertically by 400 mm. To ensure a precise positioning of the sample, all three axis are equipped with a stepper motor. The capability of cooling the sample is realized by a 400 mm long Helium-flow-cryostat (CryoVac). It can be either used with liquid N_2, so that temperatures of 80-90 K are achieved, or by liquid He allowing a sample temperature of 30-40 K.

The sample holder and the lower part of the cryostat are depicted in Fig.3.14. The metal single crystals, Ru(001) (Ø 8 mm, 2 mm thick) and Cu(111) (Ø 9 mm, 3 mm thick), are clamped between two 0.4 mm thick tantalum wires (B), that are connected to two gold coated copper legs (D). These legs are attached to a holder (E), that is connected to the helium flow cryostat (F). The copper legs are among each other and to the holder electrically insulated by sapphire plates (C). However, a good thermal connection to the cryostat is assured, because of the high heat conductivity of sapphire. The copper legs

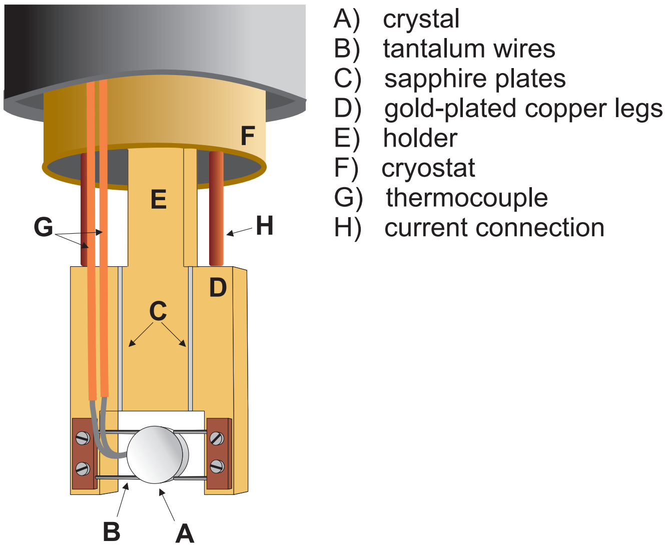

Figure 3.14: Sample holder and lower part of the He-flow cryostat. Adopted from [Stä07b].

---

[28] In this way temperatures of several thousand Kelvin can be achieved.

(D), the tantalum wires (B), and the single crystal are electrically connected current connection (H) allowing the resistive heating of the sample. The sample temperature is measured by a Type C (W/Rh) thermocouple (G) in the case of Ru(001) and by a Type K (NiCr/Ni) in the case of the Cu(111) crystal. The thermocouples are either spot-welded to the backside of the Ru(001) crystal or are inserted into a hole in the diameter of the Cu(111) crystal.

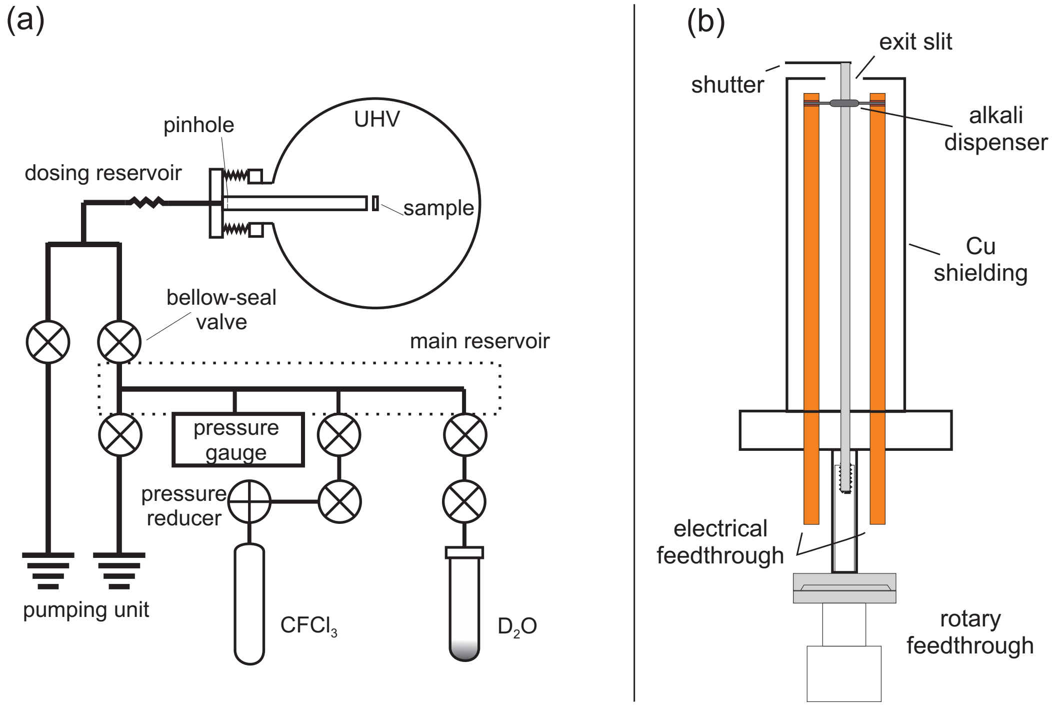

Figure 3.15: Setup of the gas system and the alkali evaporator.

For the preparation of the molecular and atomic adlayers the upper part of the UHV chamber is connected to a gas system, which allows the precise dosage of gases into the UHV chamber. The gas system is depicted schematically in Fig.3.15(a). The gases can be introduced into the UHV chamber either *via* setting a constant partial pressure of the gas adjusted by a leak valve, or directly onto the sample *via* a pinhole doser. The gas system consists of two separated parts, that can independently be pumped and filled with different gases. In this work, the dosage of water was mainly carried out *via* the pinhole doser as this method yields excellent reproducibility and only a small increase of the background pressure in the chamber during dosage. It consists of a pinhole with a diameter of 50 μm and a long steel pipe, through which the gas is evaporated onto the sample. By collisions of the molecules among each other and the wall of the pipe a homogenous molecular beam is ensured. The pinhole doser can be linearly positioned directly in front of the sample with a distance between both of ~ 5 mm. Besides water, also $CFCl_3$, Oxygen, and the noble gases Argon, Krypton, and Xenon can be introduced into the UHV chamber *via* the gas system.

The alkali metals are dosed using a home-build evaporator, which is equipped with a commercial alkali dispenser (SAES getters), that is schematically depicted in Fig.3.15(b). The dispensers are filled with an alkali metal chromate (Me_2CrO_4, where Me stands for an alkali metal) and a reducing agent. Upon heating the dispenser in a temperature range between 550 and 850°C a reduction reaction between the chromate and the reducing agent occurs and causes the free alkali metal to be evaporated. The dispenser is mounted on two steel rods, which are connected to electrical feedthroughs made of copper enabling the resistive heating of the device. In this setup heating currents of up to 9.5 A are applied to reach the designated temperatures. The device is capsuled by a Cu-shielding with an exit slit for the alkali evaporation to avoid evaporation in other directions. The exit slit can be covered by a mechanical shutter.

3.4 Sample Preparation and Characterization

3.4.1 Preparation and Characterization of the Metal Substrate

The Cu(111) surface is cleaned by cycles of ion bombardment and subsequent annealing. Argon is inserted into the UHV chamber by a leak valve setting a constant partial pressure of $p_{Ar} \simeq 2 \cdot 10^{-6}$ mbar. The Ar atoms are ionized by the filament of the sputter gun and accelerated onto the crystal by applying a high voltage of 800-900 V. For one preparation cycle the Ar^+ beam is impinging on the crystal under an angle $\leq 45°$ with respect to the surface removing the upper Cu atom layers. The sputtering is controlled by measuring the ion current flowing from the sputter gun to the sample, which is usually around $2\ \mu A$. After the sputtering procedure the rough crystal surface is smoothed by annealing the surface for 20 min at a temperature of 700-750 K. The right annealing conditions (annealing time and temperature) require a balance of smoothing the surface and the diffusion of contaminations from the crystal bulk to the surface. This preparation cycle is carried out prior to every measurement. The initial preparation of a new Cu(111) crystal consists of up to 20 sputtering and annealing cycles. The lattice structure of the crystal is checked by means of LEED. A very sensitive probe for contaminations is given by the work function and the position and width of the Cu(111) surface state, which can measured with 2PPE spectroscopy. A 2PPE spectrum of a clean Cu(111) surface is presented in Fig.3.5.

The first step of the preparation procedure for the Ru(001) surface is sputtering for 5 min with ~ 1 kV at an Ar pressure of $p_{Ar} \simeq 5 \cdot 10^{-6}$ mbar giving a sputter ion current of $\sim 4.5\ \mu A$. The sputtering is followed by annealing the sample at 1350 K in an oxygen atmosphere with a pressure of $p_{O_2} \simeq 1 \cdot 10^{-7}$ mbar for 15 min. The typical carbon contaminations of the Ru crystal react with the oxygen and form carbon monoxide, that already desorbs at temperatures below 600 K. After stopping the oxygen supply the sample is annealed to 1500 K for 2-3 min to smoothen the surface, followed by a temperature flash to 1530 K to desorb remaining oxygen from the surface [29]. This preparation procedure is performed at least once before every measurement. The surface quality is checked by means of LEED and 2PPE spectroscopy. Furthermore, the desorption of CO from Ru(001) is very sensitive to contaminations so that the surface cleanliness was as well confirmed by means of thermal desorption spectroscopy.

3.4.2 Preparation and Characterization of the Ice Layers

If not stated otherwise, the water ice layers are prepared *via* the pinhole doser. A constant pressure of 0.5 mbar is established in the main reservoir of the gas system (cf. Fig3.15)[30]. Once the cold sample is positioned in front of the doser, the valve to the dosing reservoir is opened and the dosage starts. The dosing is stopped by opening a valve to the pumping unit and evacuating the dosing reservoir within one second. Different thicknesses of the adsorbate layers are achieved by varying the dosing time at constant dosing pressure. During the dosage the partial pressure of D_2O is monitored with the QMS. Its evolution is depicted in Fig.3.16 for different dosing times. The dosing time is given by the opening of the valve to the dosing reservoir, resulting in the initial increase in the background pressure, and the evacuation of the dosing reservoir by the differential pumping, that results in the first, quick decrease of the water partial pressure.

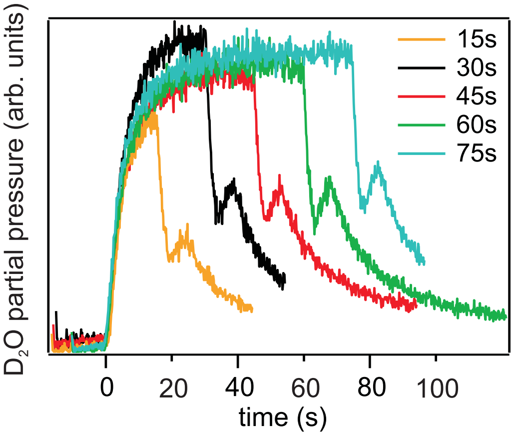

Figure 3.16: D_2O partial pressure in the preparation chamber during water dosage for different dosing times. The first pressure drop is attributed to the opening of the pump valve; the small second pressure increase corresponds to the moment, when the sample is moved away from the pinhole doser.

For the preparation of the amorphous ice layers on Cu(111) the sample was kept at a temperature of 90 K during the dosing procedure. The experiments presented in chapter 4 are conducted on amorphous ice layers, that were produced this way. To generate crystalline ice on the Ru(001) substrate for the experiments presented in chapter

---

[29] The Ru(001) crystal is heated using an electron gun (cf. Fig.3.13). Electrons are generated in a filament (I_{fil}=3.2 A) from where they are accelerated onto the back side of the crystal by applying a positive voltage of ~ 700 V at the sample.

[30] For dosage of small amounts of water ($\Theta \leq 0.5$ BL) the pressure is set to 0.1 mbar.

6, first amorphous ice was dosed employing the same procedure as for the water layers on Cu(111). Then, the sample was annealed to a temperature of ∼ 160 K for 5-10 s to induce the thermally activated crystallization of the ice. A more detailed description for the preparation of crystalline ice on Ru(001) can be found in [Gah04].

The TD spectra of various coverages of D_2O/Cu(111) dosed at a sample temperature of 90 K are presented in Fig.3.17. The spectra exhibit only one desorption peak with a coverage independent desorption onset at 150 K following zero-order desorption kinetics. The fact that the TD spectra exhibit no separated peak for the desorption of the first bilayer and multilayer is explained by similar strength of the intermolecular interaction among the water molecules and ice/metal-interaction. Hence, a direct determination of the water coverage on Cu(111) by means of TD spectroscopy is not possible. However, amorphous ice first forms in a Volmer-Weber growth before a closed wetting layer for coverages above 3 BL is established [Meh06, Gah04]. This results in a coverage dependent work function allowing to draw conclusions from the 2PPE spectra on the actual water coverage. Within the first 3 BL of water the work function decreases by ∼ 1 eV from $\Phi = 4.9$ eV for the clean Cu(111) surface to a value of $\Phi = 3.95$ eV, where the work function saturates [Gah04]. Furthermore, the work function change is accompanied by a disappearance of the Cu(111) surface state, which is a further indication of a wetting ice layer. The coverage calibration of water on Cu(111) was

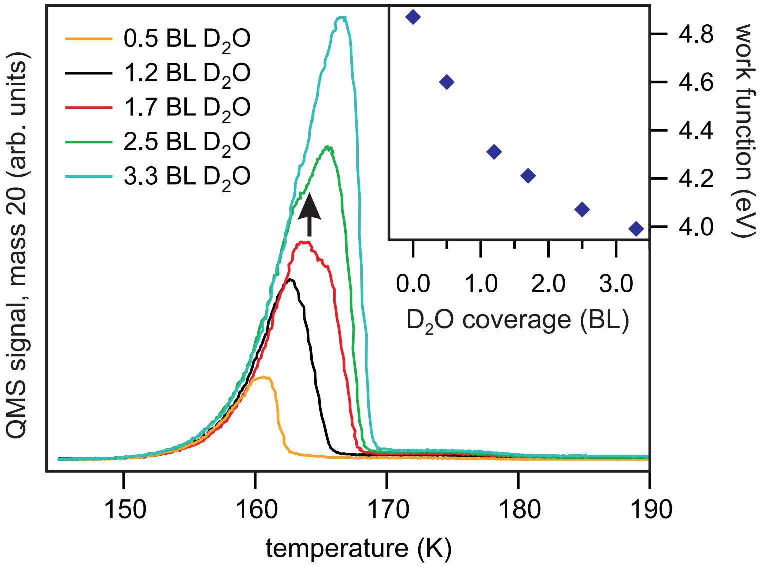

Figure 3.17: TD spectra of various ice coverages on Cu(111). The kink at T ≃ 165 K (see arrow) in the desorption peak is caused by the crystallization of the ice layer. Inset: Work function of D_2O/Cu(111) and the corresponding water coverage according to the coverage determination described in the text.

determined by comparison of the measured work function of the water covered Cu(111) surface with the coverage dependence of the work function found in [Gah04]. The work function of the respective ice layers and their assigned D_2O coverages are presented in the inset of Fig.3.17.

3.4.3 Preparation and Characterization of the Alkali Layers

The alkali atoms are deposited onto the sample using a home-build alkali evaporator, which is described in section 3.3. The alkali atoms are evaporated by sending a constant current of I=7.5-9.5 A through the alkali dispenser. This results in a typical evaporation rate of 0.01 ML/min. Different alkali coverages are achieved by varying the evaporation time, given by opening and closing the mechanical shutter of the evaporator. During the alkali deposition the back ground pressure was kept below $1 \cdot 10^{-9}$ mbar. The evaporation rate is calibrated by evaporating alkali atoms onto the bare copper crystal and comparing the measured work function with the work function shift of the Cu(111) surface as a function of alkali coverage obtained elsewhere [Dud90, Tan91, Fis94, Lu96, Are97, Gau07]. A typical coverage dependent series of 2PPE spectra for Cs/Cu(111) is depicted in Fig.3.18. The secondary edge of the spectra is clearly shifting to lower

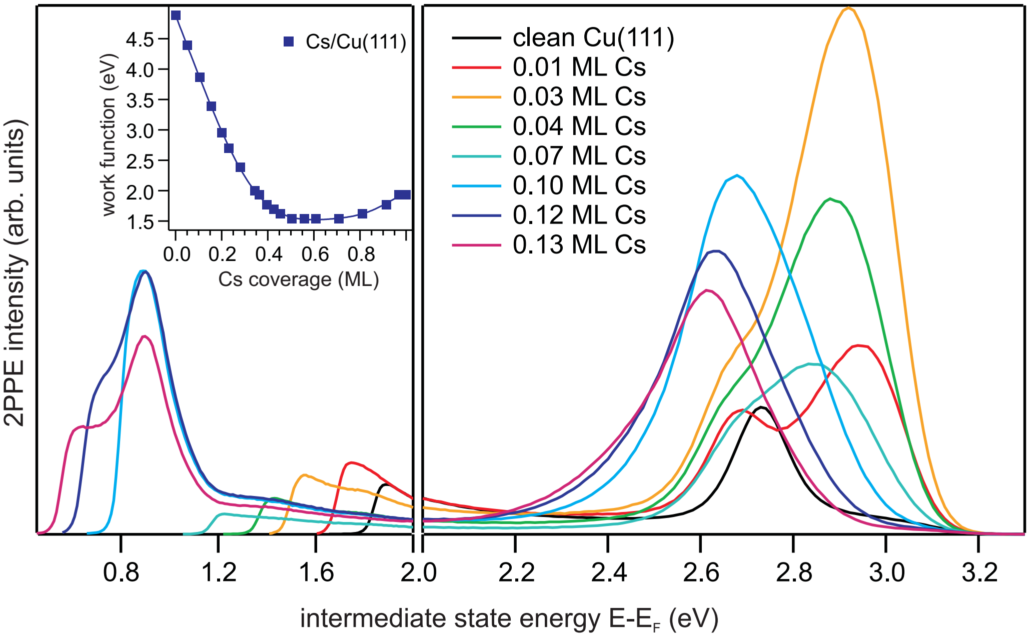

Figure 3.18: 2PPE spectra of clean Cu(111) (black solid line) and of Cs/Cu(111) for various coverages. (left panel): The work function of the system decreases with increasing alkali coverage as can be seen at the position of the secondary edge. (inset): Work function shift as a function of Cs coverage adopted from [Lu96]. (right panel): With increasing Cs coverage the alkali resonance appears and shifts to lower energies.

energies with increasing Cs coverage indicating a significant work function change of the system. For a coverage of Θ =0.13 ML Cs the work function changed by $\Delta\Phi = 1.26$ eV allowing for a precise determination of the absolute alkali coverage with an error of 0.01 ML. A calibration of the alkali coverage using a quartz balance is not possible, because of the relatively small atomic weight (Na, K) and the low alkali evaporation rates.

4 Electron Solvation at Alkali Ions Located at Ice Vacuum Interfaces

This chapter presents the electron-transfer and -solvation dynamics in wetting, amorphous ice layers adsorbed on a Cu(111) surface in the presence of co-adsorbed alkali atoms. Depending on the preparation temperature adsorption of alkali atoms on top of amorphous ice layers is accompanied by the transfer of the the *ns* valence electron to the metal substrate, leaving a positively charged alkali ion at the ice/vacuum-interface (cf. section 4.1.1). The electrostatic perturbation by the ions influences the water molecules in the vicinity leading to new initial trapping sites for excited electrons. Similar to electron dynamics in pure amorphous ice (cf. section 2.2.1) photoexcited electrons are found, that exhibit exponential decay times on the order of several tens of picoseconds and specific characteristics of solvated electrons, such as localization and energetic stabilization (cf. section 4.1.2). The charge transfer of these electrons back to the metal substrate is mediated by tunneling through a potential barrier formed by the ice film, as revealed by ice thickness-dependent measurements, presented in section 4.1.3. In contrast to the situation where alkali ions are present in the ice film, the transfer of the former *ns* valence electron of the alkali can be strongly hindered, if the alkali adlayers are prepared at temperatures below 50 K, enabling the observation of the former *ns* valence electrons (cf. section 4.2).

4.1 Ultrafast Electron Transfer and Solvation Dynamics at Alkali Ions Located at Ice Vacuum Interfaces

The experiments on alkali doped ice layers are intended to investigate the solvation of excess electron and the alkali ion in the water solvent environment. For preparation the wetting, amorphous ice layer is prepared in a first step by adsorption of D_2O onto the Cu(111) surface kept at temperatures below 100 K as described in more detail in section 3.4.2. Subsequently, the alkali atoms are evaporated from a commercial alkali dispenser (cf. section 3.4.3). The subsequent reactions of the alkali atoms with the surrounding water molecules depend on the properties of the alkali atoms, e.g. the hydration enthalpy ΔH_{hydr} of the ion, and on preparation parameters like temperature and alkali coverage [Gün02, Gle04, Bor04]. Depending on the hydration enthalpy, that is proportional to z^2/r (z is the charge and r is the effective radius of the cation), ions with a large enthalpy (Li^+) can penetrate more easily into the ice layer and bind directly to the metal substrate. Furthermore, following the detachment of the *ns* valence electron from the alkali atom, the electron and the parent ion can interact with the water molecules which may lead to their dissociation,. Dissociation can be suppressed at low sample temperature and small alkali coverages, as discussed in detail in section 2.2.4. In the framework of the present thesis all experiments were performed under temperature and alkali-coverage conditions, where no dissociation of water molecules occurs.

Fig.4.1 depicts schematically the potential energy curves of the highest occupied and the lowest unoccupied atomic orbital for sodium adsorbed on D_2O/Cu(111) as a function of the solvation coordinate q. The employed metal substrate serves as an electron donor, so that an electron from below the Fermi level is excited by absorption of a photon with energy $h\nu_{pump}$. The electron can either (i) attach to the unoccupied Na 3*s* state to form a neutral Na atom or (ii) localize in a potential minimum in the vicinity of the positively charged alkali ion and form a $Na^+(D_2O)_n^-$ complex. These attachment processes can either occur directly, as depicted in Fig.4.1 or indirectly *via* an intermediate state, *e.g.* the ice conduction band or shallow electron traps. Finally, the transient population of the excited stated is probed by photoemission after excitation with $h\nu_{probe}$. Analog to the case of solvated electrons in pure ice films, the back transfer of the excited electrons to unoccupied metal states is limiting their lifetime and presents the competing process to the photoemission.

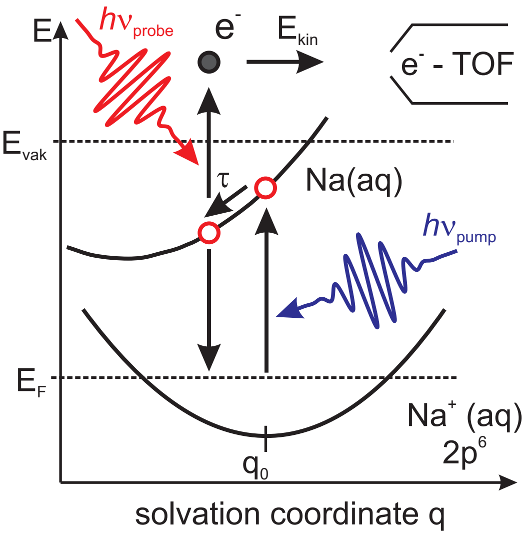

Figure 4.1: Scheme of the 2PPE experiment for solvation in Na/D_2O/Cu(111). The excitation of an electron by absorption of a photon with $h\nu_{pump}$ leads to (i) an attachment of the electron to the Na 3*s* state resulting in the neutralization of the alkali or (ii) the formation of a $Na^+(D_2O)_n^-$ complex. The transient electron population is than probed by absorption of a second photon with $h\nu_{probe}$.

In the following section 4.1.1 the autoionization of the alkali atom and the subsequent decay of the *ns* valence electron is monitored by means of a work function measurement. Having identified the ”starting conditions”, *i.e.* alkali ions and not alkali atoms, the population and stabilization dynamics of the excess electrons are discussed in section 4.1.2. In section 4.1.3 it is shown, that the new species of solvated electrons is located at the ice/vacuum-interface and that their back transfer occurs by electron tunneling through the ice layer. Alkali-coverage-dependent and temperature effects on the new species of solvated electrons are presented in section 4.1.4 and 4.1.5.

4.1.1 Autoionization of the Alkali Atom and Back Transfer of the ns Valence Electron to the Metal Substrate

One of the key questions in regard to the experiments discussed in the following is the question what species is produced by the adsorption of alkali atoms onto the amorphous ice film. There are two possibilities, (i) the alkali atoms remain neutral upon the adsorption onto the ice film, and (ii) the alkali atom is ionized and the former alkali *ns* valence electron becomes delocalized and solvated by its interaction with the surrounding water molecules. Subsequently, the solvated electron decays back to the metal substrate by tunneling through the thin ice layer and the positively charged alkali ion remains at the ice/vacuum-interface.

Indeed, Vondrak and coworkers [Von06a, Von06b, Von09] found in there investigations of co-adsorbed alkali atoms on thick (3000L) ice layers at temperatures of ~ 90 K, that the highest occupied molecular orbital (HOMO) of the alkali becomes delocalized over several water molecules (cf. Fig.2.11). In addition, this interaction leads to a reduction of the vertical ionization energy by several eV, *e.g.* for Na on ice the vertical ionization energy is lowered by ~ 2 eV compared to an isolated sodium atom to a value of 3.2 eV. Nevertheless, with increasing temperature a separation of the alkali *ns* valence electron and the parent atom is observed. For very thin ice layers (only a few BL) adsorbed at a metal surface, as investigated in this thesis, the decay of the alkali valence electrons by charge transfer to unoccupied metal bulk states becomes very efficient. In this process, the Na 3s electron will transfer to the ice and decay to the manifold of unoccupied metal states by tunneling through the thin ice layer leaving a positively charged alkali ion at the surface.

In order to be able to make a decision in favor of one of the scenarios work function measurements employing 2PPE spectroscopy were performed. As a result of the ionization of the alkali atoms the build-up of positively charged Na^+ ion layer on top of the water-ice layer would occur, and the resulting surface dipoles would lead to a lowering of the work function.

Fig.4.2 depicts the sample work function for alkali/D_2O/Cu(111) as a function of alkali coverage for Na, K, and Cs. With increasing alkali coverage, the work function Φ decreases with respect to the value for the pure ice film on Cu(111) of $\Phi = 4.0$ eV. All three investigated alkalis show a similar behavior. For instance, for a Na coverage of 0.11 ML, the work function is lowered by $\Delta\Phi = 0.35$ eV. This is in agreement with an accumulation of a positive charge at the water/vacuum interface. This positive charge at the interface and its image charge in the metal substrate form a dipole that is pointing away from the surface and hence reduces the work function for photoemitted electrons from below the charged layer. This finding experimentally confirms the ionization of the alkali atoms and the subsequent back transfer of the former *ns* valence electron to the metal substrate.

Interestingly, the work function change is relatively small compared to the work function change induced by alkali metals directly adsorbed on a metal substrate. For example, a coverage of 0.1 ML Na on bare Cu(111) reduces the work function by ~ 2 eV [Zha08] (cf. Fig.2.22 and Fig.3.18). This decrease is also a consequence of a partial

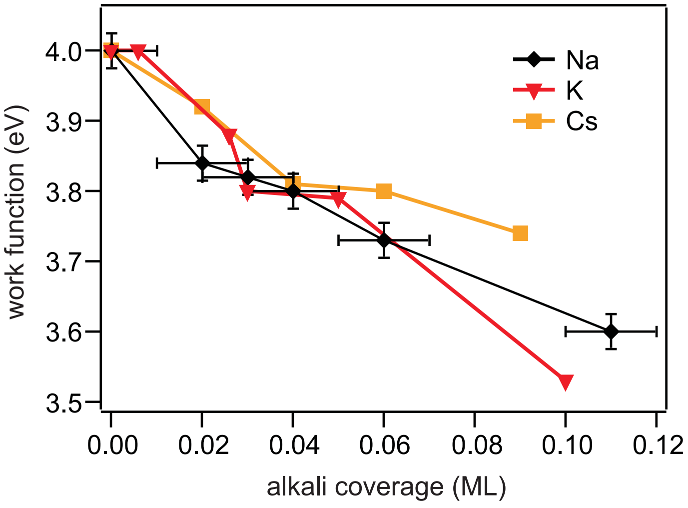

Figure 4.2: Work function change of $D_2O/Cu(111)$ as a function of alkali coverage for Na, K, and Cs adsorbed on top of the ice layer. The ice layer is ~ 4.5 BL thick.

charge transfer of the alkali metal valence electron to the metal substrate leaving a positively charged alkali at the interface. Qualitatively, one can say that a positively charged adsorbate induces an image charge in the metal. These screening charges are located at the surface and, for small adsorbate–surface distances, the whole system (ion + screening charge) can be described as a polarized alkali atom [Gau07]. The work function change is proportional to the charge density and the distance between charge and image charge. However, the change in the work function is weaker when the alkali is located at the water/vacuum interface, although the distance between the charged species is enhanced, which should give a larger dipole moment. Indeed, the net dipole moment and therefore the work function change is smaller, which is explained by the interaction of the alkali-ions with the surrounding water molecules. The water screens the excess charge by a reorientation of the dipole moments of the water molecules. Fig.4.3 depicts the relative work function change with respect to the not alkali doped ice film for Na and Cs adsorbed on ice films with various thicknesses. For both types of alkali the work function is decreasing with increasing ice layer thickness. As the alkali ions are believed to be located at the ice/vacuum interface[31] the decreasing work function of the system is explained by an increasing distance of the the charge from the surface and accordingly an increasing surface dipole moment. Using a simple model based on the formation of a dipole layer between the anion at the surface and its image charge in the metal substrate provided the observed work function change can be described. Following the Helmholtz equation he work function change ΔΦ is given by [Bru97]:

$$\Delta\Phi = -\frac{edqN_{charge}}{\varepsilon_0\varepsilon}; \tag{4.34}$$

where d is the thickness of the ice layer, N_{charge} is the surface density of alkalis, and

---

[31] Clear evidence for the alkali binding site is given in section 4.1.3.

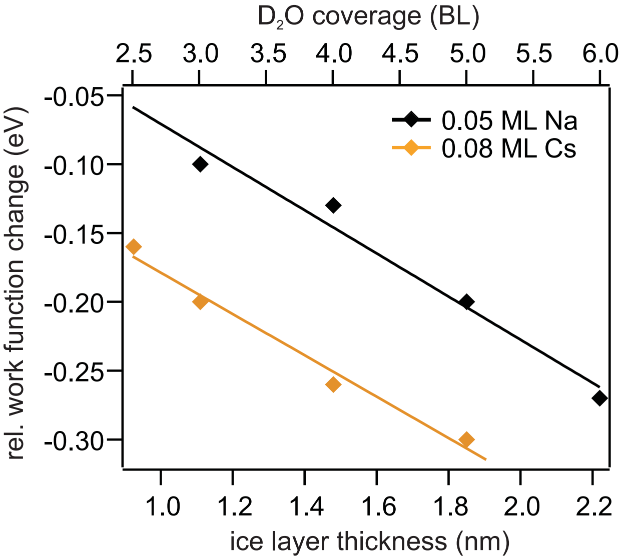

Figure 4.3: Work function change of alkali/D_2O/Cu(111) as a function of D_2O coverage for 0.05 ML Na (black diamonds) and 0.08 ML Cs (yellow diamonds) adsorbed on top of the ice layer. The solid lines depict a model fit to the data based on the formation of a dipole layer between the anion at the surface and its image charge in the metal substrate.

ε_0 is the vacuum permittivity. Having measured the work function change, equation 4.34 allows for the determination of the dielectric constant of the alkali-doped ice film. Defining a net charge q_{net} of the alkali ion, which is given by $q_{net} = q/\varepsilon_{ice}$, allows to identify the effective unscreened charge of the alkali that contributes to the dipole moment. For a fully ionized alkali atom in non-polar and non-polarizable media q_{net} would simply be the elementary charge, so that $q_{net} = 1 \cdot e$. The results of this model fit are summarized in table 4.1.

Table 4.1: Dielectric constant ε and net charge q_{net} of alkali ions adsorbed on D_2O/Cu(111)

	Na	Cs
q_{net} in e	0.02(1)	0.03(1)
ε	44(10)	37(8)

In both cases the net charge is significantly smaller than the elementary charge of the alkali ion. This clear deviation is caused by the interaction of the water dipole with the alkali ion that leads to a screening of the charge and therefore to a substantial reduction of the net charge that is forming the surface dipole. The net charge q_{net} is in the case of Cs ions $q_{net} = 0.03(1) \cdot e$, which is identical to the value for Na of $q_{net} = 0.02(1) \cdot e$. This is only a value of 3 and 2 % of the elementary charge and clearly shows how efficiently the additional charge is accommodated and compensated by the dipoles of the surrounding water network. The fact, that the net charge is slightly smaller in the case of Na compared to Cs can be explained by a better incorporation of the significantly smaller Na-ion leading to a more efficient screening in case of the smaller alkali ion. This effect especially plays a role as the alkali ions are located at the vacuum/ice interface. Hence, they are not fully coordinated (surrounded) by water molecules. The most stable configuration for Na was theoretically found for the alkali ion located within the upper half layer of the top most ice bilayer (cf. Fig.2.11) [Von06a]. A larger alkali ion might be less coordinated by water molecules and accordingly weaker screened resulting in a higher net charge q_{net}. Nevertheless, the difference is small and both values are identical within the error bars. It is noteworthy that the dielectric constant is almost on the order of the dielectric constant for liquid water, which is ~ 80. Such large values for the dielectric constant have been reported before for H_2O/Cs structures adsorbed on Cu(110), where Sass and coworkers estimated the effective dielectric constant of the water bilayer to be $\varepsilon \geq 25$ [Sas90, Sas91].

Summarizing, after the alkali atoms are deposited on top of the ice layer an ionization of the alkali atom, followed by the back transfer of the former valence electron to the metal substrate, results in the build-up of a dipole moment, that reduces the systems work function. Hence, the experiments presented in the following are conducted in the presence of alkali ions, if not stated otherwise. Nevertheless, the initial ionization of the valence electron can eventually be hindered when working at temperatures well below 60 K. In this case the neutral alkali atoms adsorbed on amorphous ice layers can be investigated, as discussed in section 4.2.

4.1.2 Stabilization and Population Dynamics

In the following, the influence of alkali ions adsorbed on top of amorphous D_2O on the electron dynamics is discussed. Fig.4.4 schematically depicts different possible species of excess electrons in the amorphous ice layer with coadsorbed alkali ions at the surface. In pure amorphous ice layers solvated electrons exist, which populate binding sites in the bulk of the ice film. These solvated electrons, referred to as species I may also be present when alkali ions are present. The next species of excess electrons are directly related to the alkali ions at the ice/vacuum interface. Whereas species II electrons are excess electrons that are solvated at the alkali-ion complex at the ice surface, species III electrons are excited to the LUMO of the alkali ion leading to its neutralization. Having introduced possible states for excess electrons in the amorphous ice layer with coadsorbed alkali ions, the results of time-dependent 2PPE spectroscopy on D_2O/Cu(111) with and without alkali ions are compared using the example of coadsorbed Na^+ ions. Starting out with the results of a bare amorphous D_2O layer on Cu(111); Fig.4.5.(a) displays a typical false-color map of the 2PPE intensity as a function of intermediate-state energy $E\text{-}E_F$ (left axis) and time delay (bottom axis) for 5 BL of D_2O adsorbed on Cu(111). The 2PPE spectra are dominated by a peak (e_s) located at $E\text{-}E_F = 2.9$ eV. With increasing time delay, the peak maximum shifts to lower energies, and its intensity decreases non-exponentially with an initial decay time of $\tau = 140$ fs, which slows down to $\tau = 320$ fs for time delays > 300 fs, in accordance with earlier work [Bov03]. This feature originates from solvated electrons in the pure water-ice layer. The reorientation of the surrounding water molecules energetically stabilizes the electron, resulting in an increased binding energy and a localization of the charge in the D_2O film. Further

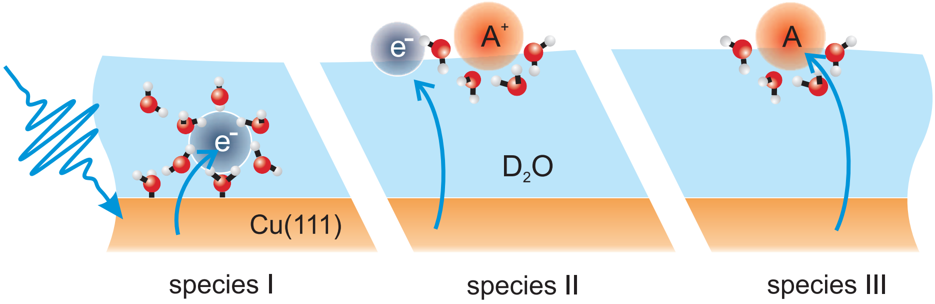

Figure 4.4: Schematic representation of the solvated electron in a pure amorphous water layer referred to as species I which occupies a binding site in the bulk of the ice film. The solvated electrons at the alkali-ion (A^+)/water complex are bound in the vicinity of the water/vacuum-interface and are referred to as species II. In addition, a neutralization of the alkali ion by a photoexcited electron may occur (species III). All excess electrons are generated by absorption of a UV photon in the metal substrate.

details on the electron solvation dynamics in amorphous D_2O can be found in section 2.2.1 or in [Stä08a]. After deposition of 0.08 ML Na onto the ice layer, pronounced changes can be seen in the time-resolved 2PPE spectra depicted in Fig.4.5.(b). The spectra are dominated by a broad and short-lived continuum at time zero and a broad peak (e_s^{alkali}) centered around $E\text{-}E_F = 2.6$ eV for the spectrum at zero time delay. With increasing time delay e_s^{alkali} shifts to lower energies with respect to the Fermi level. The qualitative behavior of the new feature is similar to that of the solvated electrons in pure water, because both a peak shift to lower energies and a decay of its intensity can be observed. However, the quantitative behavior is remarkably different even though less than a tenth of a ML alkali was evaporated onto the water-ice layer. This peak is attributed to a new species of solvated electrons that only occur in the presence of alkali ions at the ice/vacuum interface, *i.e.* photoexcitation results in the formation of an electron/alkali-ion complex that is screened by the surrounding water molecules. This new species of solvated electrons is also observed for amorphous ice films with coadsorbed K and Cs ions (not shown). In Fig.4.5.(b) one can already clearly see ,that the energetic shift of the peak, which occurs at time zero at $E\text{-}E_F = 2.6$ eV, slows down after $t \approx 400$ fs. Additionally, compared to pure amorphous D_2O the rate of the electron transfer back to the metal is significantly reduced so that the new species of solvated electrons can be observed on picosecond timescales. In the following, first a quantitative analysis of the peak shift is given before the electron population dynamics are discussed.

The positions of the peak maximum as a function of time delay for an amorphous D_2O film (red circles) and the corresponding feature for 0.08 ML Na adsorbed on top (blue diamonds) are depicted in Fig.4.6. Up to $t = 400$ fs, the distribution of solvated

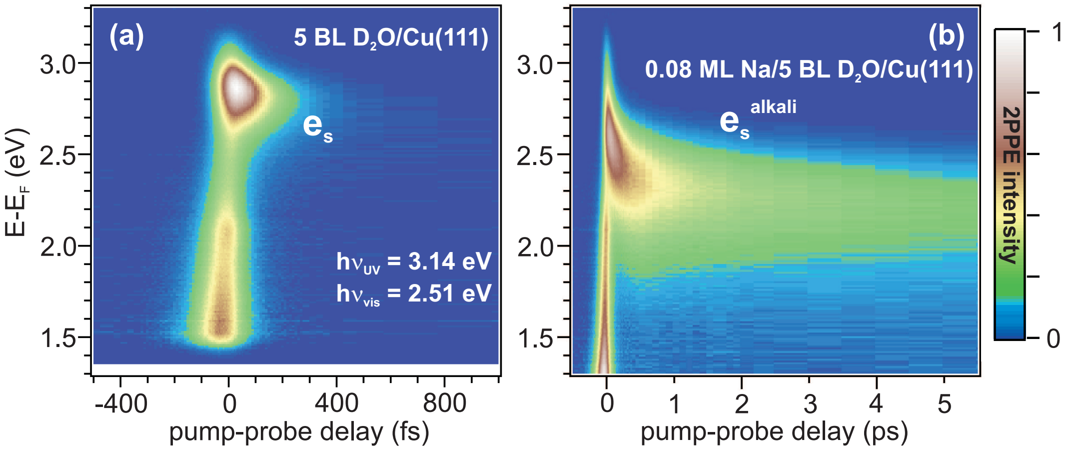

Figure 4.5: Time-resolved 2PPE spectra of D_2O/Cu(111) without and with co-adsorbed Na ions. (a): False-color map of the 2PPE intensity detected in normal emission as a function of intermediate-state energy and time delay of the visible probe pulse with respect to the UV pump pulse (positive delay times). (b): Deposition of 0.08 ML of Na on top of the ice film results in pronounced changes in the electron spectra. Please note the different scaling of the time axes.

electrons in bare D_2O has an initial energy stabilization rate of $\Sigma = 0.32(5)$ eV/ps, in accordance with earlier work [Gah02, Stä08a]. After adding Na, the initial energetic stabilization has increased compared to that of pure D_2O. Right after photoexcitation at $t = 0$ fs the maximum of e_s^{alkali} lies at E-E$_F$ = 2.62 eV followed by a shift of the peak maxima to lower intermediate state energies. This increase in the binding energy, which is related to a stronger bound electron with respect to the vacuum level of the system, is attributed to the response of the polar water molecules which screen the excess charge by molecular rearrangement, like for electron solvation in pure ice layers[32]. A linear fit of the peak position gives an initial stabilization rate of Σ_s^1 = -0.83(5) eV/ps. At longer delays, this rate significantly slows down to Σ_s^2 = -50(5) meV/ps for t = 0.4 - 2.0 ps and Σ_s^3 = -15(2) meV/ps for time delay $t > 2.0$ ps.

The fact, that the energetic peak shift slows down significantly after t = 400 fs, implies that the electron solvation at the alkali-ion/water complex proceeds via two different states, which exhibit stabilization dynamics on different times scales. Interestingly, such a scenario has been reported before for electron solvation in amorphous ammonia layers on Cu(111) [Stä07b, Stä08b]. There, the excess electron is injected to the NH_3 conduction band, where the electron subsequently localizes in a precursor state, which exhibits stabilization dynamics on femtosecond timescales, followed by a transition to

---

[32] An additional apparent peak shift, caused by energy-dependent transfer times, as observed in the case of amorphous ice adsorbed on metal surfaces [Stä06], might also contribute to the observed peak shift.

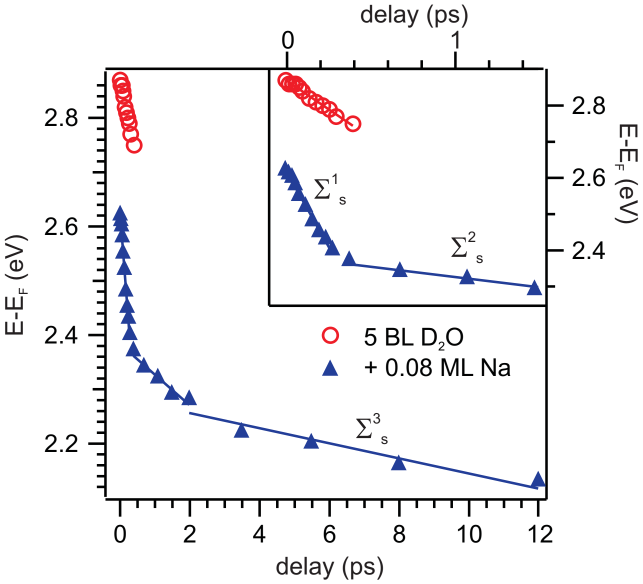

Figure 4.6: Energetic shift of the peak maximum of e_s^{alkali} for 0.08 ML on 5 Bl $D_2O/Cu(111)$ (blue diamonds) and of the peak maximum of e_s for 5 Bl $D_2O/Cu(111)$ (red circles). The energetic shift of e_s^{alkali} significantly slows down after 400 fs. The inset shows the peak positions for time delays up to 1.2 ps.

a second state with stabilization dynamics on picosecond timescales. This analogy seems reasonable as the solvated electrons are in both cases located at the ice/vacuum interface[33]. Compared to electron solvation in pure amorphous water ice, where the stabilization rate is more than two times larger, this suggests a stronger screening by the water network which surrounds the electron/alkali-ion complex. Furthermore, the more efficient screening leads to extended lifetimes of the electron/alkali-ion/water complex compared to the dynamics in pure water ice. In the case of coadsorbed K and Cs ions the energetic stabilization also proceeds on two different time scales with the same stabilization rates (not shown).

The adsorption of alkali ions not only affects the energetic stabilization of the solvated electrons but also leads to distinct changes in the population dynamics. In order to demonstrate this effect, cross-correlation (XC) traces are presented in Fig.4.7 for 5 BL D_2O layer on Cu(111) (blue open diamonds) and for the same ice layer covered with 0.08 ML Na (grey open circles). The correlation traces are obtained by integrating the 2PPE intensity over a selected energy window as a function of time delay. For the pure D_2O layer, this energy window ranges from $E-E_F = 2.3$-3.1 eV. Because of the broad distribution of excited electrons, the integration is performed in the case of the Na-covered ice layer for an energy interval of $E-E_F = 1.7$-2.8 eV. All correlation traces exhibit a non-exponential decay. In the following a model is proposed to describe the observed population dynamics and to gain insight in the involved mechanism leading to the significantly different stabilization dynamics compared to electron solvation in pure ice (cf. Fig.4.6). The model is based on fixed electronic states that can be populated

---

[33] Evidence for the binding site of the e_s^{alkali} electron at the ice/vacuum interface is given in section 4.1.3.

with a certain probability and that decay with a constant rate (single exponential decay). However, it should be noted that this assumption is a simplification in the case of excess electron states in a polar molecular environment. Here, the interaction between the dipole moments of the water molecules and the excess charge leads to a transient change of the binding energy (energetic stabilization) and of the decay rate (reduction of the wave function overlap between initial and final states). Nevertheless, although the following model is based on simplifying assumptions, it provides useful information on the population dynamics of excess electrons in amorphous ice layers with coadsorbed alkali ions and especially allows for the determination of the initial decay rates. The model description is based on a rate equation approach, which takes into account an initial state (A), *e.g.* the ice conduction band, and two states of solvated electrons e_p^{a+} and e_s^{a+}, that considers the fast electron dynamics in the first 400 fs and the slower dynamics at larger time delays, respectively. A three-level system is required as the XC trace can not be reproduced with a simpler two-level system (red solid line in the inset of Fig.4.7. The considered three level system is sketched in Fig.4.7. The new species of solvated electrons can either be excited indirectly via the initial state A with the probability $(1-p)$ or directly to the solvated electron state e_p^{a+} with the probability p. The initial localization of the excited electrons from A to e_p^{a+} is described by the localization rate $\Gamma_{trans,1}$. The electrons in e_p^{a+} can now either decay back to the metal substrate with the probability Γ_p or transfer to e_s^{a+} with the transition probability $\Gamma_{trans,2}$, from where the electrons decay back to the metal with the probability Γ_s [34]. This model was developed before to describe the transient population dynamics of solvated electrons in amorphous NH_3 [Stä08b] and leads to the following expressions for the population dynamics for both states e_p^{a+} and e_s^{a+}:

$$n_p(t) = A \cdot e^{[-(\Gamma_p+\Gamma_{trans,2})\cdot t]} + B \cdot e^{[-\Gamma_{trans,1}\cdot t]} \tag{4.35}$$

$$\begin{aligned} n_s(t) = {} & \frac{\Gamma_{trans,2}}{\Gamma_s - (\Gamma_p + \Gamma_{trans,2})} \cdot A(\cdot e^{[-(\Gamma_p+\Gamma_{trans,2})\cdot t]} - e^{-\Gamma_s \cdot t}) \\ & + \frac{\Gamma_{trans,2}}{\Gamma_s - \Gamma_{trans,1}} \cdot B \cdot (e^{[-\Gamma_{trans,1}\cdot t] - e^{\Gamma_s \cdot t}}), \end{aligned} \tag{4.36}$$

where

$$A = \frac{p(\Gamma_p + \Gamma_{trans,2}) - \Gamma_{trans,1}}{\Gamma_p + \Gamma_{trans,2} - \Gamma_{trans,1}} \tag{4.37}$$

and

$$B = \frac{(1-p)\Gamma_{trans,1}}{\Gamma_p + \Gamma_{trans,2} - \Gamma_{trans,1}}. \tag{4.38}$$

The XC trace of the solvated electron at the alkali-ion/water complex presented in Fig.4.7 is fitted with the sum of the population transients 4.35 and 4.36 convoluted

---

[34] A direct population of e_s^{a+} is not possible. For time delay > 100 fs the peak position is below E-E_F=2.5 eV, so that a direct population of this state with photon energies exceeding 2.5 eV would be possible. However, such a state at negative time delays is not observed in Fig.4.5.

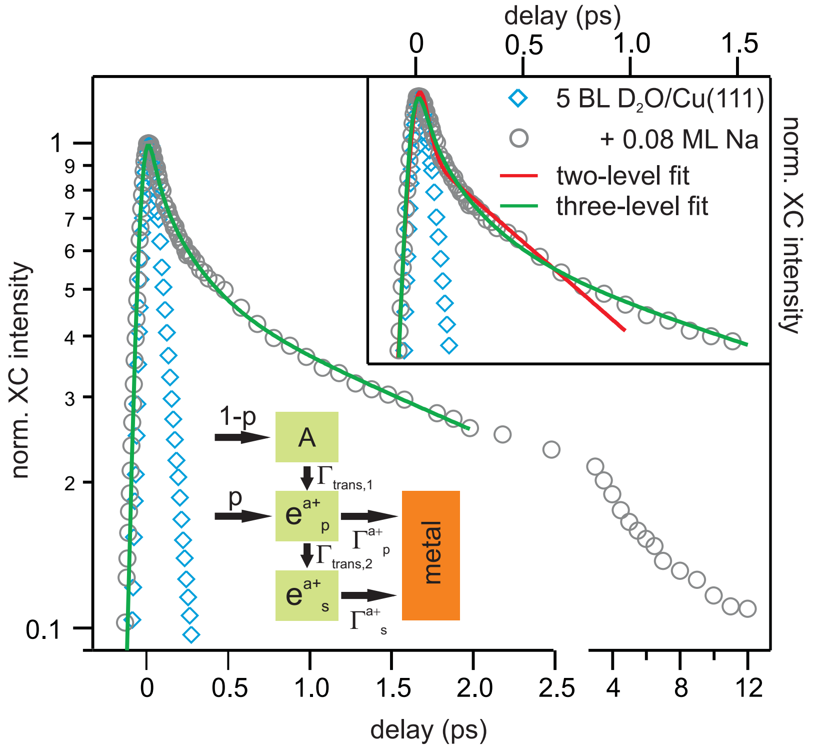

Figure 4.7: Population Dynamics of 0.08 ML Na adsorbed on D$_2$O/Cu(111). The XC of the e_s^{alkali} electrons (grey open circles) clearly shows the extended lifetime compared to the solvated electrons in pure D$_2$O/Cu(111) (blue open diamonds). The population transient is well reproduced by a three-level rate equation fit (green solid line) within the first 2 ps. (inset): A fit based on a two level system (red solid line) fails to reproduce the data. The block diagram sketches the the three-level rate equation approach.

with the laser pulses' envelope (solid green line). An additional exponential decay to negative time delays is added to take into account hot electrons, which are generated by absorption of $h\nu_{vis}$ and probed by $h\nu_{UV}$. The fit reproduces the data up to a time delay of 2 ps. The resulting fit parameters are summarized in table 4.2.

The excitation of the solvated electrons at the alkali-ion/water complex occurs via two pathways. On the one hand the e_p^{a+} state is populated indirectly via the state A of ice with a probability of 60%, on the other hand a direct population is possible with a probability of 40%. The electrons, which are excited via the state A, localize in the e_p^{a+} state with a time constant of 250 fs and subsequently cross over to e_s^{a+} with a time constant of 169 fs. Simultaneously, the electron population in both states decay back to the metal substrate with time constants of 100 fs and 2.97 ps for e_p^{a+} and e_s^{a+}, respectively. The same analysis of the population dynamics for K, and Cs adsorbed on amorphous ice yields similar fit parameters, that can be considered as identical within

Table 4.2: Fit parameters for the population decay of $Na^+/D_2O/Cu(111)$

(1-p)	0.60(5)
p	0.40(5)
$\Gamma^{-1}_{trans,1} = \tau_{trans,1}$	250(15) fs
$\Gamma^{-1}_{trans,2} = \tau_{trans,2}$	169(15) fs
$\Gamma^{-1}_{p} = \tau_{p}$	100(10) fs
$\Gamma^{-1}_{s} = \tau_{s}$	2.97(5) ps

the error bars. No clear dependence on the type of alkali is found for neither the population dynamics nor the energetic stabilization.

In the presence of alkali ions at the ice/vacuum interface a new species of solvated electrons is found, which is not present in the case of pure amorphous ice layers. On the basis of the observed energetic shift of its spectral signature, that exhibits two significantly different stabilization rates, and the population dynamics, that can be described by rate equation model, the 2PPE data can be interpreted as follows. The electron solvation at the alkali-ion/water complex occurs via two different states e_p^{a+} and e_s^{a+}, which exhibit dynamics on two different timescales. e_p^{a+} shows a strong energetic shift to lower intermediate state energies with a rate of -0.83 eV/ps and decays with a time constant of 100 fs. In contrast, the second state e_s^{a+} exhibits an energetic shift with a rate of -50 meV/ps and decays on a timescale of 3 ps. The excitation of e_p^{a+} occurs either directly with a probability of 40% or indirect by an initial state A from where the electrons cross over to e_p^{a+} with a time constant of 250 fs. To identify this state as the ice conduction band seems unreasonable, as electrons in the ice CB have a very short lifetime of only few fs, which is in contradiction to the relatively long decay time $\tau_{trans,1}$. As the electron dynamics in pure ice are significantly different and do not show such a behavior on two different time scales, state A has to be related to the alkali ions at the ice/vacuum-interface. As schematically depicted in Fig.4.4 this state could be the LUMO of the alkali ion.

Subsequently after the neutralization of the alkali it gets ionized, as discussed in section 4.1.1, and the electron is solvated at the alkali-ion/water complex, where it is further stabilized. Following this proposal, the autoionization of the alkali atom occurs with a time constant of $\tau_{trans,1}$=250(15) fs. Nevertheless, the population of these states at the ice/vacuum interface requires a wave function overlap with the initial states in the metal. Most likely, although it is not temporally resolved in the present experiments the population of state A and state e_p^{a+} proceeds via the ice conduction band with the respective probabilities (1-p) and p assuring the required wave function overlap. The population in the ice conduction band is expected to decay within the laser pulse duration, as it was also found before for electron solvation in pure amorphous ice layers on Cu(111) [Gah02].

The origin of the two states e_p^{a+} and e_s^{a+} is discussed in the following. Although, the exponential decay time of e_p^{a+} is identical to the initial decay time of solvated electrons in pure ice (species I) the state e_p^{a+} is not assigned to species I electrons, because of two reasons. (i) The initial energetic stabilization rate for e_p^{a+} is more than two times higher compared to the energetic stabilization rate of species I solvated electrons and (ii) a transition from a localized state in the bulk of the ice (species I) to a localized state at the ice/vacuum interface seems unreasonable. Hence, a different explanation for the two states e_p^{a+} and e_s^{a+} needs to be considered, when they can not be assigned to species I and species II solvated electrons. In this regard, it is noteworthy that the electron dynamics are similar to the electron dynamics in amorphous NH_3/Cu(111), where electron solvation also occurs at the adlayer/vacuum interface [Stä08b]. The two-component electron dynamics, with a fast and a slow component, seem to be a general phenomena for systems, where the solvated species is located at the vacuum interface of the polar adlayer. A possible explanation for the transition from e_p^{a+} to e_s^{a+} can be provided in analogy to the observation made for NH_3/Cu(111). As mentioned before the assumption of static states with constant decay times is a simplification in the case of solvated electrons. Here, the state is dynamically changing due to the rearrangement of the surrounding water molecules. So the transition from e_p^{a+} to e_s^{a+} can potentially be explained by the dynamic evolution of a single state, rather than by a real transition between two states. Fig.4.8 schematically depicts the modified image potential with an initial trapping site, *i.e.* a local potential minima, at the ice/vacuum interface for different time delays. Due to the solvation the potential is evolving with increasing time delay. Right after photoexcitation the energetic position of e_p^{a+} is above the potential barrier and the electronic wave function is relatively delocalized in the ice layer in the direction normal to the surface and the electron transfer is governed by its wave function overlap with unoccupied metal states (cf. Fig4.8.(a)). A reorientation of the water molecules in the vicinity of the electron leads to a further energetic stabilization, *i.e.* a deeper potential minimum, and to the formation of a potential barrier between the electron and the metal substrate (cf. Fig4.8.(b)). At larger time delays (c) the electronic wave function is screened from the substrate and the electron back transfer from the state e_s^{a+} is mainly determined by the tunneling probability through

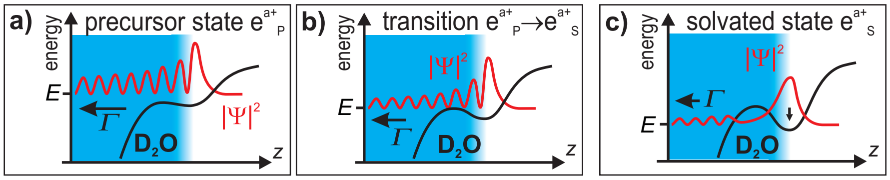

Figure 4.8: Scheme of the transition from e_p^{a+} to e_s^{a+}. The modified image potential (black solid line) and accordingly the wave function of the solvated electron (red solid line) is evolving with increasing time delay resembling the ongoing electron solvation. For details see text. Modified from [Stä08b].

the evolved potential barrier leading to slower dynamics of electrons in e_s^{a+}. In this scenario the transition time $\tau_{trans,2}$ describes the time constant of the evolution of the potential barrier between the solvated electron at the alkali-ion/water complex and the metal substrate.

In the following section further experimental evidence for the binding site of the solvated electrons in alkali ion covered ice layers is provided by the help of overlayer experiments. The dependence of the electron dynamics on the water layer thickness reveals, that the decay times at larger time delays depend exponentially on the layer thickness, indicating an electron back transfer to the metal, which is mediated by electron tunneling through a potential barrier.

4.1.3 Charge Transfer from the Alkali-Ion/Water-Interface to the Metal Substrate by Electron Tunneling

The new species of solvated electrons, introduced in the previous chapter, is clearly related to the deposition of alkalis onto the ice layer. Therefore, it is reasonable to assume, that these electrons bind in the vicinity of the alkali ions, and form a transient electron/alkali-ion/water complex located at the ice/vacuum interface. In order to verify this picture, overlayer experiments were performed to identify the binding site of the electron/alkali-ion/water complex on amorphous D_2O ice. In a previous publication, it is shown by Xenon overlayer experiments [Mey08], that for smooth amorphous water multilayers the solvated electrons reside inside the bulk of the water layer. In the case of electron solvation at the surface of the molecular adlayer the electron dynamics are strongly influenced by the additional overlayer, as it was shown for amorphous ice cluster [Stä07a, Mey08], crystalline ice structures [Bov09], and amorphous ammonia films [Stä08b]. If the long-living electrons which are observed here are bound to the alkali ions located at the ice/vacuum interface, one can expect to influence their properties also by adding an additional ice layer on top of the alkali ions[35]. Further details on overlayer experiments can also be found in section 6.1.

Fig.4.9 shows the results of such an experiment, where 3 BL of water are added on top of the Na-covered (0.08 ML) D_2O multilayer (5 BL). It shows XC traces taken before (blue diamonds) and after (green diamonds) the adsorption of the water overlayer.

The population decay of the solvated electrons at the alkali-ion/water complex is strongly affected by the additional water ice. The lifetime of these excess electrons, for simplicity determined by a single-exponential decay fit between a time delay of 1 and 2 ps is reduced from $\tau = 1.3(1)$ ps before water adsorption by 30% upon adlayer adsorption to a decay time of $\tau = 0.9(1)$ ps. In addition to changes in the population dynamics, the energetic stabilization is also modified as can be seen in Fig.4.10.

Here, the energetic positions of the peak maximum before (blue triangles) and after (green diamonds) the adsorption of the water overlayer are plotted as a function of time delays. The initial energetic stabilization rate is reduced by a factor of 4 from

---

[35] The overlayer experiment was also performed with a Xe overlayer showing a similar, but weaker effect on the electron dynamics. Therefore, only the overlayer experiment with an additional water layer is discussed, as the observed effects are much more pronounced.

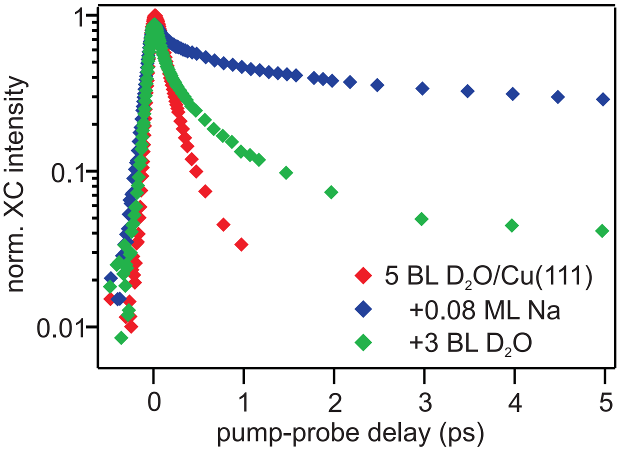

Figure 4.9: Overlayer experiment to determine the binding site of the electron/alkali-ion/water complex: Clear changes in the population dynamics of $Na^+/D_2O/Cu(111)$ occur when an additional 3 BL thick D_2O film is added on top (green diamonds). For comparison the XC traces of $Na^+/D_2O/Cu(111)$ before performing the overlayer experiment (blue diamonds) and the XC trace of solvated electrons in pure D_2O ice are depicted (red diamonds).

Σ = -0.83(5) eV/ps to Σ = -0.20(2) eV/ps by adding the top water layer. The reduced decay time and the significantly slower energetic stabilization upon adsorption of the additional water layer clearly demonstrates that the binding site of the solvated electrons is influenced by the overlayer. This interaction results in a less efficient screening of the excess charge from the substrate and a slower energetic stabilization of the charge by the surrounding water molecules. On the basis of these results, one can conclude that the excess electrons in $Na/D_2O/Cu(111)$ are located at the Na-covered ice/vacuum interface and presumably form an electron/Na^+/water complex, in contrast to the solvated electrons in amorphous ice multilayers where the solvated electrons reside in the bulk part of the layer. The fact, that the energetic stabilization of the electron at the alkali-ion/water complex proceeds more than two times faster compared to solvated electron in pure $D_2O/Cu(111)$ (cf. Fig.4.10 (red circles) can also be explained by the

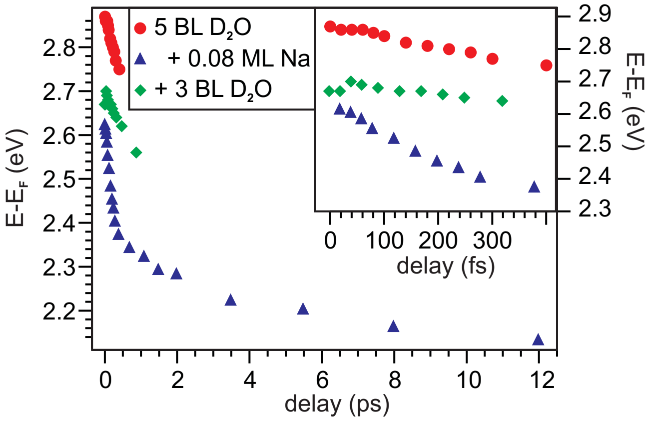

Figure 4.10: Overlayer experiment to determine the binding site of the electron/alkali-ion/water complex: Shift of the peak maximum for $Na^+/D_2O/Cu(111)$ before (blue triangles) and after (green diamonds) deposition of a 3 BL thick D_2O layer. For comparison the energetic shift of the peak maxima of solvated electrons in pure D_2O ice are depicted (red circles).

binding site difference. The energetic stabilization strongly depends on the mobility of the solvent molecules, *e.g.* the water molecules. It is known from calculations for small cluster anions, that dangling O-H bonds heavily contribute to the electron stabilization [Lee97]. The water molecules at the ice/vacuum interface are not fully coordinated in the hydrogen bond network, thus solvated electrons at the interface can exhibit a faster energetic stabilization as observed for solvated electrons in alkali$^+$/D_2O/Cu(111).

The binding site of the electron/alkali-ion/water complex at the ice/vacuum interface leads to a clear coverage dependence of the electron dynamics. This observation is also in contrast to the population dynamics of solvated electrons in pure amorphous ice, where no coverage dependence is observed for ice layer thicknesses above 2.5 BL [Gah03] [36]. Fig.4.11 presents XC traces for Cs and Na covered D_2O layers on Cu(111) of various thicknesses ranging from 2.5 to 6.0 BL. With increasing ice layer thickness the electron population dynamics in the late time regime (t>500 fs) are clearly slowing down. For a quantitative analysis of this observation single exponential decays with decay times τ_1 and τ_2 (as highlighted in Fig.4.11) were fitted to the data for different time delays of t=0.5 - 1.0 ps and t=1.0 - 2.0 ps, respectively.

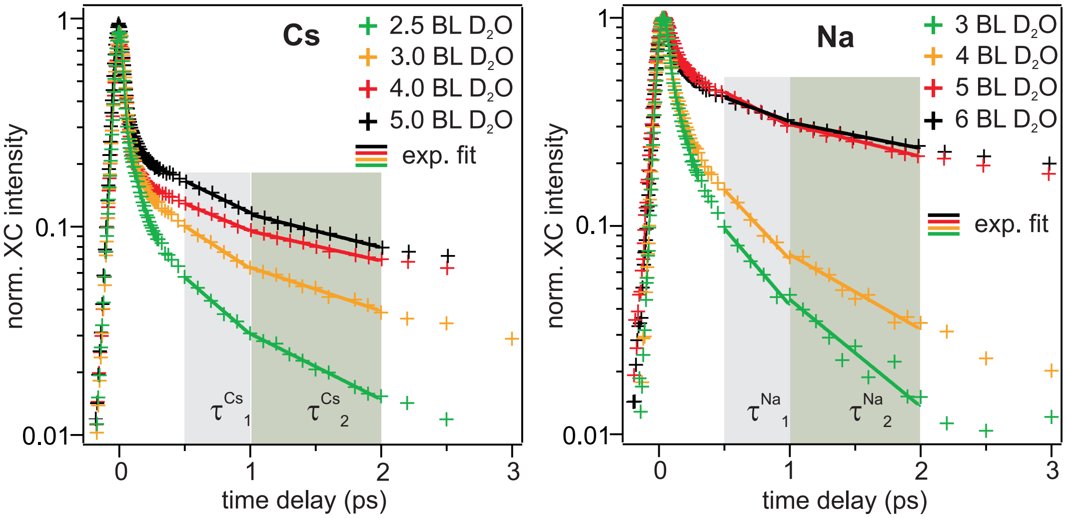

Figure 4.11: Water coverage dependence of population decay solvated electrons at the alkali-ion/water complex in amorphous D_2O/Cu(111). Solid lines present single exponential decay fits to the data for time delays of 0.5-1.0 ps and 1.0-2.0 ps, respectively.

The resulting decay times τ_1 and τ_2 for the respective time delay are plotted in Fig.4.12 as a function of ice layer thickness for Na (left panel) and Cs (right panel) adsorbed on top of the ice film. The decay times show two clear dependencies: (i) the decay times for a given water layer thickness increases with increasing time delay, and

---

[36] At a coverage of 2.5 BL D_2O on Cu(111) a transition from cluster to layer growth occurs and a wetting ice layer forms [Gah03].

(ii) for a given time delay the decay times increase with increasing ice layer thickness. The first observation can be explained by the ongoing solvation of the excess electron with increasing time delay. Due to the ongoing response of the surrounding water molecules, the energetic stabilization occurs on all investigated time scales (cf. Fig.4.6), the excess charge is further screened from the metal substrate resulting in a slow down of the back transfer. The thickness dependence of the decay times for a given time delay, *i.e.* stage of solvation, can be fitted by a single exponential decay:

$$\tau(d) \propto exp[\beta \cdot d], \tag{4.39}$$

where β is the inverse range parameter, which is a measure of the influence of the effective electron mass and the barrier height on the tunneling probability [Nit06], and d the thickness of the ice layer.

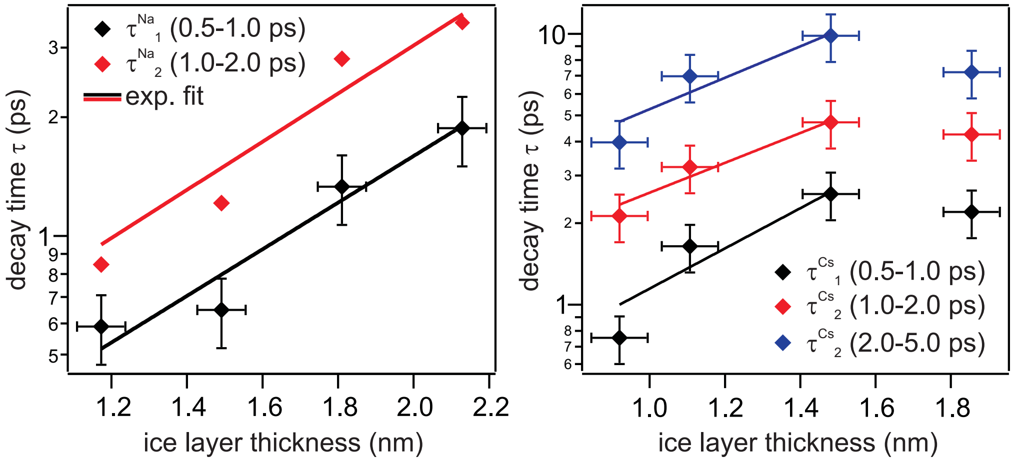

Figure 4.12: Water coverage dependent decay times derived from a single exponential decay fit to the XC data for Na (left panel) and Cs (right panel) on D_2O. The decay times depend exponentially on the ice thickness. The solid lines are exponential fits to the data.

The results of the fit are summarized in table 4.3. The inverse range parameter β shows neither a dependence on the investigated time delay nor on the type of alkali and can be considered to be constant with an average value of β=1.3(2) nm^{-1}. Recalling the fact, that the solvated electrons at the alkali-ion/water complex are located at the ice/vacuum interface, the ice thickness-dependent decay times are a strong evidence for an electron transfer proceeding by tunneling through a potential barrier, that is depending on the ice layer thickness. Accordingly, the tunneling probability depends exponentially on the barrier thickness d following equation 4.39. This scenario is schematically depicted in Fig.4.13. The alkali-ion/water complex leads to a modification of the image potential so that the potential exhibits a minimum at the ice/vacuum interface enabling for binding an excess electron. Hence, tunneling through this potential barrier determines the electron transfer time τ. For a thicker layer (2)

Table 4.3: Fit parameters of the ice thickness dependent population dynamics derived from an exponential fit to the decay times τ_1 and τ_2. Inverse range parameter in nm^{-1} and BL^{-1} .

	β_1 (nm^{-1})	β_2 (nm^{-1})	β_3 (nm^{-1})	β_1 (BL^{-1})	β_2 (BL^{-1})	β_3 (BL^{-1})
Na	1.2(2)	1.2(2)	-	0.43(7)	0.45(9)	-
Cs	1.7(3)	1.3(2)	1.3(2)	0.6(1)	0.47(9)	0.5(1)

this potential minimum is further away from the substrate and the barrier is broader than for a thinner layer (1). Accordingly, the transfer time increases exponentially with the layer thickness as it is experimentally observed.

Surface solvated electrons, which decay back to the metal substrate by tunneling through a potential barrier, are also observed in amorphous ammonia on Cu(111) [Stä07b, Stä08b]. The common binding site of the solvated electron in ammonia and the solvated electrons at alkali-ion/water complexes could be an explanation for the observed similarities in the population dynamics, the energetic stabilization, and the back transfer mechanisms of the excess charges in both systems. Nevertheless, also clear differences are observed. Whereas for NH_3 a transiently evolving potential barrier for the back transfer of solvated electrons is found, identified by an increase in the inverse range parameter β for increasing time delays, such an effect is not observed for alkali$^+$/D_2O/Cu(111), where β is constant for delay times between 0.5 and 5 ps. The evolution of the potential barrier is governed by the rearrangement of the solvent molecules, which could explain this difference. The binding strength of the H-bonds in water is much stronger with 240 meV compared to ammonia, with 100 meV. Therefore ,the water network can react faster on the excess charge and the rearrangement of the solvent molecules at later time delays is weaker. Another major difference is the

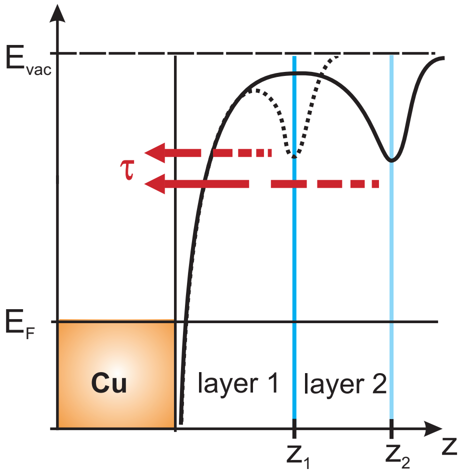

Figure 4.13: Tunneling through ice layer of the solvated electron at the alkali-ion/water complex at the ice/vacuum-interface. For thicker ice layers (2) the tunneling probability is lower than for thinner layers (1). The black solid lines are the modified image potentials with an electron trap at the ice/vacuum interface.

presence of the positively charged alkali ions at the ice/vacuum interface, that already let to a reorientation of the surrounding water molecules before an electron is attached to the alkali-ion/water complex. As a consequence the initial potential minima would already be deeper and subsequent changes would less influence the potential barrier between the charge and the metal substrate.

The following section discusses the dependence of the population dynamics on the alkali-ion coverage. This is done with the purpose to address the question if neighboring trapping sites for solvated electrons at the alkali-ion/water cluster interact with each other or can be considered to be independent.

4.1.4 Alkali Coverage Dependent Electron Dynamics

The question is raised if the number of trapping sites for species II solvated electrons linearly scale with the number of adsorbed alkali ions, implying no interaction between neighboring trapping sites or if further effects need to be considered. Therefore alkali coverage dependent 2PPE experiments were performed.

Fig.4.14 presents XC traces for an amorphous D_2O wetting layer (5 BL) (green markers) and for various coverages of Na between 0.02 and 0.08 ML adsorbed on top of the ice layer. When comparing the XC traces of the Na-covered ice layers in Fig.4.14 with the ones of the solvated electrons in pure water ice, a new component can be observed which exhibits significantly longer lifetimes. With increasing Na^+ coverage, this component becomes more dominant. For the largest investigated Na coverage of 0.08 ML Na, the electron population can be observed up to a time delay of t=20 ps. In section 4.1.2 the population dynamics of the solvated electron at the alkali-ion/water complex was discussed using the example of $Na^+/D_2O/Cu(111)$. As shown in Fig.4.7 the population dynamics can be described within the first 2.5 ps by means of a rate equation model considering two solvated electron states e_p^{a+} and e_s^{a+}, that take into account the fast and the slow component of the observed dynamics. As an approximation, the XC traces in Fig.4.14 are fitted with a triexponential decay within the first 5 ps after photo excitation in order to answer the question raised above. The first exponential decay takes the fast initial electron dynamics into account that are originating from electrons in the ice conduction band and eventually from species I solvated electrons[37], but as well a contribution from the alkali induced states A and e_p^{a+}. The latter two decays can clearly be assigned to the dynamics of the solvated electrons mediated by the presence of Na^+ ions e_s^{a+} and will be used as a measure of the number of species II solvated electrons. The fit yields decay times of τ_2=880(50) fs and τ_3=9.6(5) ps for the second and third exponential decay, respectively. In order to investigate the dependence of the population dynamics on the alkali ion coverage, the following assumption is made: the more Na is deposited on the ice layer, the more trapping sites are available to trap an electron at an alkali-ion/water complex. If no interaction between neighboring sites occurs, the 2PPE intensity from species II in the XC traces should scale linearly with Na coverage; that is, doubling the Na coverage

---

[37] They exhibit an initial exponential decay time of τ_1=110(10) fs derived by fitting a single exponential decay to the XC trace of the solvated electrons in pure ice (green markers)

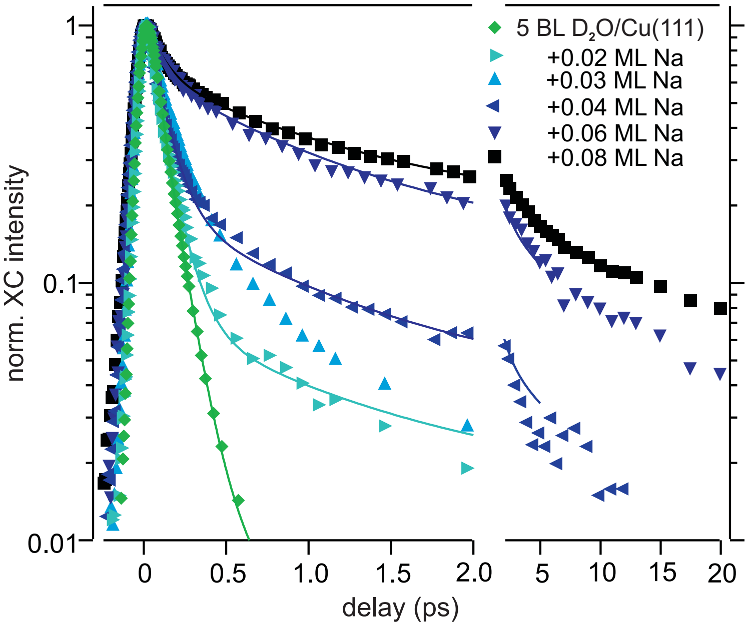

Figure 4.14: XC traces for pure water ice adsorbed on Cu(111) and for different coverages with Na co-adsorbed on top of the amorphous ice layer. The XC traces are normalized to one for the maximum intensity. The solid lines are exponential decay fits to the data. For further details, see the text.

should lead to a doubling of the amplitudes of the corresponding components in the fit of the decay dynamics. To verify this assumption, the XC trace of the 0.04 ML Na-covered water surface is fitted to determine the decay times and amplitudes mentioned before. For the other Na coverages, fits were obtained for fixed decay times τ_1, τ_2, and τ_3, only allowing the amplitudes A_1, A_2, and A_3 to be adjusted. The results of this analysis are plotted in Fig. 4.15.(a). The amplitudes of the second and third decay (A_2 and A_3, respectively) are normalized with respect to the amplitude of the first decay, yielding the ratios A_2/A_1 and $A_3/\ A_1$ as a function of Na coverage. A_1 is assumed to be independent of Na coverage, whereas species II is expected to scale according to the increased number of available sites with Na coverage. Indeed, such an increase in A_2/A_1 and $A_3/\ A_1$ is observed, which depends, however, nonlinearly on Na coverage. For comparison, the dashed lines depict the expected linear dependence of the amplitude on the Na coverage for both ratios A_2/A_1 and $A_3/\ A_1$. A similar behavior is also found for Cs presented in Fig.4.15.(c), where the same analysis as for Na was performed. However, the trend in these data set is not as clear as in the case of Na.

Different possible explanations for the observed nonlinear increase are considered, which are discussed in the following. The dependence of the population dynamics on the alkali ion coverage can be understood when the decrease in the work function for in-

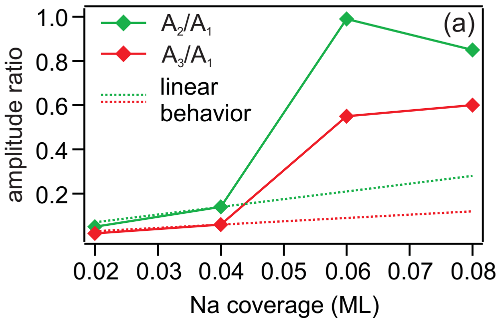

Figure 4.15: Amplitude ratio of the tri-exponential decay fit for Na (a) and Cs (b) coadsorbed on amorphous ice. A_2/A_1 and $A_3/\ A_1$ describe the proportion of the amplitude of the second and third decay, which describe the dynamics of the species II electrons, with respect to the first one, respectively. The behavior of the dashed lines would be achieved if the amplitude scaled linearly with the amount of alkali ions, i.e., the alkali coverage.

creasing alkali coverage is taken into account (see Fig.4.2). This change in the electronic structure of the system, *e.g.* from Φ=3.80 eV for 0.04 ML Na to Φ=3.65 eV for 0.08 ML Na, can lead to changes in the matrix elements involved in both the pump steps and the probe steps of the photoemission process, which can result in a higher probability to detect an excited electron. In addition, because the state of the electron/alkali-ion/water complex is pinned to the vacuum level of the system, it shifts to lower energies with respect to the Fermi level if the work function is decreased. This downshift can lead to an increased efficiency of the electron transfer in the pump step (e.g., because of a higher abundance of photoexcited electron in the substrate) and thus to an enhanced population build-up of the alkali-induced species II sites.

Besides these global effects on the population and probing efficiency, also local effects at the solvation sites can have an influence on the relative amplitude of species II. By assuming a random distribution of Na ions on the ice surface, the mean distance of neighboring Na ions would be 17.9 or 14.6 Å for coverages of 0.04 or 0.06 ML Na^+, respectively. On the basis of angle-resolved 2PPE measurements performed at solvated electrons in pure D_2O ice, the spatial extent of the electronic wave function of the species I electrons was estimated in an earlier work with a diameter on the order of 10-20 Å [Bov03]. By assuming that the spatial extend of the electronic wave function of the species II electrons is similar, it seems likely that, above a critical Na coverage of 0.05 ML Na^+, an interaction of the delocalized species II electron with two neighboring Na ions sets in. This interaction could result in energetically more favorable solvation sites in the proximity of neighboring Na ions. These trapping sites including two Na ions within the extend of the electron wave function can result in a higher population efficiency, because the better initial trapping of the excited electron reduces the back-transfer probability to the metal substrate. At even higher Na coverages exceeding the coverages investigated in the present work (>0.15 ML), the formation of Na dimers is possible. Mundy et al. showed in their theoretical work on $Na(H_2O)_6$ clusters that the autoionization process of the Na atom is more likely if they form Na_2 dimers [Mun00]. Hence, the 3s electron of the Na is better stabilized, which means that, in the vicinity of the ionized Na_2 dimer, an energetically favorable solvation site is formed.

Although a general trend is observed that higher alkali coverages, *i.e.* a higher number of trapping sites, lead to more solvated electrons at the alkali-ion/water complex (species II) a quantitative analysis of this dependence is difficult as global and local effect can have a strong influence on the population dynamics.

4.1.5 Thermally Activated Diffusion of Na-ions through an Amorphous Ice Layer

In section 4.1.1 it was shown that the adsorbed alkalis are bound at the ice/vacuum interface and in section 4.1.3 it was demonstrated that the solvated electrons at the alkali-ion/water clusters are also located at the interface to the vacuum. Nevertheless, the location of the alkali ions strongly depend on the preparation temperature as the diffusion of the alkali into the ice layer can be thermally activated. In order to investigate the effect of this diffusion on the dynamics of the solvated electrons at the alkali-ion/water clusters the following experiment was performed. An amorphous ice layer of 7 BL thickness was deposited onto the Cu(111) crystal kept at 100 K (a) followed by a temperature flash to 140 K, where the temperature was kept constant for 5 s. At this temperature no water desorption or crystallization of the ice layer occurs. After taking a time-resolved 2PPE spectrum, 0.05 ML Na were deposited on top of the ice layer (b) followed by another time-resolved 2PPE acquisition. Subsequently, the sample was flashed to temperatures of 120 and 140 K followed each time by a 2PPE measurement after the sample has cooled down again to 60 K, (c) and (d), respectively. The corresponding XC traces are depicted in Fig.4.16. In the inset the work function of the system to the corresponding steps (a)-(d) is plotted. The XC trace for 7 BL D_2O ice shows the typical initial exponential decay time of solvated electrons in amorphous ice with a time constant of $\sim$ 120 fs. The work function of this ice layer is Φ_a=4.05(5) eV. The coadsorption of 0.05 ML Na leads to a clear slowdown of the population dynamics, which is attributed to the dynamics of a solvated electron at an alkali-ion/watter complex at the ice/vacuum interface (see sec.4.1.2). Due to the presence of Na^+ at the ice surface, the work function is reduced to Φ_b=3.74(5) eV. A temperature flash to 120 K leads to a reduction of the XC intensity at larger time delays by a factor of $\sim$ 3. This reduction is accompanied by an increase of the work function by $\sim$ 100 meV. After a temperature flash to 140 K the long living component in the XC trace is almost vanished and the XC trace resembles the XC trace for amorphous D_2O ice without coadsorbed alkali ions. In addition, the work function further increased to Φ_d=4.00(5) eV, a value that is very close to the initial work function Φ_a of the pure ice film.

These observations can be explained by a diffusion of the alkali ion into the ice layer, where the ion is efficiently screened by the solvent molecules. At a temperature

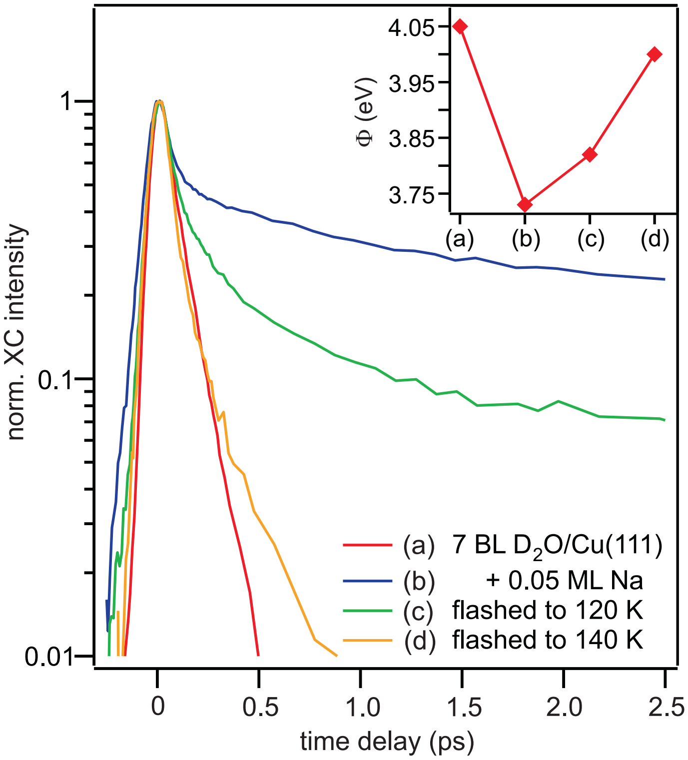

Figure 4.16: Incorporation of Na ions in amorphous D_2O ice. (Main panel): XC traces for amorphous 7 BL D_2O ice ((a), red line) and for 0.05 ML Na coadsorbed on top of the amorphous ice film ((b), blue line). Temperature flashes to 120 and 140 K and subsequent cooling of the sample to T≈60 K, ((c), green line) and ((d), yellow line), respectively, lead to an increase of the population dynamics. (Inset): Work function Φ of the sample for the indicated steps (a)-(d) of the experiment. See text for details.

of 120 K the diffusion of the alkali ions into the ice layer is activated. Nevertheless, not all ions are incorporated in the ice film and the remaining alkali-ion/water complexes at the ice/vacuum interface can further trap excess electrons. However, due to the smaller number of surface located alkali ions, *i.e.* smaller number of electron traps, the XC intensity in the slow component at larger time delays is reduced. This interpretation is in agreement with the alkali-coverage dependence of the population dynamics discussed in section 4.1.4. As less alkali ions are located at the ice/vacuum interface the work function of the system increases. After the temperature flash to 140 K all alkali ions have diffused into the ice layer and no alkali-ion/water complexes are available at the surface to bind excess electrons and allow for their subsequent screening and energetic stabilization. The XC trace (d) is now almost identical to the one for pure amorphous D_2O ice (a). Obviously, the surface character of the alkali-ion/water complexes is crucial for the ability to bind an excess charge, which is not possible anymore once the alkali-ion is completely incorporated in the water network. Probably, the alkali ion will diffuse to the metal substrate as this results in a very strong binding. The resulting dipole moment of the positively charged alkali ion and its image charge in the metal, which would lead to a reduction of the systems work function, is, however, screened by the surrounding water molecules, so that the work function is similar to the one of a pure amorphous ice layer on Cu(111). This process, which can be understand as the solvation of the ion, is discussed in detail in section 5.1.

4.2 Photoemission of the Alkali *ns* Valence Electron

As the autoionization process of alkali atoms at the ice surface is thermally activated one may expect that at sufficiently low temperatures neutral alkali atoms may be present at the surface.

Fig.4.17.(a) presents one-color 2PPE spectra of K atoms deposited at a sample temperature of T=40 K onto amorphous $D_2O/Cu(111)$ as a function of final state energy E_{fin}-E_F for various temperatures to which the sample was heated to for 2 s. Before turning to the temperature dependence, first the spectral signatures of the initial spectrum at T=45 K (black solid line) are discussed. The spectrum can be separated into two parts. The first part lies in the range from E_{fin}-E_F = 3.7 to 7.0 eV and originates from two-photon photoemission processes. Besides the secondary edge at a final state energy of 3.75 eV, resembling the work function of the system, and the Fermi edge at an energy of E_{fin}-E_F=6.86 eV, equal to two times the UV photon energy, the spectrum exhibit a feature at E_{fin}-E_F=4.6 eV, that originates from the Cu d-bands, and a peak at E_{fin}-E_F=6.3 eV (see inset of Fig.4.17.(a)). This feature is

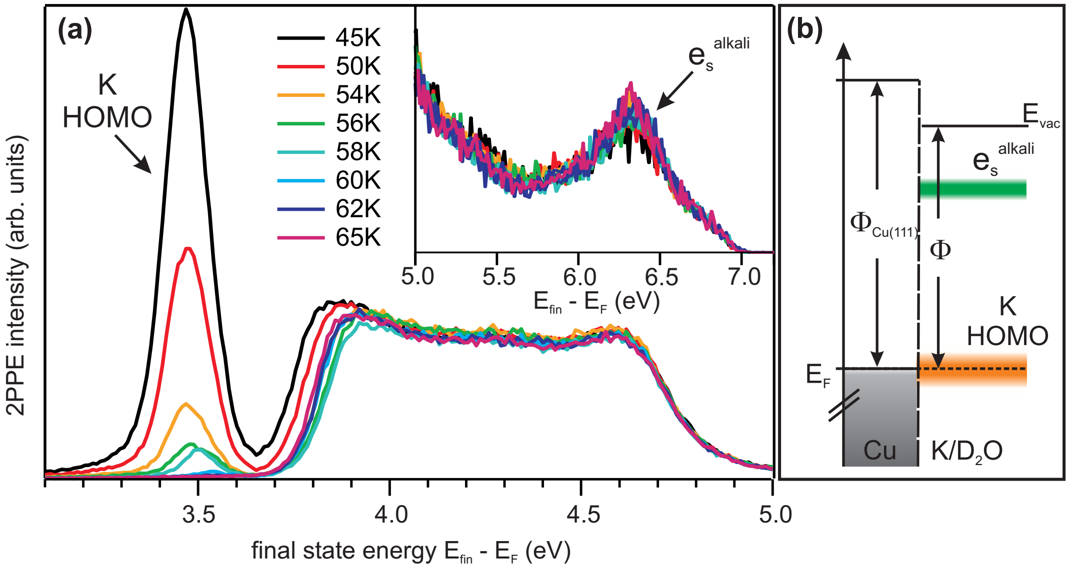

Figure 4.17: (a): Temperature-dependent 2PPE spectra of 0.07 ML K adsorbed on top of $D_2O/Cu(111)$. Prior to the acquisition of the 2PPE spectrum at 40 K, the sample was flashed to the indicated temperatures for 2 s. Each spectrum is taken on a non-irradiated spot. The Spectra were taken with UV photons with a photon energy of $h\nu$=3.43 eV. (Inset): Expanded view of the high energy part of the spectrum. (b): Energy scheme of $K/D_2O/Cu(111)$ with the occupied HOMO of the potassium located at the Fermi level (E-E_F=0 eV) and the solvated electron at the alkali-ion/water complex e_s^{alkali} at E-E_F=2.9 eV.

attributed to solvated electrons at alkali-ion/water complexes discussed in the previous sections. Its energetic position at E-E_F=2.9 eV is shown in a schematic energy diagram in Fig.4.17.(b). However, in the second part of the spectrum, below E_{fin}-E_F=3.65 eV, lies the most dominant feature of the spectrum, which is a peak located at an energy of E_{fin}-E_F=3.47 eV. In contrast to the first part, the photoelectrons in the second part are generated by absorption of a single photon, *i.e.* by direct photoemission. Hence, this peak is located at the Fermi level of the Cu(111) surface as depicted in Fig.4.17.(b). [38] Direct photoemission can only occur when the work function of the sample is below the photon energy. Here, the position of the secondary edge of the two-photon spectrum indicates a work function of Φ=3.75 eV, which is clearly above the photon energy of hν=3.43 eV. A possible explanation for this observation is given later in this section. First, evidence for the direct photoemission from the state at E_{fin}-E_F=3.47 eV is given and possible scenarios for the origin of this state are discussed.

In direct photoemission the photoemission yield scales linearly with the laser pulse intensity, whereas it depends quadratically on the laser pulse intensity when the photoemission occurs via a two photon process. Hence, for low laser fluences no second order photoemission is observed. Fig.4.18.(a) presents a series of photoemission spectra in a false color representation of K/D_2O/Cu(111) as a function of energy (left axis) and illumination time (bottom axis). The spectra were taken by illumination of the sample with UV photons with a photon energy of $h\nu = 3.02$ eV and a laser fluence of $8 \cdot 10^{-5}\ J/cm^2$. For such a low fluence no two photon photoemission signal is observed and solely the direct photoemission peak occurs in the spectrum. In addition, a clear decrease of the photoemission signal with illumination time is observed. In Fig.4.18.(b) the intensity of the direct photoemission peak is plotted as a function of illumination time. The decay of the PE signal is well described by a bi-exponential decay (red solid line) with an initial decay rate of $5.7(2)\times10^{-3}s^{-1}$ and a decay on a longer timescales with a rate of $6.4(2)\times10^{-4}s^{-1}$. The decay of the PE signal can be understand in terms of a depopulation of an occupied initial state in a direct photoemission step by absorption of UV photons. Obviously, the depopulation of this state is a very efficient process. It seems that a re-population of the initial state is either not possible at all or very inefficient by absorption of UV photons. Although the initial state can efficiently be depopulated by UV irradiation, its population decays with a low decay rate when the sample is not irradiated. After keeping the sample one hour in the dark (no UV irradiation) the PE intensity has decreased by less than 10% compared to the initial intensity (data not shown). This finding is reasonable as the initial state is located at the Fermi level of the Cu(111) substrate (cf. Fig.4.17.(b)). The direct PE signal can be quenched by heating the sample. As presented in Fig.4.17 the PE intensity depends strongly on the sample temperature. Flashing the sample to temperatures of up to 65 K and cooling down again to 40 K results in the spectra depicted in Fig.4.17. After the final heating step to 65 K the peak at E_{fin}-E_F=3.5 eV has completely vanished. In contrast, the 2PPE part of the spectra is only weakly affected by the temperature

---

[38] The corresponding feature after two photon absorption is not observed, because the cross section for the two-step process is about four orders of magnitude smaller than the one for the one-step photoemission [Fau94].

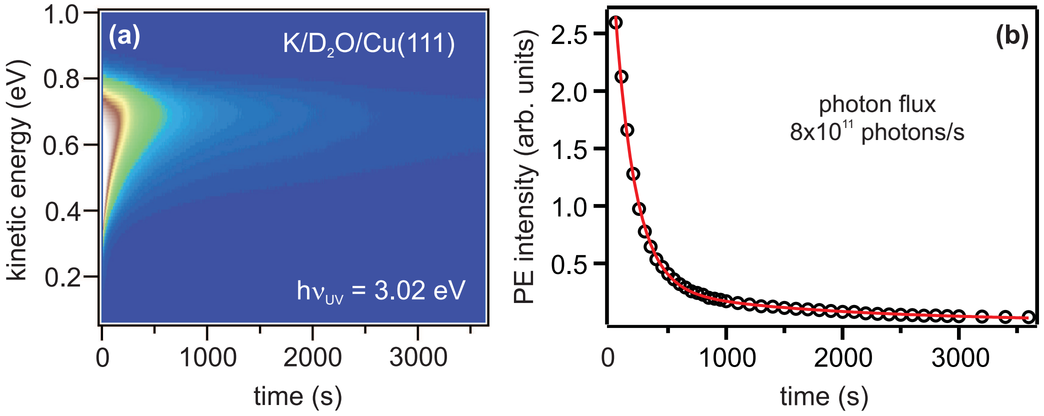

Figure 4.18: Depopulation of the K 4s state. (a): False-color plot of the PE intensity as a function of illumination time. The sample is irradiated with a fluence of $8 \cdot 10^{-5}\ J/cm^2$ by UV photons with a photon energy of $h\nu = 3.02$ eV. (b): Peak intensity of the direct PE peak as a function of illumination time. The data is fitted by a bi-exponential decay (solid red line). The initial decay rate is $5.7(2)\times10^{-3}s^{-1}$ followed by a significantly slower decay with a rate of $6.4(2)\times10^{-4}s^{-1}$. The photon flux is $8 \cdot 10^{11}\frac{photons}{s}$.

changes and shows only a shift in the position of the secondary edge to higher energies by $\sim$ 100 meV, indicating an increase of the work function.

The peak at E_{fin}-E_F=3.47 eV in the photoemission spectrum presented in Fig.4.17 can be attributed to a direct photoemission from the highest molecular orbital (HOMO) of the K atom, which mainly consists of the 4*s* orbital of K. Although for an isolated K atom the ionization potential (IP) is IP=4.34 eV [Lid93] and hence almost 1 eV above the photon energies used in the present experiment, a direct PE seems, however, possible, taking into account the screening of the surrounding water molecules. Indeed, it is known from experiments that the IP potential of Na(H_2O)$_n$ cluster with n=4 to n=23 is reduced to a value of IP=3.17 eV compared to the IP of an isolated Na atom (IP=5.14 eV [Lid93]) [Her91]. Similar systems have been investigated also theoretically for alkali-(H_2O)$_{18}$ clusters for Li, K, and Na atoms, where comparable vertical ionization potentials of $\sim$ 3 eV were found [Von06a, Von09]. For K(H_2O)$_{18}$ a vertical IP of 3.0 eV has been found [Von09]. This finding is in excellent agreement with the present experimental finding, which shows that the direct photoemission signal is observable using UV photons with a photon energy of $h\nu = 3.02$ eV (cf. Fig.4.18). Indeed, as mentioned earlier the initial state of the observed photoemission is located at the Fermi level of the sample, which corresponds to a binding energy of 2.95(5) eV with respect to the vacuum level. It seems that the simple Schottky-Mott limit, where vacuum level alignment applies, is a good assumption for K(H_2O)$_n$ cluster on a Cu(111) surface. In contrast to the isolated K atom, the theoretical calculations of Vondrak *et al.* implies that the HOMO of the K atom is more delocalized in the presence of water molecules extending to about 8 Å in diameter. The depopulation of this state, found in the present thesis, occurs with a rate of $5.7(2)\times10^{-3}s^{-1}$, which is in agreement with the decay rate of the photoionization cross section of $5(2)\times10^{-3}s^{-1}$ for 0.02 ML of K on 3000 L of H_2O found by Vondrak *et al.* [Von09]. In the present case a population of the HOMO of the K atom after the initial ionization seems not possible. This might be explainable by the fact that the presence of the alkali ion leads to a reorientation of the surrounding water molecules that screen the alkali ion from the metal substrate. As the substrate serves as an electron donor, a certain wave function overlap of the initial state of the electron in the metal and the HOMO of the K atom is required. So the screening of the alkali ion by the water molecules seems to hinder a re-population of the HOMO of the alkali ion.

The major difference of the experiments presented in this section to the ones discussed in the previous sections of this chapter is the lower sample temperature of ~ 40 K during the alkali deposition, which have been deposited at ~ 60 K in the case of the experiments discussed in section 4.1. This difference in temperature leads to a significant difference in the starting conditions of the experiment although in both cases alkali atoms are deposited onto an amorphous ice layer. When deposited at higher temperature the ionization of the alkali atom and the subsequent back transfer of the electron to the metal substrate leads to positively charged alkali ions at the ice/vacuum interface, whereas this ionization is hindered when less thermal energy is available, so that the alkali atoms remain neutral at the surface. Nevertheless, for the case of K atoms on amorphous ice, 40 K is still not cold enough to completely prevent the ionization, as the peak at E_{fin}-E_F=6.3 eV (see inset of Fig.4.17), attributed to solvated electrons at alkali-ion water cluster, is also detectable at 40 K. The temperature dependent decrease of the direct PE signal implies that the ionization of the alkali atom could be a thermally assisted process.

As mentioned earlier in this section the work function of the current system, derived from the position of the secondary edge of the two photon photoemission part of the spectrum presented in Fig.4.17, is Φ=3.75 eV, which seems to contradict the fact that a direct photoemission is observed for photon energies of $h\nu$=3.43 eV or even $h\nu$=3.02 eV. A possible explanation for this apparent contradiction considers the different origins of the photoemitted electrons and the effect of a dipole layer at the ice/vacuum interface. The investigated system is not a homogenous sample, but rather consists of different areas. The investigated sample consists of different patches, where besides areas of solely D_2O ice, patches with alkali ions and neutral alkali atoms at the surface coexist. The positively charged alkali ions at the ice surface are partially screened by the surrounding water molecules such that a dipole layer is formed at the ice/vacuum interface at z_D as schematically depicted in Fig.4.19.(b). This dipole layer at the surface leads to a modification of the image potential in front of the metal surface, which is depicted in Fig.4.19.(a). The contribution of the dipole moment ΔV_{dipole} to the potential is sketched in Fig.4.19.(c) as a function of the distance to the surface z parallel to the surface normal. It has a repulsive and an attractive part for electron passing through the dipole layer. In contrast to the work function of the pure ice layer on Cu(111) Φ^{ice} the global work function Φ is reduced by $\Delta\Phi_{alkali}$ as a consequence of the positively

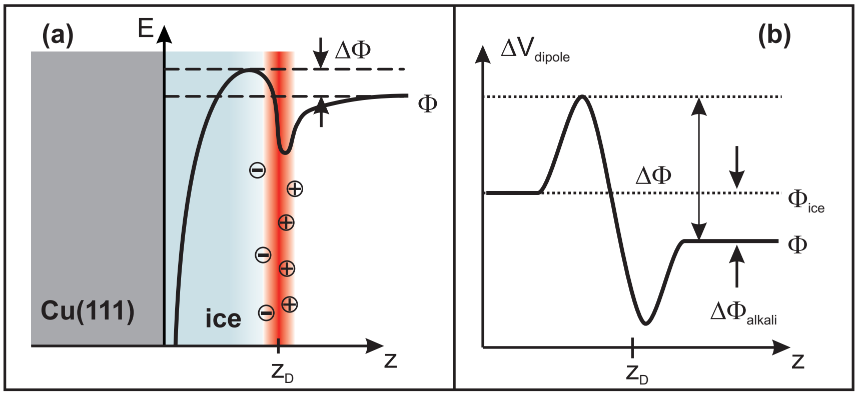

Figure 4.19: Influence of the surface dipole layer on the systems work function. (a): Side view of the layer structure of K/D_2O/Cu(111). At the ice/vacuum interface a distance z_D to the surface plane a dipole layer is formed by the positively charged alkali ions and the surrounding water molecules that screen the ions. The image potential is modified such that potential minima occur at the interface. (b): Dipole potential ΔV_{dipole} as a function of the distance to the surface z. The dipole layer at the surface leads to a repulsive and an attractive part of the potential for electrons that propagate through the dipole layer. The minimum energy for an electron, that passes through this layer, needed to overcome the systems work function Φ is increased by ΔΦ. See text for details.

charged alkali ions at the surface. However, all photoelectrons, that are generated by absorption of two photons, originate from the metal substrate, as an excitation within the ice layer can be ruled out due to the large band gap of ice. Hence, these electrons have to pass through the dipole layer at the surface, where they have to overcome the barrier that lies above the global vacuum level, defining the work function Φ, by ΔΦ, *i.e.* these electrons need an energy of Φ+ΔΦ to overcome the global work function of the sample. The electrons originating from the HOMO of the K atom, however, are not excited from the metal substrate, but directly from the K atom at the ice/vacuum interface around z_D. Hence, they do not propagate through the entire dipole layer at the surface and they do not experience the potential barrier formed by the dipole layer. So, these electrons only need to overcome the work function of Φ. In this scenario, the apparently different work function for electrons from the neutral K atoms (one photon photoemission) and for electrons initially excited in the metal substrate (two photon photoemission) is explainable.

4.3 Conclusion

The adsorption of alkali atoms on top of wetting, amorphous ice layers on Cu(111) leads to pronounced changes in the dynamics of excess electrons compared to electron solvation in pure D_2O layers. On the basis of the presented results, the following scenario is proposed: adsorption of low coverages ($<$ 0.15 ML) of alkali atoms on amorphous D_2O ice at temperatures between 60 and 100 K leads to the formation of alkali ions located at the ice/vacuum interface. The accumulation of positive charge at the ice/vacuum interface is identified by an alkali coverage dependent work function change. Due to screening of the alkali ions by the surrounding water molecules the net charge q_{net}, contributing to the work function decrease, is significantly smaller than the elementary charge of the alkali. For Cs a value of $q_{net} = 0.03(1) \cdot e$ is found, which is identical to the value for Na of $q_{net} = 0.02(1) \cdot e$. Photoinjection of excess electrons into these alkali-ion covered amorphous ice layers, results in the formation of a solvated electron at an alkali-ion/water complex located at the ice/vacuum interface, which is identified by a signature in the two-photon photoemission spectra. The solvation of the electron at this complex proceeds *via* two different states e_p^{a+} and e_s^{a+}, which exhibit dynamics on two different timescales. Whereas, the first state e_p^{a+} is energetically stabilized with a rate of Σ=-0.83 eV/ps, the latter state e_s^{a+} exhibits an energetic shift of Σ=-50 meV/ps. In addition, the population dynamics of the solvated electron at the alkali-ion/water complex can be described by a rate equation model, including an injection channel and the two states e_p^{a+} and e_s^{a+}, which decay with different time constants of 100 fs and 3 ps, respectively. The injection is expected to occur via the ice conduction band, which however can not be temporally resolved as the population in the ice CB decays too fast. The injection into the state e_p^{a+} can occur directly *via* the ice CB or indirectly *via* a state A, which can be assigned to the LUMO of the alkali ion and is as well populated *via* the ice CB. The observed behavior of an electron solvation on two different time scales seem to be a general phenomena for systems, where the solvated species is located at the interface of the polar adlayer to the vacuum, as it is also observed for NH_3/Cu(111). In analogy to this system, the two states e_p^{a+} and e_s^{a+} can be interpreted as (i) a state, where the electron transfer is determined by the wave function overlap of the solvated electron state e_p^{a+} with unoccupied metal states, and (ii) a state, where an electron transfer occurs, which is determined by the tunneling probability through the evolved potential barrier, that is due to the ongoing screening of the electron by the surrounding water molecules, leading to slower dynamics of electrons in state e_s^{a+}. This interpretation is further corroborated by ice layer thickness dependent measurements, where for time delays $>$ 500 fs an exponential dependence of the decay times on the ice layer thickness is found, in agreement with an electron transfer proceeding by tunneling through a potential barrier that is depending on the ice layer thickness. An inverse range parameter of β=1.3(2) nm^{-1} is found that neither depends on the time delay, i.e. stage of solvation, nor on the type of alkali.

When the alkali atoms are deposited onto the ice film at temperatures of $\sim$ 40 K a new spectral feature is observed, that originates from an occupied state at the Fermi level. This feature is interpreted as the HOMO of the K atom in the solvent environment. In contrast to most experiments conducted at temperatures between 60 and 100 K, the alkali atom is not autoionized and remains neutral at the surface. The interaction of the water molecules with the K atom leads to a reduction of the ionization potential from IP=4.34 eV for the isolated K atom to a value of IP=2.95 eV, which is a consequence of the interaction between alkali atom and the surrounding water molecules. The photoemission signal from this state can be depopulated by absorption of UV photons with an initial time constant of $5.7(2){\times}10^{-3}s^{-1}$. However, a re-population of the state seems not possible, or occurs with a very low efficiency, which can be explained by a very efficient screening of this state by the water molecules. In addition to this time dependence, the photoemission from the HOMO of the K atom strongly depends on the temperature and completely disappears for temperatures above ~ 60 K. This shows, that the autoionization of the alkali atom in the solvent environment is an thermally activated process.

5 Electron Dynamics at Alkali-Water-Clusters Adsorbed on a Metal Surface

In this chapter the electronic structure of alkali-water-cluster adsorbed on a Cu(111) surface and the corresponding electron dynamics in these systems are presented. By means of TPD spectroscopy and work function measurements it is shown that alkali atoms which are directly adsorbed on the metal substrate can be hydrated by surrounding water molecules. In addition, continually monitoring the transient change of the electronic structure as a function of water coverage reveals pronounced changes as the water coverage increases. The most striking effect is the appearance of a new state which can be attributed to excess electrons at the alkali-water-cluster which are stabilized by response of the polar environment. The ability of an alkali-water-cluster to bind such an electron depends on the type of alkali and increases with increasing dipole moment of the adsorbed alkali along the sequence Na, K, Cs. In the last part of this chapter the energetic stabilization and the population dynamics of the excess electrons at the alkali-water-cluster are investigated by means of time-resolved 2PPE. The population dynamics of the excess electron is pre-dominantly governed by the ratio of water molecules per alkali atom.

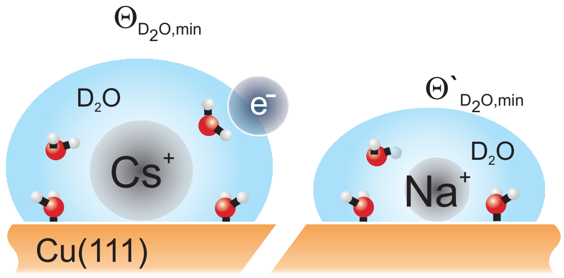

Figure 5.1: Schematic presentation of the alkali-water-cluster adsorbed on a Cu(111) surface. The alkali ion is hydrated by the water molecules. In addition an excess electron can bind to the complex if a sufficient number of water molecules are present at the alkali ion.

Alkali atoms adsorbed on a metal surface are a well studied model system for chemisorbed species. In section 2.5 a brief overview of the electronic structure and the adsorbate dynamics has been given. Less is known about the properties of adsorbed alkali atoms in the presence of polar molecules such like water. In Fig.5.1 a schematic representation of the alkali-water-cluster supported on a metal substrate is depicted. The following questions will be discussed in the present chapter:

(i) How do water molecules adsorb on the surface in the presence of alkali atoms? And is it possible to spectroscopically probe the formation of a solvation shell of water molecules around the alkali ion adsorbed on the metal substrate?

(ii) How does the adsorption of water molecules affect the unoccupied alkali resonances? As the wave function of this state is localized at the individual alkali atoms with a significant electron density extending into the vacuum region, an interaction of this state with the polar water molecules is expected to occur. Is this interaction leading to an energetic stabilization of the resonance and is the resonance eventually quenched in the presence of water molecules?

(iii) Water cluster adsorbed on a bare metal substrate can bind solvated electrons (see appendix A) at an mass equivalent of ~ 1.5 BL D_2O. Are initial traps in the potential energy surface, which serve as a 'seed' for electron solvation, influenced by the response of the water molecules on the alkalis? Is it possible to bind an excess electron to the alkali-water cluster?

5.1 Adsorption of Water Adsorbed on Alkali Pre-Covered Cu(111) and Alkali Hydration

The previous raised questions can only be addressed if one presumes a situation where the water molecules bind to the substrate in the vicinity of the alkali ions in order to form alkali-water-clusters. In order to verify this scenario TPD spectroscopy of D_2O on alkali pre-covered Cu(111) has been employed.

The alkali atoms were deposited on the Cu(111) surface following the preparation routine which has been described in detail in section 3.4.3. For the experiments presented in this chapter the alkali coverage was kept below 0.15 ML. The reason for the low coverage is to avoid alkali-induced water dissociation, which has been reported for coadsorbed water above a critical alkali coverage depending on the alkali and the metal substrate [Hen02]. In addition alkali-alkali interaction should not occur. The water molecules were dosed on to the alkali pre-covered Cu(111) surface which is kept at 35 K. TPD spectra of D_2O (m=20) adsorbed on Na, K, and Cs pre-covered Cu(111) are presented in Fig.5.2. The temperature of the sample was increased with a constant heating ramp of 1 K/s.

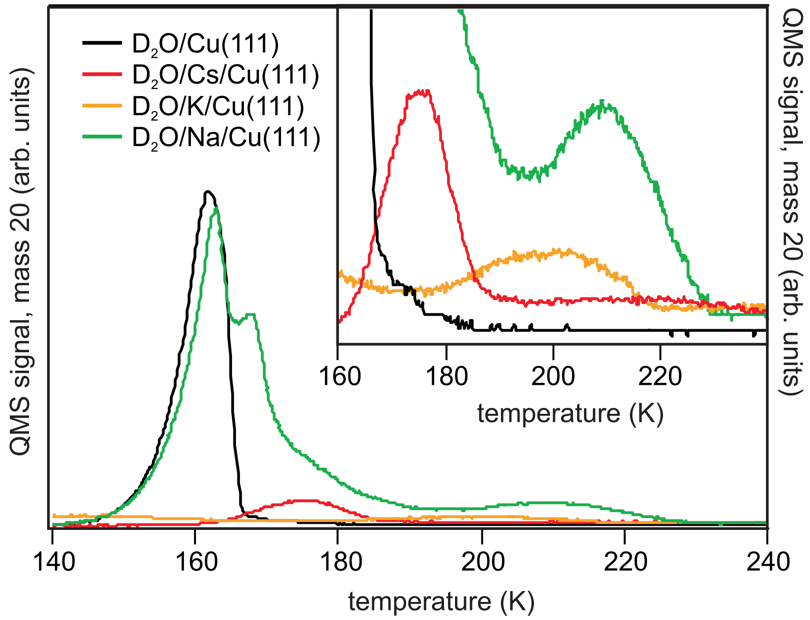

Figure 5.2: TPD spectra of D_2O on clean and alkali pre-covered Cu(111). The inset shows a magnified detail of the high temperature peak associated with water bound to the alkali atoms. For details see the text.

The black trace represents the thermal desorption spectrum of 4 BL D_2O adsorbed on clean Cu(111). The water was dosed at a sample temperature of 40 K. The spectrum exhibits a single broad peak between 140 and 165 K which is attributed to the desorption of water from the first bilayer and additional multilayers (cf. characterization of the adsorbate layers in section 3.4.2). The water desorption is clearly influenced when a sub-monolayer coverage of alkali atoms is pre-adsorbed leading to the appearance of a high temperature peak. This feature can be seen in the inset of Fig.5.2 for pre-adsorbed Caesium (red trace), Potassium (yellow trace) and Sodium (green trace). For Cs and K the integrated water coverage is 0.5 and 0.2 BL, respectively. Here the adsorbed water solely desorbs in the high temperature peak. If the alkali atoms are co-adsorbed with a higher water coverage, as it is the case for the TPD spectrum of 4.5 BL of water on the Na pre-covered surface, an additional broadening of the high temperature peak to lower desorption temperatures is observed. The desorption temperature of the water molecules in the high temperature peak increases along the sequence Cs, K, Na. For Cs the high temperature peak is centered around 175 K, whereas for K and Na it is centered around 200 K and 210 K, respectively.

These changes in the TPD spectra of water induced by co-adsorbed alkali atoms imply that water molecules are stabilized by an attractive interaction with the alkali. This effect was observed previously on other metal substrates like Ag(111) [Bla90], Cu(110) [Sas91], Ni(111) [Bor91], and Pt(111) [Vil96, Wea97]. The adsorbed alkali atoms exhibit a huge dipole moment which is due to a partial charge transfer of the alkali valence electron to the metal (cf. section 2.5). This dipole moment interacts with the water dipole moment. The most stable structure of the water molecules is governed by the competition between dipole-dipole (alkali-water) and hydrogen-bonding interactions. As can be deduced from the appearance of the high temperature peak in the TPD spectra the alkali-water interaction is stronger than the water-water interaction and therefore the orientation of the water molecules is rather governed by the alkali than the neighboring water molecules. The stronger binding of water molecules due to water/alkali interaction leads to a preferential binding of D_2O molecules at these sites. For low water coverages water adsorbs only at the preferential sites and no water desorption from the 'clean surface' is observed, see TPD spectra for K and Cs in Fig.5.2. The amount of water molecules which are stabilized by the alkali and the amount of alkali adsorbed is governed by a hydration like interaction leading to the formation of a solvation shell around the alkali [Hen02]. Accordingly, the water molecules in the high temperature desorption state can be attributed to water molecules in a hydration shell around the alkali. The desorption kinetics of the water molecules influenced by the alkalis are complicated. For a higher water coverage an additional TPD feature and broadening to lower temperatures is observed as apparent in the thermal desorption spectrum for co-adsorbed Na presented in Fig.5.2. This may result from water molecules in outer hydration shells where the water molecules are less influenced by alkali dipoles. Nevertheless, only a finite amount of water is affected as still a fraction of the water molecules desorb in the normal 'clean surface' peak. Describing the desorption kinetics of the solvating water molecules is complicated, as desorption of one molecule from the hydration shell changes the binding energies of the remaining water molecules leading to a coverage dependent potential energy landscape for desorption [Bor91, Kuc94]. The fact that water molecules from alkali-influenced adsorption sites desorb at higher temperatures clearly shows that a preferential binding at theses sites occurs. Hence in a low water coverage regime formation of alkali-water clusters on the metal substrate takes place. The interpretation of the origin of the high temperature peak in the TPD spectra as caused by the formation of a solvation shell around the alkali is further corroborated by work function measurements.

The relative work function change $\Delta\phi$ is depicted in Fig.5.3 as a function of D_2O coverage for various pre-coverages of Na (red symbols), K (yellow symbols), and Cs (green symbols) adsorbed on Cu(111) . The work function was measured by means of 2PPE spectroscopy. The water deposition onto a sub-monolayer coverage of alkalis on Cu(111) leads initially to an increase of the work function. After passing a maximum the work function decreases. This behavior is considerably different from the work function evolution when water is dosed on the clean Cu(111) surface (cf. blue symbols in Fig.5.3). Here, the work function is monotonically decreasing by 0.5 eV upon adsorption of the first water bilayer. Finally, a constant work function of $\phi = 3.95$ eV is reached when a wetting ice layer forms at a coverage of 3 BL [Bov03]. Without the alkali pre-coverage the water molecules orient such that every second water molecule is bound to the metal substrate by the oxygen lone pair[39]. As a consequence a positive

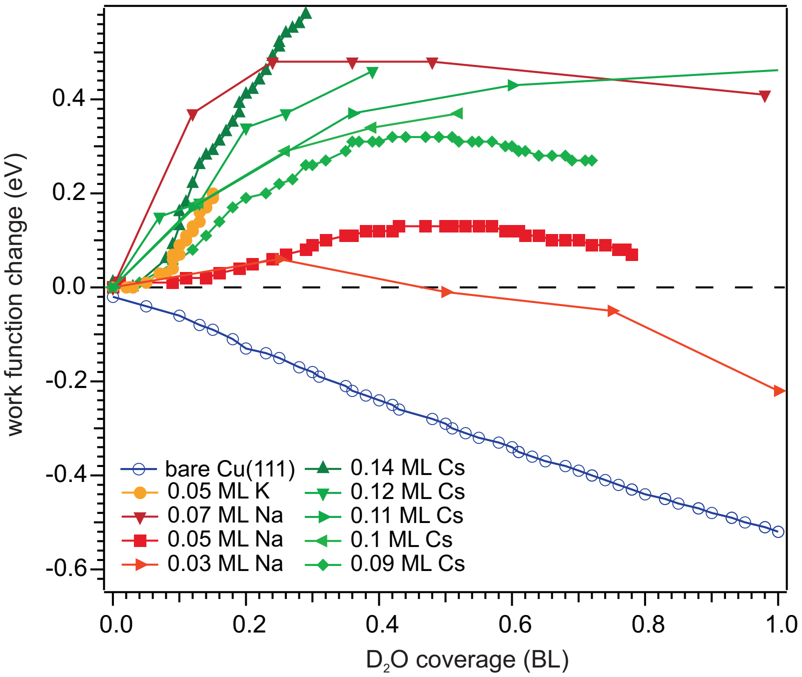

Figure 5.3: Relative work function change versus D_2O coverage for various pre-coverages of Na, K, and Cs. The water was dosed at 35 K. The blue circles represent data obtained by deposition of D_2O on clean Cu(111).

---

[39] For details on the adsorption structure of water on clean Cu(111) see section 2.4.2.

dipole moment pointing away from the surface forms which reduces the work function of the system as apparent from the data represented by the blue symbols in Fig.5.3. The same behavior would be expected if no interaction between water and alkali would occur. In fact, the initial increase of the work function is based on the same dipole-dipole interaction between the water molecules and the alkali atoms which leads to the appearance of the high temperature peak in the TPD spectrum of water(see Fig.5.2). In the presence of the alkalis the orientation of the water molecules is governed by the alkali-water interaction that dominates the water-water interaction and water adsorption results in an increase of the work function and not in a decrease. So the dipole moment induced by the water molecules changes towards the opposite direction and decreases the net surface dipole moment of the system. Nevertheless, the net surface dipole is still oriented such that it points away from the surface as the negative $\Delta\phi$ induced by the alkali is greater. In other words, the co-adsorbed water molecules screen the contribution of the alkali to the work function. As can be seen in Fig.5.3 the maximum increase in work function is proportional to the alkali pre-coverage. For example, the maximum of $\Delta\phi$ for 0.03 ML Na is $\Delta\phi = 0.06$ eV, whereas the maximum work function increase for 0.05 and 0.07 ML Na is $\Delta\phi = 0.13$ eV and $\Delta\phi = 0.48$ eV, respectively. This behavior is as well an indication of the hydration of the alkali ions by the adsorbed water molecules. As long as the water molecules adsorb in a hydration shell-like structure in the vicinity of the alkali, identified by the desorption in the TDS high temperature peak, the orientation of the water molecules result in a screening of the alkali-induced dipole moment and the work function change reaches a maximum. Additional water molecules are now not directly influenced by the alkali, desorption occurs in the normal D_2O/Cu(111) desorption peak, and the work function is decreasing again. The work function decrease with increasing water coverage is now similar to the behavior on the clean Cu(111) surface. The hydration of the alkali could also involve the braking of the alkali-metal bond and the lift-up of the alkali species by surrounding water as was reported for potassium on Pt(111) investigated by XPS [Bon85]. However, a direct proof of this effect can not be given with the techniques employed in the framework of this thesis.

5.2 Electronic Structure of Water Adsorbed on Alkali Pre-Covered Cu(111)

The electronic structure of alkali atoms on a metal substrate was already described earlier in section 2.5. The most prominent feature is attributed to the unoccupied alkali resonance. Fig.5.4 presents angle-resolved 2PPE spectra from 0.1 ML Cs adsorbed on a Cu(111) surface. The Cs resonance at $E - E_F = 2.85$ eV does not show a dispersion with parallel momentum $k_{\|}$ as expected for a state localized at the alkali atoms[40]. The energetic position of the alkali resonance strongly depends on the alkali coverage. In the zero coverage limit the resonance is located at $E - E_F = 3.0$ eV. With increasing coverage the work function of the system decreases and the resonance is shifting accordingly to lower intermediate state energies. The surface state of Cu(111) can clearly be separated from the Cs resonance. The SS shows the well-known quasi-free electron like behavior around the center of the Brillouin zone at $k_{\|}$=0.

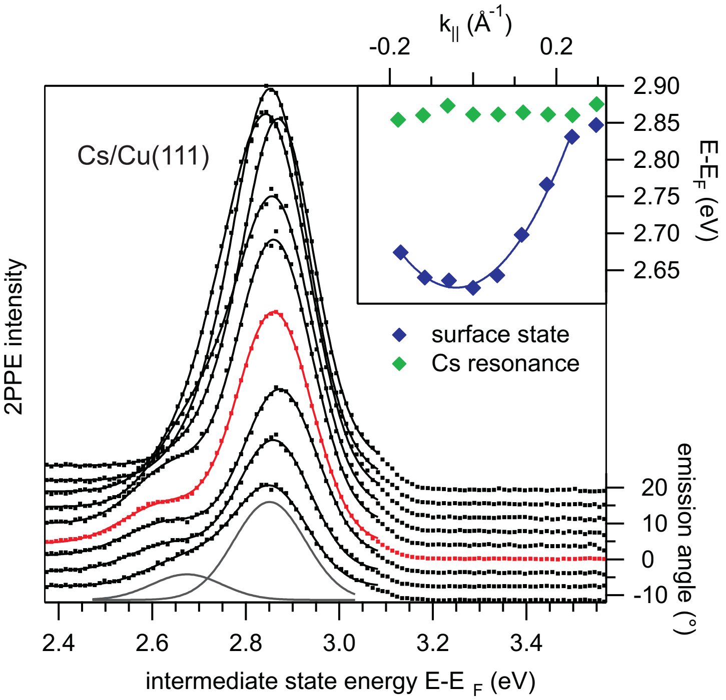

Figure 5.4: Angle-resolved 2PPE spectra from 0.1 ML Cs adsorbed on Cu(111). The 2PPE spectrum in normal emission (red trace) shows peaks attributed to the occupied surface state and the unoccupied alkali resonance. The inset shows the peak positions as a function of parallel momentum $k_{\|}$. The Cs resonance shows no dispersion along $k_{\|}$.

In order to follow the evolution of the electronic structure of alkali/Cu(111) continuously as a function of water exposure the deposition of the water was not carried out via dosing through a pinhole doser but by setting a water background pressure in the vacuum chamber which was controlled by a leak valve. The sample was kept at 35 K in the measurement position in front of the TOF spectrometer and spectra were

---

[40] Details on angle-resolved photoemission can be found in the experimental details section 3.1.3.

continuously acquired during the water deposition. The D_2O partial pressure and the exposure time was chosen such that the desired final water coverage was obtained in a exposure time below 15 min. For example, the sample was exposed to a D_2O partial pressure of $1.33 \cdot 10^{-9}$ mbar for 500 s yielding an exposure of 0.5 L[41]. Assuming a sticking coefficient of the water molecules on the Cu substrate equal to one, this exposure gives a water coverage of 0.5 BL. For a calibration of the water coverage a test experiment was performed where water was deposited on bare Cu(111). Here, the work function change in dependency of the water coverage is known [Gah04] allowing for a conversion of water exposure into water coverage. The result of this experiment is depicted in Fig.5.5 where the work function is plotted as a function of water exposure and water coverage[42]. In this way the water exposure onto an alkali pre-covered metal surface can be converted to the corresponding water ice coverage under the assumption that the sticking coefficient of water is the same for adsorption on bare or sub-monolayer alkali covered Cu(111).

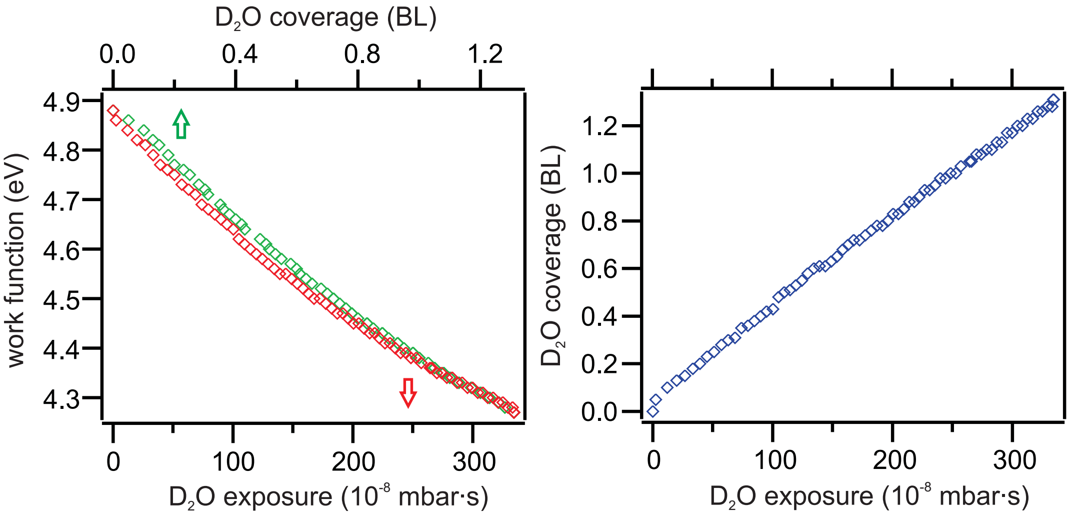

Figure 5.5: Water coverage determination during in situ deposition. (left panel): Work function of the system as a function of D_2O coverage (top axis) and D_2O exposure (bottom axis). (right panel): D_2O coverage as a function of D_2O exposure. As the water coverage dependent work function change is known from previous experiments [Gah04] the water exposure can be converted into a water coverage.

The change of the electronic structure of 0.14 ML Cs/Cu(111) as a function of water exposure is presented in the top panel of Fig.5.6. The TOF spectra are plotted as a function of intermediate state energy $E - E_F$ (left axis) and D_2O exposure

---

[41] Langmuir L is a unit for exposure. $1\text{ L} = 1.33 \cdot 10^{-6}$ mbars.

[42] The fact that exposure of 1 L water does not result in a water ice layer of 1 BL can be explained by a pressure gradient form the QMS to the μ-metal shielding where the sample is kept during the experiment. For the experimental setup please see section 3.3.

(bottom axis) in a false color representation. The bottom panel of Fig.5.6 presents the water exposure which was simultaneously detected by the QMS. On the basis of the above described coverage calibration, the water exposure can be converted into a water coverage.

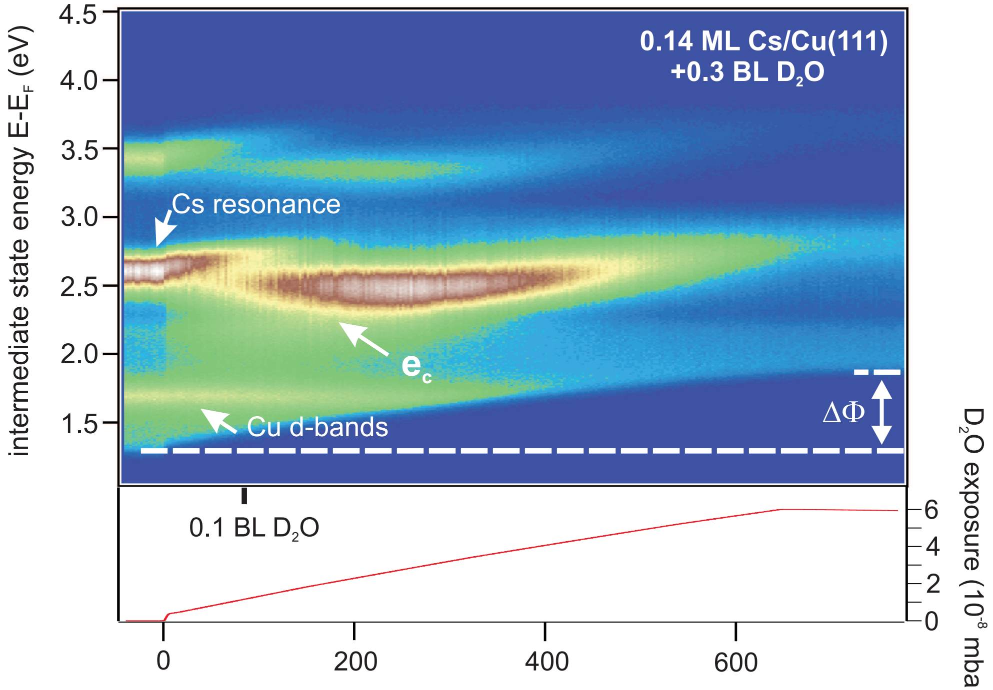

Figure 5.6: Evolution of the electronic structure of 0.14 ML Cs/Cu(111) upon water deposition. Top: 2PPE intensity in false color representation as a function of intermediate state energy and water exposure (for hν_{UV} = 3.08 eV and hν_{VIS} = 2.26 eV at t=0 fs). The final water coverage is 0.3 BL. At a coverage of 0.1 BL water the Cs resonance disappears together with the appearance of a new feature e_c which is attributed to stabilized electrons at the alkali-ion/water complex. Bottom: Water exposure as a function of exposure time simultaneously measured.

Distinct changes in the electronic structure can be observed as the water coverage increases.

- The work function of the system increases upon water deposition, as can be seen by the position of the secondary edge in the 2PPE spectra. The secondary edge is located at $E - E_F = 1.30$ eV when no water is co-adsorbed. This corresponds to a work function of $\phi = 3.56$ eV. When the water exposure starts the secondary edge is shifting to higher intermediate state energies. At the final coverage of 0.3 BL D_2O the work function has increased by almost 600 meV to $\phi = 4.14$ eV.

The work function increase is associated with an interaction of the dipole moments of the water molecules with the alkali-induced dipole moments at the alkali ions and reflects the formation of a hydration shell of water molecules around the alkali as discussed in section 5.1.

- The alkali resonance is located at an intermediate state energy of $E-E_F = 2.61$ eV before water is deposited. Upon water adsorption the position of the resonance first shifts towards higher energies and is then gradually losing intensity. At a D_2O coverage of 0.3 BL the Cs resonance is completely "quenched".

- The most striking change in the TOF spectra is the appearance of a new state(e_c) which first appears at a water coverage of 0.1 BL at an intermediate state energy of $E - E_F = 2.57$ eV, see Fig. 5.6. The state e_c is an unoccupied state which can be attributed to excess electrons stabilized at the alkali-ion/water complex.

- The spectral signature of the latter two states appear twice in the 2PPE spectra. The Cs resonance and the e_c peak occur also at a higher intermediate state energy of $E-E_F \sim 3.4$ eV. Here, the electrons are excited by two UV photons in contrast to an excitation by one UV and one VIS photon. Accordingly, the same state appears higher in energy by photon energy difference $\Delta h\nu = 0.82$ eV. The peak at $E - E_F = 1.70$ eV originates from the Cu d-bands which have a maximum in the density of states ~ 2.1 eV below the Fermi level.

In conclusion, by acquiring TOF spectra during water is deposited on a sub-monolayer alkali covered metal surface, the evolution of the electronic structure upon increasing water coverage can directly be followed. The work function change observed is attributed to the hydration of the alkali as discussed in the previous section. In addition it was found that excess electrons can be stabilized by the alkali-ion/water complex.

5.2.1 Stabilized Electrons at Alkali-Ion/Water Complexes

The nature of the electrons in the state e_c is *a priori* not clear. Two scenarios are most probable and will be discussed in the following.

(i) The e_c state could be a modified alkali resonance state. Initially, without water co-adsorbed, the alkali resonance mainly formed by the ns and np_z orbitals of the alkali [Bau98, Gau07, Zha08]. It can be transiently populated leading to a transient neutralization of the alkali. The adsorbed water molecules around the alkali can influence the electron density of this state. Therefore, the physical properties of this state, like the binding energy, can be altered in the presence of the polar water molecules. The subsequent dynamics could be initiated by a 'de-solvation'. Here, the water molecules react in order to energetically stabilize the transiently neutralized alkali/water cluster.

(ii) Similar to electron solvation in polar media as introduced in section 2.2.1, the e_c state could be a collective state of the alkali-ion/water complex. Initial trapping sites formed by reoriented water molecules in the presence of the alkali species, *i.e.* local minima in the potential energy surface could allow to bind an excess electron to the complex.

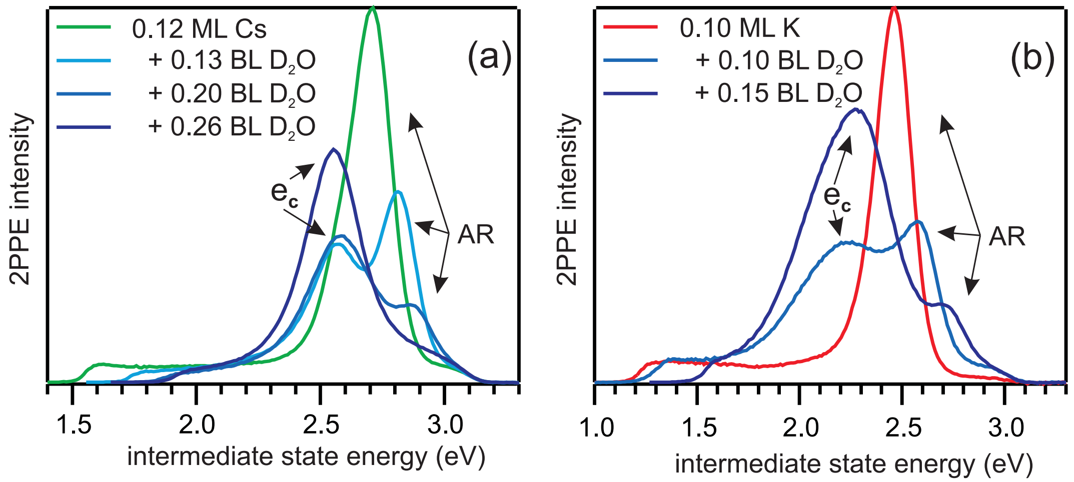

Figure 5.7: TOF spectra of Cs and K co-adsorbed with water on Cu(111). Spectra were taken using photons with energies $h\nu_{UV} = 3$ eV and $h\nu_{VIS} = 2.2$ eV at t = 0 fs. In the presence of water the state e_c appears and the intensity of the alkali resonance (AR) decreases.

TOF spectra of K and Cs adsorbed on Cu(111) with and without co-adsorbed water are depicted in Fig.5.7. The new feature is a general feature for all investigated alkali/water clusters, but is best resolved in the case of K and Cs. The unoccupied Na resonance has a broad line width of ~ 0.3 eV, because of the considerable shorter lifetime in Na/Cu(111) of ~ 2 fs [Bor02], compared to the unoccupied resonances for K and Cs, where the line width is well below 0.2 eV. Hence, a discrimination of the unoccupied Na resonance and the new appearing e_c peak on the basis of the TOF spectrum is hindered (spectra not shown). However, an assignment is possible on the basis of the population dynamics as will be discussed in section 5.3. For K and Cs co-adsorbed with small water coverages the unoccupied alkali resonance and the e_c peak are clearly separated. The e_c state lies at intermediate state energies of $E - E_F > 2.0$ eV but always at a lower energy than the alkali resonance. The energetic position of both states shifts differently with increasing water coverage.

Water Coverage Dependence

Fig.5.8 depicts the energetic position, the intensity and the peak width of the alkali resonance and of the e_c state together with the work function of the system as a function of water deposition[43]. The values depicted are obtained by fitting a background

---

[43] The water coverage dependence is discussed on the basis of the system Cs/Cu(111). The behavior of the other investigated alkalis is qualitative the same, quantitative differences will be pointed out

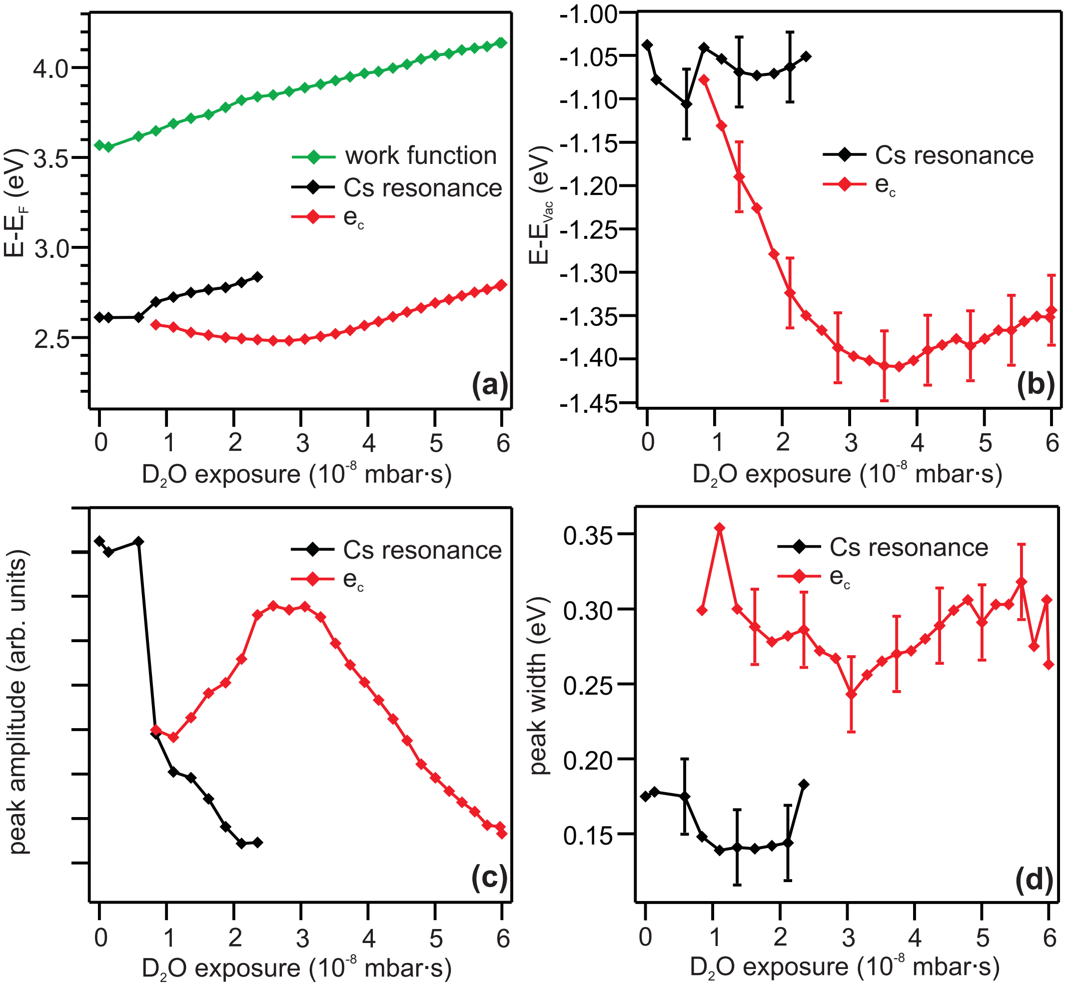

Figure 5.8: Work function, and amplitude, peak width and energetic position of the Cs resonance and the stabilized electron peak of D$_2$O/Cs/Cu(111). (a) Energetic position of the Cs resonance and the stabilized excess electron e_c with respect to the Fermi level and (b) with respect to the vacuum level as a function of water coverage. (c) and (d) Peak intensity and peak width as a function of water coverage.

and two gaussian peaks to the spectra to account for the observed electronic states. In panel (a) and (b) of Fig.5.8 the energetic position of the Cs resonance (black markers) and of the stabilized excess electron e_c (red markers) are plotted with respect to the Fermi level and the vacuum level as a function of water exposure. Both features behave significantly different upon water deposition. The energetic shift of the alkali resonance is linked to the change in the work function. The alkali resonance is pinned to the

---

individually.

vacuum level of the system [Zha08]. Hence, when the energetic position of the alkali resonance is plotted with respect to the vacuum level no change in the binding energy of this state is observed. In contrast, the e_c state becomes energetically more strongly bound with increasing water coverage. At a water exposure of $3.5 \cdot 10^{-6}$ mbars, which corresponds to $\sim$ 0.2 BL D_2O, the electrons in the e_c state gain more than 0.3 eV with respect to E_{vac}. At the same time the intensity of the Cs resonance is decreasing quickly, while the intensity of the e_c state increases (cf. Fig.5.8(c)). With further D_2O exposure the decrease is caused by an attenuation of the entire 2PPE signal (cf. Fig.5.6). The width of the Cs resonance is not affected by water co-adsorption. As long as the resonance is observable the peak width is constant within the error bars and centered around 0.17 eV. The e_c state is considerable broader with a peak width of 0.3 eV which is as well independent of the water coverage

The fact that electrons in the e_c state gain binding energy with increasing water coverage can be explained in terms of electron solvation. The excess charge at the alkali/water cluster gets stabilized by a reorientation of the surrounding water dipoles. The most stable structure of an excess charge in a polar liquid is commonly described as a solvation shell with the charge in its center (see section 2.1). With an increasing number of water molecules the coordination number of water molecules around the excess electron increases. When the first solvation shell is completed the most stable structure is reached and the binding energy increase, *i.e.* the shift towards the Fermi level, is maximized. Fig.5.9 depicts the potential energy curve of the alkali resonance (A) and the excess electron state e_c (B) as a function of D_2O coverage Θ. In this case the water coverage is a measure for the solvation/stabilization capability of the solvent cluster or in other words the number of water molecules in the solvation shell around the excess charge.

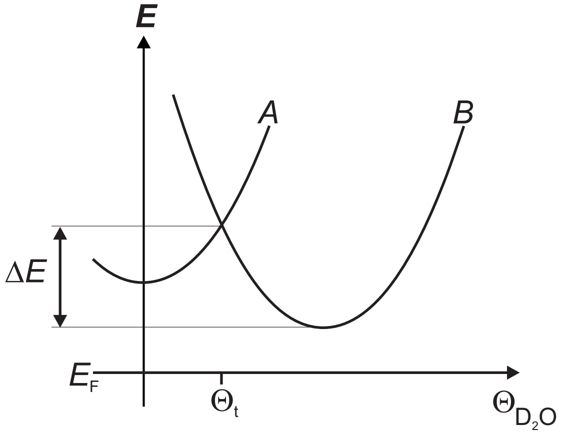

Figure 5.9: Potential energy curves of the unoccupied alkali-induced state (A) and the e_c state related to the alkali-ion/water-complex (B) as a function of D_2O coverage Θ. At Θ_t the levels are crossing and state B becomes energetically more favorable compared to state A.

In this picture the observed transition from the alkali resonance to the newly evolved state e_c can be explained. Starting with a constant alkali coverage and without water at $\Theta = 0$ the system presents one excited state (A) which corresponds to the alkali resonance. Increasing the water coverage leads to an energetic upshift of the state, because the work function of the system is getting bigger. When approaching the transition region at Θ_t the potential energy parabola (B) of the e_c state crosses the one of state A. Around Θ_t both states are observable, depending on their population and depopulation probability, in the 2PPE spectra (see for instance Fig.5.7). After the level crossing the e_c state evolves along the potential energy parabola B towards higher binding energies, whereas the alkali resonance shifts to higher intermediate state energies with increasing work function (see Fig.5.8.(a)). One possible explanation for the fact that the alkali resonance is not observable anymore after adsorption of a sub-monolayer coverage of water is this interchange in the binding energies of the two states. As both are localized at the alkali/water cluster[44] the probability to populate the energetically favorable state could be enhanced. Another possible explanation is based on the hydration of the alkali ion. As reported in section 5.1 during the hydration of the alkali ion, the alkali-metal bond might brake and the alkali is lifted off from the surface [Bon85]. As a consequence the alkali resonance will be altered which could as well lead to a quenching of the state.

Although the qualitative behavior of all three investigated alkalis upon water deposition is the same a significant trend is observed when comparing the three systems quantitatively. The amount of water molecules per alkali needed to stabilize an excess charge at the alkali/water-clusters in the e_c state depends on the type of alkali. Considering an equal distribution of the deposited water molecules at the alkali sites one can estimate the mean number of water molecules per alkali ion when the alkali and the water coverage are known. To obtain this water/alkali ratio the electronic structure was monitored during water deposition onto the alkali covered metal substrate, as presented in Fig.5.6 for Cs, also for K and Na. The minimum water coverage is defined by the coverage where the e_c state first appears in the TOF spectra. In Fig.5.6 this point is marked with the corresponding water coverage of 0.1 BL at the bottom axis. Table 5.1 presents the minimum number of water molecules required in a water/alkali cluster in order to bind an excess electron in the e_c state. For the case of adsorbed Cs on average only 2-3 water molecules are needed in the alkali/water cluster to observe the formation of the e_c state. Along the sequence Cs, K and Na the minimum size of the solvation shell increases to 3-4 molecules for K and 6-7 water molecules for Na.

At first, this trend may seem counterintuitive as one could expect that the number of water molecules needed to stabilize an excess charge would scale with the size of the alkalis to form a solvation shell. However, a complete solvation shell around the alkali is apparently not a prerequisite for the trapping of an excess charge at the cluster. For Na, K, and Cs the e_c state appears before the alkali is fully hydrated, i.e. before the work function change upon water deposition reaches its maximum. Actually, the minimum number of water molecules is inversely proportional to the surface dipole moment which is induced by the adsorbed alkalis. The induced surface dipole μ is proportional

---

[44] Angle-resolved 2PPE spectra will be shown in the following to investigate the dispersion of the e_c state along $k_\parallel$.

Table 5.1: Minimum number of water molecules per alkali needed in order to stabilize an excess electron in the e_c state and induced alkali dipole moment in the limit of zero coverage from [Ver97].

	Na	K	Cs
D_2O per alkali	$6-7$	$3-4$	$2-3$
dipole moment (D)	4.3	6.7	8.5

to the adsorption distance of the alkali to the metal substrate r_{ads} following $\mu = q \cdot r_{ads}$ and increases along the sequence Na, K ,and Cs [Ran87, Ver97, Bor02, Zha08][45]. So the alkali species with the highest induced surface dipole moment requires the lowest number of water molecules to stabilize an excess charge at an alkali/water cluster.

Without a pre-coverage of alkali atoms water forms clusters on the Cu(111) surface for coverages below 2 BL [Gah02, Stä07a]. Nevertheless, the structure of pure water clusters is quite different from the structure of the alkali/water cluster. In order to stabilize an excess charge (solvated electron) in pure water ice cluster a nominal coverage of more than 1 BL is needed. The clusters exhibit a height of 3-4 BL [Stä07a]. In contrast, for alkali/water cluster a nominal water coverage of 0.1 BL is sufficient. This is attributed to the fact that the alkali strongly influences the surrounding water molecules, as can bee seen by TDS (see Fig.5.2) or the work function change (see Fig.5.3). These changes lead to new, energetically favorable trapping sites, which are not present without the alkali. The stronger the induced surface dipole of the alkali, the stronger is the reorientation of the water molecules in the alkali/water cluster. Hence, for Cs (where the surface dipole is larger than for Na and K) only 2-3 water molecules are necessary before trapping of an excess electron in the e_c state is possible. If the perturbation is weaker more water molecules are required in the cluster to allow for the initial trapping of the excess electron.

Localization

In order to investigate the degree of localization of the e_c state angle-resolved 2PPE experiments were performed. As described in section 3.1.3 the dispersion of an electronic state parallel to the surface plane can be determined by measuring the parallel momentum of the photo electrons. According to equation 3.17 the parallel momentum $\hbar k_{\|}$ depends on the emission angle of the photo electrons with respect to the normal emission direction. The dispersion of an electronic state can be written analogous to the one of a free electron:

$$E(\vec{k}) = \frac{\hbar^2 k^2}{2m_{eff}(\vec{k})}, \tag{5.40}$$

where m_{eff} is the effective mass. Localized and delocalized states can be distinguished by their effective mass. For delocalized states it has a finite value, whereas in the case

---

[45] In this case q corresponds to the transferred charge from the alkali atom to the metal substrate.

of a localized state it becomes infinite. The group velocity of a localized electronic state is:

$$\frac{d\omega}{dk} = \frac{1}{\hbar}\frac{dE}{dk} = 0. \tag{5.41}$$

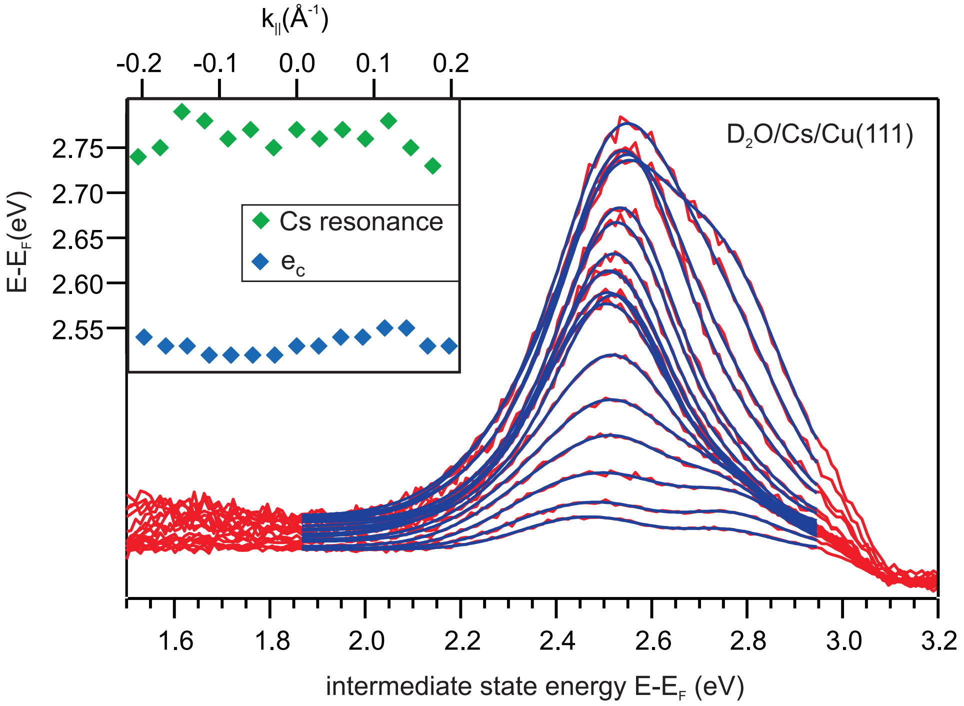

Figure 5.10: Dispersion of excess electrons in D_2O/Cs/Cu(111): Angle-resolved spectra (red traces) showing no energetic shift of the e_c peak as a function of emission angle. The inset presents the energetic position of the e_c state (blue marker) and the Cs resonance (green marker) as a function of parallel momentum $k_{\|}$.

Fig.5.10 depicts angle-resolved 2PPE data of D_2O/Cs/Cu(111) at a time delay of 0 fs for a series of emission angles from $-14°$ to $+14°$. The photon energies used are $h\nu_{UV} = 3.02$ eV and $h\nu_{VIS} = 2.22$ eV. The spectra (red traces) exhibit two distinct features at an intermediate state energy of $E - E_F = 2.55$ eV and $E - E_F = 2.75$ eV, which can be attributed to the stabilized electron distribution e_c and the Cs resonance, respectively. The positions of the e_c peak (blue markers) and the Cs resonance (green markers) as a function of parallel momentum $k_{\|}$ are depicted in the inset of Fig.5.10. The energetic positions have been derived from the 2PPE spectra by fitting gaussian distributions for both peaks and a constant 2PPE background between $E - E_F = 1.9$ eV and $E - E_F = 2.9$ eV. The fits are represented by blue traces in Fig.5.10. Obviously, the energetic position of e_c does not shift as a function of parallel momentum $k_{\|}$.

Based on the flat dispersion of the spectral feature of the excess electrons e_c it can be concluded that stabilized electrons at the Cs/water cluster reside in localized states. This is expected for an electron bound to a localized alkali/water cluster at the Cu(111) surface. Experiments for Na and K co-adsorbed with water show that the e_c electrons are as well localized in these systems. This is in agreement with solvated electrons in water ice or ammonia which are as well localized [Gah02, Stä07b] and show similar properties especially in their dynamics as can be seen in the following section.

5.3 Excess Electron Dynamics at Alkali-Ion/Water Complexes

The present section focuses on the dynamics of the excess electrons in the state e_c at the alkali/water clusters. Similar to electron solvation in pure water ice clusters an energetic stabilization of the e_c electron distribution as a function of pump-probe delay occurs (5.3.1). This is attributed to a dynamical reorientation of the water molecules and depends on the type of alkali. Additionally, it is shown that the lifetime of the electrons in e_c is in the range of several tens of femtoseconds and changes when the amount of water molecules in the alkali/water cluster is varied (5.3.2).

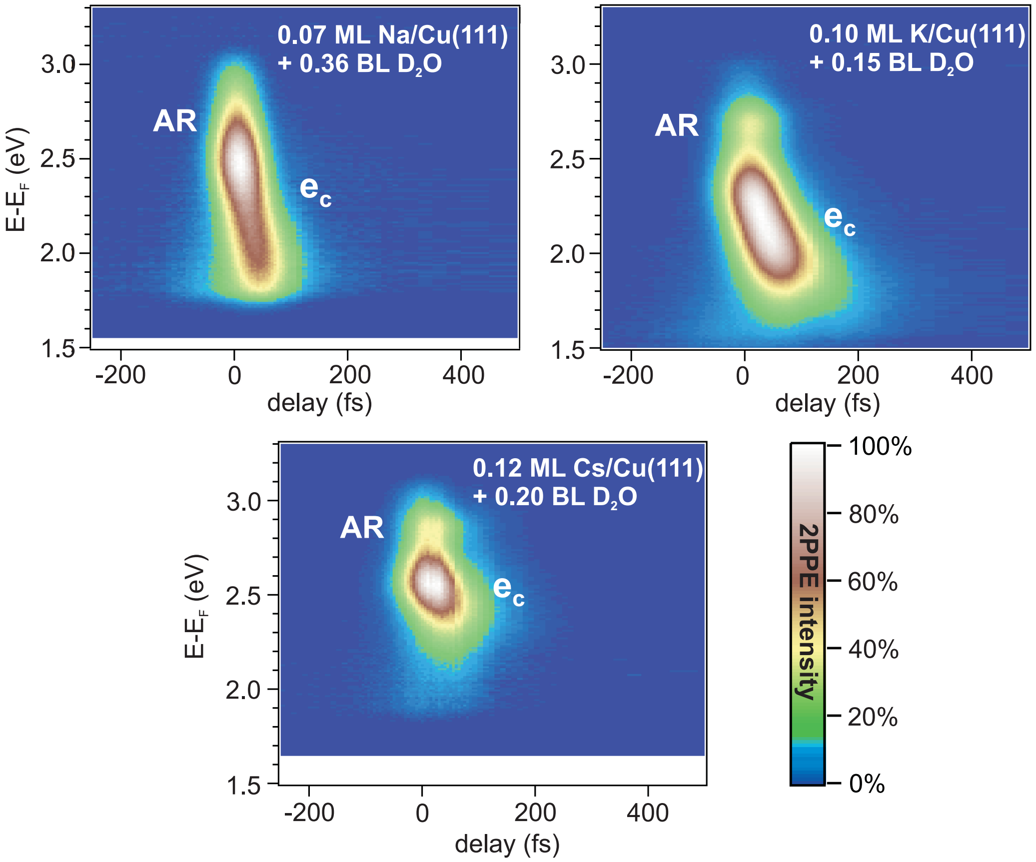

Figure 5.11: Time-resolved 2PPE data of different alkali/water clusters on Cu(111). 2PPE intensity in false color representation as a function of intermediate state energy (left axis) and pump-probe delay (bottom axis). The spectra for Na, K, and Cs exhibit a short-lived state attributed to the alkali resonance and a broader feature shifting to lower energies with increasing time delay, which is associated with excess electrons at the alkali/water cluster.

Fig.5.11 presents time- and energy-resolved 2PPE spectra of Na, K, and Cs/water clusters adsorbed on a Cu(111) surface in false color representation (intensity scale in the lower right panel). The photon energies used for these experiments were; for Na: $h\nu_{UV} = 3.03$ eV and $h\nu_{VIS} = 2.36$ eV for K: $h\nu_{UV} = 3.01$ eV and $h\nu_{VIS} = 2.28$ eV and for Cs: $h\nu_{UV} = 3.09$ eV and $h\nu_{VIS} = 2.22$ eV. The measurements were acquired at a sample temperature of 45 K. As reported before for the static measurement, two features are observed: (i) the short-lived alkali resonance (AR) and (ii) the stabilized excess electron state e_c that exhibits a finite lifetime and shifts down to lower energies with increasing time delay. The feature e_c exhibits a finite lifetime towards positive time delay, which means that it is excited by $h\nu_{UV}$. For K the e_c state is located at $E - E_F = 2.28$ eV. Nevertheless, at negative delays, the state is not excited by $h\nu_{VIS} = 2.28$ eV. It can be concluded that the electrons are not directly excited into the state e_c but via higher lying states. This indirect excitation of excess electrons occurs also for the other investigated alkalis and is in accordance with electron dynamics at ice-metal and ammonia-metal interfaces, where the excitation of solvated electrons occurs via the conduction band of the solvent (D_2O or NH_3) [Gah02, Stä08b]. Directly after the excitation the electron is localized in the state e_c as can be seen in the dispersion measurement presented in Fig.5.10 in section 5.2.1. The subsequent energetic stabilization of the electrons in e_c is observed for all investigated systems. The energetic stabilization rate is very strong as compared to stabilization dynamics of solvated electrons in water ice. The stabilization persists as long as the population in the e_c state has decayed back to the metal substrate. The stabilization dynamics are discussed in section 5.3.1. Compared to the lifetime of the AR the back transfer of the population in the e_c is considerably slowed down. The lifetime of the alkali resonance is not altered upon water deposition. For the Cs resonance it is $\tau = 33(5)$ fs, consistent with literature [Bau97, Oga99, Bor02], and decreases along the sequence Cs, K, and Na. For K the lifetime of the resonance is $\tau = 14(5)$ fs. Whereas, for Na the lifetime of the resonance is below the time resolution of our experiment. The electron transfer dynamics of the stabilized excess electron at the alkali/water complex is discussed in detail in section 5.3.2.

5.3.1 Stabilization Dynamics

The time evolution of the energetic position of the e_c peak for Na, K, and Cs co-adsorbed with water on Cu(111) as a function of pump-probe delay is depicted in Fig.5.12. The energetic position of the e_c peak was derived from fits to the TOF spectra. The spectra were fitted in the energy range around the e_c state with a constant background and one or two Gaussians depending on whether or not the alkali resonance is observed. The difference in the initial energetic position at t = 0 fs for the different alkalis is due to differences in the work function caused by varying water and alkali coverages. However, the ratio of water molecules per alkali atom is similar for all three data sets and below 10:1. For all investigated alkalis the energetic position of the e_c state is shifting to lower energies with respect to the Fermi level with increasing time delay, which corresponds to an increase in the binding energy of the state. This dynamic peak shift can be described as a solvation of an excess charge by the water molecules of the alkali/water cluster. At the alkali/water cluster the excited electron gets localized and neighboring water molecules stabilize the excess charge by a reorientation. The energetic stabilization proceeds as long as the electron reaches a potential minimum or it decays back to the metal substrate. However, an equilibrium situation is not observed in the experiments. So one can conclude that the population in the e_c state decays before the energetic minimum is reached.

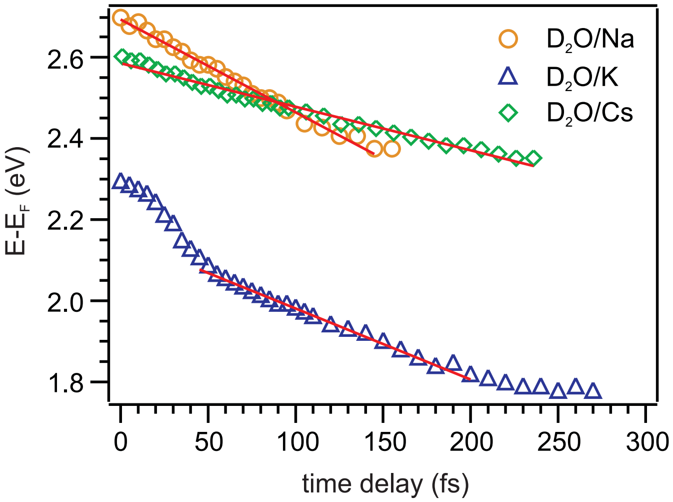

Figure 5.12: Energetic shift of the e_c peak position for Na, K, and Cs co-adsorbed with water on Cu(111). The peak positions of e_c are obtained by fitting the TOF spectra using two Gaussians and a constant background. The red lines are linear fits to the data points.

The energetic stabilization rate is described by a linear fit to the data points. The fits (red solid lines) are depicted in Fig.5.12. The shift of the e_c peak is well reproduced by the linear fit in the case of Na/water- and Cs/water-clusters. Within the first 50 fs after photoexcitation the peak shift for the K/water cluster does not follow the linear dependency. Here, the linear fit is restricted to time delays $t \geq 50$ fs. The rate of the energetic stabilization Σ differs significantly for the different alkalis. The stabilization rate for Cs is $\Sigma_{Cs} = -1.3(2)$ eV/ps and the highest rate is observed for Na where it is $\Sigma_{Cs} = -2.2(3)$ eV/ps. The results are summarized in Tab.5.2.

Table 5.2: Energetic stabilization rate of e_c.

	Na	K	Cs
stabilization rate Σ (eV/ps)	$-2.2(2)$	$-1.7(2)$	$-1.3(2)$

The energetic stabilization for the e_c state is of the same order of magnitude as for solvated electrons in amorphous ice in the presence of alkali ions at the ice/vacuum interface reported in chapter 4, but compared to solvated electrons in pure amorphous water the stabilization of e_c proceeds ~ 4 times faster [Gah03, Mey11]. The energetic stabilization is a result of the response of the polar molecules to the excess charge in its vicinity [46]. Therefore, the stabilization of the charge is influenced directly by the structure of the surrounding water molecules. The timescale on which the stabilization occurs is strongly connected to the mobility of the solvent molecules. As the investigated alkali/water cluster contains only small amounts of water, the electronic state e_c is most likely located at the alkali/water cluster surface. Accordingly, the water molecules forming the solvation shell around e_c are not fully coordinated in the H-bond network. Theoretically it was shown for small water cluster anions that dangling O-H bonds contribute strongly to the stabilization [Lee97]. Hence, a fast energetic stabilization of the electrons in e_c is reasonable. Furthermore, the presence of the alkali is as well influencing the energetic stabilization of e_c. As already discussed before, the water molecules interact with the induced surface dipole of the alkalis. The strongest interaction occurs for Cs, where the induced dipole moment is largest, and allows for binding of excess electrons at the clusters containing only 2-3 water molecules. However, the energetic stabilization rate of e_c decreases along the sequence Na, K, and Cs. This dependency is consistent with the increase of the induced dipole moment. As a consequence of the stronger interaction of the alkali with the water molecules, the water network is more stiff and the water molecules react slower and less strongly on the presence of the excess charge.

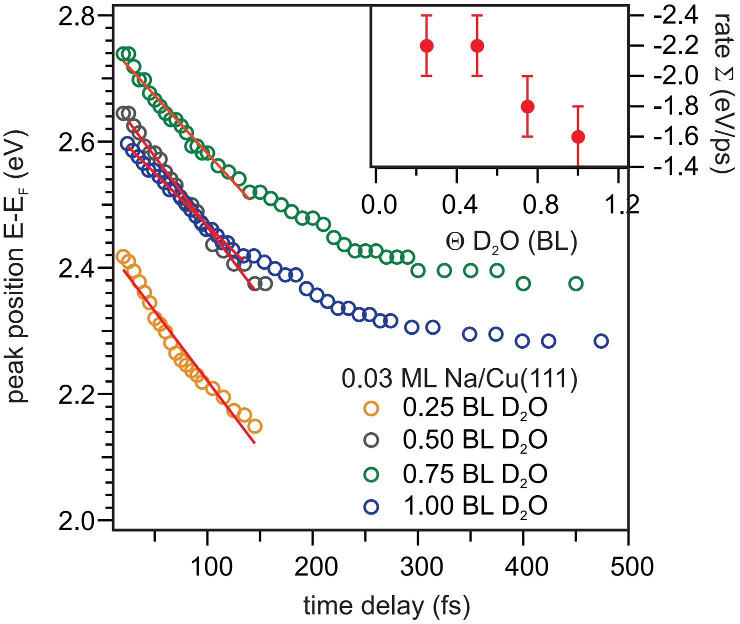

Figure 5.13: Energetic shift of the e_c peak position for Na co-adsorbed with various water coverages on Cu(111). The stabilization rates Σ, obtained by linear fits to the peak position for time delay up to $t = 150$ fs, as a function of D_2O coverage.

---

[46] An additional apparent peak shift, caused by energy-dependent transfer times, as observed in the case of amorphous ice adsorbed on metal surfaces [Stä06], might also contribute to the observed peak shift.

When increasing the water coverage, the stabilization rate shows a dependence on the water coverage. Fig.5.13 depicts the energetic shift of the e_c peak as a function of pump-probe delay for 0.03 ML of Na co-adsorbed with different amounts of D_2O ranging from 0.25 BL to 1.0 BL. The red lines are linear fits to the data for time delays between t = 20 fs and t = 150 fs. The corresponding stabilization rates are plotted in the inset of Fig.5.13 as a function of water coverage. Initially the stabilization rate is constant for water coverages below 0.5 BL, then it decreases to Σ = -1.8(2) eV/ps for 0.75 BL D_2O and Σ = -1.6(2) eV/ps for 1.0 BL D_2O. This decrease in the stabilization rate by almost 30 % is an indication for an increase in the coordination number of the water molecules which are involved in the formation of the solvation shell around the excess charge. Although the water network is more rigid for higher coordinated water molecules, *i.e.* the energetic stabilization proceeds slower, the screening of the excess charge from the metal substrate is more efficient and hence the back transfer probability to the metal is reduced. This more efficient screening leads to the fact that the e_c state can be observed up to time delays of t = 500 fs (see Fig.5.13). In this case after $t \approx 150$ fs a slowing down of the energetic stabilization by one order of magnitude is observed. For time delay > 150 fs the peak shifts with a rate of only Σ = 0.28(4) eV/ps. One possible explanation for these different stabilization rates for early (< 150 fs) and later delays is the different response of water molecules in the inner and outer solvation shells. The fast response within the initial 150 fs can be interpreted as direct response of the water molecules within the inner solvation shell around the excess charge and is mainly mediated by a rotation of the D_2O molecules. But, also water molecules residing at a larger distance to the excess charge contribute to the energetic stabilization by a rotational response although to a smaller extend. For larger time delays the diffusive motion of water molecules governs the energetic stabilization. The diffusive motion occurs significantly slower than the rotation of the molecule, as the entire molecule has to move.

The fact that the evolution of the e_c state can be followed for longer time delays with increasing water coverage is, as already mentioned, linked to the fact that the excess charge is better screened from the metal substrate. Hence, the population dynamics of the e_c state is presented in the following section.

5.3.2 Population Dynamics

In competition to the localization and the energetic stabilization, the excess electrons in e_c decay back to unoccupied electronic states in the metal substrate. The back transfer probability critically depends on the wave function overlap of the e_c electrons with electronic states of the substrate. Fig.5.14 presents cross correlation traces of stabilized excess electron at the alkali/water cluster e_c for 0.12 ML Cs and 0.07 ML Na as a function of pump-probe delay t for various water coverages. The XC traces are achieved by integrating the 2PPE intensity over the energy window that includes the entire population of the e_c state for all time delays[47]. The XC traces are vertical

---

[47] The required energy windows differ due to different work functions of the systems and hence different energetic positions of the e_c state with respect to the Fermi level.

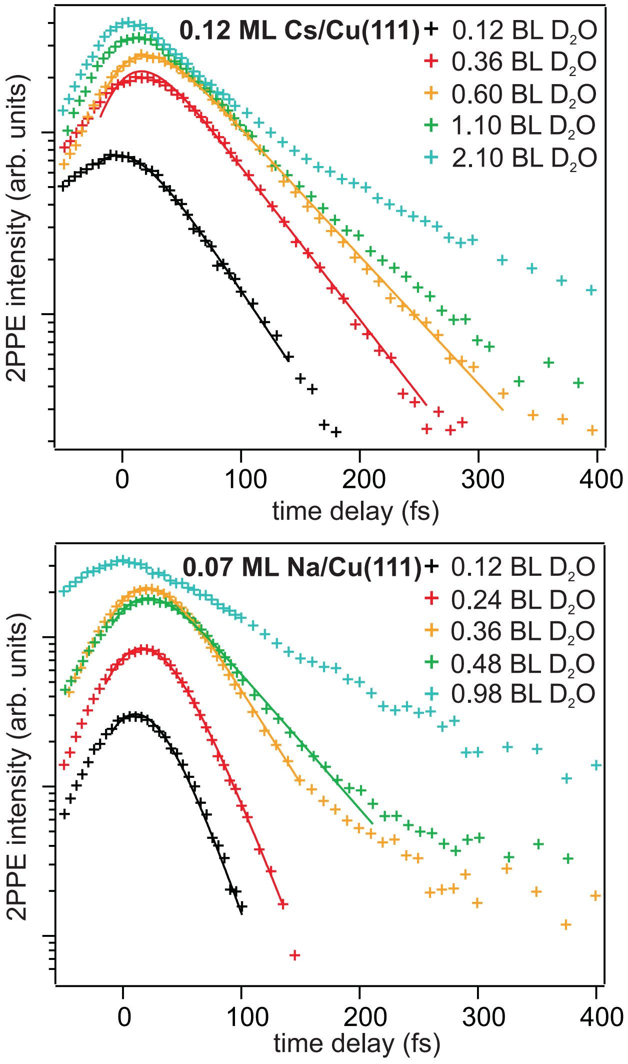

Figure 5.14: Population dynamics of e_c for Na/water- and Cs/water-clusters on Cu(111). The solid lines represent fits to the data considering an exponential decay convoluted with the envelope of the laser pulse XC. The alkali coverage is 0.07 and 0.12 ML for Na and Cs, respectively.

shifted for clarity. For small water coverages the population transient of e_c is very well reproduced by a single-exponential decay following:

$$n_{ec} = A \cdot exp(-\frac{t}{\tau_{ec}}), \tag{5.42}$$

which is convolved with the temporal shape of the laser pulse. A describes the amplitude and τ_{ec} is the decay time of the population of e_c. The results of the fit are depicted as well in Fig.5.14 (solid lines). The deviation of the data points at negative time delays is caused by hot electrons, which are excited by absorption of $h\nu_{VIS}$ and probed by $h\nu_{UV}$. Although the description of the population decay of e_c by a single exponential decay is matching the data perfectly for low water coverages, *i.e.* a low ratio of water moelcules per alkali atom, clear deviations are seen when the relative water coverage increases. Obviously, for higher relative water coverages the back transfer rate of e_c slows down with increasing time delay and the population is decaying non-exponentially. Fig.5.15 depicts the population transients of e_c for 0.03 ML Na co-adsorbed with up to 1 BL of D_2O. Compared to the data set presented in the lower panel of Fig.5.14, where 0.07 ML Na are co-adsorbed with up to 1 BL of D_2O, the relative water coverage is higher by a factor of 2. So that for the highest depicted water coverage of 1 BL the mean ratio of water molecules per alkali in the cluster is on the order of $\sim$ 100. In a first approximation the XC traces are fitted with a bi-exponential decay to the data (solid lines), that reproduces the XC traces quite well. The slowing down of the back transfer with increasing time delay has also been observed for electron solvation in pure

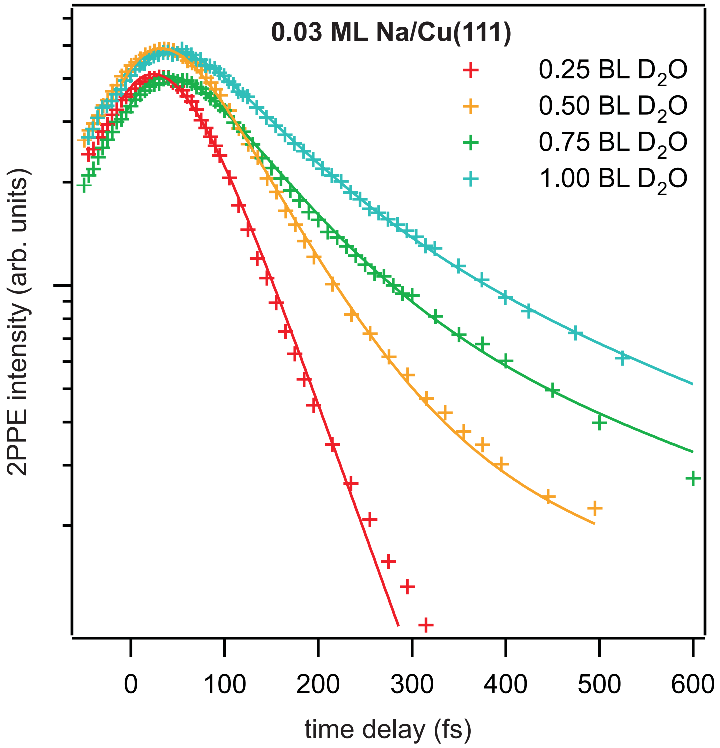

Figure 5.15: Population dynamics of e_c for 0.03 ML Na/water on Cu(111) for a higher alkali/water ratio. The solid lines represent fits to the data considering a double exponential decay convoluted with the envelope of the laser pulse XC.

water [Stä08a] and ammonia [Stä08b]. With ongoing solvation, the excess electrons get more stabilized in energy, and the wave function of the solvated electron becomes more confined. This leads to a reduced wave-function overlap of the electron with unoccupied metal states and therefore to a smaller back-transfer probability.

When looking at the initial decay times of e_c one finds a distinct increase with increasing water coverage that is already apparent in the XC traces in Fig.5.14 and Fig.5.15. The initial exponential decay rate for different coverages of Na is plotted in Fig.5.16 as a function of D_2O coverage.

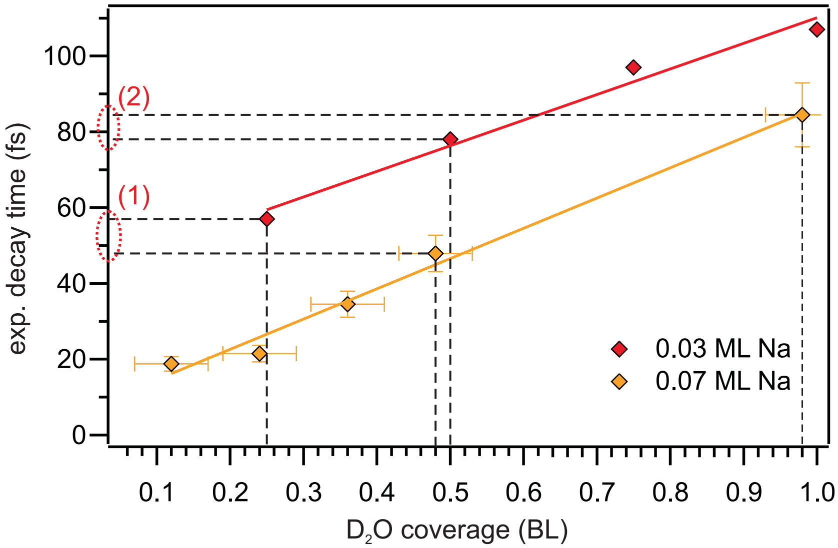

Figure 5.16: Exponential decay times τ_{ec} of the initial decay of e_c for Na as a function of water coverage. The dashed lines mark pairs (1) and (2) of equal Na/water ratio. The solid red and orange lines are a guide to the eye.

For 0.07 ML Na (yellow diamonds) the decay times are ranging from $\tau_{ec} = 19(3)$ fs for 0.12 BL D_2O to $\tau_{ec} = 85(9)$ fs for 1.0 BL D_2O. If the Na coverage is smaller by approximately a factor of 2 one finds decay times for 0.03 ML Na (red diamonds) of $\tau_{ec} = 57(6)$ fs for 0.25 BL D_2O up to $\tau_{ec} = 107(11)$ fs for 1.0 BL D_2O. The solid lines are guides to the eye. Comparing the decay times for both Na data sets at a fixed water coverage, one finds that the decay times τ_{ec} of the 0.03 ML Na data set are always bigger than the according τ_{ec} of the 0.07 ML Na. However, if one compares pairs of data points, where the water/alkali ratio is approximately the same, (1): 0.5 BL D_2O/0.07 ML Na and 0.25 BL D_2O/0.03 ML Na and (2): 1.0 BL D_2O/0.07 ML Na and 0.48 BL D_2O/0.03 ML Na, the corresponding decay times are equal within the error bars, (1): $\tau_{ec} = 48(5)$ fs and $\tau_{ec} = 57(6)$ fs and (2): $\tau_{ec} = 85(9)$ fs and $\tau_{ec} = 78(8)$ fs, respectively. Hence, one can conclude that the decay time τ_{ec} of the excess electron at the alkali/water cluster e_c is governed by the ratio of water molecules per alkali in the cluster. In this way it is directly possible to influence the lifetime of the e_c by changing the amount of water molecules per alkali/water cluster.

Fig.5.17 gives an overview of the exponential decay times τ_{ec} of the state e_c for Na, K, and Cs as a function of water coverage. In all cases the exponential decay time τ_{ec} is increasing for higher water coverages. The slope of the increase of τ_{ec} vs Θ_{D_2O} varies for all data sets. Hence, a clear systematic dependency of τ_{ec} on the type of alkali is not found, which is in contrast to the clear dependency of the energetic stabilization of e_c on the type of alkali discussed in section 5.3.1.

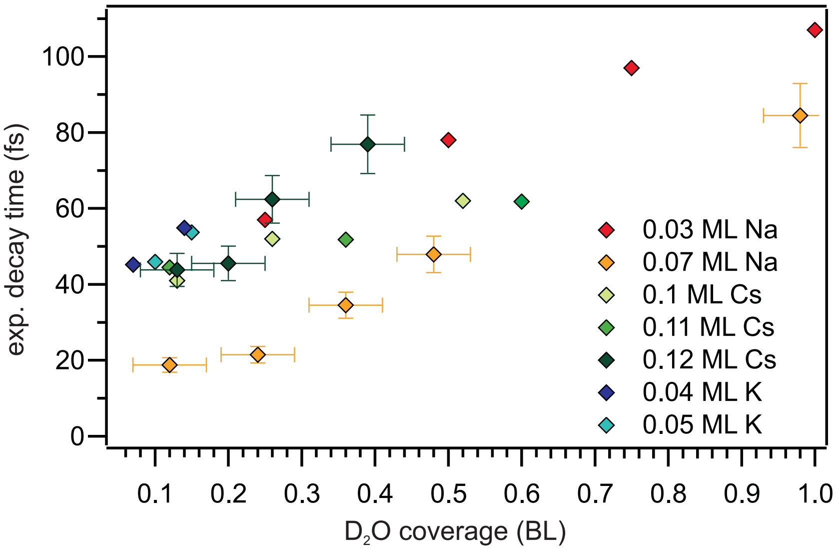

Figure 5.17: Overview of the exponential decay times τ_{ec} of the initial decay of e_c for Na, K, and Cs as a function of water coverage.

The effect of the increasing lifetime of e_c with increasing D_2O coverage can be explained by the screening of the electron by the surrounding water molecules from the metal substrate. Fig.5.18 depicts the modified image potential in which the excess charge at the alkali/water cluster is bound in a potential minimum at the distance z_i from the metal surface. Each curve depicts the potential for a fixed D_2O coverage, i.e. the evolution of the potential is caused by the different surrounding of the electron and not by the proceeding stabilization (increasing time delay). With increasing water coverage, the potential minima becomes deeper and the e_c state is shifting towards the Fermi level and the electron is gaining binding energy (cf. Fig.5.8.(b)). Hence, the potential barrier height V_0 that screens the electronic wave function from the metal substrate increases. Additionally, the barrier height V_0 can further increase with increasing water coverage although e_c is not shifting down in energy anymore when the local maximum at z_j increases. In other words, more water molecules in the solvation shell around the excess charge can screen the electronic wave function more efficiently

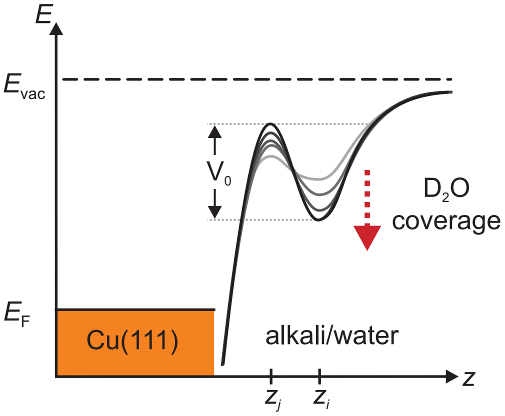

Figure 5.18: Screening of the electron in e_c for increasing water coverages. The potential perpendicular to the metal surface evolves as a function of increasing water coverage. A potential barrier with the height V_0 is formed that transiently changes its height as the local maximum at z_j and the potential minimum at z_i evolve. See text for details.

from the metal substrate, the back transfer probability of e_c is reduced and the lifetime increases. The fact that a complete solvation shell is screening an excess charge better than a fractional solvation shell seems obvious, but the possibility to vary the amount of water molecules in a solvation shell around an excess charge on a metal substrate directly enables the possibility to control the lifetime of the excited state.

5.4 Conclusion

The adsorption of water molecules ($\Theta_{D_2O} < 1$ BL) on an alkali pre-covered metal surfaces ($\Theta_{alkali} < 0.15$ ML) leads to the formation of alkali-water clusters. The adsorbed alkali atoms exhibit a huge dipole moment which is due to a partial charge transfer of the alkali valence electron to the metal. An attractive interaction between these alkali-induced dipole moments and the dipole moments of the water molecules leads to stronger and preferential binding of the D_2O molecules in the vicinity of pre-adsorbed alkali atoms. The ratio of the amount of water molecules which are stabilized by the alkali and the amount of pre-adsorbed alkali atoms are governed by a hydration like interaction that is leading to the formation of a solvation shell around the alkali. The number of water molecules in the solvation shell can be directly controlled by the D_2O coverage. The hydration of the alkalis by the water molecules is observed by means of TPD spectroscopy and work function measurements. The interaction between the dipole moments of the water molecules and the alkalis is stronger than the water-water interaction leading to the appearance of a high temperature peak in the TPD spectra. Additionally, an increasing work function upon water adsorption reveals the formation of a solvation shell of water molecules around the alkali. The dipole moments of the water is screening the alkali-induced dipole moment and the work function increases accordingly.

Water deposition on a alkali pre-covered is not only leading to the hydration of the alkali by surrounding water molecules, it also strongly influences the electronic structure of the system. The alkali/water clusters adsorbed on a Cu(111) surface can also bind photoexcited excess electrons, which are identified by a new signature e_c in the 2PPE spectrum. This new state e_c has to be related to the alkalis, because it is not observed in the low coverage regime for pure water cluster. Angle-resolved 2PPE spectroscopy shows that the spectral feature of the excess electrons e_c exhibit a flat dispersion in accordance with a localized state at the alkali/water cluster. It can be concluded the alkali strongly influences the surrounding water molecules leading to new, energetically favorable trapping sites for electrons, which are not present without the alkali. Water-coverage dependent measurements of the electronic structure for three different alkalis (Na, K, Cs) show that the minimum number of water molecules per alkali needed in order to stabilize an excess electron in the e_c state depends on the type of alkali and is inversely proportional to the alkali-induced dipole moment. Whereas 2-3 water molecules are needed in the case of Cs, the minimum number of water molecules in an alkali/water cluster for K and Na are 3-4 and 6-7 water molecules, respectively. This finding implies that a larger induced dipole moment leads to a stronger reorientation of the water molecules in the alkali/water cluster, which is responsible for the formation of the trapping sites. Hence, less water molecules are required to allow for the initial trapping of the excess electrons when the alkali-induced reorientation of the water molecules, *i.e.* the alkali-induced dipole moment, is stronger.

Similar to electron solvation in pure water ice cluster on metal surfaces an energetic stabilization of the e_c state as a function of pump-probe delay occurs. This is attributed to a dynamical reorientation of the water molecules and depends on the type of alkali. The strongest energetic stabilization is found for Na with a rate of -2.2 eV/ps. As the alkali-induced dipole moment increases, the water network is more rigid and the water molecules react slower and less strongly to the presence of the excess electron. For K and Cs the energetic stabilization rate of e_c is -1.7 and -1.3 eV/ps, respectively. The high energetic stabilization rate of the excess electrons e_c is related to the fact that dangling OH-bonds contribute strongly to the energetic stabilization. The clusters contain only small amounts of water so that the water molecules in the alkali/water cluster are not fully coordinated in the H-bond network and many dangling OH-bonds are present in the vicinity of the excess electron.

In competition to the localization and energetic stabilization, the stabilized electrons in e_c can decay back to unoccupied electronic states in the metal substrate. The decay time τ_{ec} of the excess electron at the alkali/water cluster e_c is governed by the ratio of water molecules per alkali in the cluster. With increasing water coverage the lifetime τ_{ec} increases; *e.g.* for 0.07 ML Na the exponential decay time is $\tau_{ec} = 19$ fs at a water coverage of 0.12 BL and $\tau_{ec} = 85$ fs at a coverage of 1.0 BL. Similar decay times are found for the three investigated alkalis. The increase of the decay time of the excess electron with increasing water coverage shows that more water molecules in the alkali/water cluster can screen the electronic wave function of the e_c electrons more efficiently from the metal substrate. Accordingly, the back transfer probability of the e_c electrons decreases and their decay time increases.

6 Reactivity of Water-Electron Complexes on Crystalline Ice Surfaces

The interaction between long-living electrons trapped in defects at the surface of crystalline ice and electronegative molecules, such as trichloromonofluoromethane ($CFCl_3$), is discussed in this chapter. Before addressing the chemical reactivity of these electrons, the determination of the binding site by adsorption of a Xe overlayer is presented in section 6.1. In the following the $CFCl_3$ deposition is characterized by means of TD-spectroscopy on the clean Ru(001) substrate and on crystalline ice. Finally in section 6.3, the dissociative electron attachment (DEA) of the trapped electron to coadsorbed $CFCl_3$ molecules leading to the formation of $\bullet$ $CFCl_2$ and Cl^- is followed by means 2PPE spectroscopy. This process is very efficient since it is observed for very low coverages of $CFCl_3$ molecules.

6.1 Binding Site Determination of Trapped Electrons in Crystalline Ice

In crystalline D_2O structures on metal surfaces, trapped electrons are generated by photoexcitation in the metal substrate followed by a transfer to trapping sites at the ice/vacuum interface. As has been shown in previous work these electrons exhibit extraordinary long lifetimes on the order of minutes indicating the efficient decoupling of the electron wave-function from the metal substrate. Trapped electrons seem to be a general property of polar molecule-metal interfaces as they are as well observed for crystalline ammonia [Bov09, Stä11]. Further details on their properties have already been given in section 2.2.2. The trapped electrons can be utilized to trigger chemical reactions with co-adsorbed molecules. In the present case the DEA of trapped electrons to $CFCl_3$ molecules is investigated. The DEA cross section is very high and benefits from two characteristics of trapped electrons in crystalline ice, (i) their very long lifetime, which is in the order of minutes and (ii) their binding site at the ice/vacuum interface as discussed in the following.

To answer the question of the electron binding site a surface science approach is employed in the present work to discriminate between surface and bulk trapping sites. It is realized by adsorption of Xe adlayers on top of the crystalline ice as depicted in Fig.6.1. The experiment is based on differing interactions of bulk- and surface-bound solvated electrons with the Xe atoms, which allows determination of the binding site. For trapped electrons at the ice/vacuum interface distinct changes of the photoelectron spectra are expected. As the rare gas atoms are inert, no chemical reaction takes place. Thus, observed modifications in the properties of the excess charge are caused by a perturbation of the potential of the excess electron. This electrostatic perturbation is attributed to the polarizability of the xenon atoms and might be accompanied by a modification of the spatial confinement of the e_T wave function. On the other hand, if the trapped electrons are located in the bulk of the crystalline ice, no significant changes in the photoelectron spectra are expected. Due to the efficient screening of the trapped electron, only the net electric field of the screened charge interacts with the Xe. Hence, if at all only minor changes in the properties of the trapped electrons are expected. Xe overlayer experiments for amorphous water ice clusters and wetting ice layers adsorbed on Cu(111) showed that the spectral signature of the solvated electrons is modified by titration of surface binding sites with xenon atoms [Stä07a, Mey08]. In order to investigate the adsorption characteristics of Xe on ice TD spectroscopy was performed. Although the dynamics of trapped electrons on crystalline ice has been studied on Ru(001) as a substrate, the following TD spectra were performed on a Cu(111) surface. However, the desorption energies of Xe on Ru(001) and Cu(111) are very similar, especially for the desorption of the monolayer [Sch92, Sch93, Ber04]. Additionally, both experiments were performed on closed ice layers, which decouple the Xe adlayer from the substrate, so that the interaction of Xe with water molecules will be, if at all, only slightly influenced by the metal substrate.

Figure 6.1: Xe overlayer experiment. Different interactions of bulk- and surface bound electrons with the adsorbed rare gas layer allow for a discrimination of the binding sites.

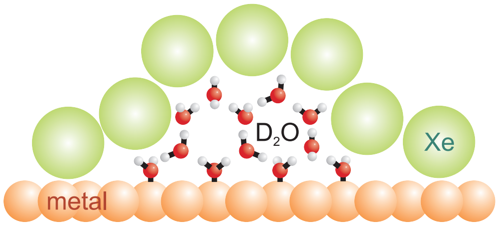

The Xe adlayers were prepared by exposure of the surface to a partial pressure of Xe at 30 K. The TDS of Xe/Cu(111) (blue line) is depicted in Fig.6.1 and exhibits three peaks. In good agreement with literature [Ber04], the peak at 82 K is associated with the desorption of the first monolayer of Xe. Features at 64 K and 62 K are attributed to the second monolayer and additional multilayers of Xe, respectively. For Ru(001) as a substrate the first monolayer of Xe desorbs at 88 K and multilayer desorption occurs at 60 K [Sch92]. The xenon coverage is determined from the TD spectrum by normalization of the integrated intensity to the high temperature peak, i.e. to one complete monolayer of xenon adsorbed on the bare Cu(111) surface.

In contrast to these observations, no separate monolayer desorption peak for Xe adsorbed on D_2O/Cu(111) is found (Fig.6.1, green curve). The Xe adsorbed on the ice layer desorbs exclusively via zero order desorption kinetics at a sample temperature of 60 K, suggesting that the interaction strength between the Xe atoms and the water ice is similar to the interatomic interaction within the Xe layer. This further justifies the fact that the substrate plays only a minor role. Because the interatomic interaction of Xe is independent of the substrate, as can be seen by multilayer desorption peak at temperatures of 62 K for Xe/Cu(111) and 59 K for Xe/Ru(001), which can be considered identical within the error bars.

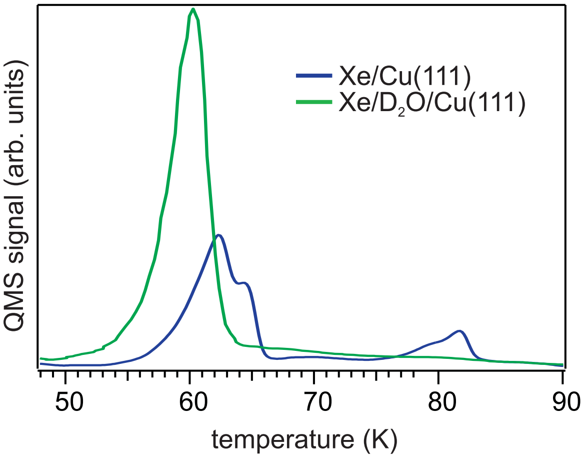

Figure 6.2: Thermal desorption spectra of 4 ML xenon on Cu(111) (blue curve) and 6 ML xenon adsorbed on a D_2O layer on Cu(111) (green curve). The spectrum of Xe/Cu(111) shows three peaks at 62 K, 64 K and 82 K attributed to xenon atoms adsorbed in multilayers, second monolayer and first monolayer, respectively. In the case of xenon adsorbed on water, the TDS exhibits only one peak at around 60 K and is attributed to sublimation from a multilayer. The heating rate is 1 K/s.

Fig.6.3 compares 2PPE spectra of the crystalline ice layer, after deposition of 3 and 6 ML of Xe and after flashing the sample to 100 K, respectively. The spectra are taken at a sample temperature of 30 K in one-color 2PPE using photons with an energy of $h\nu = 3.69$ eV. The 2PPE spectrum of 4.5 BL crystalline ice on Ru(001) exhibits three distinct features. The peak at $E - E_F = 0.9$ eV is originating from the occupied Ru d-band. The feature at $E - E_F = 3.2$ eV is attributed to the first image potential state of the D_2O/Ru(001) interface. The broad peak which is centered around $E - E_F = 2.1$ eV is attributed to trapped electrons in crystalline ice. As observed from the 2PPE spectra, the adsorption of 6 ML of Xe results in a total quenching of the long-living electrons signal, which unambiguously shows that the e_T electrons are localized on the surface of the ice layer. A coverage of 3 ML results in a relative decrease of the e_T peak only. The observed quenching can be understood as an electrostatic perturbation of the trapping sites (defects) by the surrounding Xe atoms, therefore inducing the quenching of the e_T signal in the 2PPE spectra. The relatively high Xe coverage (6 ML) needed for quenching can be explained by (i) the fact that each trapping site has to be surrounded by Xe atoms to generate the required electrostatic perturbation to induce the change in the 2PPE spectra and (ii) the structure of the crystalline D_2O layer. Indeed, as mentioned in section 2.2.2, for coverages of more than one bilayer, the D_2O molecules form clusters on top of the first wetting bilayer, thus increasing the effective interface area between D_2O and Xe atoms. Beside quenching the long-living electrons signal, the Xe coverage does not have a significant effect on the system work function. Nevertheless, the $n = 1$ IPS is affected by the adsorption of Xe and its energetic position shifts to higher energies with respect to E_F by $\sim$ 200 meV. Already at a Xe coverage of 3 ML, where the intensity of the e_T peak is only slightly decreased, the energetic shift of the

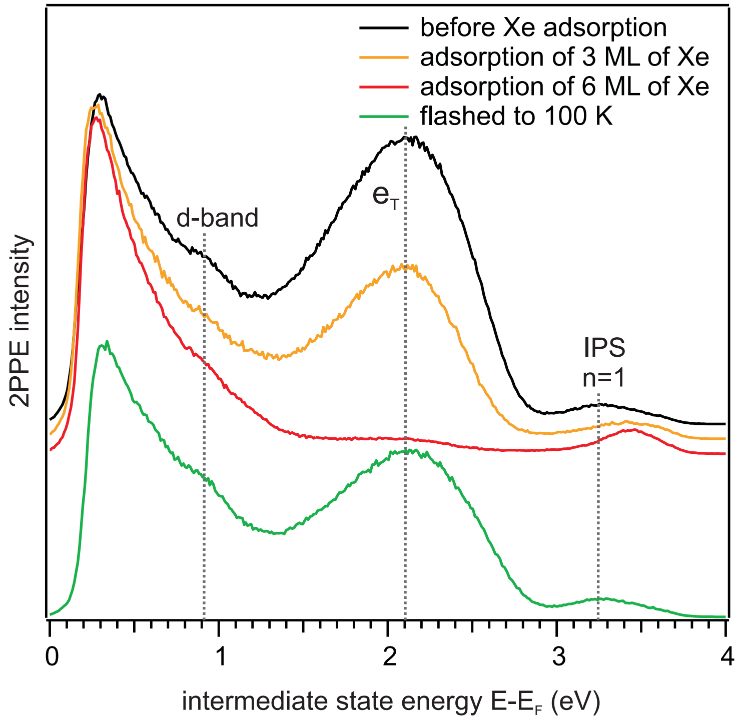

Figure 6.3: Determination of the trapped electrons binding site. 2PPE spectra of 4.5 BL of crystalline D_2O adsorbed on Ru(001) taken at a sample temperature of 30 K (black line), after deposition of 3 ML of Xe (yellow line), after deposition of 6 ML of Xe (red line) and after flashing the sample to ~ 100 K.

IPS is completed and stays unchanged for further Xe adsorption. This is in agreement with the growth of crystalline towers on a first wetting BL and the fact that the wave function of the IPS is confined to lateral regions of the bare first BL [Bov09]. Hence, only these regions need to be in contact with the adsorbed Xe atoms.

Furthermore, it is noteworthy that the interaction of the Xe atoms with the trapping sites is not destructive, as the e_T peak is recovered after desorption of the Xe adlayer at 100 K. Nevertheless, the e_T peak is less intense after the flash than in the case of freshly prepared crystalline ice. This intensity difference might be related to thermal induced modifications of the surface trapping sites upon annealing to 100 K.

6.2 Characterization of $CFCl_3$ Deposition

The adsorption of $CFCl_3$ on clean Ru(001) and on crystalline D_2O are characterized by means of TD spectroscopy in the present section. Fig.6.4 presents TD spectra of $CFCl_3$ adsorbed on Ru(001) for various coverages ranging from 0.1 ML to 5.7 ML. The desorption of $CFCl_3$ was monitored by following the most abundant fragment $CFCl_2$ with m/e = 101, which was identified by a residual gas analysis during deposition of $CFCl_3$. The TD spectra exhibit two separate peaks for coverages exceeding 1 ML. The peak α at 135 K is attributed to desorption from the first monolayer and saturates with increasing coverage. In contrast, the intensity of the peak labeled γ further increases with increasing $CFCl_3$ coverage. The γ-peak originates from molecules in the multilayer which desorb via zero order desorption kinetics as apparent by the coverage-independent onset of desorption at 105 K. The fact, that the desorption of the first ML of $CFCl_3$ occurs at temperatures which are higher by ~ 30 K compared to the

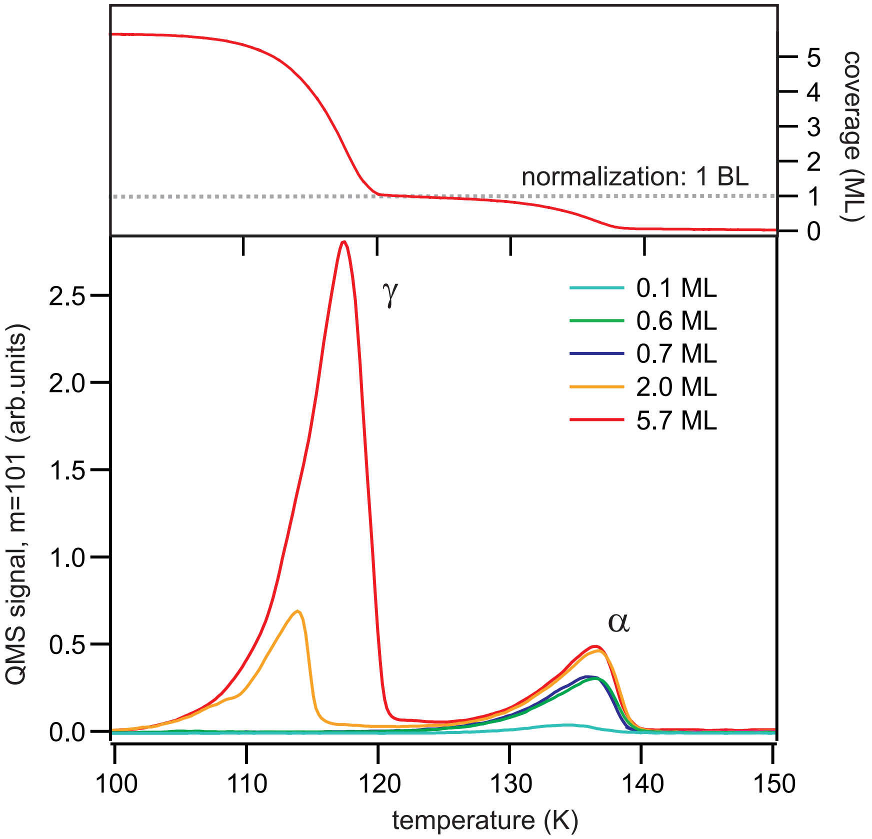

Figure 6.4: TD Spectra of $CFCl_3$ on Ru(001). The spectrum exhibits two peaks which are attributed to $CFCl_3$ adsorbed in multilayers γ and first monolayer α, respectively. The top panel shows the integrated QMS signal for the 5.7 ML coverage. For details see text.

multilayer desorption indicate a significantly stronger $CFCl_3$-Ru interaction than the intermolecular interaction within the $CFCl_3$ layer.

The absolute $CFCl_3$ coverage is determined using the desorption yield of the first monolayer as a mass equivalent. The integrated QMS signal for the 5.7 ML coverage is shown in the top panel of Fig.6.4. The kink at 120 K is caused by the decrease of the $CFCl_3$ desorption yield between multilayer and monolayer desorption and it is used to define the mass equivalent of 1.0 ML. The experiments to investigate the reactivity of the trapped electrons in crystalline ice were conducted with very low $CFCl_3$ coverages (< 0.02 ML). The $CFCl_3$ coverage on top of the crystalline ice was determined by the above described procedure and by assuming a constant sticking coefficient in the low coverage regime.

TD spectroscopy of $CFCl_3$ adsorbed on ice was performed and the results are presented in Fig.6.5. For comparison the TD spectrum of 1.7 ML $CFCl_3$ adsorbed on 4.5 BL D_2O/Ru(001) (red line) is plotted together with the TDS of 2.0 ML $CFCl_3$/Ru(001) (black line). The TDS exhibits also two separated peaks which can be attributed to $CFCl_3$ desorption from the first monolayer and multilayers. The onset of the zero order multilayer desorption at 105 K is identical to the one in absence of co-adsorbed ice, which indicates that the intermolecular interaction of the $CFCl_3$ molecules is not altered by the ice layer. The $CFCl_3$-D_2O interaction is slightly weaker than the D_2O-Ru interaction as apparent by the shift to lower desorption energies of the monolayer peak at 130 K. Nevertheless, the desorption temperature for the monolayer is 25 K higher than that observed for multilayer species indicating the significant interaction between

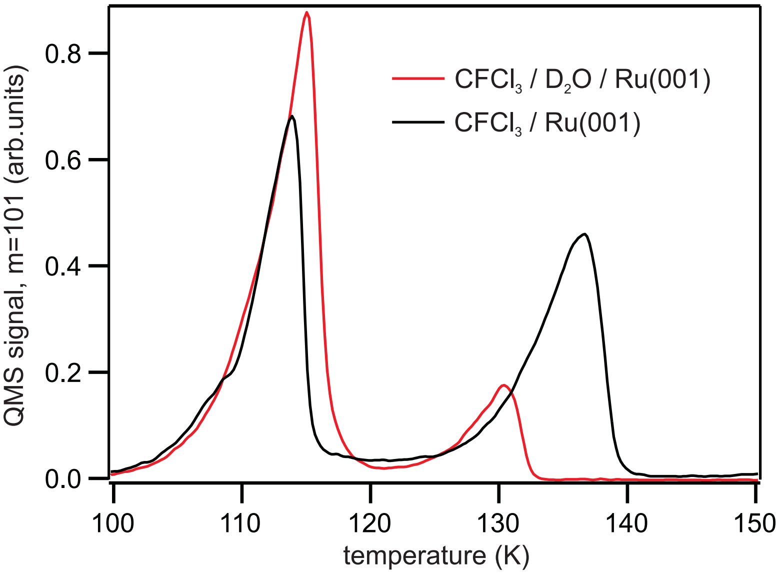

Figure 6.5: TD spectra of $CFCl_3$ adsorbed on ice (red line) and directly on Ru(001) (black line). The heating rate is 1 K/s.

the adsorbate and the ice surface. This finding is in good agreement with literature [Oga02b] and can be explained by the hydrogen bonding between $CFCl_3$ and the ice surface.

6.3 Reactivity of Trapped Electrons in Crystalline Ice with Coadsorbed $CFCl_3$

Having identified the surface character of the trapped electron's binding site and the adsorption properties of $CFCl_3$ molecules on the metal substrate and on crystalline ice, the reactivity of these trapped electrons with co-adsorbed chlorofluorocarbons is investigated by means of 2PPE spectroscopy.

One-color 2PPE spectra of 4.5 BL of crystalline D_2O adsorbed on Ru(001) for various coverages of co-adsorbed $CFCl_3$ are presented in Fig.6.6. The energy of the photons is $h\nu = 3.60$ eV. The spectra were acquired during *in situ* exposure of the sample kept at ~ 30 K to a partial pressure of $CFCl_3$ ($p_{CFC} = 1 \times 10^{-9}$ mbar). The $CFCl_3$ background pressure was controlled by a leak valve in the preparation chamber[48]. During the $CFCl_3$ adsorption the sample is illuminated so that electrons are permanently excited by absorption of UV photons. Fig.6.6 (a) presents a 2D plot of the 2PPE intensity in false color representation as a function of intermediate state energy $E - E_F$ and $CFCl_3$ coverage. The most prominent feature before $CFCl_3$ introduction is a broad and intense peak centered around $E - E_F \sim 2.2$ eV which is attributed to trapped electrons e_T in pure crystalline ice. Directly after the $CFCl_3$ deposition begins the intensity of the e_T is quickly vanishing. Additionally, the low energy cut-off of the spectrum, which is related to an increase of the work function Φ of the system, is shifting towards higher energies with respect to the Fermi level. Both effects can as well be clearly seen in Fig.6.6 (b) where 2PPE spectra as a function of $E - E_F$ are presented for several $CFCl_3$ coverages. The spectra are achieved by taking vertical cuts of the 2D plot in (a) for a given $CFCl_3$ coverage. Furthermore, the Ru d-band at $E - E_F = 1.0$ eV and the first IPS of the D_2O/Ru(001) interface at $E - E_F = 3.3$ eV can be observed. The quick decrease of the e_T peak intensity and the increase in the work function with increasing $CFCl_3$ exposure are very remarkable as both occur for an extremely small $CFCl_3$ coverage. The e_T peak becomes completely quenched for a coverage as small as ~ 0.004 ML. For this coverage the work function increases by $\Delta\Phi = +250$ meV. Such an increase of the system work function has to be related to the presence of an effective negative charge density on the surface, inducing a surface dipolar potential that raises the vacuum energy with respect to the Fermi level.

Although $CFCl_3$ deposition leads as well to the quenching of the long living electron peak, as in the case of Xe adsorption (cf. Fig.6.3, a simple electrostatic perturbation of the trapping site by surrounding $CFCl_3$ molecules can not solely explain the effect. In contrast to the Xe overlayer experiment where a coverage of 6 ML is required to quench the e_T signal, the low $CFCl_3$ coverage of $\leq 10^{-2}$ ML cannot induce such a strong elec-

---

[48] The setup of the UHV system is described in section 3.3

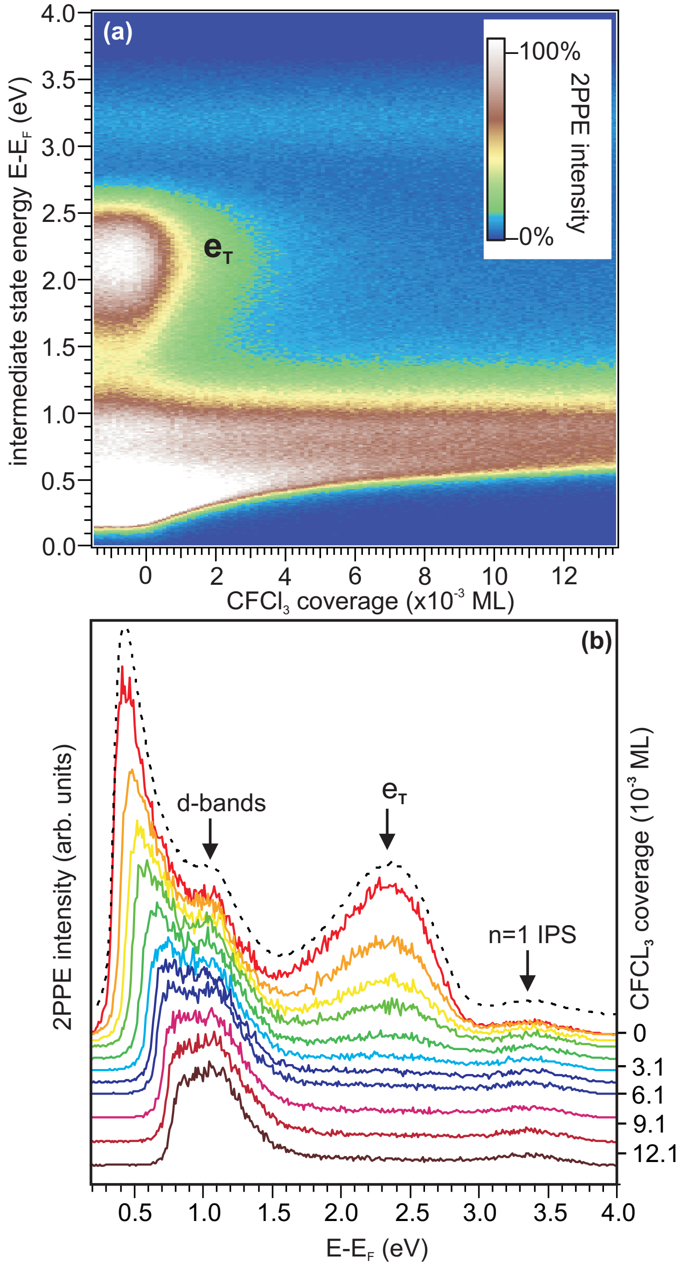

Figure 6.6: 2PPE spectra of $CFCl_3$ adsorbed on 4.5 BL crystalline ice deposited on Ru(001). (a) 2D plot of the 2PPE intensity in a false color representation as a function of $E - E_F$ and $CFCl_3$ coverage. (b) Vertical cuts of the 2D plot presented in (a) for different $CFCl_3$ coverages. The dashed black line is the 2PPE spectrum of 4.5 BL crystalline D_2O before $CFCl_3$ deposition.

trostatic effect on the surface trapping sites. Moreover, the work function increase which appears simultaneously with the quenching of the e_T peak, cannot be based on the dipole moment of the intact $CFCl_3$ molecules at such low coverage. Indeed, the $CFCl_3$ dipole moment is 0.45 Debye [Kao95], i.e. lower than the D_2O dipole moment of 1.86 Debye [Clo73], and is therefore expected to have little impact on the system work function due to the low density of molecules and screening by the underlying 4.5 BL of crystalline ice. In addition, the UV irradiation performed on crystalline ice alone leads to a work function increase of $\sim$ 50 meV for a coverage of 4.5 BL, due to the charging of the layer which is five times smaller than the one observed in the present case. Finally, any process triggered by the direct photodissociation of the $CFCl_3$ can not be operative in our case, since the photon energy employed (3.6 eV) is below the dissociation threshold of the intact molecule which is $\sim$ 5 eV [Ryu06].

Indeed, the quenching of the e_T peak and the increase of the work function can be explained by a reactive interaction between the $CFCl_3$ molecules and the long-living electrons trapped at the ice/vacuum interface. Fig.6.7 presents a scheme of the DEA reaction of $CFCl_3$ with the trapped electrons. In this process, an electron can attach to the molecule, leading to the formation of a transient negative ion, which can subsequently decay either via the auto detachment of the electron, or via a C-Cl bond cleavage and the formation of a Cl^- ion and a $\bullet$ $CFCl_2$ radical, following the equation:

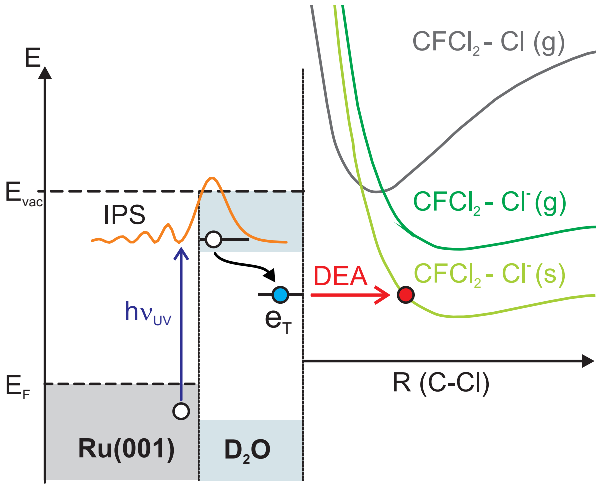

Figure 6.7: Scheme DEA reaction of $CFCl_3$ with trapped electrons in crystalline ice. The trapped electrons are injected into the D_2O ice by photo excitation in the metal substrate followed by charge transfer via the IPS. The energy of the negative ion state is lowered compared to the gas phase allowing the trapped electrons to attach to $CFCl_3$ via the stabilized ion resonance (DEA) leading to the dissociation of the molecule.

$$e^- + CFCl_3 \leftrightarrow CFCl_3^{*-} \rightarrow Cl^- + \bullet CFCl_2. \tag{6.43}$$

Due to polarization effects (image-charge potential due to the metal substrate and polarizability of the surrounding molecules) [Sam87], the energy of the negative ion state in the condensed phase is lowered compared to the gas phase by the polarization potential E_p of 1-2 eV [Lu10] [49]. As a consequence the potential energy curve of the molecule becomes resonant with the trapped electrons enabling the DEA of trapped electrons to the condensed $CFCl_3$ molecules. Thus, in the present case, the concomitant quenching of the e_T peak and increasing of the work function can be understood as follows. The lowering and quenching of the e_T peak's intensity in the 2PPE spectra can be related to the dissociative attachment of the long-living electrons to the $CFCl_3$ molecules. This dissociation is then accompanied by the formation of stable Cl^- anions at the surface of the ice and the density of negative charge present on the surface is then responsible for the observed increase of the work function. Furthermore, the very weak coupling of the trapped electrons with the metal substrate, i.e. their extraordinary long residence times, lead to a very inefficient decay channel of auto detachment of the electron and therefore favors the dissociative decay channel.

The work function change and the intensity of the e_T peak of the data set presented in Fig.6.6 are depicted in Fig.6.8 as a function of $CFCl_3$ coverage. The work function change saturates at $\Delta\Phi = +500$ meV. As discussed above the e_T peak is totally quenched for a $CFCl_3$ coverage of 0.004 ML, which corresponds to a surface density of $N_{CFC} = 2.3 \times 10^{12}\ cm^{-2}$, considering a surface density of $5.8 \times 10^{13}\ cm^{-2}$ for 0.1 ML [Lu04]. The corresponding work function change for this coverage is 250 meV. Indeed, considering a model based on the formation of a dipole layer between the Cl^- anion at the surface and its image in the metal substrate can explain the strength of the work function change $\Delta\Phi$ [Bha10]. It can be described according to the following equation:

$$\Delta\Phi = -\frac{4\pi d N_{CFC} q}{\varepsilon_{ice}}, \tag{6.44}$$

where d is the thickness of the ice, N_{CFC} is the surface density of the Cl^- anions, q is the charge and ε_{ice} is the dielectric constant of ice. Taking the above mentioned surface density N, a thickness for 4.5 BL crystalline ice of approximately $d \sim 20$ Å, a charge of q = -1 and ε_{ice} =4, gives a work function change of $\Delta\Phi = 210$ meV. This result is in very good agreement with the experimental value of $\Delta\Phi = 250$ meV.

In this context the question of the cross section for the DEA of the $CFCl_3$ adsorbed on the crystalline ice is of great interest. In order to determine the cross section for the DEA knowledge of the electron trapping density is required. The surface density of trapping sites was estimated from a fluence-dependent study on the e_T peak intensity [Gah04]. Rate equations, involving the equilibrium between excitation probability and probing probability of the trapping sites, were used, assuming a photoelectron detection probability of 10^{-4}. The estimated surface density of trapping sites is $N_{trap} \sim 2.5 \times 10^{12}\ cm^{-2}$ and hence on the same order of magnitude as the surface density N_{CFC} of the CFC molecules. This gives a lower limit of the cross of $\sigma \geq 4 \times 10^{-13}\ cm^2$, where every trap has interacted with one CFC. The cross section is at least one order of magnitude larger compared to the corresponding cross section in the gas [Ill79] and condensed phase without water ice [Lu10]. This finding shows the

---

[49] Taking CF_2Cl_2 adsorbed on an H_2O ice surface as an example the polarization potential is $E_p \sim 1.3$ eV [Lu02]

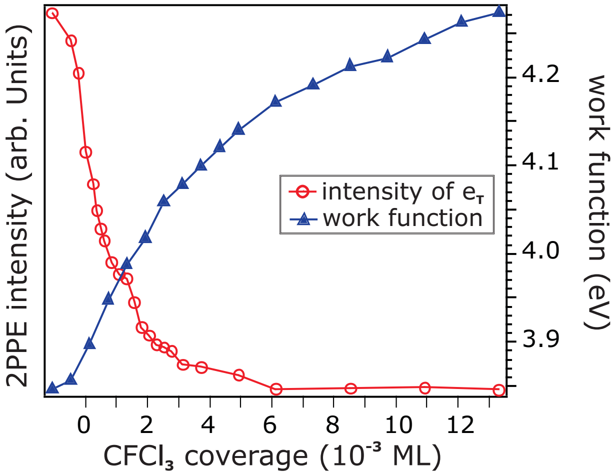

Figure 6.8: Work function change and intensity change of e_T as a function of CFCl$_3$ coverage derived from the 2PPE data presented in Fig.6.6.

high reactive character of the long-living electrons. The fact that the work function change continues with increasing CFCl$_3$ coverage after the e_T peak already vanished (cf. Fig.6.8) and saturates at $\Delta\Phi = +500$ meV for 0.015 ML of CFCl$_3$ suggests that several dissociation events may occur at one electron trap and that the trap is not inactive although the e_T peak cannot be observed anymore. Hence, one needs to understand how the blocking or deactivation of the trapping site works.

In order to get a better insight into the interactions involved between the e_T electrons and the CFCl$_3$ molecules, 2PPE has been performed on crystalline D$_2$O covered by 0.01 ML of CFCl$_3$ and subsequently annealed to different temperatures below the multilayer desorption temperature of crystalline ice. The resulting spectra are plotted in Fig.6.9 as a function of energy with respect to the Fermi level. All spectra were taken after cooling the sample to 30 K following the initial temperature increase to the indicated temperature. The spectra are vertically shifted for clarity. The black solid line represents the spectrum of 4.5 BL crystalline D$_2$O/Ru(001) with the pronounced feature e_T. The adsorption of 0.1 ML CFCl$_3$ (red solid line) is accompanied by a quenching of the e_T peak and an increase in the work function as described above. Again, the experiments are performed under UV irradiation that is generating the trapped electrons. Subsequently, these electrons can react with the adsorbed CFCl$_3$ molecules and lead to their dissociation. For flashing temperatures of 60 and 140 K, Fig.6.9 shows spectra acquired on a fresh spot, i.e. where no UV irradiation has lead to the trapping sites population by e_T electrons prior to the flashing (dashed curve), and pre-irradiated spot, i.e. where UV irradiation has already been realized before the annealing, and therefore where the reaction could already have taken place (solid curve). After the first flash to 60 K, the work function increased slightly by ~ 50 meV on the pre-irradiated spot (solid line) compared to the spectrum before the flash, whereas the spectrum taken on the non-irradiated spot (dashed line) is basically identical to the one before the flash. After the flash to 140 K, the work function has decreased slightly on the pre- and non-irradiated spot and is now considered as identical to the value of pure crystalline ice. However, the spectrum taken on the pre-irradiated spot shows no feature which is related to the trapped electrons, whereas the spectrum on the non-irradiated spot exhibits a peak at $E - E_F = 2.2$ eV attributed to the e_T electrons. The final flash to 160 K leads to the complete recovery of the e_T peak in the spectra taken on the fresh and pre-irradiated spot.

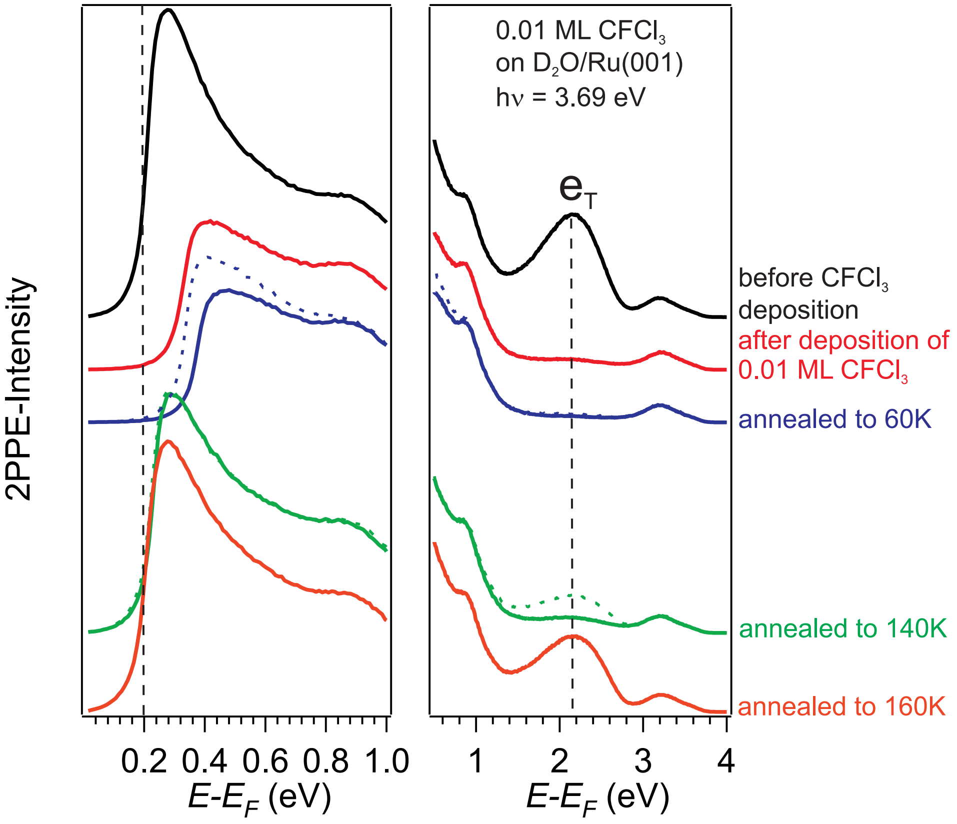

Figure 6.9: Temperature dependence of e_T-quenching. 2PPE spectra of 4.5 BL of crystalline D_2O before and after deposition of 0.01 ML $CFCl_3$. Subsequently, the sample was flashed to 60, 140 and 160 K and the spectra were recorded after cooling down to 30 K. After flashing to 60 and 140 K the spectra were taken on pre-irradiated spots before the flash (solid lines) and on non-irradiated spots (dashed line). The vertical dashed lines represent the position of the low energy cut-off and the position of e_T of the pure crystalline ice, respectively.

The temperature dependent change of the work function and the vanishing and reappearing of the e_T peak are signatures of a reactive process and corroborate the interpretation as a dissociative electron attachment of the trapped electron to the $CFCl_3$ molecules. Nevertheless, the exact nature of the subsequent reaction is *a priori* not clear. Several options can be considered to explain the decrease of the e_T peak intensity as well as the flashing-temperature dependency of the 2PPE spectra. The observed quenching of the e_T peak can indeed be explained with (i) a significant reduction of the lifetime of the trapped electron caused by an attachment to the $CFCl_3$ molecule whereas the trapping sites can still be populated by excited electrons during the illumination. When the lifetime of the state is reduced below the inverse repetition rate of the laser system (3 μs) the population and depopulation is not carried out by subsequent laser pulses. Therefore this process can only occur by absorption of photons within one laser pulse which is then a non-linear process and the intensity of the e_T peak can be drastically reduced. Another mechanism which can lead to the quenching of the e_T signal (ii) is based on an energetic or chemical modification of the trapping site that prevents further population of this site by photoexcited electrons.

If the quenching of the e_T would be solely caused by the attachment of the trapped electron to the intact CFC molecule, one could observe a recovery of the e_T signal upon illuminating the sample at a constant $CFCl_3$ coverage after all $CFCl_3$ molecules around the trapping site were dissociated. Nevertheless, such a recovery with illumination time was never observed in the experiments. Hence, a blocking of the site involving solely mechanism (i) can be excluded. Hence, the DEA process leads as well to a chemical modification and a deactivation of the trapping site. The deactivation mechanism is discussed in the following for two proposed scenarios.

(i) After one single cycle of population of the site and attachment of the electron to the $CFCl_3$, the resulting Cl^- is trapped at the site and therefore blocks it with regard to further population. This scenario is depicted schematically in Fig.6.10. Note that, the overall surface charge density is higher after the dissociation; after one complete cycle all traps are occupied by a Cl^- anion. In contrast, in equilibrium of population and depopulation of the traps with excess electrons not all trapping sites are occupied by an electron, so that the overall surface charge density $N_{electron} \leq N_{Cl}$. The work function increase for the e_T population of pure ice without $CFCl_3$ molecules is $\Delta\Phi = 50$ meV [Gah04], whereas the work function change is $\Delta\Phi = 250$ meV when 0.004 ML $CFCl_3$ is adsorbed. In addition, the observed change of the work function can as well originate from the different screening of the trapped electron and the anions by the surrounding water molecules at the ice/vacuum interface. Finally, the fact that a total quenching of the e_T peak is observed for a number of $CFCl_3$ molecules which is similar as the number of trapping sites fits with the above interpretation.

(ii) At one given trapping site several dissociations of CFC molecules could occur so that more than one Cl^- anion can be produced at one single trap. The blocking of the site can then be caused by a high density of Cl^- formed in the vicinity of the trapping defect, resulting in a strong electrostatic perturbation which leads to its deactivation. This scenario is depicted schematically in Fig.6.11. In this case, the work function increase is caused by a higher number of negative charges, *i.e.* Cl^- anions, present on the surface. To explain the work function change due to the Cl^- formation ($\Delta\Phi = 250$ meV) in comparison to the one due to the charging of the pure crystalline

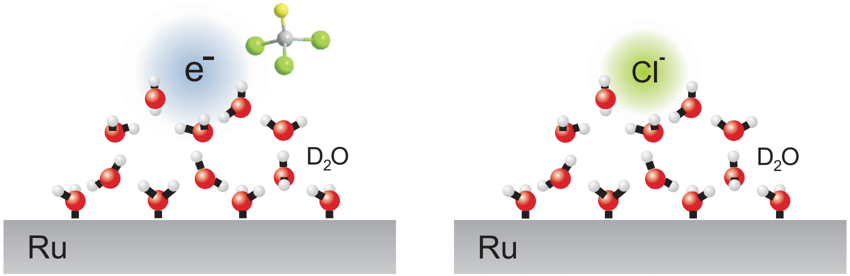

Figure 6.10: Deactivation of trapping site after one single dissociation

D_2O layer by the e_T electrons ($\Delta\Phi = 50$ meV), at least five Cl^- would need to be formed per trapping site. Although in the case of a total quenching of the e_T peak the number of $CFCl_3$ molecules is estimated to be comparable to the number of e_T electron sites, the uncertainty inherent to the determination of the density of sites — principally the determination of the detection sensitivity in the 2PPE experiment — does not allow us to exclude unambiguously the possibility that several dissociation processes can occur per surface defect. Furthermore, as apparent from Fig.6.8 the work function change continues after the e_T peak is completely quenched and saturates for coverages exceeding 0.015 ML at $\Delta\Phi = 500$ meV. So, assuming a similar screening of trapped electrons and Cl^- anions at the ice surface, at each trap on average 10 molecules could dissociate.

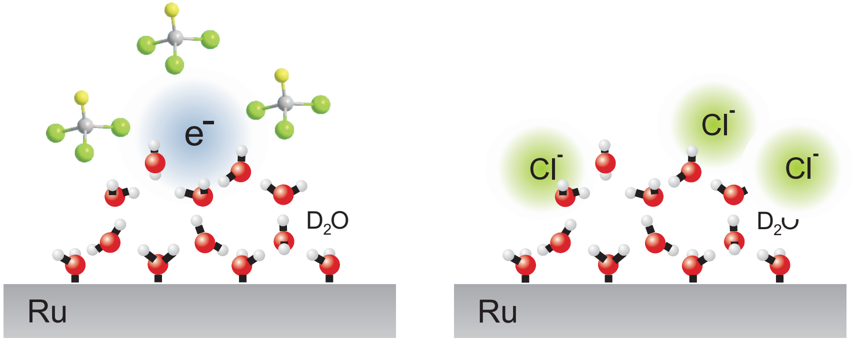

Figure 6.11: Deactivation of trapping site after several dissociations

As no scenario can strictly be ruled out the temperature dependent behavior of the work function change and the e_T peak intensity, presented in Fig.6.9 are discussed for both suggested scenarios. The flashing to 60 K promotes the diffusion of intact $CFCl_3$ molecules to available sites. In the pre-irradiated spot, where a certain number of sites are already blocked by the irradiation before the flashing, the temperature flash may activate the diffusion of intact $CFCl_3$ to some remaining available sites. The reaction is therefore enhanced and results in a larger amount of trapped Cl^- compared to the one present before flashing. The higher amount of Cl^- increases the local work function of the system. In the non-irradiated spot, as no dissociation took place before the flash, the diffusion of $CFCl_3$ prior to the reaction has no effect on the 2PPE spectrum. The flash of the system to 140 K desorbs the majority of the intact $CFCl_3$, as can be seen by the TD spectrum presented in Fig.6.5, which is seen on the non-irradiated spot where the e_T signal is again observed after the flash. For the pre-irradiated spot, one can conclude that the trapping sites are still blocked as no e_T signal is present in the 2PPE spectrum. However, the work function of the system is now very close to the one of the pure crystalline ice. Considering the first scenario, the work function increase is due to a less effective screening of the Cl^- by the water molecules of the e_T electron sites. The decrease of the work function upon flashing to 140 K means then that the thermal energy brought to the system allows the D_2O molecules to re-orient around the Cl^-, therefore enhancing the charge screening, and thus decreasing the work function. This scenario is thus capable of explaining the flashing-temperature dependence of the 2PPE spectra. Considering the second scenario, where the work function increase and the deactivation of the trapping site is due to the accumulation of several Cl^- ions, the interpretation of the behavior observed after the annealing at 140 K becomes more complex. Indeed, the work function reduction in the pre-irradiated spot could be explained by the thermal-induced diffusion of the Cl^- ions on the surface which would then decrease the local density of surface negative charge. However, the blocking of the trapping sites cannot be explained by the anions' density any more and other mechanisms, like a thermal-induced reaction (e.g. involving $\bullet CFCl_2$ radicals) leading to the chemical modification of the sites, have to be invoked. After flashing to 160 K, the 2PPE spectra are identical to the one of the pure crystalline ice. Indeed, as annealing to this temperature results in considerable D_2O desorption, in both scenarios one can expect the Cl^- to diffuse on the whole surface or in the bulk of the ice, therefore drastically decreasing its local density on the surface due to its weak concentration, and the surface defects to be regenerated.

Additionally, other blocking mechanisms involving a chemical modification of the trapping site are possible, although they seem to be less likely. The radical $\bullet CFCl_2$, which is a product in the DEA reaction, could react with the water molecules in the vicinity of the e_T traps, leading to their chemical modification. Indeed, it was shown that radicals $\bullet CF_xCl_{4-x}$ (x = 0, 2), formed from electron dissociative attachment on CF_2Cl_2 or CCl_4 coadsorbed with water, are at the origin of subsequent chemical reactions with H_2O molecules, leading in particular to CO_2 formation [Per04]. In contrast to the present experiment, this findings were realized on amorphous ice upon X-ray and 200 eV irradiation. In this case other electron-induced dissociations are involved. Hence, a direct comparison of this chemistry induced by higher energy irradiation to our case should be considered with caution. Furthermore, in infrared adsorption spectroscopy performed on crystalline ice co-adsorbed with $CFCl_3$ no evidence for a C-F stretching mode was found after illumination with 193 nm light[50], indicating that the $CFCl_2$ species were removed from the surface due to photodecomposition [Oga02b]. In the case of amorphous ice it was as well shown that two neighboring $\bullet CFCl_2$ radicals can recombine and form stable $C_2F_2Cl_4$ [Ryu06], but due to the low concentration of $CFCl_3$ in the present experiment a recombination seems very unlikely. Because of the very small coverage of $CFCl_3$ used here, attempts to find direct evidence of any product of a possible chemical reaction by TDS were not successful since the small amount desorbed is below the sensitivity threshold of the employed QMS.

6.4 Conclusion

Trapped electrons in crystalline ice exhibit pronounced characteristics which makes them a chemically very reactive species. First of all, a very efficient decoupling of the excess electrons from the metal substrate leads to lifetimes on the order of several minutes of the trapped electrons, so that they are available for a reaction over a large timescale. Furthermore, overlayer experiments with Xe adlayers revealed that these electrons are trapped at the ice/vacuum interface. When electronegative molecules like $CFCl_3$ are coadsorbed with crystalline ice a reactive interaction between the $CFCl_3$ molecules and the trapped electrons *via* a dissociative electron attachment process occurs, resulting in the formation of $\bullet CFCl_2$ radicals and Cl^- anions. This process results in the deactivation of the trapping sites and in the increase of the system work function which saturates at $\Delta\Phi = +500$ meV, which is a consequence of the accumulation of Cl^- at the ice surface. The deactivation of the trapping sites can be explained by (i) a blocking of the site by a Cl^- which is occupying the site or (ii) by a electrostatic perturbation of the site resulting from a high density of Cl^- anions formed by several dissociation processes in the vicinity of the trap. Both scenarios are capable to explain the flashing-temperature dependence of the e_T peak intensity and the work function change. The deactivation of the trapping sites and the concomitant work function change of $\Delta\Phi = +250$ meV are observed for very low coverages of $CFCl_3$ (~ 0.004 ML), which corresponds to a density of molecules comparable to the density of trapping sites. Following a conservative estimation where one trapping site dissociates one $CFCl_3$ molecule shows the high efficiency of the DEA process and leads to a cross section of $\sigma \geq 4 \times 10^{-13}\ cm^2$, that is at least one order of magnitude larger compared to the DEA cross section in the gas phase and in the condensed phase without coadsorbed ice. This large cross section is related to the long lifetime of the trapped electrons and their binding site at the ice/vacuum interface. Furthermore, the energy of the negative ion state in the condensed phase is lowered compared to the gas phase due to polarization effects. As a consequence the potential energy curve of the negative ion state of the molecule becomes resonant with the trapped electrons enabling the DEA of trapped electrons to the condensed $CFCl_3$ molecules, which enhances the DEA

---

[50] The experiments were performed with a $CFCl_3$ coverage which is 2 orders of magnitude larger compared to the coverage used in the present experiments. This and the fact that the sample was irradiated by light with a significantly higher photon energy of $h\nu = 6.4$ eV hinder a direct comparison as new photon-dissociation channel may be involved.

cross section significantly. These results suggest that the photo excited trapped electrons can play an important role in the heterogeneous chemical processes on condensed water surfaces and could be relevant in the polar stratosphere chemistry.

7 Summary

The present work focuses on the interaction between excess electrons in water ice structures adsorbed on metal surfaces and other charged or neutral species, like alkali ions, or chemically reactive molecules, like chlorofluorocarbons (CFC), respectively. In this thesis three different systems have been investigated by time-resolved 2PPE spectroscopy. The influence of alkali adsorption on electron solvation and transfer dynamics in ice structures has been observed for three different alkalis. The electrostatic interaction between the positively charged alkali ions and the water dipole moments leads to a strong perturbation of the H-bond network of the ice structures. This leads to the formation of new minima in the potential energy landscape which allows for the initial trapping of excess electrons in the ice. Finally, the capability of localized solvated electrons at the adsorbate/vacuum interface to mediate chemical reactions by electron attachment is demonstrated for coadsorbed CFCs on crystalline ice.

In the first part of this study the effect of coadsorption of alkali atoms/ions at the ice surface on the electron solvation dynamics at ice/metal interfaces is investigated. The adsorption of low coverages (< 0.15 ML) of alkali atoms on amorphous D_2O ice at temperatures between 60 and 100 K leads to in the formation of positively charged alkali ions at the ice/vacuum interface. In this temperature range the alkali atoms undergo an autoionization and the former *ns* valence electron decays to unoccupied states in the metal substrate leaving alkali ions at the surface, which are identified by an alkali coverage dependent work function change. It has been shown that the autoionization of the alkali atoms at the amorphous ice surface is a thermally activated process and that it can be at least partially suppressed at temperatures around 40 K for coadsorbed potassium atoms, whereby the 4s electrons of the neutral K atoms can be probed by direct photoemission spectroscopy.

The interaction between the alkali ions at the surface and the dipole moments of the surrounding water molecules results in an reorientation of the water molecules. As a consequence new electron trapping sites, i.e. at local potential minima, at the ice/vacuum interface are formed. Photoinjection of excess electrons into these alkali-ion covered amorphous ice layers, results in the trapping of a solvated electron at an alkali-ion/water complex located at the ice/vacuum interface. Compared to electron solvation in pure amorphous ice layers these electrons exhibit remarkably different population and stabilization dynamics. Directly after photoinjection the electrons stabilize with a rate of Σ=-0.83 eV/ps, which is more than two times higher than the stabilization rate for electron solvation in pure ice. However, after t$\approx$400 fs the solvation is significantly slowed down to Σ=-50 meV/ps accompanied by a strongly reduced population decay. The energetic stabilization is caused by nuclear rearrangement in the environment of the excess electron. The comparison of the initial stabilization rates of the solvated electrons in pure ice suggests a stronger molecular reorientation of the water molecules that surround the alkali-ion/water complex. This can be explained by a higher number of dangling OH-bonds at the ice/vacuum interface, that strongly contribute to the energetic stabilization. Furthermore, the more efficient screening leads to extended lifetimes of the solvated electrons at the alkali-ion/water complex compared to the dynamics in pure water ice. The population dynamics are described by means of a rate equation model that includes two different states e_p^{a+} and e_s^{a+}. The first state exhibits the faster stabilization dynamic and exponential decay times on fs-timescales, whereas the latter one exhibits dynamics on ps-timescales. The photoinjection into the ice layer proceeds via the ice conduction band directly into the initial trapping state e_p^{a+} or via an additional state, which is assigned to the LUMO of the alkali ion from where the electron is transferred to e_p^{a+} with a time constant of τ=250 fs. Both pathways occur with an equal probability. The latter time constant is assigned to the time constant of the autoionization of the alkali atom in an amorphous ice layer at a sample temperature of 60 K. The first state e_p^{a+} can be interpreted as a state, where the electron transfer is determined by the wave function overlap of the solvated electron state e_p^{a+} with unoccupied metal states. The electron transfer in the second state e_s^{a+} is determined by the tunneling probability through the evolved potential barrier, which is due to the ongoing screening of the electron by the surrounding water molecules. This leads to slower dynamics of electrons in state e_s^{a+}.

Coverage dependent measurements reveal that the decay time of the state e_s^{a+}, *i.e.* for time delays > 500 fs, increases exponentially with the layer thickness. In addition, overlayer experiments with D_2O or Xe adlayer show that the solvated electrons at the alkali-ion/water complexes are located at the ice/vacuum interface. Hence, the tunneling barrier, which separates e_s^{a+} from the metal substrate is determined by the thickness of the ice layer.

Changing the type of alkali from Na to K and Cs does not qualitatively influence the population and stabilization dynamics of the solvated electrons at the alkali-ion/water complex. As long as the alkali atoms autoionize after the initial preparation and the resulting alkali ions are not diffusing into the ice layer, excess electrons can be trapped at the alkali-ion water complexes located at the ice/vacuum interface. This is reasonable as the reorientation of the water molecules in the surrounding of the alkali ions is responsible for the formation of the initial trapping sites. This reorientation is induced by the electrostatic interaction between the dipole moments of the water and the positive charge of the alkali, which is identical for all types of alkalis.

In the second part of this study another approach enabled the investigation of electron solvation at small alkali/water clusters directly adsorbed on a metal substrate. In this way it is possible to control the number of water molecules in such a cluster and to investigate the population and stabilization dynamics of excess electrons as a function of D_2O coverage and hence the size of the solvation shell around the alkali atom. The clusters are prepared by adsorption of water molecules ($\Theta_{D_2O} < 1$ BL) on an alkali pre-covered metal surface ($\Theta_{alkali} < 0.15$ ML). An attractive interaction between the alkali-induced dipole moments and the dipole moments of the water molecules leads to stronger and preferential binding of the D_2O molecules in the vicinity of pre-adsorbed alkali atoms. The ratio of the amount of water molecules which are stabilized by the alkali and the amount of pre-adsorbed alkali atoms are governed by a hydration like interaction that is leading to the formation of a solvation shell around the adsorbed alkali. The ratio is typically in the range between 5:1 and 10:1 and does not show a pronounced dependence on the type of alkali.

In contrast, another critical ratio of water molecules to alkali atoms is found that depends on the type of alkali. Above a minimum number of water molecules per alkali in a cluster photoexcited excess electrons can be trapped at the alkali/water cluster identified by a new state e_c in the 2PPE spectra. This minimum cluster size depends on the type of alkali and is inversely proportional to the alkali-induced dipole moment. In the case of Cs only 2-3 water molecules are needed to stabilize an excess electron. For Na, where the induced dipole moment is only half of the one for Cs, 6-7 water molecules are required to allow for the initial trapping of an electron. This implies that the capability to bind an excess electron at the cluster is related to the reorientation of the water molecules caused by the alkali-induced dipole moment.

These localized excess electrons show, similar to electron solvation in ice layers, an energetic stabilization that is attributed to a dynamical reorientation of the water molecules in the cluster. In contrast to the electron solvation at alkali-ion/water complexes on wetting amorphous ice layers, the rate of energetic stabilization depends on the type of alkali. The strongest energetic stabilization is found for Na/water clusters with a rate of Σ=-2.2 eV/ps. A possible explanation could be that, as the alkali-induced dipole moment increases, the water network is more rigid and the water molecules react slower and less strongly to the presence of the excess electron. So the energetic stabilization rate decreases to Σ=-1.7 and Σ=-1.3 eV/ps for K and Cs, respectively. In the regime of small water coverages this strong energetic stabilization is possible because the water molecules in the alkali/water cluster are not fully coordinated in an H-bond network and many dangling OH-bonds are present in the vicinity of the excess electron. The screening of the electrons by the molecular reorientation of the water molecules leads to a reduction of the overlap of their wave function with unoccupied metal states and therefore to an increase of their lifetime. The decay time τ_{ec} of the excess electron at the alklai/water cluster is governed by the ratio of water molecules per alkali in the cluster, *e.g.* for 0.07 ML Na the exponential decay time is $\tau_{ec} = 19$ fs at a water coverage of 0.12 BL and $\tau_{ec} = 85$ fs at a coverage of 1.0 BL. Obviously, more water molecules in the alkali/water cluster can screen the electronic wave function of the e_c electrons more efficiently from the metal substrate leading to an increased lifetime.

In a third part of this thesis, excess electrons at interfaces, as found in the case of alkalis coadsorbed with water ice structures, can be utilized to mediate chemical reactions at surfaces. Trapped electrons in crystalline ice structures are a model system to investigate such reactions because these electrons exhibit characteristics which makes them a chemically very reactive species: (i) they exhibit lifetimes on the order of several minutes and (ii) they are trapped at the ice/vacuum interface. The high reactivity of such electrons has been demonstrated for the case of coadsorbed $CFCl_3$. Adsorption of 0.004 ML $CFCl_3$ leads to the quenching of the long-living electron signal in the 2PPE experiment. Simultaneously, the work function of the system increases by $\Delta\Phi = +250$ meV. These effects are attributed to the dissociative electron attachment (DEA) of the trapped electrons to intact $CFCl_3$ molecules, resulting in the formation of $\bullet CFCl_2$ radicals and Cl^- anions. The formation of the Cl^- results in the increase of the systems work function because of an enhancement in the effective surface negative charge density. Following a conservative estimation where one trapping site dissociates one $CFCl_3$ molecule shows the high efficiency of the DEA process and leads to a cross section of $\sigma \geq 4 \times 10^{-13}\ cm^2$. That is at least one order of magnitude larger compared to the DEA cross section in the gas phase and in the condensed phase without coadsorbed ice. The efficiency of this process has to be related to the very long lifetime, the surface location, and the weak coupling to the metal substrate. Furthermore, the energy of the negative ion state in the condensed phase is lowered compared to the gas phase due to polarization effects. As a consequence the potential energy curve of the negative ion state of the molecule becomes resonant with the trapped electrons enabling the DEA of trapped electrons to the condensed $CFCl_3$ molecules, which enhances the DEA cross section significantly. These results suggest that the photoexcited trapped electrons can play an important role in the heterogeneous chemical processes on condensed water surfaces and could be relevant in the polar stratosphere chemistry.

Summarizing, the presence of alkali ions in water ice strongly influences the population, localization, and stabilization dynamics of excess electrons in ice structures adsorbed on metal surfaces. It could be demonstrated that the understanding of the interactions of charged species and water molecules is a key parameter to describe the dynamics of excess electrons in polar molecular ices. Furthermore, it has been shown that trapped electrons need to be taken into account when describing chemistry at ice structure surfaces, as they can very efficiently mediate chemical reactions *via* dissociative electron attachment.

A route for future investigations would be to expand the doping of ice layers to other impurities and to study as well salts and alkaline earth metals. This would offer the possibility to study the dynamics of excess electrons in amorphous ice layers in the presence of positively and negatively charged parent ions. It was shown for alkali ions that the solvation dynamics mainly depend on the charge of the coadsorbed species. Hence, a doubly charged ion could influence the dynamics significantly different than a single charged one and would provide new insides. Similar experiments would also be beneficial for the understanding of electron trapping at doped water clusters directly adsorbed on the metal substrate. Finally, electron-induced chemical reactions require a systematic investigation with different reactive molecules to identify crucial parameters such as ionization energy or dissociation energy governing the efficiency of the reactions.

A Electron Solvation in Pure Amorphous D_2O - Minimum Water Coverage

In the presence of pre-adsorbed alkali atoms on Cu(111) stabilized excess electrons e_c are found, which exhibit similar characteristics as solvated electrons, for water coverages of 0.1-0.2 BL, as discussed in chapter 5. At this small water coverage binding of an solvated electron is not possible in pure ice layers without coadsorbed alkali atoms. In order to determine the minimum water coverage required to observe a solvated electron in pure ice, 2PPE spectra are recorded while D_2O is exposed to the cold sample setting a constant water background pressure of $p_{D_2O} \simeq 5 \cdot 10^{-9}$ mbar. The resulting 2PPE spectra are presented in Fig.A.1 as a function of final state energy $E_{fin} - E_F$ (left axis) and D_2O exposure (bottom axis). Upon increasing water coverage the secondary edge of the spectra is shifting to larger energies indicating a decreasing work function. The water-coverage-dependent work function change of Cu(111) is known [Gah04] and can be seen in the inset of Fig.3.17. This dependency is used to determine the water coverage in this experiment. The peak at $E_{fin} - E_F = 5.75$ eV is attributed to the occupied Cu(111) surface state. With increasing water coverage its intensity is gradually decreasing. At higher water coverage a new spectral feature arises at an energy of $E_{fin} - E_F = 6.1$ eV that is associated with solvated electrons e_s. From the work function

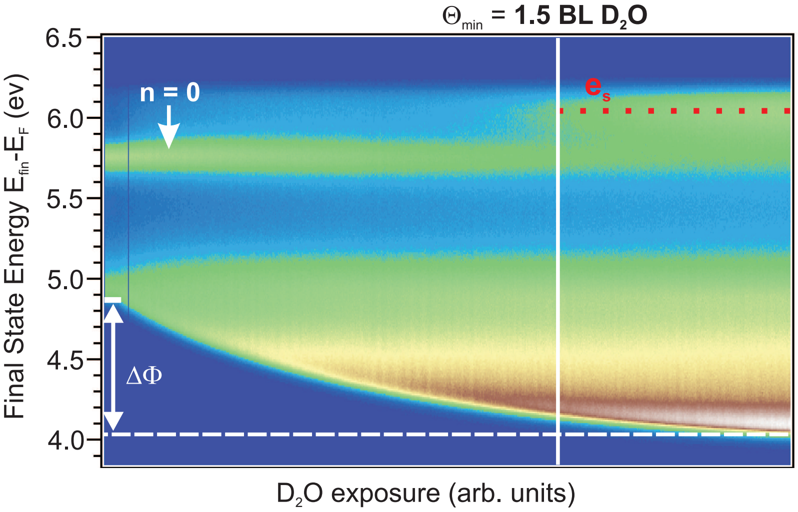

Figure A.1: Evolution of the 2PPE spectrum of Cu(111) as a function of D_2O exposure. The spectra are recorded using a photon energy of $h\nu_{UV}$ 3.09 eV.

at this water exposure of $\Phi = 4.2$ eV a corresponding water coverage of $\Theta_{min} = 1.5$ BL is derived, which is one order of magnitude higher than in the case of alkali pre-coverage. This finding emphasizes the strong influence of the alkalis on the water network.

References

[Are97] D. A. Arena, F. G. Curti, & R. A. Bartynski. *Unoccupied electronic states of the Cs/Cu(100) and Cs/Cu(111) adsorption systems.* Phys. Rev. B **56**, 23, (1997) 15404.

[Ass99] M. Assel, R. Laenen, & A. Laubereau. *Retrapping and solvation dynamics after femtosecond UV excitation of the solvated electron in water.* The Journal of Chemical Physics **111**, 15, (1999) 6869. URL `http://link.aip.org/link/?JCP/111/6869/1`.

[Bal99] A. Baltuska, M.F. Emde, M.S. Pshenichnikov, & D.A. Wiersma. *Early-Time Dynamics of the Photoexcited Hydrated Electron.* Journal of Physical Chemistry A **103**, (1999) 10065.

[Bar78] Bill Baron, Dale Hoover, & Ferd Williams. *Vacuum ultraviolet photoelectric emission from amorphous ice.* The Journal of Chemical Physics **68**, 4, (1978) 1997. URL `http://link.aip.org/link/?JCP/68/1997/1`.

[Bar88] R.N. Barnett, U. Landmann, C.L. Cleveland, & J. Jortner. *Dynamics and spectra of a solvated electron in water clusters.* Journal of Chemical Physics **88**, 4, (1988) 4429.

[Bar93] R. N. Barnett & Uzi Landman. *Hydration of sodium in water clusters.* Phys. Rev. Lett. **70**, 12, (1993) 1775.

[Bau97] M. Bauer, S. Pawlik, & M. Aeschlimann. *Resonance lifetime and energy of an excited Cs state on Cu(111).* Phys. Rev. B **55**, 15, (1997) 10040.

[Bau98] M. Bauer, S. Pawlik, R. Burgermeister, & M. Aeschlimann. *Symmetry properties of an electronic alkali excitation at a noble metal surface as investigated by two-photon photoemission.* Surface Science **402-404**, (1998) 62 . URL `http://www.sciencedirect.com/science/article/B6TVX-3X82696-B/2/20c0eaa528f269f34e9557687bf5ac15`.

[Bau99] M. Bauer, S. Pawlik, & M. Aeschlimann. *Decay dynamics of photoexcited alkali chemisorbates: Real-time investigations in the femtosecond regime.* Phys. Rev. B **60**, 7, (1999) 5016.

[Ber33] J.D. Bernal & R.H. Fowler. *A theory of water and ionic solutions, with particular reference to hydrogen and hydroxyl ions.* Journal of Chemical Physics **1**, (1933) 515.

[Ber64a] C. N. Berglund & W. E. Spicer. *Photoemission Studies of Copper and Silver: Experiment.* Phys. Rev. **136**, 4A, (1964) A1044.

[Ber64b] C. N. Berglund & W. E. Spicer. *Photoemission Studies of Copper and Silver: Theory.* Phys. Rev. **136**, 4A, (1964) A1030.

[Ber00] W. Berthold, U. Höfer, P. Feulner, & D. Menzel. *Influence of Xe adlayer morphology and electronic structure on image-potential state lifetimes of Ru(0001)*. Chemical Physics **251**, 1-3, (2000) 123 . URL `http://www.sciencedirect.com/science/article/B6TFM-3YDFYFW-9/2/9de45f4e0ef63ca948bc8d938c6a958f`.

[Ber04] W. Berthold, F. Rebentrost, P. Feulner, & U. Höfer. *Influence of Ar, Kr, and Xe layers on the energies and lifetimes of image-potential states on Cu(100)*. Applied Physics A: Materials Science & Processing **78**, (2004) 131. URL `http://dx.doi.org/10.1007/s00339-003-2310-6`. 10.1007/s00339-003-2310-6.

[Bha10] Somesh Kr. Bhattacharya, James M. Finn, Vinh P. Diep, Francesca Baletto, & Sandro Scandolo. *CCl_4 dissociation on the ice I_h surface: an excess electron mediated process*. Physical Chemistry Chemical Physics **12**, (2010) 13034 . URL `http://pubs.rsc.org/en/Content/ArticleLanding/2010/CP/c0cp00439a`.

[Bla90] P. M. Blass, X. L. Zhou, & J. M. White. *Coadsorption and reaction of water and potassium on silver(III)*. The Journal of Physical Chemistry **94**, 7, (1990) 3054. URL `http://pubs.acs.org/doi/abs/10.1021/j100370a058`.

[Bon85] H. P. Bonzel, G. Pirug, & A. Winkler. *Hydration of K and OH on Pt(111) during the adsorption of H_2O at 100 K*. Chemical Physics Letters **116**, 2-3, (1985) 133 . URL `http://www.sciencedirect.com/science/article/pii/0009261485801408`.

[Bor91] T. Bornemann, H.-P. Steinrück, W. Huber, K. Eberle, M. Glanz, & D. Menzel. *The adsorption of H_2O on K precovered Ni(111) studied by ARUPS and TPD*. Surface Science **254**, 1-3, (1991) 105 . URL `http://www.sciencedirect.com/science/article/B6TVX-46T3BM0-230/2/d21452cc094c08663d09afb838a125ac`.

[Bor01] A. G. Borisov, J. P. Gauyacq, A. K. Kazansky, E. V. Chulkov, V. M. Silkin, & P. M. Echenique. *Long-Lived Excited States at Surfaces:* Cs/Cu(111) *and* Cs/Cu(100) *Systems*. Phys. Rev. Lett. **86**, (2001) 488. URL `http://link.aps.org/doi/10.1103/PhysRevLett.86.488`.

[Bor02] A. G. Borisov, J. P. Gauyacq, E. V. Chulkov, V. M. Silkin, & P. M. Echenique. *Lifetime of excited electronic states at surfaces: Comparison between the alkali/Cu(111) systems*. Phys. Rev. B **65**, 23, (2002) 235434.

[Bor04] A. Borodin, O. Höfft, U. Kahnert, V. Kempter, & A. Allouche. *Electron spectroscopy (UPS(HeI and II) and metastable impact electron spectroscopy (MIES)) applied to molecular surfaces: the interaction of atoms and molecules with solid water*. Vacuum **73**, 1, (2004) 15 . URL `http://www.sciencedirect.com/science/article/`

`B6TW4-4BH625W-8/2/238de178d811c1a06a148a428a326818`. 16th Ion-Surface Interactions Conference.

[Bor08] A. G. Borisov, V. Sametoglu, A. Winkelmann, A. Kubo, N. Pontius, J. Zhao, V. M. Silkin, J. P. Gauyacq, E. V. Chulkov, P. M. Echenique, & H. Petek. *π Resonance of Chemisorbed Alkali Atoms on Noble Metals*. Phys. Rev. Lett. **101**, 26, (2008) 266801.

[Bov03] Uwe Bovensiepen, Cornelius Gahl, & Martin Wolf. *Solvation Dynamics and Evolution of the Spatial Extent of Photoinjected Electrons in $D_2O/Cu(111)$*. Journal of Physical Chemistry B **107**, (2003) 8706. URL `http://pubs.acs.org/doi/full/10.1021/jp034654g`.

[Bov09] U. Bovensiepen, C. Gahl, J. Stähler, M. Bockstedte, M. Meyer, F. Baletto, S. Scandolo, X.-Y. Zhu, A. Rubio, & M. Wolf. *A Dynamic Landscape from Femtoseconds to Minutes for Excess Electrons at Ice-Metal Interfaces*. The Journal of Physical Chemistry C **113**, 3, (2009) 979. URL `http://pubs.acs.org/doi/abs/10.1021/jp806997d`.

[Bra04] A. E. Bragg, J. R. R. Verlet, A. Kammrath, O. Cheshnovsky, & D. M. Neumark. *Hydrated Electron Dynamics: From Clusters to Bulk*. Science **306**, 5696, (2004) 669. URL `http://www.sciencemag.org/content/306/5696/669.abstract`.

[Bru97] Merlin Bruening, Rami Cohen, Jean FranÃfÂ§ois Guillemoles, Tamar Moav, Jacqueline Libman, Abraham Shanzer, & David Cahen. *Simultaneous Control of Surface Potential and Wetting of Solids with Chemisorbed Multifunctional Ligands*. Journal of the American Chemical Society **119**, 24, (1997) 5720. URL `http://pubs.acs.org/doi/abs/10.1021/ja964434z`.

[But05] G. Butti, S. Caravati, G. P. Brivio, M. I. Trioni, & H. Ishida. *Image potential states and electronic structure of Na/Cu(111)*. Phys. Rev. B **72**, 12, (2005) 125402.

[Car97] A. Carlsson, B. Hellsing, S.-Å. Lindgren, & L. Walldén. *High-resolution photoemission from a tunable quantum well: Cu(111)/Na*. Phys. Rev. B **56**, 3, (1997) 1593.

[Cha] Martin Chaplin. URL `http://www.lsbu.ac.uk/water`.

[Cha01] D. V. Chakarov, M. A. Gleeson, & B. Kasemo. *Photoreactions of water and carbon at 90 K*. The Journal of Chemical Physics **115**, 20, (2001) 9477. URL `http://link.aip.org/link/?JCP/115/9477/1`.

[Chu06] E. V. Chulkov, A. G. Borisov, J. P. Gauyacq, D. Sánchez-Portal, V. M. Silkin, V. P. Zhukov, & P. M. Echenique. *Electronic Excitations in Metals and at Metal Surfaces*. Chemical Reviews **106**, 10, (2006) 4160. URL `http://pubs.acs.org/doi/abs/10.1021/cr050166o`.

[Cla04] C. Clay, S. Haq, & A. Hodgson. *Intact and dissociative adsorption of water on Ru(0001).* Chemical Physics Letters **388**, 1-3, (2004) 89 . URL `http://www.sciencedirect.com/science/article/B6TFN-4BYK2DD-9/2/2d7fa256e263dff9c15e70de423c739a`.

[Clo73] Shepard A. Clough, Yardley Beers, Gerald P. Klein, & Laurence S. Rothman. *Dipole moment of water from Stark measurements of* H_2O*, HDO, and* D_2O*.* The Journal of Chemical Physics **59**, 5, (1973) 2254. URL `http://link.aip.org/link/?JCP/59/2254/1`.

[Coe90] J.V. Coe, G.H. Lee, J.G. Eaton, S.T. Arnold, H.W. Sarkas, & K.H. Bowen. *Photoelectron spectroscopy of hydrated electron cluster anions,* $(H_2O)^-_{n=2-67}$. Journal of Chemical Physics **92**, 6, (1990) 3980.

[Coe06] James V. Coe, Susan T. Arnold, Joseph G. Eaton, Gang Ho Lee, & Kit H. Bowen. *Photoelectron spectra of hydrated electron clusters: Fitting line shapes and grouping isomers.* The Journal of Chemical Physics **125**, 1, (2006) 014315. URL `http://link.aip.org/link/?JCP/125/014315/1`.

[Coh96] Coherent Laser Group, SantaClara. *Operator's Manual. The Coherent Mira Seed Laser* (1996).

[Dav08] H. Davy. Phil. Trans. R. Soc. A **98**, (1808) 333.

[Den03] D. N. Denzler, Ch. Hess, R. Dudek, S. Wagner, Ch. Frischkorn, M. Wolf, & G. Ertl. *Interfacial structure of water on Ru(001) investigated by vibrational spectroscopy.* Chemical Physics Letters **376**, 5-6, (2003) 618 . URL `http://www.sciencedirect.com/science/article/B6TFN-492083V-1/2/de25135332ed002191d9f534fe7e81be`.

[Dud90] R. Dudde, K. H. Frank, & B. Reihl. *Unoccupied electronic band structure of an ordered potassium layer on copper: Cu(111)-(2x2)K.* Phys. Rev. B **41**, 8, (1990) 4897.

[Ech78] P.M. Echenique & J.B. Bendry. *The existence and detection of Rydberg states at surfaces.* Journal of Physics C **11**, (1978) 2065.

[Ech00] P. M. Echenique, J. M. Pitarke, E. V. Chulkov, & A. Rubio. *Theory of inelastic lifetimes of low-energy electrons in metals.* Chemical Physics **251**, 1-3, (2000) 1 . URL `http://www.sciencedirect.com/science/article/B6TFM-3YDFYFW-2/2/5ff94eb0d98398762c0ae56f2f37624f`.

[Ech04] P. M. Echenique, R. Berndt, E. V. Chulkov, Th. Fauster, A. Goldmann, & U. Höfer. *Decay of electronic excitations at metal surfaces.* Surface Science Reports **52**, 7-8, (2004) 219 . URL `http://www.sciencedirect.com/science/article/B6TVY-4CB0CX3-1/2/67195f2cb92916a84304f99b21c7c42c`.

[Eck84] H. Eckhardt, L. Fritsche, & J. Noffke. *Self-consistent relativistic bandstructure of noble metals*. Journal of Physics F .

[Emd98] Michel F. Emde, Andrius Baltusˇka, Andreas Kummrow, Maxim S. Pshenichnikov, & Douwe A. Wiersma. *Ultrafast Librational Dynamics of the Hydrated Electron*. Phys. Rev. Lett. **80**, (1998) 4645. URL `http://link.aps.org/doi/10.1103/PhysRevLett.80.4645`.

[Far04] N. S. Faradzhev, C. C. Perry, D. O. Kusmierek, D. H. Fairbrother, & T. E. Madey. *Kinetics of electron-induced decomposition of CF_2Cl_2 coadsorbed with water (ice): A comparison with CCl_4*. The Journal of Chemical Physics **121**, 17, (2004) 8547. URL `http://link.aip.org/link/?JCP/121/8547/1`.

[Fau94] Thomas Fauster. *Two-photon photoemission*. Progress in Surface Science **46**, 2-3, (1994) 177 . URL `http://www.sciencedirect.com/science/article/pii/0079681694900779`.

[Fau95] Th. Fauster & W. Steinmann. *Two-photon photoemission spectroscopy of image states*. Electromagnetic Waves: Recent Developments in Research, P. Halevi, Ed., Elsevier, Amsterdam **2**, (1995) 347.

[Fei02] Peter J. Feibelman. *Partial Dissociation of Water on Ru(0001)*. Science **295**, 5552, (2002) 99. URL `http://www.sciencemag.org/content/295/5552/99.abstract`.

[Fei03] Peter J. Feibelman. *Vibrations of a water adlayer on Ru(0001)*. Phys. Rev. B **67**, 3, (2003) 035420.

[Fei04] P.J. Feibelmann. *What the stretch frequency spectrum of D_2O/Ru(001) does and does not mean*. Chemical Physics Letters **389**, (2004) 92.

[Fer91] C. Ferradini & J. Jay-Garin (Hg.). *Excess Electrons in Dielectric Media*. CRC, Boca Raton, 1991.

[Fer03] Y. Ferro & A. Allouche. *Sodium hydroxide formation in water clusters: The role of hydrated electrons and the influence of electric field*. The Journal of Chemical Physics **118**, 23, (2003) 10461. URL `http://link.aip.org/link/?JCP/118/10461/1`.

[Fin02] J. L. Finney, A. Hallbrucker, I. Kohl, A. K. Soper, & D. T. Bowron. *Structures of High and Low Density Amorphous Ice by Neutron Diffraction*. Phys. Rev. Lett. **88**, 22, (2002) 225503.

[Fis94] N. Fischer, S. Schuppler, Th. Fauster, & W. Steinmann. *Coverage-dependent electronic structure of Na on Cu(111)*. Surface Science **314**, 1, (1994) 89 . URL `http://www.sciencedirect.com/science/article/B6TVX-46P3NJN-27/2/999b15544e4c1a7c48f9e71bacd6ecc9`.

[Fri08] Tomaso Frigato, Joost VandeVondele, Burkhard Schmidt, Christof Schütte, & Pavel Jungwirth. *Ab Initio Molecular Dynamics Simulation of a Medium-Sized Water Cluster Anion: From an Interior to a Surface-Located Excess Electron via a Delocalized State*. The Journal of Physical Chemistry A **112**, 27, (2008) 6125. URL `http://pubs.acs.org/doi/abs/10.1021/jp711545s`. PMID: 18547038.

[Gah02] C. Gahl, U. Bovensiepen, C. Frischkorn, & M. Wolf. *Ultrafast Dynamics of Electron Localization and Solvation in Ice Layers on Cu(111)*. Physical Review Letters **89**, (2002) 107402.

[Gah03] C. Gahl, U. Bovensiepen, C. Frischkorn, K. Morgenstern, K. H. Rieder, & M. Wolf. *Ultrafast electron solvation dynamics in* D_2O*/Cu(111): influence of coverage and structure*. Surface Science **532-535**, (2003) 108 . URL `http://www.sciencedirect.com/science/article/B6TVX-47X1HPY-5/2/d24bd98bfb15f8a3363b65a45adcfc47`. Proceedings of the 7th International Conference on Nanometer-Scale Science and Technology and the 21st European Conference on Surface Science.

[Gah04] Cornelius Gahl. *Elektronentransfer- und Solvatisierungsdynamik in Eis adsorbierten Metalloberflächen*. Dissertation, Freie Universität Berlin (2004).

[Gal09] Mark Gallagher, Ahmed Omer, George R. Darling, & Andrew Hodgson. *Order and Disorder in the Wetting Layer on Ru(0001)*. Fara **141**, (2009) 231. URL `http://pubs.rsc.org/en/content/articlelanding/2009/fd/b807809b`.

[Gar98] Eric E. Gard, Michael J. Kleeman, Deborah S. Gross, Lara S. Hughes, Jonathan O. Allen, Bradley D. Morrical, David P. Fergenson, Tas Dienes, Markus E. Gälli, Robert J. Johnson, Glen R. Cass, & Kimberly A. Prather. *Direct Observation of Heterogeneous Chemistry in the Atmosphere*. Science **279**, 5354, (1998) 1184. URL `http://www.sciencemag.org/content/279/5354/1184.abstract`.

[Gar05] Bruce C. Garrett, David A. Dixon, Donald M. Camaioni, Daniel M. Chipman, Mark A. Johnson, Charles D. Jonah, Gregory A. Kimmel, John H. Miller, Thomas N. Rescigno, Peter J. Rossky, Sotiris S. Xantheas, Steven D. Colson, Allan H. Laufer, Douglas Ray, Paul F. Barbara, David M. Bartels, Kurt H. Becker, Kit H. Bowen, Stephen E. Bradforth, Ian Carmichael, James V. Coe, L. Rene Corrales, James P. Cowin, Michel Dupuis, Kenneth B. Eisenthal, James A. Franz, Maciej S. Gutowski, Kenneth D. Jordan, Bruce D. Kay, Jay A. LaVerne, Sergei V. Lymar, Theodore E. Madey, C. William McCurdy, Dan Meisel, Shaul Mukamel, Anders R. Nilsson, Thomas M. Orlando, Nikolay G. Petrik, Simon M. Pimblott, James R. Rustad, Gregory K. Schenter, Sherwin J. Singer, Andrei Tokmakoff, Lai-Sheng Wang, , & Timothy S. Zwier. *Role of Water in Electron-Initiated Processes and Radical Chemistry:*

Issues and Scientific Advances. Chemical Reviews **105**, 1, (2005) 355. URL http://pubs.acs.org/doi/abs/10.1021/cr030453x. PMID: 15720157.

[Gau07] J.P. Gauyacq, A.G. Borisov, & M. Bauer. *Excited states in the alkali/noble metal surface systems: A model system for the study of charge transfer dynamics at surfaces*. Progress in Surface Science **82**, 4-6, (2007) 244 . URL http://www.sciencedirect.com/science/article/B6TJF-4NP3P01-2/2/917c224fdf60f9d4b7b49bdf0642b290. Dynamics of Electron Transfer Processes at Surfaces.

[Ge98] N.-H. Ge, C.M.Wong, R.L. Lingle Jr., J.D. McNeill, K. J. Gaffney, & C.B. Harris. *Femtosecond Dynamics of Electron Localization at Interfaces*. Sience **279**, (1998) 202.

[Ge00] Nien-Hui Ge, Chung M. Wong, & Charles B. Harris. *Femtosecond Studies of Electron Dynamics at Interfaces*. Accounts of Chemical Research **33**, 2, (2000) 111. URL http://pubs.acs.org/doi/abs/10.1021/ar980138a.

[Gle04] M. A. Gleeson, K. Martensson, B. Kasemo, & D. V. Chakarov. *Co-adsorption and reactions of Na and H_2O on graphite*. Applied Surface Science **235**, 1-2, (2004) 91 . URL http://www.sciencedirect.com/science/article/B6THY-4CSP54F-B/2/88431db8d598356cbdb394057d97ce0b. 8th European Vacuum Conference and 2nd Annual Conference of the German Vacuum Society.

[Gou90] T. Goulet, A. Bernas, C. Ferradini, & J.-P. Jay-Gerin. *On the electronic structure of liquid water: Conduction-band tail revealed by photoionization data*. Chemical Physics Letters **170**, 5-6, (1990) 492 . URL http://www.sciencedirect.com/science/article/B6TFN-44FDCPJ-3B/2/8e42d7bc4e7cb6b659c776a63c61b0c4.

[Gro11] Jens-Uwe GrooÃŸ & Rolf MÃ¼ller. *Do cosmic-ray-driven electron-induced reactions impact stratospheric ozone depletion and global climate change?* Atmospheric Environment **45**, 20, (2011) 3508 . URL http://www.sciencedirect.com/science/article/pii/S135223101100330X.

[Gün02] J. Günster, S. Krischok, V. Kempter, J. Stultz, & D. W. Goodman. *Characterization of Coadsorbed Molecular Species in a Multilayer Solvent Envirnment on Insulating Surfaces*. Surface Revi **9**, 3&4, (2002) 1511.

[Gün03] Jens Günster & Ryutaro Souda. *Thickness dependent reactivity of amorphous water layers on Pt(111) interacting with sodium*. Chemical Physics Letters **371**, 5-6, (2003) 534 . URL http://www.sciencedirect.com/science/article/B6TFN-484SW45-2/2/1a4dc4b209995623b43f1c7fe3f6b459.

[Guo02] J.-H. Guo, Y. Luo, A. Augustsson, J.-E. Rubensson, C. Såthe, H. Ågren, H. Siegbahn, & J. Nordgren. *X-Ray Emission Spectroscopy of Hydrogen*

Bonding and Electronic Structure of Liquid Water. Phys. Rev. Lett. **89**, 13, (2002) 137402.

[Hal89] A. Hallbrucker, E. Mayer, & G.P. Johari. *Glas-Liquid transition and the enthalpy of devitrification of annealed vapour-deposited solid water: A comparison with hyperquenched glassy water*. Journal of Physical Chemistry **93**, (1989) 4986.

[Haq06] S. Haq, C. Clay, G. R. Darling, G. Zimbitas, & A. Hodgson. *Growth of intact water ice on* Ru(0001) *between 140 and* 160K *: Experiment and density-functional theory calculations*. Phys. Rev. B **73**, 11, (2006) 115414.

[Haq07] Sam Haq & Andrew Hodgson. *Multilayer Growth and Wetting of Ru(0001)*. The Journal of Physical Chemistry C **111**, 16, (2007) 5946. URL `http://pubs.acs.org/doi/abs/10.1021/jp065328e`.

[Har62] E.J. Hart & J.W. Boag. Journal of the American Chemical Society **84**, (1962) 4090.

[Har97] Yoshiya Harada, Shigeru Masuda, & Hiroyuki Ozaki. *Electron Spectroscopy Using Metastable Atoms as Probes for Solid Surfaces*. Chemical Reviews **97**, 6, (1997) 1897. URL `http://pubs.acs.org/doi/abs/10.1021/cr940315v`.

[Hel94] G. Held & D. Menzel. *The structure of the* $p(\sqrt{3} \times \sqrt{3})R30°$ *bilayer of* D_2O *on Ru(001)*. Surface Science **316**, 1-2, (1994) 92 . URL `http://www.sciencedirect.com/science/article/B6TVX-46SXVNK-15B/2/cf126890d396b40bcbdad0da28a976b9`.

[Hel95] G. Held & D. Menzel. *Isotope effects in structure and kinetics of water adsorbates on Ru(001)*. Surface Science **327**, 3, (1995) 301 . URL `http://www.sciencedirect.com/science/article/B6TVX-3YKM3T7-H/2/703cfd013acdb1fffc2febbac5bd695a`.

[Hen02] Michael A. Henderson. *The interaction of water with solid surfaces: fundamental aspects revisited*. Surface Science Reports **46**, 1-8, (2002) 1 . URL `http://www.sciencedirect.com/science/article/B6TVY-44TVHCS-1/2/a6aca6f52ff0de7b134704b09d935610`.

[Her91] I. V. Hertel, C. Hüglin, C. Nitsch, & C. P. Schulz. *Photoionization of* $Na(\mathrm{NH}_3)_n$ *and* $Na(\mathrm{H}_2O)_n$ *clusters: A step towards the liquid phase?* Phys. Rev. Lett. **67**, (1991) 1767. URL `http://link.aps.org/doi/10.1103/PhysRevLett.67.1767`.

[Hod09] A. Hodgson & S. Haq. *Water adsorption and the wetting of metal surfaces*. Surface Science Reports **64**, 9, (2009) 381 . URL `http://www.sciencedirect.com/science/article/B6TVY-4X49MV5-1/2/5eb1a8d268d7a2f9384765d26244d9cc`.

[Hof03] Germar Hoffmann, Richard Berndt, & Peter Johansson. *Two-Electron Photon Emission from Metallic Quantum Wells*. Phys. Rev. Lett. **90**, 4, (2003) 046803.

[Hot99] Arthur Hotzel. *Elektronendynamik der adsorbatbedeckten Cu(111) Oberfläche*. Dissertation, Freie Universität Berlin (1999).

[Hüf95] St. Hüfner. *Photoelectron Spectroscopy: Principles and Applications*. Springer Verlag Berlin Heidelberg, 1995.

[Iba90] H. Ibach & H. Lüth. *Festkörperphysik: Einführung in die Grundlagen*. Springer Verlag Berlin, Heidelberg, 1990, 3. Aufl.

[Ill79] E. Illenberger, H.-U. Scheunemann, & H. Baumgärtel. *Negative ion formation in CF_2Cl_2, CF_3Cl and $CFCl_3$ following low energy (0–10 eV) impact with near monoenergetic electrons*. Chemical Physics **37**, 1, (1979) 21 . URL `http://www.sciencedirect.com/science/article/B6TFM-44XDXH8-7G/2/8b5e81912c3e419e73274c9d5bb36e61`.

[Jen94] P. Jenniskens & D.F. Blake. *Structural transitions in amorphous water ice and astrophysical implications*. Science **265**, (1994) 753.

[Joh02] Peter Johansson, Germar Hoffmann, & Richard Berndt. *Light emission from Na/Cu(111) induced by a scanning tunneling microscope*. Phys. Rev. B **66**, 24, (2002) 245415.

[Kam06] Aster Kammrath, Jan R. R. Verlet, Graham B. Griffin, & Daniel M. Neumark. *Photoelectron spectroscopy of large (water)$_n{}^-$ (n = 50–200) clusters at 4.7 eV*. The Journal of Chemical Physics **125**, 7, (2006) 076101. URL `http://link.aip.org/link/?JCP/125/076101/1`.

[Kao95] C. P. Chai Kao, M. E. Paulaitis, G. A. Sweany, & M. Yokozeki. *An equation of state/chemical association model for fluorinated hydrocarbons and HF*. Fluid Phase Equilibria **108**, 1-2, (1995) 27 . URL `http://www.sciencedirect.com/science/article/B6TG2-3XVH330-V/2/b8809cc53e87ee65f1bc05fc251466e0`.

[Kev81] Larry Kevan. *Solvated electron structure in glassy matrixes*. Accounts of Chemical Research **14**, 5, (1981) 138. URL `http://pubs.acs.org/doi/abs/10.1021/ar00065a002`.

[Kim05] Greg A. Kimmel, Nikolay G. Petrik, Zdenek Dohnálek, & Bruce D. Kay. *Crystalline Ice Growth on Pt(111): Observation of a Hydrophobic Water Monolayer*. Phys. Rev. Lett. **95**, 16, (2005) 166102.

[Kir08] P.S. Kirchmann. *Ultrafast Electron Dynamics in Low-Dimensional Materials*. Dissertation, Freie Universität Berlin (2008).

[Kit05] Ch. Kittel. *Einführung in die Festkörperphysik*. Oldenbourg Verlag München, 2005.

[Kla01] D. Klar, M.-W. Ruf, I. I. Fabrikant, & H. Hotop. *Dissociative electron attachment to dipolar molecules at low energies with meV resolution: $CFCl_3$, 1,1,1-$C_2Cl_3F_3$, and HI.* Journal of Physics B: Atomic, Molecular and Optical Physics **34**, 19, (2001) 3855. URL `http://stacks.iop.org/0953-4075/34/i=19/a=309`.

[Kno97] Ernst Knoesel. *Ultrakurzzeit-Dynamik elektronischer Anregungen auf Metalloberflächen.* Dissertation, Freie Universität Berlin (1997).

[Kno98] E. Knoesel, A. Hotzel, & M. Wolf. *Temperature dependence of surface state lifetimes, dephasing rates and binding energies on Cu(111) studied with time-resolved photoemission.* Journal of Electron Spectroscopy and Related Phenomena **88-91**, (1998) 577 . URL `http://www.sciencedirect.com/science/article/B6TGC-40B7Y9K-3G/2/9d600b108b6c9d72f1a3c9cbdff5a1d9`. Proceedings of the Seventh International Conference on Electron Spectroscopy.

[Koo34] T. Koopmans. *Über die Zuordnung von Wellenfunktionen und Eigenwerten zu den Einzelnen Elektronen Eines Atoms.* Physica **1**, 1-6, (1934) 104 . URL `http://www.sciencedirect.com/science/article/pii/S0031891434900112`.

[Kra08] C.A. Kraus. *Solutions of Metals in Non-Metallic Solvents.* Journal of the American Chemical Society **30**, (1908) 1323.

[Kri03] S. Krischok, O. Höfft, J. Günster, R. Souda, & V. Kempter. *The chemistry of alkali atoms on solid water: a study with MIES and UPS.* Nuclear Instruments and Methods in Physics Research Section B: Beam Interactions with Materials and Atoms **203**, (2003) 124 . URL `http://www.sciencedirect.com/science/article/B6TJN-47MSDG7-C/2/91a76478d2feefbccc4bc59652ed2095`. 14th International Workshop on Inelastic Ion-Surface Collisions.

[Krö07] D. Kröner, T. Klamroth, M. Nest, & P. Saalfrank. *Laser-induced charge transfer and photodesorption of Cs at Cu(111): quantum dynamical model simulations.* Applied Physics A: Materials Science & Processing **88**, (2007) 535. URL `http://dx.doi.org/10.1007/s00339-007-4071-0`. 10.1007/s00339-007-4071-0.

[Kuc94] W. Kuch, W. Schnurnberger, M. Schulze, & K. Bolwin. *Equlibrium determination of H_2O desorption kinetic parameters of $H_2O/K/Ni(111)$.* Journal of Chemical Physics **101**, 2, (1994) 1687. URL `http://jcp.aip.org/resource/1/jcpsa6/v101/i2/p1687_s1`.

[Lae00] R. Laenen, T. Roth, & A. Laubereau. *Novel Precursors of Solvated Electrons in Water: Evidence for a Charge Transfer Process*. Physical Review Letters **85**, 1, (2000) 50.

[Lan73] N. D. Lang & W. Kohn. *Theory of Metal Surfaces: Induced Surface Charge and Image Potential*. Phys. Rev. B **7**, 8, (1973) 3541.

[Lar10] Ross E. Larsen, William J. Glover, & Benjamin J. Schwartz. *Does the Hydrated Electron Occupy a Cavity?* Science **329**, 5987, (2010) 65. URL `http://www.sciencemag.org/content/329/5987/65.abstract`.

[Lee97] Sik Lee, Jongseob Kim, Sang Joo Lee, & Kwang S. Kim. *Novel Structures for the Excess Electron State of the Water Hexamer and the Interaction Forces Governing the Structures*. Phys. Rev. Lett. **79**, 11, (1997) 2038.

[Li06] Bin Li, Jin Zhao, Ken Onda, Kenneth D. Jordan, Jinlong Yang, & Hrvoje Petek. *Ultrafast Interfacial Proton-Coupled Electron Transfer*. Science **311**, 5766, (2006) 1436. URL `http://www.sciencemag.org/content/311/5766/1436.abstract`.

[Lid93] D.R. Lide (Hg.). *CRC Handbook of Chemistry and Physics*. CRC, Boca Raton, FL, 1993.

[Lis04] M. Lisowski, P.A. Loukakos, U. Bovensiepen, J. Stähler, C. Gahl, & M. Wolf. *Ultra-fast dynamics of electron thermalization, cooling and transport effects in Ru(001)*. Applied Physics A: Materials Science & Processing **78**, (2004) 165. URL `http://dx.doi.org/10.1007/s00339-003-2301-7`. 10.1007/s00339-003-2301-7.

[Loe06] Thomas Loerting & Nicolas Giovambattista. *Amorphous ices: experiments and numerical simulations*. Journal of Physics: Condensed Matter **18**, 50, (2006) R919. URL `http://stacks.iop.org/0953-8984/18/i=50/a=R01`.

[Lon90] F.H. Long, H. Lu, & K.B. Eisenthal. *Femtosecond Studies of the Presolvated Electron: An Excited State of the Solvated Electron?* Physical Review Letters **64**, 12, (1990) 1469.

[Lou00] R. Loudon. *The Quantum Theory of Light*. Oxford University Press, Oxford, 2000.

[Lu96] Q. B. Lu, D. J. O'Connor, B. V. King, & R. J. MacDonald. *Local electrostatic potential determination of Cs/Cu(111) surfaces by negative ion spectroscopy*. Surface Science **347**, 3, (1996) L61 . URL `http://www.sciencedirect.com/science/article/pii/0039602895010394`.

[Lu99a] Q.-B. Lu & Theodore E. Madey. *Giant enhancement of electron-induced dissociation of chlorofluorocarbons coadsorbed with water or ammonia ices: Implications for atmospheric ozone depletion*. The Journal of Chemical Physics **111**, 7, (1999) 2861. URL `http://link.aip.org/link/?JCP/111/2861/1`.

[Lu99b] Q.-B. Lu & Theodore E. Madey. *Negative-Ion Enhancements in Electron-Stimulated Desorption of CF_2Cl_2 Coadsorbed with Nonpolar and Polar Gases on Ru(0001).* Phys. Rev. Lett. **82**, 20, (1999) 4122.

[Lu01a] Q.-B. Lu & Theodore E. Madey. *Factors Influencing Cl^- and F^- Enhancements in Electron-Stimulated Desorption of CF_2Cl_2 Coadsorbed with Other Gases.* The Journal of Physical Chemistry B **105**, 14, (2001) 2779. URL `http://pubs.acs.org/doi/abs/10.1021/jp003161y`.

[Lu01b] Q.-B. Lu & L. Sanche. *Effects of Cosmic Rays on Atmospheric Chlorofluorocarbon Dissociation and Ozone Depletion.* Phys. Rev. Lett. **87**, 7, (2001) 078501.

[Lu01c] Q.-B. Lu & L. Sanche. *Enhanced dissociative electron attachment to CF_2Cl_2 by transfer of electrons in precursors to the solvated state in water and ammonia ice.* Phys. Rev. B **63**, 15, (2001) 153403.

[Lu02] Q.-B Lu, A. D. Bass, & L. Sanche. *Superinelastic Electron Transfer: Electron Trapping in H_2O Ice via the $N_2^-(^2\Pi_g)$ Resonance.* Phys. Rev. Lett. **88**, 14, (2002) 147601.

[Lu04] Q.-B. Lu & L. Sanche. *Enhancements in dissociative electron attachment to CF_4, chlorofluorocarbons and hydrochlorofluorocarbons adsorbed on H_2O ice.* The Journal of Chemical Physics **120**, 5, (2004) 2434. URL `http://link.aip.org/link/?JCP/120/2434/1`.

[Lu09] Q.-B. Lu. *Correlation between Cosmic Rays and Ozone Depletion.* Phys. Rev. Lett. **102**, 11, (2009) 118501.

[Lu10] Qing-Bin Lu. *Cosmic-ray-driven electron-induced reactions of halogenated molecules adsorbed on ice surfaces: Implications for atmospheric ozone depletion and global climate change.* Physics Reports **487**, 5, (2010) 141 . URL `http://www.sciencedirect.com/science/article/B6TVP-4XVC4M5-1/2/643db802d858c3d6e2ec9b78627fea24`.

[Lud01] R. Ludwig. *Water: From clusters to bulk.* Angewandte Chemie International Edition **40**, (2001) 1808.

[Lud04] Valdemir Ludwig, Kaline Coutinho, & Sylvio Canuto. *Sequential classical-quantum description of the absorption spectrum of the hydrated electron.* Phys. Rev. B **70**, 21, (2004) 214110.

[Mal09] George Malenkov. *Liquid water and ices: understanding the structure and physical properties.* Journal of Physics: Condensed Matter **21**, 28, (2009) 283101. URL `http://stacks.iop.org/0953-8984/21/i=28/a=283101`.

[Mar99] W. Marbach, A. N. Asaad, & P. Krebs. *Optical Absorption of Solvated Electrons in Water and Tetrahydrofuran/Water Mixtures.* The Journal of Physical

Chemistry A **103**, 1, (1999) 28. URL `http://pubs.acs.org/doi/abs/10.1021/jp983520d`.

[Mar10] Ondrej Marsalek, Frank Uhlig, Tomaso Frigato, Burkhard Schmidt, & Pavel Jungwirth. *Dynamics of Electron Localization in Warm versus Cold Water Clusters*. Phys. Rev. Lett. **105**, 4, (2010) 043002.

[Meh06] Michael Mehlhorn. *Dynamik von CO und D_2O auf Cu(111)*. Dissertation, Freie Universität Berlin (2006).

[Men05] Sheng Meng, E.G. Wang, Ch. Frischkorn, M. Wolf, & Shiwu Gao. *Consistent picture for the wetting structure of water/Ru(0001)*. Chemical Physics Letters **402**, 4-6, (2005) 384 . URL `http://www.sciencedirect.com/science/article/B6TFN-4F60NH4-B/2/91e450f60b500c73be91eec477cec973`.

[Mey08] Michael Meyer, Julia Stähler, Daniela O. Kusmierek, Martin Wolf, & Uwe Bovensiepen. *Determination of the electrons solvation site on D_2O/Cu(111) using Xe overlayers and femtosecond photoelectron spectroscopy*. Physical Chemistry Chemical Physics **10**, 32, (2008) 4932. URL `http://pubs.rsc.org/en/Content/ArticleLanding/2008/CP/b807314g`.

[Mey11] Michael Meyer, Mathieu Bertin, Uwe Bovensiepen, Daniel Wegkamp, Marcel Krenz, & Martin Wolf. *Ultrafast Dynamics at the Na/D_2O/Cu(111) Interface: Electron Solvation in Ice Layers and Na^+-Mediated Surface Solvation*. The Journal of Physical Chemistry C **115**, 1, (2011) 204. URL `http://pubs.acs.org/doi/abs/10.1021/jp107253g`.

[Mol74] M. J. Molina & F. S. Rowland. *Stratospheric sink for chlorofluoromethanes: chlorine atomc-atalysed destruction of ozone*. Nature **249**, (1974) 810.

[Mun00] Christopher J. Mundy, Jürg Hutter, & Michele Parrinello. *Microsolvation and Chemical Reactivity of Sodium and Water Clusters*. Journal of the American Chemical Society **122**, 19, (2000) 4837. URL `http://pubs.acs.org/doi/abs/10.1021/ja994507p`.

[Nit06] A. Nitzan. *Chemical Dynamics in Condensed Phases*. Oxford University Press, New York, 2006.

[Nor07] D. Nordlund, H. Ogasawara, H. Bluhm, O. Takahashi, M. Odelius, M. Nagasono, L. G. M. Pettersson, & A. Nilsson. *Probing the Electron Delocalization in Liquid Water and Ice at Attosecond Time Scales*. Phys. Rev. Lett. **99**, 21, (2007) 217406.

[Oga99] S. Ogawa, H. Nagano, & H. Petek. *Phase and Energy Relaxation in an Antibonding Surface State: Cs/Cu(111)*. Phys. Rev. Lett. **82**, 9, (1999) 1931.

[Oga02a] H. Ogasawara, B. Brena, D. Nordlund, M. Nyberg, A. Pelmenschikov, L. G. M. Pettersson, & A. Nilsson. *Structure and Bonding of Water on Pt(111)*. Phys. Rev. Lett. **89**, 27, (2002) 276102.

[Oga02b] Hirohito Ogasawara & Maki Kawai. *Photochemistry of $CFCl_3$ on ice surface: surface chlorine reservoir species*. Surface Science **502-503**, (2002) 285 . URL `http://www.sciencedirect.com/science/article/pii/S0039602801019653`.

[Pai04] D. Hern Paik, I-Ren Lee, Ding-Shyue Yang, J. Spencer Baskin, & Ahmed H. Zewail. *Electrons in Finite-Sized Water Cavities: Hydration Dynamics Observed in Real Time*. Science **306**, 5696, (2004) 672. URL `http://www.sciencemag.org/content/306/5696/672.abstract`.

[Par00] Seong-Chan Park, T. Pradeep, & H. Kang. *Ionic dissociation of NaCl on frozen water*. The Journal of Chemical Physics **113**, 21, (2000) 9373. URL `http://link.aip.org/link/?JCP/113/9373/1`.

[Pat02] Prabir K. Patra & M. S. Santhanam. *Comment on "Effects of Cosmic Rays on Atmospheric Chlorofluorocarbon Dissociation and Ozone Depletion"*. Phys. Rev. Lett. **89**, 21, (2002) 219803.

[Pau35] L. Pauling. *The structure and entropy of ice and other crystals with some randomness of atomic arrangements*. Journal of the American Chemical Society **57**, (1935) 2680.

[Pel00] T. Pelzer, G. Ceballos, F. Zbikowski, B. Willerding, K. Wandelt, U. Thomann, Ch. Reuß, Th. Fauster, & J. Braun. *Electronic structure of the Ru(0001) surface*. Journal of Physics: Condensed Matter **12**, 10, (2000) 2193. URL `http://stacks.iop.org/0953-8984/12/i=10/a=305`.

[Per04] C. C. Perry, N. S. Faradzhev, D. H. Fairbrother, & T. E. Madey. *Electron-driven chemistry of halogenated compounds in condensed phases: Effects of solvent matrices on reaction dynamics and kinetics*. International Reviews in Physical Chemistry **23**, 2, (2004) 289 . URL `http://search.ebscohost.com/login.aspx?direct=true&db=aph&AN=15059227&site=ehost-live`.

[Pet97] H. Petek & S. Ogawa. *Femtosecond time-resolved two-photon photoemission studies of electron dynamics in metals*. Progress in Surface Science **56**, 4, (1997) 239 . URL `http://www.sciencedirect.com/science/article/B6TJF-3T0V40N-1/2/7a7a1eb9814c7370cb2fc9a2ad847f11`.

[Pet99] V.F. Petrenko & R.W. Whitworth. *Physics of ice*. Oxford University Press, New York, 1999.

[Pet00] Hrvoje Petek, Miles J. Weida, Hisashi Nagano, & Susumu Ogawa. *Real-Time Observation of Adsorbate Atom Motion Above a Metal Surface*. Science **288**, 5470, (2000) 1402. URL `http://www.sciencemag.org/content/288/5470/1402.abstract`.

[Pla03] John M. C. Plane. *Atmospheric Chemistry of Meteoric Metals*. Chemical Reviews **103**, 12, (2003) 4963. URL `http://pubs.acs.org/doi/abs/10.1021/cr0205309`.

[Pol07] A. Politano, R. G. Agostino, E. Colavita, V. Formoso, & G. Chiarello. *High resolution electron energy loss measurements of Na/Cu(111) and H_2O/Na/Cu(111): Dependence of water reactivity as a function of Na coverage*. The Journal of Chemical Physics **126**, 24, (2007) 244712. URL `http://link.aip.org/link/?JCP/126/244712/1`.

[Pra90] M. J. Prather & R. T. Watson. *Stratospheric ozone depletion and future levels of atmospheric chlorine and bromine*. Nature **344**, (1990) 729.

[Pui03] S.R. Puisto, T.J. Lerotholi, G. Held, & D. Menzel. *Analysis of Water on Ru(0001): Experimental Test of the Partial Dissociation Model*. Surface Review and Letters **10**, 2-3, (2003) 487.

[Ran87] G. Rangelov & L. Surnev. *Alkali metal adsorption on Ru(001)*. Surface Science **185**, 3, (1987) 457 . URL `http://www.sciencedirect.com/science/article/pii/S003960288780170X`.

[Rav97] A. R. Ravishankara. *Heterogeneous and Multiphase Chemistry in the Troposphere*. Science **276**, 5315, (1997) 1058. URL `http://www.sciencemag.org/content/276/5315/1058.abstract`.

[Row91] S.F. Rowland. *Stratospheric Ozone Depletion*. Annu **42**, (1991) 731.

[Ryu06] Sunmin Ryu, Jinyoung Chang, Hyuksang Kwon, & Seong Keun Kim. *Dynamics of Solvated Electron Transfer in Thin Ice Film Leading to a Large Enhancement in Photodissociation of $CFCl_3$*. Journal of the American Chemical Society **128**, 11, (2006) 3500. URL `http://pubs.acs.org/doi/abs/10.1021/ja058323o`.

[Sam87] H. Sambe, D. E. Ramaker, L. Parenteau, & L. Sanche. *Electron-stimulated desorption enhanced by coherent scattering*. Phys. Rev. Lett. **59**, 4, (1987) 505.

[Sas90] J.K. Sass, J. Schott, & D. Lackey. *Prospects for the direct determination of the dielectric constant of water in the double layer using model adsorption experiments in UHV: coadsorption of Cs and H2O on Cu (110)*. Journal of Electroanalytical Chemistry and Interfacial Electrochemistry **283**, 1-2, (1990) 441 . URL `http://www.sciencedirect.com/science/article/pii/002207289087408C`.

[Sas91] J.K. Sass, D. Lackey, & J. Schott. *Electrochemical hydration and reaction processes on metal surfaces studied by gas phase adsorption*. Electrochimica Acta **36**, 11-12, (1991) 1883 . URL `http://www.sciencedirect.com/science/article/pii/001346869185062C`.

[Sch68] U. Schindewolf. *Bildungsreaktionen und Eigenschaften solvatisierter Elektronen.* Angewandte Chemie **80**, 5, (1968) 165. URL `http://dx.doi.org/10.1002/ange.19680800502`.

[Sch92] Hartmut Schlichting & Dietrich Menzel. *High resolution, wide range, thermal desorption spectrometry of rare gas layers: sticking, desorption kinetics, layer growth, phase transitions, and exchange processes.* Surface Science **272**, 1-3, (1992) 27 . URL `http://www.sciencedirect.com/science/article/pii/003960289291418B`.

[Sch93] H. Schlichting & D. Menzel. *Techniques for attainment, control, and calibration of cryogenic temperatures at small single-crystal samples under ultrahigh vacuum* **64**, 7, (1993) 2013. URL `http://dx.doi.org/doi/10.1063/1.1143992`.

[Sch03] M. Schattke & M. A. Van Hove. *Solid-State Photoemission and Related Methods.* Wiley VCH, 2003.

[Sei00] Ari P. Seitsonen. *Theoretical Investigations into Adsorpion and Co-adsorption on Transition-Metal Surfaces as Models to Heterogeneous Catalysis.* Dissertation, Technische Universität Berlin (2000). URL `http://opus.kobv.de/tuberlin/volltexte/2002/152/`.

[Shi77] Takashi Shibaguchi, Hideo Onuki, & Ryumyo Onaka. *Electronic Structures of Water and Ice.* Journal of the Physical Society of Japan **42**, 1, (1977) 152. URL `http://jpsj.ipap.jp/link?JPSJ/42/152/`.

[Sie10] Katrin R. Siefermann, Yaxing Liu, Evgeny Lugovoy, Oliver Link, Manfred Faubel, Udo Buck, Bernd Winter, & Bernd Abel. *Binding energies, lifetimes and implications of bulk and interface solvated electrons in water.* Nat Chem **2**, 4, (2010) 274. URL `http://dx.doi.org/10.1038/nchem.580`.

[Sil98] Carlos Silva, Peter K. Walhout, Kazushige Yokoyama, & Paul F. Barbara. *Femtosecond Solvation Dynamics of the Hydrated Electron.* Phys. Rev. Lett. **80**, (1998) 1086. URL `http://link.aps.org/doi/10.1103/PhysRevLett.80.1086`.

[Smi85] N. V. Smith. *Phase analysis of image states and surface states associated with nearly-free-electron band gaps.* Physical Review B **32**, 6, (1985) 3549.

[Smi89] N. V. Smith & C. T. Chen. *Distance of the Image Plan from Metal Surfaces.* Physical Review B **40**, 11, (1989) 7565.

[Son01] Dong Hee Son, Patanjali Kambhampati, Tak W. Kee, & Paul F. Barbara. *Delocalizing Electrons in Water with Light.* The Journal of Physical Chemistry A **105**, 36, (2001) 8269. URL `http://pubs.acs.org/doi/abs/10.1021/jp012431p`.

[Stä06] J. Stähler, C. Gahl, U. Bovensiepen, & M. Wolf. *Ultrafast Electron Dynamics at Ice-Metal Interfaces: Competition between Heterogeneous Electron Transfer and Solvation.* Journal of Physical Chemistry B **110**, (2006) 9637.

[Stä07a] J. Stähler, M. Mehlhorn, U. Bovensiepen, M. Meyer, D. O. Kusmierek, K. Morgenstern, & M. Wolf. *Impact of Ice Structure on Ultrafast Electron Dynamics in D_2O Clusters on Cu(111).* Phys. Rev. Lett. **98**, 20, (2007) 206105.

[Stä07b] Julia Stähler. *Electron Transfer and Solvation Dynamics at Ice- and Ammonia-Metal Interfaces: Freezing Hot Electrons.* Dissertation, Freie Universität Berlin (2007). Dissertation.

[Stä08a] Julia Stähler, Uwe Bovensiepen, Michael Meyer, & Martin Wolf. *A surface science approach to ultrafast electron transfer and solvation dynamics at interfaces.* Chemical Society Reviews **37**, (2008) 2180. URL `http://pubs.rsc.org/en/Content/ArticleLanding/2008/CS/b800257f`.

[Stä08b] Julia Stähler, Michael Meyer, Daniela O. Kusmierek, Uwe Bovensiepen, & Martin Wolf. *Ultrafast Electron Transfer Dynamics at NH_3/Cu(111) Interfaces: Determination of the Transient Tunneling Barrier.* Journal of the American Chemical Society **130**, 27, (2008) 8797. URL `http://pubs.acs.org/doi/abs/10.1021/ja801682u`. PMID: 18597434.

[Stä11] Julia Stähler, Michael Meyer, Uwe Bovensiepen, & Martin Wolf. *Solvation dynamics of surface-trapped electrons at NH_3 and D_2O crystallites adsorbed on metals: from femtosecond to minute timescales.* Chemical Science URL `http://pubs.rsc.org/en/Content/ArticleLanding/2011/SC/c0sc00644k`.

[Ste99] K.P. Stevenson, G.A. Kimmel, Z. Dohnalek, R.S. Smith, & B.D. Kay. *Controlling the Morphology of Amorphous Solid Water.* Science **283**, (1999) 1505.

[Ste10] F. Steeb, S. Mathias, M. Wiesenmayer, A. Fischer, M. Aeschlimann, M. Bauer, & J. P. Gauyacq. *Probing adsorbate dynamics with chirped laser pulses in a single-pulse scheme.* Phys. Rev. B **82**, 16, (2010) 165430.

[Szy05] P. Szymanski, S. Garret-Roe, & C.B. Harris. *Time- and angle-resolved two-photon photoemission studies of electron localization and solvation at interfaces.* Progress in Surface Science **78**, (2005) 1.

[Tan91] D. Tang, D. McIlroy, X. Shi, C. Su, & D. Heskett. *The structure of Na overlayers on Cu(111) at room temperature.* Surface Science Letters **255**, 1-2, (1991) L497 . URL `http://www.sciencedirect.com/science/article/pii/016725849190158N`.

[Thi87] Patricia A. Thiel & Theodore E. Madey. *The interaction of water with solid surfaces: Fundamental aspects.* Surface Science Reports **7**, 6-8,

(1987) 211 . URL `http://www.sciencedirect.com/science/article/B6TVY-46CC7D9-2/2/c8cc77e1dd0bcb3a149cedef9220cbb0`.

[Too91] Owen B. Toon & Richard P. Turco. *Polar Stratospheric Clouds and Ozone Depletion*. Scientific American **264**, 6, (1991) 68.

[Tur05a] Lazlo. Turi, Wen-Shyan Sheu, & Peter J Rossky. *Characterization of Excess Electrons in Water-Cluster Anions by Quantum Simulations*. Science **309**, (2005) 914.

[Tur05b] Lazlo Turi, Wen-Shyan Sheu, & Peter J. Rossky. *Response to Comment on "Characterization of Excess Electrons in Water-Cluster Anions by Quantum Simulations"*. Science **310**, 5755, (2005) 1769. URL `http://www.sciencemag.org/content/310/5755/1769.3.abstract`.

[Ver97] R. W. Verhoef & M. Asscher. *The work function of adsorbed alkalis on metals revisited: a coverage-dependent polarizability approach*. Surface Science **391**, 1-3, (1997) 11 . URL `http://www.sciencedirect.com/science/article/B6TVX-412S0YX-K/2/0876fe852b2d92dad16ac71a02a3aa72`.

[Ver05a] J. R. R. Verlet, A. E. Bragg, A. Kammrath, O. Cheshnovsky, & D. M. Neumark. *Comment on "Characterization of Excess Electrons in Water-Cluster Anions by Quantum Simulations"*. Science **310**, 5755, (2005) 1769. URL `http://www.sciencemag.org/content/310/5755/1769.2.abstract`.

[Ver05b] J. R. R. Verlet, A. E. Bragg, A. Kammrath, O. Cheshnovsky, & D. M. Neumark. *Observation of Large Water-Cluster Anions with Surface-Bound Excess Electrons*. Science **307**, (2005) 93.

[Vil96] Ignacio Villegas & Michael J. Weaver. *Progressive cation solvation at Pt(111) model electrochemical interfaces in ultrahigh vacuum as probed by infrared spectroscopy and work-function measurements*. Electrochimica Acta **41**, 5, (1996) 661 . URL `http://www.sciencedirect.com/science/article/pii/0013468695003541`. Infrared Spectroscopy in Electrochemistry.

[Von06a] Tomas Vondrak, John M. C. Plane, & Stephen R. Meech. *Influence of submonolayer sodium adsorption on the photoemission of the Cu(111)/water ice surface*. The Journal of Chemical Physics **125**, 22, (2006) 224702. URL `http://link.aip.org/link/?JCP/125/224702/1`.

[Von06b] Tomas Vondrak, John M. C. Plane, & Stephen R. Meech. *Photoemission from Sodium on Ice: A Mechanism for Positive and Negative Charge Coexistence in the Mesosphere*. The Journal of Physical Chemistry B **110**, 9, (2006) 3860. URL `http://pubs.acs.org/doi/abs/10.1021/jp0571630`. PMID: 16509666.

[Von09] Tomas Vondrak, Stephen R. Meech, & John M. C. Plane. *Photoelectric emission from the alkali metal doped vacuum-ice interface*. The Journal of Chemical Physics **130**, 5, (2009) 054702. URL `http://link.aip.org/link/?JCP/130/054702/1`.

[Wan08] C.-R. Wang, K. Drew, T. Luo, M.-J. Lu, & Q.-B. Lu. *Resonant dissociative electron transfer of the presolvated electron to CCl_4 in liquid: Direct observation and lifetime of the ${CCl_4}^{*-}$ transition state*. The Journal of Chemical Physics **128**, 4, (2008) 041102. URL `http://link.aip.org/link/?JCP/128/041102/1`.

[Wea97] Michael J. Weaver & Ignacio Villegas. *Modeling Electrochemical Interfaces in Ultrahigh Vacuum: Influence of Progressive Cation and Surface Solvation upon Charge-Potential Double-Layer Behavior on Pt(111)*. Langmuir **13**, 25, (1997) 6836. URL `http://pubs.acs.org/doi/abs/10.1021/la970820y`.

[Weg09] Daniel Wegkamp. *Schnelle Elektronendynamiken an Grenzflächen untersucht mit einer NOPA-basierenden Femtosekunden-Lichtquelle*. Diplomarbeit, Freie Universität Berlin (2009).

[Yok98] Kazushige Yokoyama, Carlos Silva, Dong Hee Son, Peter K. Walhout, & Paul F. Barbara. *Detailed Investigation of the Femtosecond Pump-Probe Spectroscopy of the Hydrated Electron*. The Journal of Physical Chemistry A **102**, 35, (1998) 6957. URL `http://pubs.acs.org/doi/abs/10.1021/jp981809p`.

[Zal98] R.b Zallen. *The Physics of Amorphous Solids*. Wiley VCH, 1998.

[Zan88] A. Zangwill. *Physics at Surfaces*. Cambridge Iniversity Press, Cambridge, 1988.

[Zha03] Chang-Guo Zhan & David A. Dixon. *The Nature and Absolute Hydration Free Energy of the Solvated Electron in Water*. The Journal of Physical Chemistry B **107**, 18, (2003) 4403. URL `http://pubs.acs.org/doi/abs/10.1021/jp022326v`.

[Zha06a] Jin Zhao, Bin Li, Kenneth D. Jordan, Jinlong Yang, & Hrvoje Petek. *Interplay between hydrogen bonding and electron solvation on hydrated TiO_2(110)*. Phys. Rev. B **73**, 19, (2006) 195309.

[Zha06b] Jin Zhao, Bin Li, Ken Onda, Min Feng, & Hrvoje Petek. *Solvated Electrons on Metal Oxide Surfaces*. Chemical Reviews **106**, 10, (2006) 4402. URL `http://pubs.acs.org/doi/abs/10.1021/cr050173c`.

[Zha08] Jin Zhao, Niko Pontius, Aimo Winkelmann, Vahit Sametoglu, Atsushi Kubo, Andrei G. Borisov, Daniel Sánchez-Portal, V. M. Silkin, Eugene V. Chulkov, Pedro M. Echenique, & Hrvoje Petek. *Electronic potential of a chemisorption interface*. Phys. Rev. B **78**, 8, (2008) 085419.

[Zhu04] X.-Y. Zhu. *Charge Transport at Metal-Molecule Interfaces:A Spectroscopic View*. The Journal of Physical Chemistry B **108**, 26, (2004) 8778. URL `http://pubs.acs.org/doi/abs/10.1021/jp0370876`.

List of Publications

Publications within this thesis

M. Bertin, M. Meyer, J. Stähler, C. Gahl, M. Wolf, and U. Bovensiepen, *Reactivity of water-electron complexes on crystalline ice surfaces*, Faraday Discuss. **141** , (2009), pp 293 - 307.

M. Meyer, M. Bertin, U. Bovensiepen, D. Wegkamp, M. Krenz, and M. Wolf, *Ultrafast Dynamics at the Na/D_2O/Cu(111) Interface: Electron Solvation in Ice Layers and Na^+- Mediated Surface Solvation*, J. Phys. Chem. C, **115**(1), (2011), pp 204-209; DOI: 10.1021/jp107253g.

M. Meyer, U. Bovensiepen, and M. Wolf, *Stabilized excess electrons at alkali/water clusters*, in preparation.

Publications concerning other topics

J. Stähler, M. Mehlhorn, U. Bovensiepen, M. Meyer, D. O. Kusmierek, K. Morgenstern, M. Wolf *Impact of Ice Structure on Ultrafast Electron Dynamics in D_2O Clusters on Cu(111)*, Phys. Rev. Lett. **98**, 206105 (2007) pp. 1-4.

J. Stähler, M. Meyer, X.Y. Zhu, U. Bovensiepen, and M. Wolf *Dynamics of electron transfer at polar molecule-metal interfaces: The role of thermally activated tunnelling*, New J. Phys. **9**, 394 (2007) pp. 1-13.

J. Stähler, M. Meyer, D. O. Kusmierek, U. Bovensiepen, and M. Wolf *Ultrafast electron transfer dynamics at NH_3/Cu(111) interfaces: Determination of the transient tunneling barrier*, J. Am. Chem. Soc. **130**, 27 (2008) pp. 8797-8803.

M. Meyer, J. Stähler, D. O. Kusmierek, M. Wolf, and U. Bovensiepen *Determination of the electron's solvation site on D_2O/Cu(111) using Xe overlayers and femtosecond photoelectron spectroscopy*, Phys. Chem. Chem. Phys. **10**, (2008) pp. 4932-4938.

J. Stähler, U. Bovensiepen, M. Meyer, and M. Wolf *A Surface Science Approach To Ultrafast Electron Transfer and Solvation Dynamics at Interfaces*, Chem. Soc. Rev **37** (10), (2008) pp. 2180 - 2190.

U. Bovensiepen, C. Gahl, J. Stähler, M. Bockstedte, M. Meyer, F. Baletto, S. Scandolo, X.-Y. Zhu, A. Rubio, M. Wolf *A dynamic landscape from femtoseconds to minutes for excess electrons at ice-metal interfaces*, J. Phys. Chem. C **113** (3), (2009); pp. 979–988.

J. Stähler, M. Meyer, U. Bovensiepen, M. Wolf *Solvation dynamics of surface-trapped*

electrons at NH_3 and D_2O crystallites adsorbed on metals: From femtosecond to minute timescales, Chemical Science **2** (6), (2011); pp. 1644-1673; DOI: 10.1039/C0SC00644K.

Academic curriculum vitae

The curriculum vitae is omitted in this online version due to data privacy.

Acknowledgments

Während eines so komplexen und langwierigen Projekts wie einer Promotion gibt es zum Glück viele Menschen, die einen unterstützen und es einem ermöglichen, diese Arbeit erfolgreich abzuschließen. Diesen Menschen möchte ich an dieser Stelle danken.

Zuerst möchte ich mich bei Martin Wolf bedanken, der es mir ermöglicht, hat nach meiner Diplomarbeit auch noch meine Doktorarbeit in seiner Arbeitsgruppe durchzuführen. Sein Engagement und seine Begeisterung für die Physik ermöglichten ein wissenschaftliches Arbeiten unter exzellenten Rahmenbedingungen. Gerade in der Endphase meiner Arbeit war er eine große Unterstützung. Diskussionen mit ihm waren immer sehr fordernd, aber auch bereichernd.

Martin Weinelt danke ich für seine Bereitschaft, mein Zweitgutachter zu werden und für sein Interesse an meiner Arbeit. Er hatte immer ein offenes Ohr für meine Fragen und offenbar kaum enden wollende gute Laune.

Uwe Bovensiepen war mein Betreuer und bevor er nach Duisburg ging, auch mein Büronachbar. Ich danke ihm für seine tolle Unterstützung, die er mir über die ganze Zeit meiner Arbeit gegeben hat. Es war immer sehr erhellend und motivierend mit ihm zu diskutieren und von seinem großen Wissen zu profitieren. Und ja, das mit dem zweiten Pinhole Doser bin ich dir bisher wohl noch schuldig geblieben. Aber man soll die Hoffnung ja nie aufgeben.

Petra Tegeder danke ich dafür, dass sie mir nach dem Wegzug von Uwe und Martin Asyl gewährt hat, sowohl was mein Experiment angeht als auch einen Platz für meinen Schreibtisch und mich. Deine freundliche und hilfsbereite Art und deine Bereitschaft meine Fragen zu beantworten, die jetzt auf Dich als erste zukamen, hat die Anwesenheit in deiner Arbeitsgruppe sehr angenehm gemacht.

Julia Stähler danke ich an dieser Stelle auch noch einmal. Sie hat mich damals in das 2PPE Labor eingeführt und hat meine Fragen zu dem Experiment und den wissenschaftlichen Fragestellungen mit viel Geduld und Wissen beantwortet.

Mathieu Bertin worked the first year on the new projects in the lab with me as a post doc and we had a very good and efficient time. I thank you for your enthusiasm, for science you shared with me, for your good mood, for reading this manuscript, and a little less for your ”wonderful” singing.

Felix Leyßner danke ich dafür, dass wir seit der 1.Klasse unseren beruflichen Werdegang zusammen bestreiten und so auch schon seit 25 Jahren gute Freunde sind. Du hast mir geholfen, doch immer weiter zu machen und Spaß an der Arbeit zu haben. Mal gucken, wie es so weiter geht.

Dank gebührt natürlich auch Dietgard Mallwitz und Peter West, die die guten Seelen der AG Wolf waren und sind. Beide waren eine große Hilfe bei der Bewältigung der organisatorischen Aufgaben an der Uni und es war immer schön, mit euch ein kleines Pläuschchen zu halten.

Ich möchte mich auch bei allen anderen ehemaligen und aktuellen Mitgliedern der AG Wolf und AG Tegeder bedanken, mit denen ich zusammenarbeiten durfte. Von den "alten Hasen" Patrick Kirchmann, Sebastian Hagen und Marcel Krenz habe ich viel gelernt, sie waren stets hilfsbereit und haben für eine gute Atmosphäre im Labor gesorgt. Dank geht auch an die aktuelle Besetzung, Lea Bogner, Chris Bronner, meinen Bruder Stephan Meyer, Laurenz Rettig, Michael Schulze und Erwan Varene, für die gute und freundliche Arbeitsatmosphäre und für unterhaltsame Mittags-, Kaffee- und sonstige Pausen.

Ein riesen großes Dankeschön gebührt meiner Familie, die immer an mich geglaubt hat und mich immer unterstützt hat. Ich danke meinen Eltern, dass sie es mir ermöglicht haben, diesen Weg zu gehen. Danken möchte ich hier auch noch mal meinem Bruder Stephan für seine Unterstützung und für das Korrekturlesen meiner Arbeit. Ich danke meiner geliebten Marie für alles und ich freue mich darauf, was das Leben als nächstes für uns bringt. Auch meiner kleinen Ida danke ich. Obwohl sie mir auch viele sehr kurze Nächte beschert hat, hat ihr Lachen und ihre Liebe mich so oft wieder aufgebaut und glücklich gemacht.